DEVELOPMENT AND EXPLOITATION OF GPS ATTITUDE DETERMINATION FOR MICROSATELLITES

Thesis Submitted for the Degree of Doctor of Philosophy

Stuart Duncan

University of Surrey,

Surrey Space Centre

Academic Supervisor: Dr Stephen Hodgart
Industrial Supervisor: Dr Martin Unwin

June 2010

Abstract

In this research a robust real-time GPS attitude determination sensor has been developed and implemented onboard an SSTL SGR-20 GPS receiver in Low Earth Orbit.

To permit the development of this new attitude sensor the performance factors and measurement errors, such as receiver noise, line bias and multipath that effect GPS attitude determination were analysed using data logged in Low Earth Orbit.

A new integer ambiguity algorithm was developed that requires no *a priori* information regarding the attitude of the platform and is designed to operate in real-time onboard the SGR-20 GPS receiver. The algorithm uses the known length of the antenna baselines in conjunction with a series of pre-calculated statistical thresholds to rapidly eliminate many false integer ambiguities. The design of the algorithm allows the GPS satellites to rise and set whilst performing a multi-epoch comparison. The algorithm was tested using both Monte-Carlo simulation and through the post-processing of in-orbit data. The results of this testing showed that the new algorithm is robust in the presence of GPS measurement errors; it can solve the integer ambiguities during large angle manoeuvres and is fast enough to run in real-time onboard the SGR-20 GPS receiver.

Once the integer ambiguities are solved a double-difference point solution algorithm was used to estimate the attitude. The performance of this algorithm on real data logged in-orbit is demonstrated, including tracking of large angle manoeuvres. The various performance factors affecting GPS attitude on a microsatellite are also analysed.

A new version of flight software for the SGR-20 was developed that enables real-time stand-alone GPS attitude determination. In-orbit results demonstrate that the GPS attitude solution on Topsat had an expected accuracy of around 1 degree RMS, with increased availability with respect to other spacecraft attitude sensors such as sun-sensors, magnetometers and Earth horizon sensors.

Acknowledgements

This research has been supported by the EPSRC, the Location and Timing Knowledge Transfer Network, Surrey Satellite Technology Limited and the University of Surrey. The Topsat microsatellite mission was funded by the UK MOD and built by a consortium of UK companies including QinetiQ, Surrey Satellite Technology Limited, Rutherford Appleton Laboratories and Infoterra. I acknowledge the support of this consortium in allowing the GPS attitude experiments to be conducted on the Topsat microsatellite.

I would like to thank my academic supervisor Dr Stephen Hodgart for his assistance in suggesting paths to research and increasing my understanding of statistical theory. I would also like to thank my industrial supervisor Dr Martin Unwin, whose enthusiasm for developing the SSTL SGR GPS receivers resulted in the unique opportunity to develop and test my algorithms using in-orbit hardware. His support was vital in gaining the permission to use the SGR-20 on Topsat for this work.

The ground operations team at SSTL provided invaluable assistance throughout this work. In the early stages of this work, James Wilhelm and Neville Bean assisted my work on planning experiments for Bilsat, as well as answering my many questions about satellite operations. I am particularly indebted to Richard Hebden who kindly scheduled most of the experiments on Topsat, mostly in his free time. Without Richard's support and patience the in-orbit experiments would not have been possible.

My work colleagues Paul Blunt, Rob Myatt and Reynolt De Vos Van Steenwijk have also supported me in a number of ways throughout this work. They have aided my research by providing a useful sounding board for receiver related discussions, as well as providing assistance in learning the flight software so that the real-time attitude experiment could be implemented.

Last, but not least, I wish to thank my wife Daisy for her endless support and encouragement throughout the time spent on this research.

Contents

List of Acronyms

ADCS	Attitude Determination and Control System
ADOP	Attitude Dilution of Precision
EHS	Earth Horizon Sensor
FOV	Field of View
GNSS	Global Navigation Satellite System
GPS	Global Positioning System
IAR	Integer Ambiguity Resolution
IGRF	International Geomagnetic Reference Field
IMU	Inertial Measurement Unit
LEO	Low Earth Orbit
LNA	Low Noise Amplifier
LOS	Line of Sight
MCAD	Mechanical Computer Aided Design
OBC	Onboard Computer
PDOP	Position Dilution of Precision
PLL	Phase-Locked-Loop
PRN	Pseudo Random Noise
PVT	Position, Velocity and Time
QEKF	Quaternion Extended Kalman Filter for ADCS attitude system
RF	Radio Frequency
RMS	Root Mean Squared
SGR	Space GPS Receiver
SLSE	Scalar Least Squares Estimation
SNR	Signal to Noise Ratio
SSTL	Surrey Satellite Technology Ltd
SSC	Surrey Space Centre
SV	Space Vehicle
TTFA	Time To First Attitude
TTFF	Time To First Fix

List of Symbols

Hat Notations:

$\tilde{x}$	trial x
$\hat{x}$	estimated/predicted x
$\bar{x}$	measured x
$\breve{x}$	nominal x
x	true x

Subscript Notations:

$(\text{sub})_{(B)}$	with respect to spacecraft body-defined coordinates
$(\text{sub})_{(O)}$	with respect to orbit-defined coordinates
$(\text{sub})_{i}$	index to baseline
$(\text{sub})_{j}$	index to measurement/satellite

GPS Attitude Parameters:

$\mathbf{s}$	single-difference line-of-sight (LOS) vector to GPS satellite
$\mathbf{v}$	double-difference line-of-sight (LOS) vector
$\mathbf{b}$	baseline vector
λ_{L1}	GPS carrier wavelength at L_1 frequency 1.57542 GHz
α	angle between baseline vector and line-of-sight vector to GPS satellite

GPS Measurements:

φ	fractional carrier phase difference, in cycles
$\vec{r}$	path difference, in cycles
$\bar{r}$	measured single-difference accumulated carrier phase, in cycles
r	true single-difference accumulated carrier phase, in cycles
$\Delta\bar{r}$	measured double-difference accumulated carrier phase, in cycles
Δr	true double-difference accumulated carrier phase, in cycles
i	index to baseline vector
j	index to measurement for a GPS satellite
J	total number of measurements
k	index to epoch in which measurements were taken
K	total number of epochs
v	receiver noise
u	multipath
w	total measurement noise
β	line bias
β^*	effective line bias
N	integer ambiguity
B_n	noise bandwidth
C/N_0	carrier to noise density ratio

ω	GPS measurement residual
T_{int}	integration time of loop filter
$\Delta\varphi$	carrier phase shift (due to multipath)

Integer Ambiguity Resolution:

$\mathbf{R}$	covariance matrix of GPS measurements
$\mathbf{P}$	state covariance matrix
$\mathbf{H}$	observation matrix
$\mathbf{H}_p$	observation matrix for primary set of measurements
$\mathbf{D}$	design matrix for selecting integers in float solution
$\Delta\rho$	double-difference code-phase (pseudorange) measurement
Ω	weight least-squares cost
λ_p	parameter used in baseline vector estimation
$a_{p,q}$	co-efficient used in baseline vector estimation
$\mathbf{b}_\perp$	component of baseline vector normal to the plane
ε_{ML}	maximum likelihood cost
x_j	real-valued estimate for double-difference carrier phase ambiguity
z	number of standard deviations from mean
t	threshold for confidence interval
m	index to list of trial integer ambiguity solutions
M	number of trial integer ambiguity solutions
d_j	ambiguity residual

Mathematical Notation and Operators:

$(\text{sup})^{\times}$	anti-symmetric matrix
tr	trace of matrix
$(\text{sup})^{\text{T}}$	transpose of matrix
det	determinant of matrix
$\times$	vector cross product
$\bullet$	vector dot product
$\lVert\ \rVert$	vector norm
$\lvert\ \rvert$	absolute value for scalar
$\langle\ \rangle$	expected value
$\mathbf{1}$	Identity matrix

Attitude Representations and Rate Parameters:

$\mathbf{A}$	attitude transformation matrix from orbit-defined coordinates to spacecraft body-defined coordinates
$\hat{\mathbf{A}}_{ADCS}$	attitude matrix computed by ADCS
$\delta\mathbf{A}$	attitude correction matrix
ϕ	roll angle
θ	pitch angle

ψ	yaw angle
$\mathbf{q}$	quaternion vector
$\Delta\xi$	attitude error vector
$\mathbf{\Delta}$	constant rotational error of ADCS reference frame
$\boldsymbol{\alpha}$	attitude controller noise
$\boldsymbol{\delta}$	attitude measurement noise

List of Figures

List of Tables

1 Introduction

This chapter provides a brief history and context to the research presented in this thesis, including some background on the contributing parties. Following this, a short description of the content in the subsequent chapters of this report is given.

1.1 The CASE PhD studentship

The CASE PhD studentship was created by the Electrical and Physical Sciences Research Council (EPSRC) to promote collaboration between industry and academia through research with common goals. The EPSRC set up a number of special interest groups to develop the link between industry and academia for a specific subject area. The CASE studentship was partially funded by the Pinpoint Faraday partnership which is specifically interested in research into the applications of the Global Navigation Satellite Systems (GNSS). During the course of this research Pinpoint Faraday was renamed the Location and Timing Knowledge Transfer Network.

The goals of the research conducted under the CASE studentship are expected to satisfy both the industrial and academic partners. For this reason the CASE projects tend to involve more practical work than the traditional theoretical PhD. The industrial partner of this CASE studentship was Surrey Satellite Technology Ltd (SSTL). SSTL was formed as a spin-off company from the University of Surrey inn 1985. Since then SSTL has been involved in over thirty-five satellite missions and is the world leader in supplying small satellite platforms. SSTL manufactures its own range of GNSS receivers which are operated on-board SSTL satellites and supplied externally as sub-systems.

The academic partner, Surrey Space Centre, specialises in all areas of space research at the University of Surrey. Surrey Space Centre works closely with SSTL on many projects, providing both practical and blue-skies research to aid SSTL in maintaining its position as leader in the world of small satellites and to help in the goal of changing the economics of space.

1.2 GPS attitude determination

In the 1990s the use of interferometric GPS carrier phase measurements for attitude determination was the subject of much research, and was of particular interest for use onboard spacecraft. Much research was conducted into the various aspects of GPS attitude determination such as integer ambiguity resolution, satellite selection and mitigation of errors.

Interest in the area peaked around 1994 with much research published at the conferences that year, but then tailed off with little effort on the subject in recent years. In the mid 1990s ESA contributed towards the development of the SGR-20, a specifically designed GPS attitude receiver, at SSTL. The SGR-20 flew on UoSat-12 as a GPS attitude validation experiment.

The UoSAT-12 experiment was the basis for two previous PhDs at the University of Surrey. The first PhD by Somphop Purivigraipong analysed data from the UoSAT-12 experiment and showed that in principle it was possible to determine attitude from GPS carrier phase measurements. His thesis highlighted the problems of integer ambiguity resolution and multipath, but didn't tackle either subject conclusively.

The problem of multipath was looked at in a later PhD by Ronald Wong, who used the data collected on UoSAT-12 to construct a spherical harmonic based multipath calibration map. The results of this work showed that the map could describe the multipath in a given direction to within 1.0mm, and so potentially mitigate most of the multipath error present on UoSAT-12.

While it was shown possible to construct a multipath mitigation map for calibrating a GPS attitude sensor, no robust method for solving the integer ambiguity problem was available. In order to have a useable sensor in space the whole GPS attitude system must be made robust. Other factors such as optimal satellite selection, real-time operation of the algorithms and the need for real-time validation must be considered.

This thesis describes the work carried out to develop and exploit GPS attitude determination for use on microsatellites. This research aims to build on the work done by Purivigraipong and Wong so that GPS attitude determination could be exploited by SSTL for use on their small satellite platforms. In the original scope for this PhD it was expected to use a number of microsatellites for conducting GPS attitude experiments. By the start of this PhD UoSat-12 was no longer operational, but Bilsat-1 was launched in October 2004, carrying an SGR-20 and a star-camera for the attitude reference. Unfortunately, due to technical problems only a couple of experiments were carried out on Bilsat-1 before it became inoperable in 2005. In November 2005, Topsat was launched carrying an SGR-20, but it was not until February 2007, after the main imagery mission had achieved its goals, that GPS attitude experiments were permitted on Topsat.

1.3 Outline of thesis

This thesis consists of eight chapters with the following content.

Chapter 2 provides the necessary background information for understanding the problems inherent in GPS attitude determination. The general concepts and terminology used throughout the thesis are introduced. An overview of past research into GPS attitude determination is provided via a review of the literature on the subject. A historical review of GPS attitude experiments on spacecraft is also provided. Chapter 2 also details the mathematical models used to study and use GPS carrier phase measurements for attitude determination. The measurement model used to relate GPS carrier phase measurements to the attitude of a spacecraft is discussed, and the important error terms are explained. Methods for solving for attitude using GPS measurements are described and the concept of dilution of precision is discussed. Other factors that affect the performance of GPS attitude determination are also described.

Chapter 3 provides an analysis of real data logged on an SGR-20 flown on the Topsat microsatellite. Firstly the onboard reference attitude from the Attitude Determination and Control System (ADCS) is discussed. Next, the ADCS reference attitude is used to estimate the GPS antenna baselines to determine if they differ from the vectors measured from the mechanical drawings of the satellite. Following this, the GPS carrier phase measurement residuals are used to estimate the measurement noise observed by the SGR-20 on Topsat. The disparity between the GPS carrier phase measurements and predicted measurements from the ADCS are also analysed. This was done to provide a comparison between the GPS and ADCS and to look for potential systematic errors in either system. The GPS residuals are then used to demonstrate the presence of multipath in the GPS carrier phase measurements. Finally the issue of line bias is examined, and the ADCS reference attitude is used to estimate the line bias for a number of experimental data sets to determine if there is an analytical solution to the line bias problem. A brief analysis of the satellite visibility in Low Earth Orbit is also given.

Chapter 4 examines the problem of integer ambiguity resolution. An overview of the main issues relating to integer ambiguity resolution is given and the problems specific to integer ambiguity resolution on a microsatellite are discussed. The suitability of previous methods from the literature, including the standard 'Least Squares Ambiguity Decorrelation Adjustment' (LAMBDA) method, for use on microsatellites and specifically on the SGR-20 receiver is discussed. A new method for integer ambiguity resolution using only six single-frequency GPS carrier phase measurements per baseline, and short time-spans of data is then developed.

Chapter 5 details the simulation and testing of the new integer ambiguity resolution algorithm. A MATLAB based simulator (described in Appendix A) is used to test the robustness of the new integer ambiguity resolution algorithm for different levels of receiver noise and multipath. Realistic levels of measurement noise are simulated based on the results of the analysis of spaceflight data performed in Chapter 3. The performance of the new algorithm is analysed in detail, including a break down of the performance at each stage of the algorithm to identify any weaknesses or instabilities in the proposed method. Following this, real GPS measurements logged on a number of in-orbit experiments on the Topsat microsatellite are used to demonstrate the real-life performance of the algorithm. The robustness of the new algorithm when subjected to the subtleties of processing measurements from a real GPS receiver is analysed, and the ability of the algorithm to solve for the integer ambiguities even during large angle manoeuvres is demonstrated.

Chapter 6 contains a short study on a number of performance factors affecting GPS attitude determination. The effect of baseline geometry on the Attitude Dilution of Precision (ADOP) is studied and the potential attitude accuracy of a GPS attitude receiver that can track all satellites in view is demonstrated via simulation. The second issue studied is the use of the ADCS to initialise the line bias estimate. It is shown that this can lead to systematic offsets in the ADCS also being present in the GPS attitude solution. This removes the potential advantage of GPS attitude as a stand-alone attitude sensor. The third performance factor is the effect of the elevation mask on the number of visible satellites. A numerical simulation is used to demonstrate that at least eight satellites are visible at all times and therefore the SGR-20 on Topsat should be able to track six satellites on each baseline in every epoch.

Finally, post-processing of the data logged in-orbit is used to demonstrate the potential performance of GPS attitude determination on Topsat.

Chapter 7 covers the implementation and testing of the real-time attitude determination flight software on the SGR-20. An overview of the software changes made to the SGR-20 flight code is provided. The method used for implementing and testing the new software is discussed. Finally stand-alone GPS attitude determination is demonstrated using an SGR-20 on Topsat via a number of real-time in-orbit experiments. The real-time attitude determination results are analysed to highlight a number of issues raised by the in-orbit experiments and the results are compared with the ADCS reference attitude.

Chapter 8 discusses the outcomes of this research and what it means for future use of GPS attitude determination on small satellites. The contributions made by this research are detailed and proposals for future work are listed.

Appendix A details the implementation of a MATLAB based simulator which uses the knowledge gained from the analysis of the space-flight data to recreate more accurately the measurement environment experienced on Topsat.

Appendix B provides a description of the 'Attitude Determination using the Standard Method' (ADSM) integer ambiguity resolution technique devised by Dr Hodgart on which the robust integer ambiguity resolution algorithm detailed in Chapter 4 is based.

Appendix C describes the procedure for rotating between the WGS-84 frame in which the GPS Navigation solution is based and the Orbit-Referenced Frame (ORF) used for GPS attitude determination.

Appendix D contains a list of all the GPS attitude experiments conducted on Topsat to date, including which sensors were used for the ADCS; the manoeuvres conducted; settings relevant to the GPS attitude algorithms such as the elevation mask used as well as a description of the mode of operation of the SGR-20.

Appendix E provides details of the new SBPP commands and packets implemented on the SGR-20 in order to control the real-time attitude determination algorithms and log the results.

1.4 Research Motivation

Attitude determination on microsatellites is normally achieved via a combination of sensors which are combined via a filter to provide a three-axis attitude estimate. The application of GPS attitude determination on a microsatellite platform permits real-time kinematic three-axis attitude information from a single-sensor, whilst requiring minimal additional hardware and minimal additional cost. Previous work, including a number of experiments in space, has shown that GPS attitude determination is feasible, but these experiments either did not demonstrate onboard processing or used proprietary algorithms which were not published in the literature.

If GPS attitude determination can be proven to be both robust and accurate on small satellites also, then it could potentially be employed on all future small satellites in order to augment or replace some of the other attitude sensors discussed in this chapter. Since a GPS receiver is typically flown on every small satellite mission there would be minimal additional cost or mass penalty from using GPS attitude determination. If GPS was used to augment current attitude sensors then it could act as a back-up in the case of other attitude sensors failing, or could potentially be used to enable low cost missions where attitude information is required throughout the whole orbit – such as Synthetic Aperture Radar missions. If GPS attitude was used to replace other attitude sensors then there would be savings in both cost and mass which would permit the savings to be used for the main payload or additional payloads.

It is important to note that even if the accuracy of the GPS attitude solution were no better than the standard sun-sensor and magnetometer combination used on most SSTL satellites, it may provide a beneficial augmentation or replacement. The GPS attitude solution has a number of advantages over the sun-sensor and magnetometer combination. These advantages include:

- Increased availability since sun-sensors do not work during eclipse and magnetometers have problems over the Earth's poles.
- A more consistent attitude solution since the errors affecting the GPS attitude solution are a fixed function of the receiver and spacecraft (i.e. receiver noise and multipath)
- The GPS attitude solution provides a three-axis attitude solution from a single sensor.
- To provide a GPS attitude capability only requires two additional GPS antennas and the fitting of the additional RF front ends, thereby saving on the mass and cost of the hardware required for sun-sensors and magnetometers.

The SGR-20 GPS receiver on Topsat provides a unique opportunity to develop and test new algorithms for GPS attitude determination. Proving that GPS attitude determination can operate reliably and in real-time onboard an operational imaging satellite should aid the acceptance of the technology and it is hoped lead to its inclusion in the baseline for future small satellite missions. This should also increase support for the development of future GNSS attitude receivers to take advantage of the Galileo and Modernized GPS constellations once they are operational which should improve the performance and availability of GPS attitude.

1.5 Research Aims

The aim of this research was to use the Topsat microsatellite, launched in October 2005, to demonstrate and exploit GPS attitude determination for a useful purpose on a microsatellite.

The specific goals of this research are as follows:

1. Analysis of spaceflight data from a small satellite, including quantification of measurement errors such as line bias error, multipath and receiver noise.

2. Design and implementation of a robust integer ambiguity resolution technique for single frequency single epoch GPS measurements.
3. Analysis of the performance factors affecting GPS attitude determination on small satellites.
4. Implementation of a robust real time onboard GPS attitude determination system based on the SGR-20.
5. Demonstration of real-time in-orbit GPS attitude determination on a microsatellite, and comparison of the GPS attitude solution with the ADCS reference attitude.

2 Background

In this chapter the necessary background information for understanding the GPS attitude determination problem is covered. The concept of attitude is defined, along with a definition for the different reference frames used in this work.

An overview of current attitude sensors used on small satellites is provided with a brief description of each sensor's advantages and disadvantages. The fundamentals of using GPS measurements to determine attitude are then explained. The measurement model used to describe the GPS measurements is defined, including the various error sources that affect GPS measurements. Methods for estimating attitude based on this measurement model are also described.

Details of the hardware used during this thesis are given, including the limitations it imposes on the work. An explanation of how the GPS receiver hardware provides the measurements necessary for attitude determination is provided.

A literature review is undertaken to provide context for this research and highlight areas worthy of further study. The history of space-based GPS attitude experiments is documented, and information on the microsatellites used for SSTL's GPS attitude experiments is also given. Finally the motivation for this research, the research aims and the contributions from this research are discussed.

2.1 Attitude

Most small satellite missions, particularly Earth Observation missions, require precise knowledge of the orientation of the satellite body with respect to a reference frame, for example the surface of the Earth being imaged. The orientation of the body of the satellite with respect to a reference frame is known as the *attitude* of the satellite. The definition of the attitude is given below.

2.1.1 Coordinate systems

The *orbit-defined* coordinate system is a system of coordinates that maintains its orientation relative to the Earth as the spacecraft moves in its orbit [Wertz, 1978]. An orthogonal triad of vectors, denoted $\mathbf{X}_O$, $\mathbf{Y}_O$ and $\mathbf{Z}_O$ defines the reference axes in the orbit-defined coordinate system. Roll, pitch and yaw are defined as right-handed rotations about these three axes, with roll corresponding to a rotation about the $\mathbf{X}_O$ axis, pitch a rotation about the $\mathbf{Y}_O$ axis and yaw a rotation about the $\mathbf{Z}_O$ axis.

Since the orientation of the axes remains fixed relative to the Earth, they are defined in the following way. The $\mathbf{Z}_O$, or yaw axis, is directed towards the centre of the Earth (nadir), the $\mathbf{Y}_O$ or pitch axis is directed toward the negative orbit normal, and the $\mathbf{X}_O$ or roll axis completes the orthogonal set.

A second set of vectors, $\mathbf{X}_\mathrm{B}$, $\mathbf{Y}_\mathrm{B}$, $\mathbf{Z}_\mathrm{B}$ define a second coordinate system termed the *body-fixed* coordinate system that is defined relative to the spacecraft body itself.

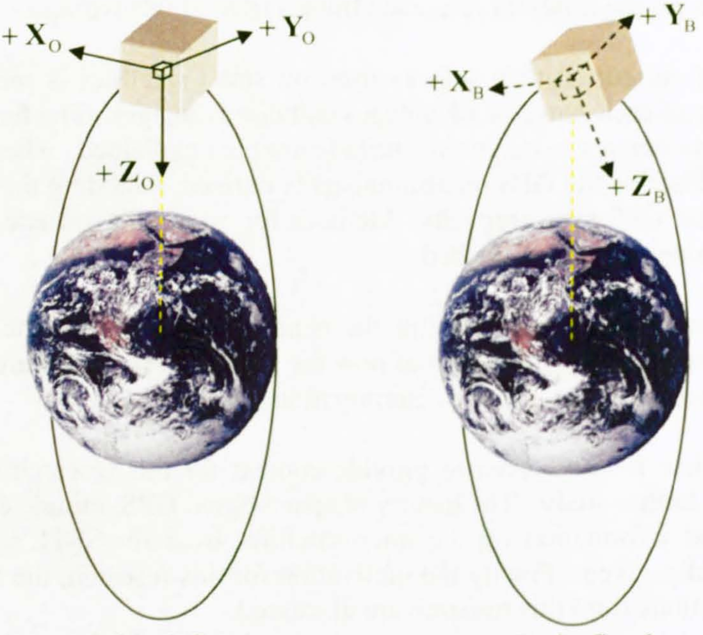

Orbit-defined coordinate system

Body-fixed coordinate system

Figure 2-1 Coordinate system definition

The attitude of the spacecraft is the orientation of the body-fixed coordinate system relative to the orbit-defined coordinate system. It can be described in a number of ways, which are discussed in detail in [Wertz, 1978] and adapted below.

2.1.2 Attitude representations

A common method for describing the attitude of a rigid body is the *direct cosine matrix* or *attitude matrix*. This matrix is a coordinate transformation matrix that maps vectors from the reference frame to the body frame. If $\mathbf{a}_\mathrm{O}$ is a vector with components a_1, a_2, and a_3 in the orbit-defined coordinate system, then

$$\mathbf{A}\mathbf{a}_\mathrm{O} = \begin{bmatrix} u_1 & u_2 & u_3 \\ v_1 & v_2 & v_3 \\ w_1 & w_2 & w_3 \end{bmatrix} \begin{bmatrix} a_1 \\ a_2 \\ a_3 \end{bmatrix} = \begin{bmatrix} a_u \\ a_v \\ a_w \end{bmatrix} = \mathbf{a}_\mathrm{B} \qquad \text{2-1}$$

where $\mathbf{a}_\mathrm{B}$ is the same vector in body-fixed coordinates. The direct cosine matrix can be parameterised in a number of ways, the most common being Euler Angles and Euler Symmetric Parameters or *Quaternions*. These are described below.

2.1.2.1 Euler Angles

The direct cosine matrix can be parameterised in terms of three rotation angles, commonly known as Euler angles. This allows the orientation of the spacecraft to be defined in terms of three angles: roll, pitch and yaw as defined in the explanation of the coordinate systems above. The spacecraft body-fixed coordinate system is rotated to the orbit-defined coordinate system using three consecutive right-hand positive rotations.

The rotations are defined about the three axes $\mathbf{X}_O$, $\mathbf{Y}_O$ and $\mathbf{Z}_O$, and can be described by the following rotation matrices

$$\mathbf{R}_X(\phi)=\begin{bmatrix}1 & 0 & 0\\ 0 & \cos\phi & \sin\phi\\ 0 & -\sin\phi & \cos\phi\end{bmatrix} \tag{2-2}$$

$$\mathbf{R}_Y(\theta)=\begin{bmatrix}\cos\theta & 0 & \sin\theta\\ 0 & 1 & 0\\ -\sin\theta & 0 & \cos\theta\end{bmatrix}$$

$$\mathbf{R}_Z(\psi)=\begin{bmatrix}\cos\psi & \sin\psi & 0\\ -\sin\psi & \cos\psi & 0\\ 0 & 0 & 1\end{bmatrix}$$

where ϕ, θ and ψ represent the rotation angles about the roll, pitch and yaw axes respectively. These rotation matrices can be combined into a single matrix by finding their product. There are six permutations. For example, the 2-1-3 sequence is defined by a rotation θ about the pitch axis $\mathbf{Y}_O$, followed by a rotation ϕ about the roll axis $\mathbf{X}_O$, followed by a rotation ψ about the yaw axis $\mathbf{Z}_O$.

This gives

$$\mathbf{A}_{213}(\phi,\theta,\psi)=\mathbf{R}_Y(\theta)\mathbf{R}_X(\phi)\mathbf{R}_Z(\psi) \tag{2-3}$$

or

$$\mathbf{A}=\begin{bmatrix}\cos\psi\cos\theta+\sin\psi\sin\phi\sin\theta & \sin\psi\cos\phi & -\cos\psi\sin\theta+\sin\psi\sin\phi\cos\theta\\ -\sin\psi\cos\theta+\cos\psi\sin\phi\cos\theta & \cos\psi\cos\phi & \sin\psi\sin\theta+\cos\psi\sin\phi\cos\theta\\ \cos\phi\sin\theta & -\sin\phi & \cos\phi\cos\theta\end{bmatrix} \tag{2-4}$$

The 2-1-3 Euler angles can be obtained from the elements of the attitude matrix, $\mathbf{A}$, by

$$\phi=\sin^{-1}(-\mathbf{A}_{3,2}) \qquad \theta=\tan^{-1}\left(\frac{\mathbf{A}_{3,1}}{\mathbf{A}_{3,3}}\right) \qquad \psi=\tan^{-1}\left(\frac{\mathbf{A}_{1,2}}{\mathbf{A}_{2,2}}\right) \tag{2-5}$$

There is a two-fold ambiguity in ϕ, corresponding to $\sin\phi$ being positive or negative. This ambiguity is resolved by choosing $0 \leq \phi < 180$ degrees, which allows θ and ψ to be determined uniquely (modulo 360 degrees) unless ϕ is a multiple of 180 degrees when only the sum or difference of θ and ψ can be determined.

A second group of Euler angle rotations uses only two of the axes and one of which is necessarily used twice, resulting in another six permutations. Classically the most well-known is the 3-1-3 sequence of rotations which is closely identified with the natural motions of an axially symmetric body nutating in gravity free space.

2.1.2.2 Quaternions

A more fundamental means of defining an attitude is in terms of an Euler axis and angle parameterization. On completion of an attitude rotation there is one specific axis, the unit Euler axis $\mathbf{e}$, whose components are the same in both reference and body-axis coordinates. A rotation ϕ about this axis is all that is needed then to complete the description.

Quaternions or Euler Symmetric Parameters provide a convenient parameterization of the attitude based on the Euler axis and angle. They are defined by

$$\mathbf{q} = \begin{bmatrix} \mathbf{e}\sin(\phi/2) \\ \cos(\phi/2) \end{bmatrix} = \begin{bmatrix} q_1 & q_2 & q_3 & q_4 \end{bmatrix}^T \tag{2-6}$$

The four parameters are not independent, but satisfy the constraint equation

$$\mathbf{q}^T\mathbf{q} = q_1^2 + q_2^2 + q_3^2 + q_4^2 = 1 \tag{2-7}$$

The direct cosine matrix can be expressed in terms of quaternions according to:

$$A(\mathbf{q}) = \begin{bmatrix} q_1^2 - q_2^2 - q_3^2 - q_4^2 & 2(q_1q_2 + q_3q_4) & 2(q_1q_3 - q_2q_4) \\ 2(q_1q_2 - q_3q_4) & -q_1^2 + q_2^2 - q_3^2 + q_4^2 & 2(q_2q_3 + q_1q_4) \\ 2(q_1q_3 + q_2q_4) & 2(q_2q_3 - q_1q_4) & -q_1^2 - q_2^2 + q_3^2 + q_4^2 \end{bmatrix} \tag{2-8}$$

Quaternions have found widespread use in spacecraft work due to the numerous advantages they provide over other methods:

1. They avoid the singularities of trigonometric functions.
2. They are more convenient than other parameterizations such as the Euler axis and angle method, because they do not require the use of trigonometric functions.
3. They are more compact than the direct cosine matrix because only four parameters are needed instead of nine (when storing the full direct cosine matrix).

4. The algebra associated with combining multiple rotations is relatively straight-forward. The product of two rotations:

$$A(\mathbf{q}'') = A(\mathbf{q}')A(\mathbf{q}) \qquad \textbf{2-9}$$

then

$$\mathbf{q}'' = \begin{bmatrix} q_4' & q_3' & -q_2' & q_1' \\ -q_3' & q_4' & q_1' & q_2' \\ q_2' & -q_1' & q_4' & q_3' \\ -q_1' & -q_2' & -q_3' & q_4' \end{bmatrix} \mathbf{q} \qquad \textbf{2-10}$$

2.2 *Attitude sensors found on small satellites*

Spacecraft attitude determination depends on attitude sensors, the selection of which depends on the required pointing mode of the mission (e.g. inertial or Earth pointing), the required accuracy, the spacecraft's power budget and cost.

The first SSTL satellites - the UoSAT series - achieved adequate attitude control using only a passive gravity-gradient boom and active magnetic torquing [Hodgart, 1982], [Hodgart, 1989], [Hodgart *et al.*, 1997], [Steyn and Hashida, 1999]. Since the launch of UoSat-12 SSTL has changed its approach to using reaction wheels, cold-gas thrusters and magnetorquers as the primary actuators.

Currently, small satellites tend to use a combination of sensors to provide attitude knowledge. More accurate sensors are now deployed including sun-sensors, Earth Horizon sensors and Star Trackers. The performance of each sensor is outlined and a brief description given in the following sections.

2.2.1 Sun-sensors

Sun-sensors are the most widely used sensor type for attitude determination on spacecraft. Sun-sensors measure the angle or vector to the Sun in body-fixed coordinates and provide a two axis measurement. This Sun vector is typically combined with measurements from other sensors such as magnetometers to determine the attitude of the spacecraft. SSTL manufactures its own model of Sun-sensor, the first being flown on UoSat-3. The latest evolution was first flown on FASAT-Bravo, launched in 1998, and has flown on all missions since then, including Topsat. The stated accuracy of the SSTL sun-sensor is one degree (95%), and it has a field of view of ±50°.

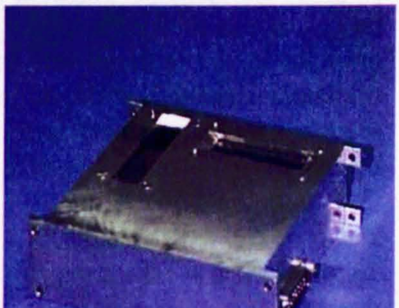

Figure 2-2 SSTL Sun-sensor

One disadvantage of Sun-sensors is that depending on the orbit of the spacecraft the sun may be eclipsed by the Earth for large periods of the orbit resulting in periods during which no Sun-sensor data is available.

2.2.2 Magnetometers

Magnetometers are widely used as spacecraft attitude sensors for a variety of reasons: they are vector sensors, providing both the direction and magnitude of the magnetic field; they are reliable, lightweight, and have low power requirements; they operate over a wide temperature range; and they have no moving parts.

However, magnetometers are not accurate attitude sensors because the magnetic field is not completely known and the models used to predict the magnetic field direction and magnitude at the spacecraft's position are subject to relatively substantial errors [Wertz, 1978].

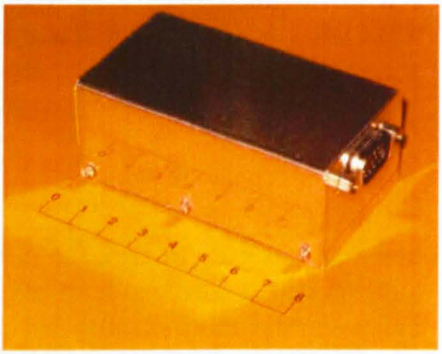

Figure 2-3 SSTL magnetometer

2.2.3 Earth horizon sensors (EHS)

Earth Horizon sensors provide attitude information by using infra-red sensors to determine the location of the Earth's horizon. Horizon sensors require a Sun rejection capability due to the Sun having an intensity of 400 times that of the Earth in the infra-red band, which can cause errors in the Horizon sensor output.

The Earth Horizon sensors used on SSTL microsatellites consist of three infra-red sensors which output a voltage depending on the amount of radiation impinging on them. When they are nominally aligned with the horizon one sensor is looking at the Earth, one at the horizon and the other at cold space, which allows the three sensors' measurements to be combined to determine the attitude to within 0.1-0.2 degree [Wertz, 1978]. The accuracy of the horizon sensor depends on the accuracy of the model of the thickness of the Earth's atmosphere because the atmosphere causes a gradient in the radiated intensity rather than a hard boundary and will also vary in thickness during the day/night cycle. The main disadvantage of Earth Horizon sensors is their very narrow field of view, which is around 5 degrees for the type used by SSTL. Any slew will cause the Earth Horizon Sensors to lose lock on the horizon.

2.2.4 Star cameras

Star cameras measure star coordinates in the spacecraft frame and compare them with a star catalogue to provide three-axis attitude information, typically achieving accuracies in the arc-second range. The main disadvantages of star cameras are that they are heavy, expensive and require more power than most other attitude

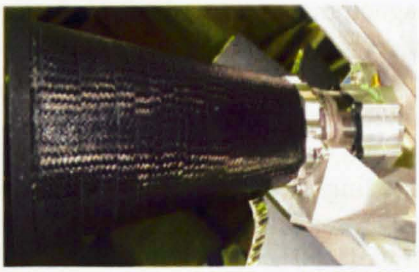

Figure 2-4 SSTL ALTAIR HB+ Star camera

sensors. For example, the SSTL star camera requires 8.5W [SSTL, 2009a]. The other major draw-back of star cameras is that they require large baffles to prevent them being blinded by the Sun, Earth or other bright sources. They must maintain minimum exclusion angles in order to prevent interference from these bright objects affecting the attitude solution. For the SSTL star camera the exclusion angles are fifty-five degrees for the Sun and thirty degrees for the Earth.

2.2.5 Inertial measurement units (IMUs)

Inertial measurement units are generally a combination of accelerometers and gyros which are used to measure the linear and rotational acceleration of the body to which they are mounted. By integrating the output of the IMU it is possible to calculate the change in attitude (and position) of a spacecraft in the inertial frame. The disadvantages of IMUs are that they only measure the change in attitude, so must be initialised with an absolute attitude sensor; they are expensive and consume a lot of power; they are prone to drift and so can only be used for short periods without correction.

2.3 Attitude from GPS measurements

GPS is now ubiquitous for navigation for both terrestrial and space-based users. It provides reliable real-time position, velocity and time information which, in the case of low earth orbiting satellites, can be used for orbit determination and image geo-location. With suitable hardware the same GPS signals used for general navigation can also be used attitude determination, using the principle of interferometry between multiple antennas.

2.3.1 GPS attitude fundamentals

The fundamental observable in GPS attitude determination is the carrier phase difference between two antennas separated by the baseline length as illustrated in . For each GPS antenna, the received carrier phase signal is measured at the apparent phase centre of the antenna. A relative phase difference between the received signals from two antennas forming a baseline is defined as the modulo carrier phase difference $\varphi_{i,j}$, where:

$$-\frac{1}{2} \leq \varphi_{i,j} \leq \frac{1}{2} (cycles) \qquad \textbf{2-11}$$

and i indexes a particular baseline and j indexes a particular GPS satellite measurement.

The GPS receiver also maintains a running sum of the number of accumulated carrier cycles since the receiver began tracking satellite j on baseline i. At each measurement epoch the accumulated cycle count, n_{acc} is summed with the modulo carrier phase difference $\varphi_{i,j}$ to give an accumulated carrier phase difference, $\bar{r}_{i,j}$:

$$\bar{r}_{i,j} = \varphi_{i,j} + n_{acc} \qquad \textbf{2-12}$$

In the first epoch

$$\bar{r}_{i,j} = \varphi_{i,j} \qquad \textbf{2-13}$$

since

$$n_{acc} = 0 \qquad \textbf{2-14}$$

This measurement is updated in all subsequent epochs in which the satellite is tracked and hence:

$$\bar{r}_{i,j}[k] = \varphi_{i,j}[k] + n_{acc}[k] \qquad \textbf{2-15}$$

More information on accumulated carrier phase measurements is given in the next section.

If the length of the baseline vector, $\|\mathbf{b}_i\|$, is larger than one carrier wavelength, the number of full cycles in the first epoch is unknown resulting in an *integer ambiguity* $N_{i,j}$ in each carrier phase difference measurement. Since the accumulated carrier phase difference accounts for any accumulated cycles in subsequent epochs, the unknown integer ambiguity is constant for as long as the satellite is tracked successfully.

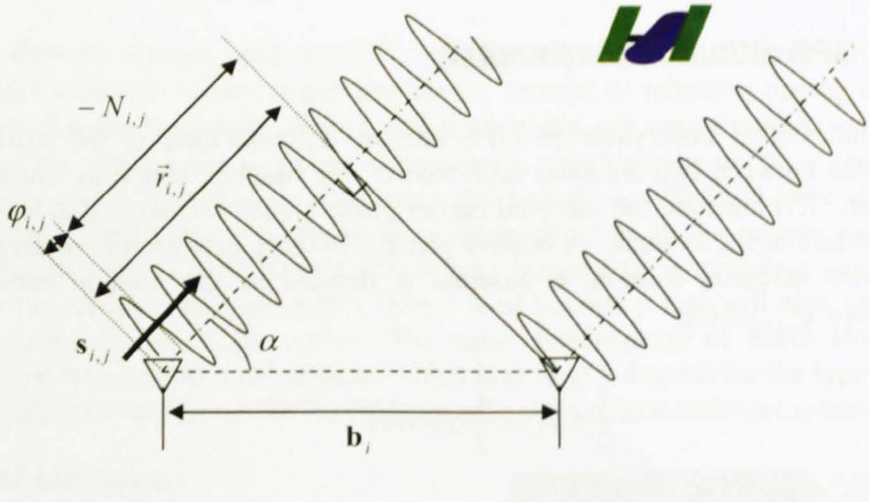

Figure 2-5 Carrier Phase Difference measurement

If the integer ambiguity $N_{i,j}$ is resolved the path difference $\vec{r}_{i,j}$ can be determined from the accumulated carrier phase difference between the two antennas (excluding measurement error)

$$\vec{r}_{i,j} = \bar{r}_{i,j} - N_{i,j} \qquad \textbf{2-16}$$

The path difference $\vec{r}_{i,j}$ can be expressed as the projection of the unit line-of-sight (LOS) vector $\mathbf{s}_{j(B)}$ onto the baseline vector $\mathbf{b}_{i(B)}$,

$$\vec{r}_{i,j} = \mathbf{s}^{T}_{j(B)}\mathbf{b}_{i(B)} = \left\|\mathbf{b}_{i(B)}\right\|\cos(\alpha) \qquad \textbf{2-17}$$

where the subscript 'B' acknowledges that both vectors are in the body-referenced coordinate system and α describes the angle between the baseline vector and the LOS vector to the GPS satellite. Substituting orbit-referenced vectors into Equation 2-17 gives

$$\vec{r}_{i,j} = \mathbf{s}^{T}_{j(O)}\mathbf{b}_{i(O)} \qquad \textbf{2-18}$$

and knowing that the attitude matrix $\mathbf{A}$ transforms vectors from the orbit-referenced frame to the body-fixed frame according to

$$\mathbf{s}_{j(B)} = \mathbf{A}\mathbf{s}_{j(O)} \qquad \textbf{2-19}$$

It follows that the path difference $\vec{r}_{i,j}$ is a function of the attitude using

$$\vec{r}_{i,j} = \mathbf{b}^{T}_{i(B)}\mathbf{A}\mathbf{s}_{j(O)} \qquad \textbf{2-20}$$

Since the baseline vector $\mathbf{b}_{i(B)}$ and the LOS vector $\mathbf{s}_{j(O)}$ are known, and given that the carrier phase differences are a function of the attitude of the spacecraft, the unknown attitude can be estimated.

2.3.2 Measurement model

The carrier phase difference measurements are perturbed by measurement errors including receiver noise, multipath error and line bias. A more complete measurement model for a given epoch k is defined as:

$$\bar{r}_{i,j}[k] - N_{i,j} + \beta_i[k] + w_{i,j}[k] = \mathbf{s}^{T}_{i,j(O)}[k]\mathbf{b}_{i(O)}[k] \qquad \textbf{2-21}$$

where i and j index the baseline and GPS satellites, respectively; all variables are in units of cycles and:

$\bar{r}_{i,j}$ is the single-difference carrier phase measurement

$N_{i,j}$ is the unknown integer ambiguity

β_i is the unknown phase offset between the GPS antennas, known as *line bias*

$w_{i,j}$ is the total measurement error (including receiver noise and multipath)

$\mathbf{s}_{i,j(O)}$ is the unit line-of-sight vector from the master antenna to the GPS satellite

$\mathbf{b}_{i(O)}$ is the unknown baseline vector between the two GPS antennas

2.3.2.1 Integer ambiguity

As mentioned above the number of cycles in the carrier phase difference measurements is unknown, and this is termed the *integer ambiguity*.

In order to track the GPS signal for a given satellite the GPS receiver must generate a replica carrier signal at the correct frequency. When measuring the carrier phase at each antenna the GPS receiver measures the fractional carrier phase (modulo one wavelength) of this replica carrier.

In the SGR-20 the carrier cycle counts and fractional phase measurements are taken by the GP2021 correlator hardware. Both measurements are based on the replica carrier created by each RF front-end in the GPS receiver. The correlator hardware keeps a running count of the number of positive-going zero crossings of the replica carrier for each tracking channel. It also stores the fractional carrier phase measurement for each channel. Both measurements are read by the SGR software every 0.1s as part of the measurement task and the summed to calculate the accumulated carrier phase for each channel.

The accumulated carrier phase on each channel approximates the change in range between the GPS patch antenna on which the satellite is being tracked and the phase centre of the GPS satellite. This is called a *delta-range* measurement. This measurement is affected by the frequency error in the GPS receiver's clock and is ambiguous due to the arbitrary time at which the tracking begins.

As shown in the path difference between two GPS patch antennas forming a baseline is a function of the angle between the baseline and the LOS vector to the GPS satellite. To calculate the path difference between the two antennas the difference in the accumulated carrier phase measurements for a pair of channels that are tracking the same GPS satellite is calculated. This results in a *single-difference* accumulated carrier phase measurement, or simply a *single-difference carrier phase measurement*. However the measurement is subject to an arbitrary and unknown offset due to the arbitrary time at which each of the channels began calculating the accumulated carrier phase measurements. To eliminate this offset the initial accumulated carrier phase difference is set to the difference in the fractional carrier phase measurements, and the accumulation of the carrier phase difference proceeds anew from this value for as long as the satellite is tracked on both channels.

If either of the channels being differenced loses lock on the satellite then the accumulated carrier phase difference is cleared and flagged as invalid. If the satellite is subsequently reacquired the initial accumulated carrier phase difference is again set to the difference in the fractional phases, and the accumulation begins anew.

This final accumulated carrier phase difference is still subject to an integer ambiguity, but this integer ambiguity remains constant for as long as the satellite is tracked on both antennas. The integer ambiguities can be resolved through a process termed *integer ambiguity resolution* (IAR).

2.3.2.2 Line of sight vectors

Line Of Sight (LOS) vectors are unit vectors directed from the master antenna to the GPS satellite. The LOS vectors are provided by the receiver in the World Geodetic System 84 (WGS-84) coordinate system [NGA, 2004], which is the reference coordinate system used by GPS. The LOS vectors are rotated to the orbit-defined coordinate system for use in determining the attitude, using the method defined in Appendix C.

2.3.2.3 Multipath

Multipath is caused by reflections of the signals arriving at the antennas from nearby surfaces, and generally the definition of multipath is broadened to include signals diffracting around nearby edges and obstacles, such as a gravity gradient boom. Specular reflections produce systematic, correlated errors that are not easily treated in a processing filter [Reichert, 1999]. For the case of a satellite platform specular multipath can only occur by the signal reflecting off the satellite structure and the multipath error can be treated as time invariant, being simply a function of the incident signal direction. Specular multipath causes phase errors equivalent to an error in electrical path length of several centimetres [Comp and Axelrad, 1998]. Diffraction multipath generally produces a rapidly varying error which is equivalent to an error in electrical path length of several millimetres [Comp and Axelrad, 1998]. This type of multipath can be possibly mitigated with the use of dynamic filtering techniques [Purivigraipong, 2000].

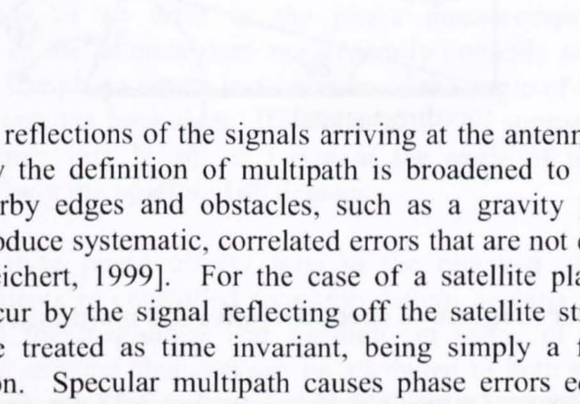

Figure 2-6 Multipath

If an antenna receives two signals: a line-of-sight signal and a reflected signal with phase shift $\Delta\varphi$ and amplitude attenuation a the error in the carrier phase measurement as a result of multipath is:

$$\delta\varphi = \tan^{-1}\left(\frac{a\sin\Delta\varphi}{1+a\cos\Delta\varphi}\right) \qquad \textbf{2-22}$$

Equation 2-22 shows that the phase of the fractional cycle of the reflected signal corrupts the phase of the fractional cycle of the direct signal, depending on its relative strength and phase. It follows that the error in the carrier phase measurements due to multipath does not exceed a quarter cycle if the reflected signal has a smaller amplitude than the direct signal.

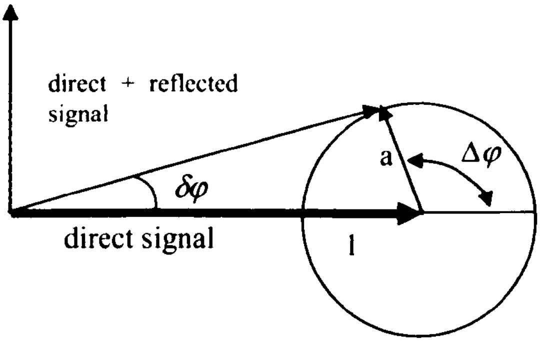

Figure 2-7 Phasor diagram of specular reflection multipath error

The phase measurement error defined in Equation 2-22 describes the error at a single antenna. For GPS attitude determination we must take carrier phase differences between two antennas, and so the errors due to multipath at each antenna will sum together in the carrier phase difference measurement.

In the measurement model used in this work multipath is assumed to be a time-invariant deterministic function of the direction of the incoming signal. The direction of the incoming signal relative to the spacecraft body frame is defined in terms of its co-elevation θ_{mp} and azimuth ϕ_{mp}. The resulting *multipath error* can then be defined according to:

$$u_{mp}[k] = f(\theta_{mp}, \phi_{mp}) \qquad \textbf{2-23}$$

Multipath can be modelled as a stochastic sequence of correlated random variables with a local mean $\langle u_{i,j} \rangle$ and a local mean square $\langle u_{i,j}^2 \rangle$ (where j represents a particular satellite and i a particular baseline).

Along any one track of an observed satellite crossing the sky the multipath error will have some local track mean and a variation about that mean. The variation is termed *multipath noise.*

In the case of spacecraft, the only source of multipath is that originating from the spacecraft itself. For UoSat-12, even after limiting the field of view to exclude the worst error (below 20 degrees elevation) the RMS multipath, with respect to a typical baseline was 9.8mm. Peak values in the worst case directions exceeded 40mm [Wong, 2004].

2.3.2.3.1 Antenna errors

SSTL's satellites generally use micro-strip patch antennas which can induce a number of different errors in the carrier phase measurements. The errors can be described in terms of *antenna phase centre variation*, the *antenna phase pattern* and *phase wind-up*, each of which is described below.

The point of reception of a radio signal at an antenna is referred to as the *phase centre*, which is the apparent electrical centre of the antenna. The antenna phase centre uncertainty leads to an error in the phase measurements because the electromagnetic centre of the antenna does not generally coincide with the physical centre of the antenna. The phase centre is a function of the angle of incidence of the incoming signal to the antenna bore-sight. [Godet et al, 1999] suggest that the phase centre of an antenna may vary by up to 3 mm as the angle of incidence of the incoming signal moves over the possible 180 degrees.

[Kim et al, 2004] analyse phase effects seen in the received phase pattern of individual antenna elements in controlled reception pattern antenna (CRPA) arrays. They demonstrate that the magnitude and location (in terms of incident signal direction) for individual antenna elements can be attributed to both the phase centre movement of the individual antenna element and fringing effects when the antenna element is placed near the edge of the ground plane. Errors in manufacturing may also lead to an offset in the antenna phase response. [Kim et al, 2004] modelled a dimensional tolerance in the construction of a micro-strip patch antenna and showed that in general manufacturing tolerances tend to introduce a constant offset in the phase response but do not affect the phase pattern of the antenna.

If one of the slave antennas were to rotate physically with respect to the master antenna the measurements may contain *phase wind-up*. This would be a problem in systems where the master and slave antennas are located on separate platforms, such as RTK systems. For the purposes of attitude determination the antennas are generally co-located rigidly on the same platform, so any phase wind-up effects are common to all antennas, and therefore cancel out in the single-difference measurements.

[Godet et al, 1999] show that the structure of the spacecraft surrounding an antenna has a significant effect on the phase variation of the antenna. In their experiments around ±18mm of error was seen purely from the immediate area around the antenna. Antenna errors are indistinguishable from physical multipath and can be treated as a single error under the general term *multipath error*. This means that *multipath error* can occur even without obstacles creating reflected signals.

2.3.2.4 Line bias

Line bias is a relative phase offset between measurements taken between two antennas. It is caused by the combination of different cables lengths between the antennas and the RF-front ends of the GPS receiver, and by differences in the RF-front ends themselves.

Line bias will be defined as whatever is the net contribution of all errors that are common to the phase measurements within one base line. It may be time-varying. A major contribution is the error induced by delays caused by the various stages of the RF section of the receiver. The line bias contribution is typically different for each baseline since differences in the electrical path length between each antenna and the RF front-ends can induce a common phase delay in the measurements that will be present in all measurements taken on that baseline. The line bias β_i is defined as

$$\beta_i = \beta_i[k] \qquad \text{2-24}$$

where k is an epoch count.

For modelling purposes it may not be possible to distinguish this physical bias from any average bias induced by the spatially correlated multipath. Accordingly, the effective line bias will also contain the local averages $\langle u_{i,j}[k]\rangle$ of the multipath error for all carrier phase measurements from $J_i[k]$ satellites tracked on baseline i in epoch k. The *effective* line bias $\beta_i^*[k]$ in epoch k is defined as

$$\beta_i^*[k] = \beta_i[k] + \frac{1}{J_i[k]}\sum_{j=1}^{J}\langle u_{i,j}[k]\rangle \qquad \text{2-25}$$

In order to use the accumulated carrier phase measurements for GPS attitude determination the line bias must either be estimated or eliminated using double-difference measurements. Past researchers that estimated the line bias included [Cohen, 1992], [Ward, 1996], [Purivigraipong, 2000] and [Buist, 2006]. [Cohen, 1992] estimated the line bias pre-flight using many hours of logged data but it was shown in [Lightsey et al, 1994] that estimating the line bias before flight was not satisfactory since its value for the RADCAL satellite changed once the satellite was operating in space. Most carrier phase users particularly those using Real-Time-Kinematic surveying techniques now utilise double-difference measurements to eliminate the line bias rather than estimating it.

[Morros, 1995] showed that the line bias in the SGR-20 is affected by temperature as a result of the GP2010/2015 RF Front-end integrated circuits. Changes in temperature cause a time-varying drift in the phase measurements. According to [Morros, 1995] as the temperature increases the phase measured by the GP2010 decreases. If the temperature remains stable the phase measured will remain constant.

2.3.2.5 Receiver noise

The code and carrier measurements are affected by random measurement noise, called *receiver* noise. This is a broad term covering the RF radiation sensed by the antenna in the band of interest unrelated to the signal; noise introduced by the antenna, amplifiers, cables, and the receiver; multi-access noise (i.e. interference from other GPS signals and GPS-like broadcasts from system augmentations); and signal quantization noise [Misra and Enge, 2001].

For the purposes of our model receiver noise is assumed to be a zero mean random noise with a mean square of

$$\langle v_{i,j} \rangle = \sigma_v^2 \qquad \textbf{2-26}$$

Receiver noise is assumed to be uncorrelated in time and across the different tracking channels in the GPS receiver.

$$\langle v[k]v[l] \rangle = 0 \quad k \neq l \qquad \textbf{2-27}$$

$$\langle v_j v_l \rangle = 0 \quad j \neq l \qquad \textbf{2-28}$$

[Kaplan, 1996] provides an equation that defines the RMS carrier phase error, σ_v, caused by receiver noise in the tracking loop of the GPS receiver:

$$\sigma_v = \frac{\lambda_{L1}}{2\pi}\sqrt{\frac{B_n}{\left(C/N_0\right)}\left(1 + \frac{1}{2\mathrm{T}_{\mathrm{int}}\left(C/N_0\right)}\right)} \qquad \textbf{2-29}$$

where

λ_{L1}	is the wavelength of the L1 frequency, 0.1903 metres
B_n	is the noise bandwidth in Hz
C/N_0	is the received carrier-to-noise power density ratio, expressed in Hz
$\mathrm{T}_{\mathrm{int}}$	is the integration time of the loop filter

For the SGR-20 GPS receiver, the phase-locked-loop (PLL) is designed with T_{int} = 1 msec and B_n = 10 Hz [SSTL, 1999]. For a C/N_0 of 45dB-Hz, the corresponding theoretical RMS (undifferenced) carrier phase error is 0.7mm. For a single-difference carrier phase measurement the carrier phase error will be $\sqrt{2}\times 0.7\text{mm} \approx 1.0\text{mm}$.

2.3.2.6 Baseline error

If the baseline vectors are measured from the mechanical drawings then potential manufacturing errors can lead to a difference between the assumed baseline vectors and the true baselines. If the baseline vectors are 'surveyed' using GPS carrier phase measurements the estimated baseline vectors will differ from the nominal vectors measured from the mechanical drawings due to the variation in the antenna phase centre which is dependent on the direction of the incoming signals. In Chapter 3 a batch least-squares algorithm uses data from the ADCS reference attitude to estimate the baseline vectors in the ADCS reference frame.

2.3.2.7 ADCS error

The ADCS attitude solution is used as a reference or 'truth' attitude throughout this thesis. If the accuracy of the ADCS attitude is not at least an order of magnitude better than the expected GPS attitude accuracy then the ADCS will make a significant contribution to the calculation of the disparity between GPS and ADCS.

The error in the ADCS reference attitude $\breve{\mathbf{A}}$ relative to the true attitude $\mathbf{A}$ is defined as

$$\breve{\mathbf{A}}[k] = \mathbf{A}[k]\left(\mathbf{1} + \boldsymbol{\Delta}^{\times} + \boldsymbol{\alpha}^{\times}[k] + \boldsymbol{\delta}^{\times}[k]\right) \qquad \textbf{2-30}$$

where

$\boldsymbol{\alpha}[k]$ is the attitude controller noise
$\boldsymbol{\Delta}$ is the constant rotational error of the ADCS effective axes relative to the true body axes
$\boldsymbol{\delta}[k]$ is the attitude measurement noise, which is assumed random with zero-mean

Note that the superscript '$\times$' defines a skew-symmetic matrix i.e.

$$\boldsymbol{\Delta}^{\times} = \begin{bmatrix} 0 & \Delta_3 & -\Delta_2 \\ -\Delta_3 & 0 & \Delta_1 \\ \Delta_2 & -\Delta_1 & 0 \end{bmatrix} \qquad \textbf{2-31}$$

The attitude controller noise $\boldsymbol{\alpha}[k]$ will be absorbed in to an effective measurement noise and so is indistinguishable from random errors in the GPS carrier phase measurements. The ADCS errors $\boldsymbol{\delta}[k]$ and $\boldsymbol{\Delta}$ will affect the estimate of the true baseline vectors and the GPS satellite line of sight vectors in the spacecraft body frame. These errors therefore contribute to an *effective baseline knowledge error* $\Delta\mathbf{b}^{*}$.

2.3.2.8 Total measurement noise

The *total measurement noise* $w_{i,j}$ is defined as the sum of the multipath noise and the receiver noise, which includes all errors affecting the system excluding any average bias

$$w_{j,i}[k] = u_{j,i}[k] + v_{j,i}[k] \qquad \textbf{2-32}$$

Note that when using single-difference carrier phase measurements the average bias is grouped with the line bias $\beta_i^{*}[k]$ as defined in section 2.3.2.4.

2.3.2.9 Double-difference measurements

The measurement model described above calculates the carrier phase difference for a single satellite measurement j between two antennas forming a baseline i. Taking two such measurements on a particular baseline and differencing them then effectively eliminates the line bias parameter. This process, known as *double-differencing* results in the following measurement model:

$$\Delta\bar{r}_{i,j}[k] - \Delta N_{i,j} + \Delta w_{i,j}[k] = \mathbf{v}^{T}_{i,j(O)}[k]\mathbf{b}_{i(O)}[k] \qquad \textbf{2-33}$$

Where:

$$\begin{aligned} \Delta\bar{r}_{i,j-1}[k] &= \bar{r}_{i,j}[k] - \bar{r}_{i,1}[k] \\ \Delta N_{i,j-1} &= N_{i,j} - N_{i,1} \\ \mathbf{v}_{i,j-1(O)}[k] &= \mathbf{s}_{i,j(O)}[k] - \mathbf{s}_{i,1(O)}[k] \\ \Delta w_{i,j-1}[k] &= w_{i,j}[k] - w_{i,1}[k] \end{aligned} \qquad \textbf{2-34}$$

for $2 \le j \le J$, where J is the number of satellites tracked on baseline i.

By removing the line bias parameter the integer ambiguities are always precisely integer in nature, which aids integer ambiguity resolution. The disadvantages of double-differencing are that the noise in each measurement is increased; typically by a factor of $\sqrt{2}$ assuming the signal to noise ratio (SNR) is the same on both antennas for a given satellite. Also, the measurements are now correlated since one measurement, known as the *pivot*, is differenced from all the rest. This results in a different noise covariance matrix when using double-differences:

$$\mathbf{R} = 2\tilde{\sigma}^2_{\varphi_u} \begin{bmatrix} 2 & 1 & \cdots & 1 \\ 1 & 2 & \cdots & 1 \\ \vdots & \vdots & \ddots & 1 \\ 1 & 1 & 1 & 2 \end{bmatrix} \qquad \textbf{2-35}$$

where $\tilde{\sigma}^2_{\varphi_u}$ is the estimated *undifferenced* GPS carrier phase measurement noise variance (i.e. the noise variance of the accumulated carrier phase measurement for a single tracking channel).

Note also that throughout this work the *highest elevation* satellite is chosen as the *pivot* satellite that is differenced from all the other measurements. Theoretically any satellite can be chosen as the pivot satellite, but it is standard practice in the literature to choose the highest elevation satellite since it is expected that it will experience the least multipath error and is more likely to be co-visible for all antennas (dependent on the attitude of the platform).

2.3.3 Attitude estimation techniques

There are two distinct approaches for estimating attitude using GPS measurements – the linear, vector based approach, and the non-linear measurements based approach. Vector based methods involve calculating the rotation matrix between vectors in two different frames. For GPS attitude determination the baseline vectors are defined in the spacecraft body-referenced frame, but are unknown in the orbit-referenced frame. Therefore in order to use the vector based methods the unknown baseline vectors must first be solved for in the orbit referenced frame.

2.3.3.1 Solving for an unknown baseline vector using GPS

The vector $\mathbf{b}_{i(O)}$ is defined that describes the unknown baseline vector i in orbit referenced coordinates. Calculating double-difference measurements using the method described in section 2.3.2.9 at each epoch k a set of equations can be formed

$$\Delta\bar{\mathbf{r}}_i[k] = \mathbf{H}_i[k]\mathbf{b}_{i(O)}[k] \tag{2-36}$$

The observation matrix $\mathbf{H}_i$ contains the LOS vectors to each of the J GPS satellites, with corresponding path difference measurements stored in $\bar{\mathbf{r}}$:

$$\mathbf{H}_i[k] = \begin{bmatrix} \mathbf{v}_{i1}^T[k] \\ \mathbf{v}_{i2}^T[k] \\ \vdots \\ \mathbf{v}_{i(J-1)}^T[k] \end{bmatrix} \qquad \Delta\bar{\mathbf{r}}_i[k] = \begin{bmatrix} \Delta\bar{r}_{i1}[k] - \Delta N_{i1} \\ \Delta\bar{r}_{i2}[k] - \Delta N_{i2} \\ \vdots \\ \Delta\bar{r}_{i(J-1)}[k] - \Delta N_{i(J-1)} \end{bmatrix} \tag{2-37}$$

where it is assumed that the integer ambiguities $\Delta N_{i,j}$ have been solved through integer ambiguity resolution as addressed in Chapter 4. The baseline vector is solved for using a weighted least squares solution

$$\hat{\mathbf{b}} = \left(\mathbf{H}_i[k]^T \mathbf{R}^{-1} \mathbf{H}_i[k]\right)^{-1} \mathbf{H}_i[k]^T \mathbf{R}^{-1} \Delta\bar{\mathbf{r}}_i \tag{2-38}$$

where $\mathbf{R}$ is the known measurement noise covariance matrix given in Equation 2-35.

The baseline vector can be estimated using least-squares for each available baseline. If two or more baseline vectors are available then the attitude can be estimated using the TRIAD or sLSE methods outlined below.

2.3.3.2 TRIAD method

The TRIAD method, also known as the 'Algebraic method' [Wertz, 1978] is based on the rotation matrix representation of the attitude. Any two vectors $\mathbf{u}$ and $\mathbf{v}$ define an orthogonal coordinate system with the basis vectors $\vec{\mathbf{a}}_1$, $\vec{\mathbf{a}}_2$ and $\vec{\mathbf{a}}_3$ given by

$$\begin{aligned}\vec{\mathbf{a}}_1 &= \mathbf{u} \\ \vec{\mathbf{a}}_2 &= \mathbf{u}\times\mathbf{v}/\|\mathbf{u}\times\mathbf{v}\| \\ \vec{\mathbf{a}}_3 &= \vec{\mathbf{a}}_1\times\vec{\mathbf{a}}_2\end{aligned} \qquad \textbf{2-39}$$

provided that $\mathbf{u}$ and $\mathbf{v}$ are not parallel, i.e.

$$\|\mathbf{u}\times\mathbf{v}\| < 1 \qquad \textbf{2-40}$$

Given two measured vectors in the orbit-referenced frame, $\mathbf{u}_{(O)}$ and $\mathbf{v}_{(O)}$, then the reference matrix $\mathbf{M}_{(O)}$ can be constructed from

$$\mathbf{M}_{(O)} = \begin{bmatrix}\vec{\mathbf{a}}_{1(O)} & \vec{\mathbf{a}}_{2(O)} & \vec{\mathbf{a}}_{3(O)}\end{bmatrix} \qquad \textbf{2-41}$$

If the same vectors are known in the spacecraft body coordinates, $\mathbf{u}_{(B)}$ and $\mathbf{v}_{(B)}$, the body matrix, $\mathbf{M}_{(B)}$ can be constructed from:

$$\mathbf{M}_{(B)} = \begin{bmatrix}\vec{\mathbf{a}}_{1(B)} & \vec{\mathbf{a}}_{2(B)} & \vec{\mathbf{a}}_{3(B)}\end{bmatrix} \qquad \textbf{2-42}$$

The attitude matrix, or direct cosine matrix, $\hat{\mathbf{A}}$ is defined as the rotation between the orbit and body referenced frames:

$$\hat{\mathbf{A}}\mathbf{M}_{(O)} = \mathbf{M}_{(B)} \qquad \textbf{2-43}$$

This equation may be solved for $\hat{\mathbf{A}}$ to give

$$\hat{\mathbf{A}} = \mathbf{M}_{(B)}\mathbf{M}_{(O)}^{-1} \qquad \textbf{2-44}$$

Because $\mathbf{M}_{(O)}$ is orthogonal, $\mathbf{M}_{(O)}^{-1} = \mathbf{M}_{(O)}^{T}$ and hence

$$\hat{\mathbf{A}} = \mathbf{M}_{(B)}\mathbf{M}_{(O)}^{T} \qquad \textbf{2-45}$$

The simplicity of this method makes it particularly suitable for real time implementation. Since the $\mathbf{u}$ vector is treated preferentially it should generally be the more accurate of the two vectors. The scalar term $\mathbf{u}_{(O)}\cdot\mathbf{v}_{(O)}$ can be compared with the known scalar $\mathbf{u}_{(B)}\cdot\mathbf{v}_{(B)}$ to provide a basic sanity check.

2.3.3.3 Scalar least-squares method

An attitude solution $\hat{\mathbf{A}}$ can be obtained by minimising the cost function in least squares form [Cohen, 1992]

$$J(\hat{\mathbf{A}}) = \sum_{i=1}^{m}\sum_{j=1}^{n}\left(\Delta\bar{r}_{i,j} - \mathbf{b}_{i(B)}^{T}\hat{\mathbf{A}}\mathbf{v}_{i,j(O)}\right)^{2} \qquad \text{2-46}$$

where $\Delta\bar{r}_{i,j}$ is the double-difference path difference for baseline i and satellite j (i.e. the double-difference carrier phase corrected for the integer ambiguity). All measurements are taken from a single epoch k.
The estimated attitude matrix is defined as

$$\hat{\mathbf{A}} = \delta\mathbf{A}\hat{\mathbf{A}}_{0} \qquad \text{2-47}$$

where $\hat{\mathbf{A}}_{0}$ is a prior estimate of the attitude matrix and $\delta\mathbf{A}$ is defined as

$$\delta\mathbf{A} = \mathbf{I}_{3\times3} + \Delta\boldsymbol{\xi}^{\times} \qquad \text{2-48}$$

and the attitude error vector and its skew-symmetric matrix are defined as [Shuster, 1993]

$$\Delta\boldsymbol{\xi} = \begin{bmatrix} \delta\phi \\ \delta\theta \\ \delta\psi \end{bmatrix} \qquad \Delta\boldsymbol{\xi}^{\times} = \begin{bmatrix} 0 & \delta\psi & -\delta\theta \\ -\delta\psi & 0 & \delta\phi \\ \delta\theta & -\delta\phi & 0 \end{bmatrix} \qquad \text{2-49}$$

For each trial in the iterative process the predicted phase difference can be expressed as

$$\Delta\hat{r}_{i,j} = \mathbf{b}_{i(B)}^{T}\hat{\mathbf{A}}\mathbf{v}_{i,j(O)} + \Delta N_{i,j} = \mathbf{b}_{i(B)}^{T}\left(\mathbf{I}_{3\times3} + \Delta\boldsymbol{\xi}^{\times}\right)\hat{\mathbf{A}}_{0}\mathbf{v}_{i,j(O)} + \Delta N_{i,j} \qquad \text{2-50}$$

The difference between the measured path difference $\Delta\bar{r}_{i,j}$ and the predicted path difference $\Delta\hat{r}_{i,j}$ is then given by

$$\Delta\bar{r}_{i,j} - \Delta\hat{r}_{i,j} = \Delta\bar{r}_{i,j} - \Delta N_{i,j} - \mathbf{b}_{i(B)}^{T}\hat{\mathbf{A}}_{0}\mathbf{v}_{i,j(O)} - \mathbf{b}_{i(B)}^{T}\Delta\hat{\boldsymbol{\xi}}^{\times}\hat{\mathbf{A}}_{0}\mathbf{v}_{i,j(O)} \qquad \text{2-51}$$

The above equation can be rewritten as

$$\Delta\bar{r}_{i,j} - \Delta\hat{r}_{i,j} = \delta r_{i,j} - \mathbf{b}_{i(B)}^{T}\Delta\hat{\boldsymbol{\xi}}^{\times}\hat{\mathbf{A}}_{0}\mathbf{v}_{i,j(O)} \qquad \text{2-52}$$

where δr is an error in measurements expressed as

$$\delta r_{i,j} = \Delta\bar{r}_{i,j} - \Delta N_{i,j} - \mathbf{b}_{i(B)}^{T}\hat{\mathbf{A}}_{0}\mathbf{v}_{i,j(O)} \qquad \text{2-53}$$

From Equation 2-52 the overall difference between the measured and predicted path difference should converge towards zero in least squares fitting. Therefore the cost function can be rewritten as

$$J(\Delta\xi) = \sum_{i=1}^{m}\sum_{j=1}^{n}\left(\delta r_{i,j} - \mathbf{h}_{i,j}\Delta\xi\right)^2 \qquad \textbf{2-54}$$

where

$$\mathbf{h}_{i,j} = \mathbf{b}_{i(B)}^T \hat{\mathbf{A}}_0 \mathbf{v}_{i,j(O)} \qquad \textbf{2-55}$$

The solution which minimises the cost of Equation 2-54 can be calculated using the standard least-squares method

$$\Delta\hat{\xi} = \left(\mathbf{H}^T\mathbf{R}^{-1}\mathbf{H}\right)^{-1}\mathbf{H}^T\mathbf{R}^{-1}\boldsymbol{\delta}\mathbf{r} \qquad \textbf{2-56}$$

where $\mathbf{R}$ is given in Equation 2-35,

$$\boldsymbol{\delta}\mathbf{r} = \left[\delta r_{1,1} \quad \cdots \quad \delta r_{I,J}\right]^T_{(I\times J)\times 1} \qquad \textbf{2-57}$$

and

$$\mathbf{H} = \begin{bmatrix} \mathbf{h}_{1,1} \\ \vdots \\ \mathbf{h}_{I,J} \end{bmatrix} = \begin{bmatrix} -\mathbf{b}_{1(B)}^T \hat{\mathbf{A}}_0 \mathbf{v}_{1,1(O)}^{\times} \\ \vdots \\ -\mathbf{b}_{I(B)}^T \hat{\mathbf{A}}_0 \mathbf{v}_{I,J(O)}^{\times} \end{bmatrix} \qquad \textbf{2-58}$$

The iterative process can in principle be initialised with the identity matrix as the *a priori* attitude matrix. The error vector will be calculated and the attitude estimate updated, and then fed back to the next iteration until it converges on a solution. If the true attitude is not close to the initial value used, then the algorithm may not converge, particularly when using real data. Also note that on each iteration the implicit axes within the attitude matrix $\hat{\mathbf{A}}$ must be orthogonalised and normalised to ensure that the matrix correctly represents a rotation matrix.

2.3.3.4 Attitude point solution

This algorithm, based on [Ward, 1996], uses a least-squares estimate with *a priori* information to solve for the attitude on an epoch-by-epoch basis, using double-difference carrier phase measurements. Note that there is no essential difference between this algorithm and the sLSE algorithm other than Ward's method solves for the quaternion rather than the direct cosine matrix.

Let the state vector be defined as:

$$\hat{\mathbf{x}}[k] = \boldsymbol{\delta}\mathbf{q} = \left[\delta q_1 \quad \delta q_2 \quad \delta q_3\right] \qquad \textbf{2-59}$$

where $\delta\mathbf{q}$ is a 3-element correction to a quaternion.

The predicted double-difference phase for baseline i observing satellite j is given by:

$$\Delta\hat{r}_{i,j}[k] = \mathbf{b}^T_{i(B)}\hat{\mathbf{A}}[k]\mathbf{v}_{i,j}[k] + \Delta N_{i,j} \qquad \textbf{2-60}$$

where the initial value of $\hat{\mathbf{A}}[k]$ is the attitude estimate from the previous epoch if available. It is assumed that the integer ambiguities are known (for example via integer ambiguity resolution).

The measurement gradient for a single observation is given by:

$$\mathbf{H}_{i,j}[k] = \left[2\left(\hat{\mathbf{A}}[k]\mathbf{v}_{i,j}[k]\right)^T\mathbf{B}^{\times}\right] \qquad \textbf{2-61}$$

where $\mathbf{B}^{\times}$ is the skew-symmetric form of the baseline vector $\mathbf{b}_{i(B)}$.

The measurement gradient vectors for all the observations at a particular measurement epoch are concatenated to form a $(J-1)\times 6$ matrix $\mathbf{H}$ where $J-1$ is the number of double-difference measurements at the epoch. The measurement residuals are then combined into vector $\mathbf{z}$ to give:

$$\mathbf{z}[k] = \begin{bmatrix} \vdots \\ \Delta\tilde{r}_{i,j}[k] - \Delta\hat{r}_{i,j}[k] \\ \vdots \end{bmatrix} \qquad \textbf{2-62}$$

At each measurement of epoch a set of equations can be formed

$$\mathbf{H}[k]\hat{\mathbf{x}}[k] = \mathbf{z}[k] \qquad \textbf{2-63}$$

which is solved for $\hat{\mathbf{x}}[k]$ using a weighted least squares solution with *a priori* information as follows:

$$\hat{\mathbf{x}}[k] = \left(\mathbf{H}^T[k]\mathbf{R}'^{-1}\mathbf{H}[k] + \mathbf{P}^{-1}[k-1]\right)^{-1}\left(\mathbf{H}^T[k]\mathbf{R}'^{-1}\mathbf{z}[k] + \mathbf{P}^{-1}[k-1]\hat{\mathbf{x}}[k-1]\right) \qquad \textbf{2-64}$$

where $\mathbf{P}[k-1]$ is the *a priori* state covariance, and $\hat{\mathbf{x}}[k-1]$ is the *a priori* estimate of the state. The weighting matrix $\mathbf{R}'$ is $(J-1)\times(J-1)$, and is sparse having the form:

$$\mathbf{R}' = \begin{bmatrix} \mathbf{R} & 0 & 0 \\ 0 & \ddots & 0 \\ 0 & 0 & \mathbf{R} \end{bmatrix} \qquad \textbf{2-65}$$

since it is assumed the measurements on individual baselines are uncorrelated. $\mathbf{R}$ is given in section 2.3.2.9.

The estimate of the 3-element correction quaternion $\boldsymbol{\delta}\mathbf{q}$ is used to form the full correction quaternion $\delta\hat{q}$ with the equation

$$\boldsymbol{\delta}\hat{\mathbf{q}} = \begin{bmatrix} \boldsymbol{\delta}\mathbf{q} \\ \hline \sqrt{1 - \delta q_1^2 - \delta q_2^2 - \delta q_3^2} \end{bmatrix} \qquad \textbf{2-66}$$

The updated quaternion estimate $\hat{\mathbf{q}}$ is computed by composing the full correction quaternion with the *a priori* estimate $\overline{\mathbf{q}}$ as follows:

$$\hat{\mathbf{q}} = \boldsymbol{\delta}\hat{\mathbf{q}} \otimes \overline{\mathbf{q}} \qquad \textbf{2-67}$$

where ⊗ represents the quaternion composition operation:

$$\mathbf{q}'' = \mathbf{q}' \otimes \mathbf{q} \qquad \textbf{2-68}$$

$$\mathbf{q}'' = \begin{bmatrix} q_4' & q_3' & -q_2' & q_1' \\ -q_3' & q_4' & q_1' & q_2' \\ q_2' & q_1' & q_4' & q_3' \\ q_1' & -q_2' & -q_3' & q_4' \end{bmatrix} \mathbf{q}$$

The line bias is updated by simply adding the correction value to the *a priori* estimate. The process is repeated until $\hat{\mathbf{x}}$ becomes sufficiently small. The best estimate of the state from the current epoch then serves as the *a priori* value for the next epoch.

2.3.4 Dilution of Precision (DOP)

Dilution of Precision (DOP) factors are commonly used to evaluate the quality of the GPS position estimate [Kaplan, 1996]. Commonly used factors are the Position Dilution of Precision (PDOP) which describes the uncertainty of the position estimate and Geometric Dilution of Precision (GDOP) which describes the uncertainty in the whole GPS solution. More information on the different dilution of precision factors can be found in [Kaplan, 1996].

2.3.4.1 Attitude Dilution of Precision (ADOP)

The quality of the GPS attitude estimate can be evaluated using the Attitude Dilution of Precision (ADOP). Assuming double-difference measurements, Equation 2-58 can be used to define a non-dimensional measurement matrix $\hat{\mathbf{H}}$ using the effective baseline length b_0:

$$\hat{\mathbf{H}} = \begin{bmatrix} \mathbf{h}_{1,1}/b_0 \\ \vdots \\ \mathbf{h}_{I,J}/b_0 \end{bmatrix} \qquad \textbf{2-69}$$

where the effective baseline length is the average length of all baselines used for GPS attitude determination. The ADOP can then be determined from

$$\mathrm{ADOP} = \sqrt{\mathrm{tr}\left(\hat{\mathbf{H}}^T \mathbf{W}^{-1} \hat{\mathbf{H}}\right)^{-1}} \qquad \textbf{2-70}$$

Where

$$\mathbf{W} = \begin{bmatrix} 2 & 1 & \cdots & 1 \\ 1 & 2 & \cdots & 1 \\ \vdots & \vdots & \ddots & 1 \\ 1 & 1 & 1 & 2 \end{bmatrix} \qquad \textbf{2-71}$$

[Yoon and Lundberg, 2001] shows how the ADOP can be broken down into Euler angle components. Using Equation 2-70 three separate DOPs can be defined to relate the effect of the GPS satellite geometry and the antenna baselines on the estimates of the Euler angles as

$$\left[\varphi\mathrm{DOP}^2 \quad \theta\mathrm{DOP}^2 \quad \psi\mathrm{DOP}^2\right] = \mathrm{diag}\left[\left(\hat{\mathbf{H}}^T \mathbf{W}^{-1} \hat{\mathbf{H}}\right)^{-1}\right] \qquad \textbf{2-72}$$

which leads to the equations

$$\begin{aligned} \sigma_\varphi &= \varphi\mathrm{DOP} \times \frac{\sigma_w}{b_0} \\ \sigma_\theta &= \theta\mathrm{DOP} \times \frac{\sigma_w}{b_0} \\ \sigma_\psi &= \psi\mathrm{DOP} \times \frac{\sigma_w}{b_0} \end{aligned} \qquad \textbf{2-73}$$

where σ_w is the double-difference RMS measurement noise. Using these equations the effect of different factors on the accuracy of the estimates of the Euler angles can be calculated (for small angles). To determine the overall pointing error the following equation can be used:

$$\sigma_{GPS} = \sqrt{\sigma_\varphi^2 + \sigma_\theta^2 + \sigma_\psi^2} \qquad \textbf{2-74}$$

Naturally the double-difference RMS measurement noise must be known in order to solve for the overall GPS pointing error.

The uncertainty in terms of roll, pitch and yaw (in radians) is determined from

$$\left[\sigma_\varphi^2 \quad \sigma_\theta^2 \quad \sigma_\psi^2\right] = \mathrm{diag}\left[\left(\mathbf{H}^T \mathbf{R}^{-1} \mathbf{H}\right)^{-1}\right] \qquad \textbf{2-75}$$

where $\mathbf{H}$ is given in Equation 2-58 and $\mathbf{R}$ is given in Equation 2-35.

2.4 SGR-20 receiver hardware

The SGR-20 (Space GPS Receiver) is SSTL's heritage GPS receiver. It is based on a parallel architecture and comprises of two 12 channel C/A code correlators and four RF front ends. It has been specifically designed for use in orbit to provide real-time positioning, velocity, time and attitude determination. It uses commercial off-the-shelf technology to provide a low-cost alternative to other receivers for space-borne applications.

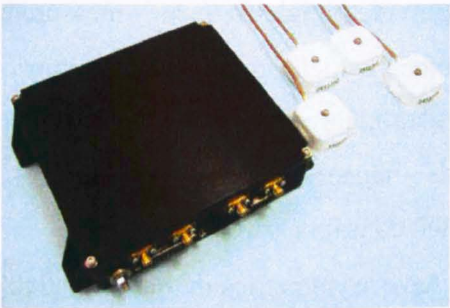

Figure 2-8 SGR-20 GPS Receiver and four patch antennas

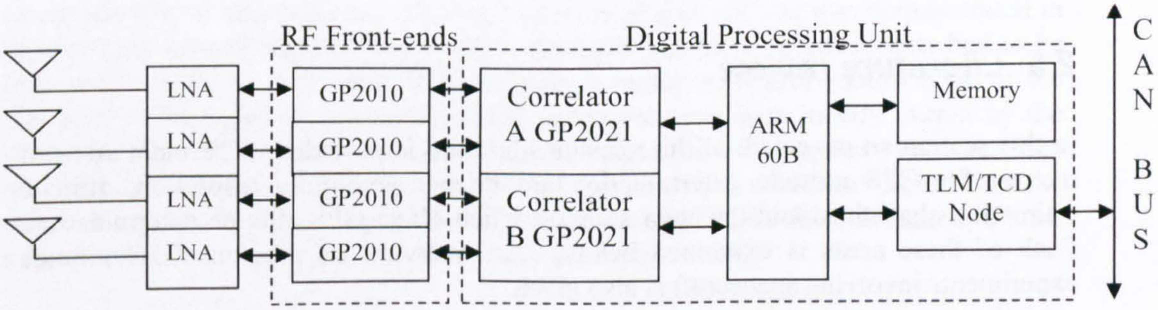

Figure 2-9 SGR-20 Hardware diagram

The SGR-20's twin correlators allow up to 24 simultaneous measurements to be taken from up to four antennas, permitting three independent baselines for use in attitude determination. The correlators are software configurable so that the number of channels assigned in each correlator can be altered depending on the application. This allows 12 channels to be assigned in each correlator for fast time-to-first-fix (TTFF) when positioning, and 6 channels to be assigned to each antenna when using the receiver to determine attitude.

The parallel architecture has a number of benefits over alternative designs such as multiplexing receivers [Cohen, 1992]. For example, the signal to noise ratio achieved by receivers with a parallel architecture is generally higher than that of multiplexing receivers. For both parallel and multiplexing architectures all measurements are referenced to a common clock, thereby removing the need for the complex modelling of the clock parameters that is needed when using multiple receivers. However, multiplexing receivers face particular problems with aliasing and data decoding, which are not an issue for parallel architectures.

The onboard ARM processor provides the flexibility to implement a multitude of different algorithms for real time operation on the receiver. The onboard software can be easily updated using the SGR-20's flash update facility, allowing new code to be uploaded to the receiver, even whilst in orbit, in order to implement new algorithms, test their robustness and improve on them over time.

There are a number of limitations caused by the SGR-20 hardware which affect the scope of this work:

- The SGR-20 only provides single-frequency measurements on L1
- It only has 24 channels which provide a maximum of six measurements per baseline when calculating three-axis attitude when in its attitude configuration
- The RF Front-ends induce an arbitrary phase bias into the carrier phase measurements, which contributes to the line bias
- All patch antennas have asymmetries in their effective phase centres which are made worse by ground plane inadequacies.

2.5 Literature review

In this section an overview of the relevant literature is provided. The main areas of interest for GPS attitude determination are integer ambiguity resolution, attitude estimation algorithms and the error sources which affect GPS attitude determination. Each of these areas is examined below. An overview of previous GPS attitude experiments involving spacecraft is also given.

2.5.1 Integer ambiguity resolution

There are a number of proposed methods for GPS attitude determination that do not require knowledge of the integer ambiguities (such as [Weill, 1995]), but most methods rely on first solving the integer ambiguity problem.

Many integer ambiguity resolution algorithms use the method first proposed in [Hatch, 1991] of splitting the available measurements in to a *primary* and *secondary* set. An integer search over two or three dimensions is conducted and the primary set is used to solve directly for a trial baseline pointing. The trial baseline solution is in turn used to estimate the integers for the secondary set of measurements and in general the trial integer solution which minimises a least-squares cost (subject to some constraints) is chosen as the correct solution.

There are two main issues with integer search techniques. One is that the search space can be prohibitively large, which is why much research has been focused on techniques to reduce this search space sufficiently, without running the risk of losing the correct solution. [Brown, 1992] and [Quinn, 1993] used the geometry of multiple baselines as a constraint to narrow the ambiguity search-space. The other issue is that search-based techniques generally aim to find the integer ambiguity solution that minimises the mean square cost. In the presence of noise this does not necessarily guarantee the correct answer [Crassidis 1999b]. [Martin-Neira, 1995] provides an excellent proof of this issue.

[Quinn, 1993] proposed a method based on double-difference measurements. The method performs a search of the ambiguity space for each baseline, using knowledge from the first baseline to constrain the second and so on. Both [Brown, 1992] and [Hatch, 1994] discuss the procedures for efficiently searching the ambiguity space, and their work forms a basis for that done by Quinn. Quinn's work only provides instantaneous ambiguity resolution when using at least four measurements, two or more baselines and multiple frequencies.

The method described in [Knight, 1994] is a proven ambiguity search technique that has been used operationally in the 'Vector' attitude determination system developed by Trimble. The ambiguity search problem is formulated as a maximum-likelihood optimisation, which attempts to maximise the probability density of the phase measurements by adjusting the vehicle attitude and carrier cycle integer parameters. An interesting feature of Knight's method is that it uses a recursive filter to create a decision tree for the possible integer solutions, which allows the large search space to be traversed in an efficient manner by pruning branches of the tree that are less likely to contain the correct solution. The performance of this method was demonstrated in the presence of multipath on the ground, although a number of constraints had to be imposed in order to guarantee the performance including a priori knowledge of the line bias. The author conceded that false solutions were occasionally output by the method, and therefore a maximum likelihood comparison of the top two solutions was necessary in order to reduce the number of false solutions. It was stated that the installation used in the testing of this algorithm resulted in no false solutions, but no mention is given of how this was practically achieved.

The Null Space method [Martin-Neira et al, 1995] uses the fact that the domain of candidate solutions lies close to the null space of the matrix of the residuals and has a dimension equal to that of the physical space. Simulator tests showed good convergence for poor initial attitude estimates and a fast solution of the integer ambiguities that could be suitable for real-time applications under certain conditions. It was suggested by the author that the method could be extended to a motion-based method to allow for increased robustness. The performance has not been verified with real GPS data [Daganzo and Pasetti, 1998].

[Cross and Ziebart, 2003] take a different approach to most integer search methods by conducting the search in the attitude domain. The position of the master antenna is first fixed using the navigation solution. The position of the slave antennas are mathematically tumbled around this point, retaining their relative geometry based on the known baseline vectors in the body-referenced frame. A cost function is used to evaluate each orientation. The orientation that minimises the cost function is used to estimate approximate Euler angles, which are in turn used to fix the integer ambiguities. This method was shown to work in simulation with up to 10mm RMS measurement noise. However, the algorithm was deemed inefficient for implementation in real-time onboard the GPS receiver hardware.

The SNUGLAD method [Kee et al, 2003] is another search based technique that is based on the technique proposed in [Hatch, 1991]. This integer ambiguity resolution algorithm uses the known baseline length to constrain the integer search space and a stochastic model of the measurement noise to test the goodness of fit of the integers in the secondary set. Multiple baselines are used to constrain the integer search further, but the work only describes a single-epoch method and no description of how to extend the method to multiple epochs to provide greater robustness is given.

The method described in [Purivigraipong, 1998] is also a search-based technique. The method follows the work done by [Hatch, 1991] in realising that the double-difference measurements from four satellites, given a trial integer set, generate a unique solution of the pointing of one. Rival solutions using different trial choices of integers are ranked in terms of a cost equal to the difference between the calculated baseline length and the true baseline length (known from body-defined geometry). The solution that minimises this cost is deemed the most likely solution. The drawback of this method is that as with other such methods the solution that minimises the cost in a single epoch is not necessarily the correct solution. Another drawback is that by adopting Gram-Schmidt orthogonalisation to generate apparent satellites in orthogonal directions the method is limited to using just four satellite measurements.

A number of methods use the relative motion of the user and the GPS constellation to aid the integer ambiguity resolution process. In general, this means that by studying a number of solutions over multiple epochs the correct answer will present itself due to changes in platform attitude or position. Such methods are deemed more robust and reliable. A number of authors testify to this including [Cohen, 1992] and [Ward, 1996].

Cohen described three methods based on different cases of motion. These were platform motion (where the timescale of platform motion is very much faster than the timescale of GPS satellite motion), SV motion (static platforms), and quasi-static motion (where the timescale of platform motion is comparable to that of the GPS satellites) [Cohen, 1992]. The quasi-static motion scenario is the one most suited to use on satellites in Low Earth Orbit. This scenario assumes the user is moving at a comparable rate to the GPS satellites. Batch processing methods are used to solve for an initial attitude and attitude rate. These are then used to refine the actual attitude using a further batch technique. Cohen states that whilst satellites moving in and out of visibility complicate the problem, the accelerated time-scales of motion seen in LEO reduce the time needed for motion-based methods to converge on a solution. The static and quasi-static cases were both tested on the GPS Attitude and Navigation experiment (GANE) [Lightsey, 1997]. The results showed that the static method did not converge to a solution, but the quasi-static solution had a reliable performance. The quasi-static method has a number of drawbacks – a prior attitude estimate must be given, and the method is an iterative batch estimator that may not converge if a wrong prior attitude is given [Purivgraipong, 2000]. However the main problem with this method is that it requires three non-coplanar baselines in order for the batch-least squares estimation to be full rank and so it not practical for most small satellite platforms which can only accommodate coplanar baselines.

Another method that relies on the relative motion of the user and GPS constellation is presented by Crassidis [Crassidis et al, 1999]. In this method, the line-of-sight vectors to the GPS satellites are represented by the sum of two vectors, one depending on the phase measurements, the other on the integer ambiguity. This method requires no prior attitude knowledge, requires less computational effort than similar techniques [Conway et al, 1996] and is non-iterative so less likely to converge on a wrong solution. It also provides an integrity check. The method was tested using a Trimble TANS Vector receiver and a dynamic hardware simulator, and was shown to produce viable results. The main disadvantage, which would preclude its use on small satellites, is that it requires three non-coplanar baselines.

Methods based on using data from multiple epochs can be shown to be more robust given measurement errors that approximate a Gaussian distribution. However, [Kee et al, 2007] found that because in reality there is no such thing as ideal Gaussian noise (because of unmodelled errors such as multipath) that even using multiple epochs problems can occur due to the residuals converging to a value close to zero rather than exactly zero when taken over many epochs. Their solution was a pseudo-moving average filter which relied on an empirical design parameter. Ideally an improved robust ambiguity algorithm would not rely on an empirical filter to ensure convergence on the correct solution.

More recently the most commonly used is to calculate a *float solution* to the ambiguities that are then fixed to integers either by a simple process such as rounding or by more advanced methods, such as the Local Minima Search Algorithm [Pratt et al, 1997] or the LAMBDA method [Teunissen, 1995]. Float solutions can be calculated using just a single-epoch of data if accurate code-phase (or *pseudo-range*) measurements are available (see section 4.1.1.1). If only carrier-phase measurements are available it is also possible to calculate float solutions using carrier phase measurements taken over multiple-epochs, with the inter-epoch time span being dependant on the relative motion of the user and GPS constellation.

The Least-squares Ambiguity Decorrelation Adjustment (LAMBDA) method has been well developed. Teunissen noted that the uncertainty in the real-valued ambiguities estimated using a float solution are highly correlated, which results in a confidence ellipsoid (representing the uncertainty in each dimension of the ambiguity problem) that is rotated with respect to the coordinate axes and highly elongated in one direction. This is particularly true in the case of short observational time spans [Teunissen, 1994]. The basic idea of the LAMBDA method is that integer ambiguity estimation becomes trivial once the confidence ellipsoid of the ambiguities equals a sphere. An excellent example of how the LAMBDA method is used to decorrelate the integer ambiguities is shown [Verhagen and Teunissen, 2004] which plots the two-dimensional probability density function of the float ambiguity residuals before and after the LAMBDA method is applied.

The LAMBDA method is widely used in surveying and real-time kinematic (RTK) applications, and its use for ground-based attitude determination has been demonstrated [Simsky et al, 2005]. Most users of the LAMBDA method rely on geodetic quality receivers with large choke ring antennas to obtain the high success rates demonstrated in the literature, and it has been shown that the success rate is much lower (~50-60%) when standard navigation quality receivers are used. This is due to the fact that most LAMBDA method users utilise both code phase (pseudo-range) and carrier phase measurements in the float solution and only geodetic quality receivers can achieve the low code phase noise required (typically less than 0.05m RMS) to ensure the high success rate of the standard LAMBDA method. Many researchers have focussed on potential improvements to the LAMBDA method, mainly on imposing baseline constraints [Moon and Verhagen, 2006], [Buist, 2007], [Monikes et al, 2005]. Such constraints generally result in a 100% success rate in simulation but a slightly lower success rate when real data is considered, particularly when standard navigation quality GPS receivers are used [Moon and Verhagen, 2006].

2.5.2 Attitude algorithms

Much research has been conducted on methods for determining the attitude of a platform based on measurements from many different types of sensors. Typically these algorithms can be classified in to two groups – those which rely on scalar measurements and those that rely on vector measurements. Both types of algorithms can be applied to the problem of GPS attitude determination.

Scalar methods are generally non-linear and so require *a priori* information in order to solve for the attitude. Examples of such methods are the sLSE algorithm devised by [Cohen, 1992] which was used in [Purivigraipong, 2000], and the Attitude Point Solution method described in [Ward, 1996]. Both methods are very similar and use an iterative least-squares approach to calculate a correction to an *a priori* attitude estimate.

Vector-based methods have the advantage that they typically do not require an initial estimate of the attitude in order to calculate the solution. Vector-based methods require knowing at least two non-collinear vectors in both the body-referenced and orbit-referenced frames. The TRIAD algorithm, detailed in 2.3.3.2, and taken from [Wertz, 1978] is a deterministic method for solving for the attitude matrix, whereas, the remainder of the methods described in this section are statistical estimators that use information from many vectors to find the optimal solution. The problem with the TRIAD method is that only two vectors can be used as inputs, meaning that when using sensors such as GPS receivers that provide many simultaneous measurements, information is discarded, and therefore the solution is sub-optimal.

The q-Method [Wertz, 1978] provides a means for calculating a statistically optimal estimate of the attitude by minimising a cost function based on Wahba's formulation [Wahba, 1965] expressed in terms of quaternions. The cost function is reformulated as an eigenvalue problem in which the optimal solution for the attitude is an eigenvector corresponding to the maximum eigenvalue of a matrix. There are a number of ways of solving for the eigenvalues and eigenvectors of a matrix, such as the QUEST algorithm described below.

The QUEST algorithm given in [Shuster and Oh, 1981] provides an efficient way of solving the eigenvector problem using an approximation of the largest eigenvalue. In the q-Method the aim was to maximise the gain function by finding the largest eigenvalue of a matrix. The QUEST algorithm uses an approximation of the largest eigenvalue to speed up the calculation of the corresponding eigenvector, which is the quaternion corresponding to the optimal attitude estimate. The QUEST algorithm does this by using Rodriguez parameters to reformulate the quaternion so that it can be solved using simple linear algebra. There are a number of problems with this approach. The first is that the Rodriguez parameters become singular when the rotation is 180 degrees. Shuster and Oh devised a method based on a series of sequential rotations to combat this problem. The second is that it requires efficient linear algebra routines to solve for the Rodriguez parameters, otherwise the benefit of QUEST over other methods of solving eigenproblems may be lost.

[Purivigraipong, 2000] describes an iterative vector based method that uses a least-squares formulation to determine the attitude by comparing multiple vectors given in both body and orbit defined coordinate frames. It does not suffer from regions of inaccuracy that hampered previous techniques, as well as not requiring an initial estimate of the attitude to guarantee convergence. Being a statistical attitude estimator it can accommodate a large number of vector measurements to produce an optimal estimate of the attitude. Previous testing was shown in [Purivigraipong, 2000] and [Urhan, 2002].

2.5.2.1.1 Multipath mitigation

The effects of multipath can be mitigated by modelling the multipath environment surrounding the antenna allowing a subtraction of the predicted errors. One method based on the Geometric Theory of Diffraction (GTD) provides an approximation of the electromagnetic field including the direct, reflected and diffracted signals [Gomez et al, 1995]. The disadvantage of this method is that it requires exact knowledge of the reflection coefficients of the surfaces surrounding the antenna, which may not be within the bounds of normal engineering tolerances. However, test results on the ground showed that the differential phase predictions using GTD are close to the measurements (cited from [Purivigraipong, 2000]).

A second method was proposed by [Cohen, 1992] who fitted an 8th order spherical harmonic model to the incoming signals and demonstrated a forty percent reduction in the carrier phase residuals. This work was re-examined by [Reichert and Axelrad, 1997] who compared the spherical harmonic model with a polynomial and a grid-based model, of which the grid was shown to provide the most improvement. Reichert and Axelrad also examined a different method using SNR measurements to characterise an effective reflector. Their method attempts to model a single reflector using a batch estimator, but it does not show a significant improvement for tests performed on the CRISTA-SPAS experiment [Reichert, 1999]. [Lopes and Milani, 2000] give an alternative map-based calibration method based on a Taylor series projection of a sphere, instead of a spherical harmonic representation. The advantage of this method is that it does not suffer from a singularity at zenith, which is important to GPS attitude determination because the antennas are usually coplanar with their boresight at zenith. This technique was taken further by [Wong, 2004] who showed that a 22nd order spherical harmonic model of the multipath environment can be used to achieve sub-millimetre accuracy in the multipath correction to carrier phase measurements. After removing the multipath error, the error of GPS attitude determination on one baseline caused by multipath is suppressed from 87.7mm^2 to 0.51mm^2.

Spectral processing through either Fast-Fourier Transforms or Wavelets has also been examined for multipath mitigation. The benefits of wavelet-based methods for carrier phase multipath are negligible due to their inability to remove low frequency multipath, as shown in [Souza, 2004].

2.6 History of space-based GPS attitude experiments

To date there have been a number of GPS attitude experiments on spacecraft. Nearly all were conducted by the United States, and many involved large spacecraft including the Space Shuttle and the International Space Station. Details of these experiments including the GPS receiver used, the baseline configuration, the reported accuracy and the reference sensors are given in the table below.

Table 2-1 Overview of space-based GPS attitude experiments

Launch	Mission	GPS Receiver	Antennas	Baseline Configuration	RMS Error	Reference Sensors
April 1993	RADCAL	Trimble Quadrex	4	Coplanar (0.67m)	Within 3 deg	Magnetometers
Nov 1994	CRISTA-SPAS	Trimble Vector	4	Non-Coplanar (1, 1.2, 0.8m)	Within 0.5 deg	Star Tracker and IMU
March 1996	REX II	Trimble Vector	4	Coplanar (0.67m for all)	Within 3 deg	Magnetometers and Coarse Sun Sensor
May 1996	GANE	Trimble Vector	4	Coplanar (1.5, 3, 3.3m)	Within 0.5 deg	Star Tracker and IMU
April 1999	UoSAT-12	SGR-20	4	Coplanar (0.65, 0.65, 0.86m)	Within 1 deg	Star Tracker, Rate Gyro, Earth Horizon Sensor, Sun Sensor and Magnetometer
May 2000	SOAR	SIGI	4	Coplanar (1.5, 3.6, 3.2m)	Within 0.5 deg	Star Tracker
Feb 2001	ISS	SIGI	4	(1.5m, 1.5m, 1.5m)	0.5 deg	Star Tracker and IMU (on Space Shuttle)
Oct 2003	SERVIS-1	INU	3	Coplanar (1.4, 0.98m)	Within 0.3 deg	Star Tracker
Oct 2005	TOPSAT	SGR-20	4	Coplanar (0.68, 0.71, 0.42m)	TBD	Earth Horizon Sensor, IMU, Sun Sensor and Magnetometer

2.6.1 Non-SSTL missions

2.6.1.1 RADCAL

RADCAL (RADar CALibration) is a gravity gradient stabilised satellite which was launched in April 1996 into a polar orbit at an altitude of 815km [Cohen *et al.*, 1993]. RADCAL had four GPS antennas mounted on the space facing facet, with each antenna canted outwards from zenith at a 17 degree angle to improve visibility and reduce multipath from the gravity gradient boom.

A Trimble TANS Quadrex receiver was used to collect measurements for GPS attitude determination in post-processing. This receiver uses a special multiplexing design so that the same RF section is used for all four antennas thereby eliminating any line bias issues related to the receiver hardware except for cable differences.

RADCAL used a motion-based method to solve the integer ambiguities [Cohen *et al.*, 1993]. Since the RADCAL satellite was constantly rotating about its yaw axis there was sufficient platform motion to allow the motion-based method to successfully resolve the integer ambiguities using eight minutes of data.

Ground experiments using the same microstrip patch antenna as was employed on RADCAL suggested an RMS multipath error of around 5mm, which was supported by the RADCAL flight data. [Cohen *et al.*, 1993] states that the RMS of the phase residuals was around 7mm which they determined should result in an attitude accuracy of around 0.5 degrees once the correct line biases and baseline lengths had been obtained. [Lightsey, 1997] estimated that the RMS residual between GPS attitude and magnetometer-derived attitude was around 3 degrees (1 sigma) for all attitude angles, but this was more likely due to the error in the magnetometer-derived attitude estimate than the GPS attitude estimate.

2.6.1.2 CRISTA-SPAS

The CRISTA-SPAS satellite was a 3-axis stabilized flight experiment built by Daimler-Benz Aerospace and flown by NASA on the Space Shuttle [Ward, 1996]. It was released by the Space Shuttle Atlantis and later retrieved and returned to Earth. During its flight its orbital altitude was approximately 300km. Attitude determination was performed by a star tracker-gyro inertial measurement unit (IRU), which provided a reference attitude claimed to have an RMS error of less than 0.05 degrees.

The CRISTA-SPAS used an Alcatel receiver provided by Space Systems/Loral to provide navigation data, and a Trimble TANS Vector GPS receiver that had been modified by Stanford University to provide GPS attitude determination. This experiment was the first demonstration of real-time GPS attitude determination in space [Reichert and Axelrad, 2001]. They demonstrated a quaternion point solution attitude estimation algorithm that gave estimates with an RMS error of less than half of one degree in all three axes for the CRISTA-SPAS mission.

Figure 2-10 CRISTA-SPAS

2.6.1.3 REX II

REX II was a gravity gradient stabilised spacecraft launched in March 1996 [Freesland *et al.*, 1996]. It successfully performed onboard attitude estimation and closed loop control using GPS measurements. The GPS attitude solution was always checked with a coarse attitude derived from magnetometer measurements to ensure that the disagreement between different sensors was less than 15 degrees [Freesland *et al.*, 1996].

The primary attitude sensors used on REX II were magnetometers and coarse sun-sensor that resulted in an RMS attitude error of 3 degrees and so the determination of the accuracy of the GPS attitude solution could only be done to this level [Lightsey *et al.*, 1996].

2.6.1.4 GANE

The GANE (GPS Attitude and Navigation Experiment) was flown on the Space Shuttle Endeavour, STS-77 [Carpenter and Hain, 1997]. Four GPS choke ring antennas formed a coplanar configuration, and were mounted on the experiment platform in the shuttle's payload bay. The platform used for GANE is an idealised system for GPS attitude determination that could not reasonably be accommodated on a microsatellite platform.

The GANE experiment used an IMU and star tracker to provide an external attitude reference and the GPS attitude solution agreed with the reference attitude to 0.2 degrees RMS in yaw and pitch, and 0.4 degrees in roll [Carpenter and Hain, 1997].

2.6.1.5 SOAR

The SOAR (SIGI Orbital Attitude Readiness) experiment flew for the first time during the STS-101 mission of the Space Shuttle Atlantis in May 2000 [Um and Lightsey, 2000]. The SOAR experiment was conducted to determine the suitability of GPS attitude determination for used on the International Space Station (ISS) and the Crew Return Vehicle (CRV).

The experiment utilised the SIGI sensor which was composed of a Trimble Force-19 GPS receiver, ring laser gyros, accelerometers and a microprocessor. The SIGI sensor could provide attitude solutions with stand-alone GPS measurements and with integrated GPS/INS measurements.

SOAR used a search-based integer ambiguity resolution method based on a maximum-likelihood estimation technique. The integer ambiguity resolution algorithm was aided by estimating the antenna boresight vector from SNR measurements and constraining the integer search space by assuming that the pitch and roll angles were within 15 degrees of the estimated antenna boresight.

The SOAR experiment performed attitude determination onboard in real-time to an accuracy of 0.41 degrees using on GPS double-difference carrier phase measurements. Using line-bias modelling the attitude error was reduced to 0.16 degrees [Um and Lightsey, 2000].

2.6.1.6 ISS

The International Space Station (ISS) carries two SIGI sensors in the U.S. lab which was launched on 7th Februrary 2001 [Gomez, 2002]. The ISS began using the GPS attitude capability on 20th April 2002.

Specific problems relating to the use of GPS attitude determination on the ISS included cable runs of over thirty metres which were connected for the first time in orbit (and so could not be pre-

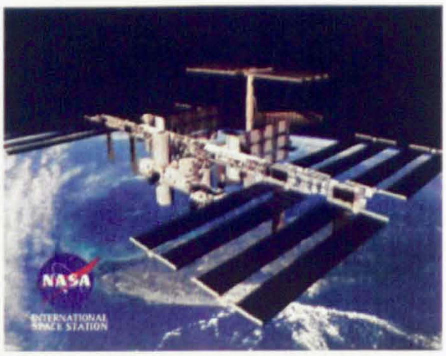

Figure 2-11 International Space Station

calibrated); the unique pointing modes used by the ISS and the multipath environment due to the large number of potential reflectors such as surrounding trusses and the large solar panels. The ISS used choke-ring antennas to help mitigate multipath, and the antennas formed a 1.533 metre rectangle.

The final GPS attitude solution onboard the ISS was based on double-difference carrier phase measurements to eliminate the line bias caused by the long cable lengths. The stand-alone GPS attitude solution was not accurate enough to meet the 0.5 degree requirement, and so the ISS's attitude determination filter combines the GPS receiver's attitude determination information with data from the ISS rate gyro assembly (RGA) to produce the ISS attitude solution [Gomez and Lammers, 2004].

2.6.1.7 SERVIS-1

Space Environment Reliability Verification Integrated System (SERVIS-1) was developed by the Institute for Unmanned Space Experiment Free Flyer (USEF) in Japan. It was launched on October 30th 2003 in to a sun-synchronised orbit with an altitude of around 1000km [Buist, 2006].

GPS attitude determination is performed on SERVIS-1 using a GPS receiver called the 'Integrated Navigation Unit' (INU) built by NEC Toshiba Space systems. The INU consists of both a GPS receiver and a star camera and in the nominal usage mode both sensors are used in a Kalman filter to provide a more robust attitude solution. The GPS receiver makes use of 18 L1 channels on 3 antennas mounted on the space facing facet of the satellite. GPS attitude initialisation took around ten seconds and comparison of the GPS attitude solution with the onboard star camera showed the GPS attitude estimate was accurate to around 0.3 degrees. The GPS attitude solution was calculated onboard the INU using a Kalman filter, which resulted in errors of up to 3 degrees due to the lag of the filter.

2.6.2 SSTL/SGR-20 missions

To date SSTL has flown three microsatellites with the necessary hardware for GPS attitude determination. Details of each satellite are given below.

2.6.2.1 UoSAT-12

The construction of the SGR-20 was sponsored by the European Space Agency to allow the investigation of the use of GPS attitude determination on a microsatellite in Low Earth Orbit. The SGR-20 flew for the first time on the UoSat-12 mission, which was a technology demonstrator carrying a number of different experimental payloads.

UoSat-12 was used to study GPS attitude determination, and resulted in the awarding of two PhDs, the first to [Purivigraipong, 2000] for his work on attitude determination using the SGR-20, and the second to [Wong, 2004] for his

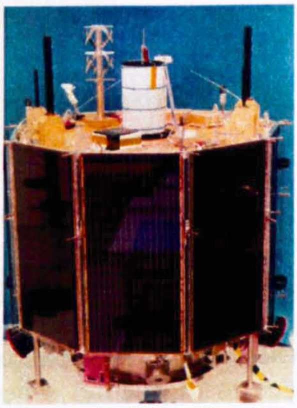
Figure 2-12 UoSat-12

work on multipath mitigation through mapping using spherical harmonics.

UoSat-12 flew four low-profile GPS patch antennas on its zenith facet to carry out the GPS attitude determination experiment.

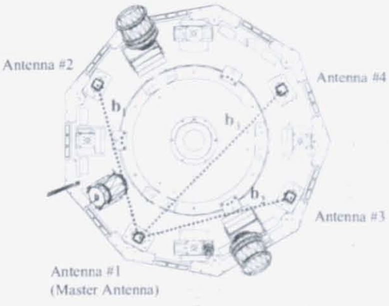

Figure 2-13 UoSat-12 Zenith Facet

Antenna 1, 2 and 3 were on the same level, while antenna 4 was placed 155 mm lower according to the mechanical drawing. The field of view for antenna 1, 2 and 3 had a 75^0 co-elevation angle.

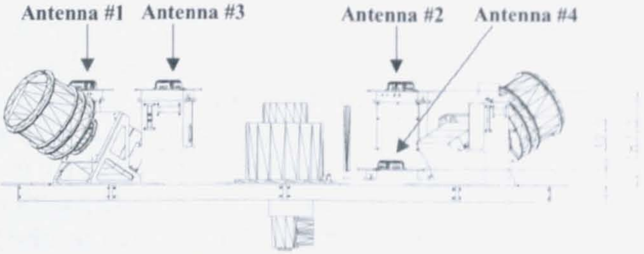

Figure 2-14 View of UoSat-12 GPS antennas from +X direction

The nominal baseline vectors derived from MCAD drawings for UoSat-12 were:

Table 2-2 UoSat-12 nominal GPS antenna baselines from mechanical drawings

Baseline	X_B(m)	Y_B (m)	Z_B (m)
1	-0.1677	-0.6257	0.0000
2	0.6257	0.1677	0.0000
3	0.5927	-0.6067	0.155

2.6.2.2 Bilsat-1

Bilsat-1 formed part of the Disaster Monitoring Constellation (DMC) and was built by SSTL for Turkey. It carried an SGR-20 with four antennas as well as a prototype star tracker. It was hoped that Bilsat could be to used during the research undertaken for this thesis, but due to difficulties scheduling GPS attitude experiments

Figure 2-15 Bilsat-1

on Bilsat only two datasets were collected before the satellite's battery reached the end of its working life.

2.6.2.3 Topsat

TopSat was built by SSTL working as part of a consortium of British companies including QinetiQ, Rutherford Appleton Laboratory (RAL) and Infoterra.

Figure 2-16 Topsat

TopSat is a specially designed agile micro-satellite, weighing just 120 kg. It carries an optical camera developed by RAL capable of delivering panchromatic images with a spatial resolution at nadir of 2.8 metres covering a 17x17 km area, and simultaneous three-band multi-spectral images, (red, green, blue), with a resolution of 5.6 metres.

TopSat has a purpose designed Attitude Determination and Control System (ADCS) utilising a combination of an IMU, Earth Horizon sensors, sun-sensors, and magnetometers, permitting pitch compensation manoeuvres, allowing imaging of low illumination scenes.

Topsat has four GPS patch antennas mounted on its space-facing facet which is defined as the –Z facet in the spacecraft body frame. The nominal antenna locations were measured from the three-dimensional MCAD mechanical drawings used in the original construction of the satellite, a snapshot of which is shown in the figure below.

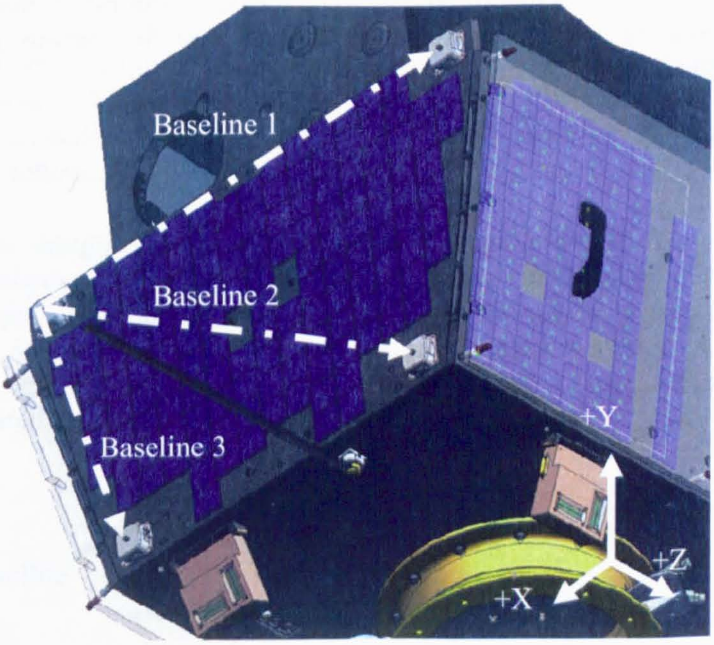

Figure 2-17 GPS antenna locations, baselines and the body-referenced frame on Topsat

The antenna locations relative to the centre of mass of the spacecraft are:

Table 2-3 GPS patch antenna locations on Topsat according to MCAD mechanical drawings

Antenna	X (m)	Y (m)	Z (m)
1	0.3385	0.43365	-0.4318
2	-0.3385	0.43365	-0.4318
3	-0.2435	0.02165	-0.4318
4	0.2435	0.02165	-0.4318

Throughout this work we define three baselines from these antennas using antenna 1 as the master antenna and antennas 2, 3 and 4 as the slave antennas. The resulting *nominal* baseline vectors are:

Table 2-4 Topsat nominal GPS antenna baselines from mechanical drawings

Baseline	X_B (m)	Y_B (m)	Z_B (m)
1	-0.6770	0.0000	0.0000
2	-0.5820	-0.4120	0.0000
3	-0.0950	-0.4120	0.0000

2.7 Conclusions

In this chapter the background to the use of GPS for attitude determination has been given. The concept of attitude has been defined, and it has been shown how attitude can be estimated using GPS measurements. The measurement model used to describe GPS carrier phase measurements has been defined and the various error sources considered in this model have been described.

3 Analysis of spaceflight data

In this chapter data logged in-orbit is analysed to quantify and characterise the various error sources affecting GPS attitude determination.

Throughout this work the ADCS attitude solution is used as 'truth' and for convenience the ADCS attitude solution is hereon referred to simply as 'ADCS'. The quality of the ADCS is analysed and the effect that ADCS error has on comparisons with the GPS attitude solution is investigated. The ADCS is then used to 'survey' the GPS antenna baselines by using a recursive least-squares filter to post-process in-orbit data and solve for the baseline vectors in the body-referenced frame.

The in-orbit data is used to quantify the measurement noise using residuals calculated from the GPS carrier phase measurements. The GPS measurement noise is compared with the GPS-ADCS disparity in order to examine the errors in both systems. A study of the cross-correlation or covariance of the GPS carrier phase measurements is used to attempt to prove that multipath is present in the measurements.

The ADCS is also used to characterise the line bias error observed in the measurements logged by the SGR-20. The effectiveness of estimating the line bias using only GPS measurements is also examined.

Finally a brief study on GPS satellite visibility is provided to demonstrate the effect of the higher relative velocity of a satellite in LEO and determine the field-of-view of each baseline.

3.1 ADCS reference attitude

The ADCS reference attitude is calculated from the combination of Earth Horizon sensors, Sun-sensors, Magnetometers and an Inertial Measurement Unit (IMU) using a Quaternion Extended Kalman Filter (QEKF). A detailed explanation of the mathematics is contained in [Steyn, 1995], [Steyn, 1998] and [Hashida, 1997].

Topsat is a new design of agile microsatellite. It regularly performs a Time-Delay Integration manoeuvre (TDI) which allows it to image for longer periods in order to gather more light. The manoeuvre involves the satellite pitching forward to look at the target as it approaches it. As the satellite passes over the target, it performs an opn-loop slew in pitch in order to 'stare' at the target. Once the manoeuvre is complete the satellite returns to its nominal nadir pointing mode.

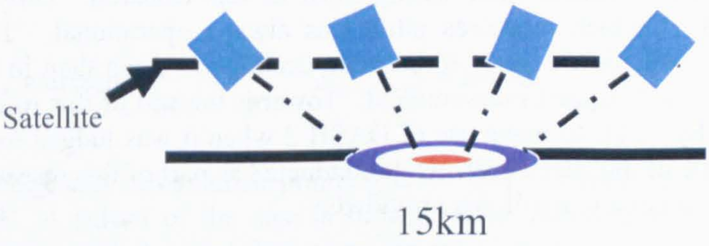

Figure 3-1 Time-Delay Integration Manoeuvre

During the TDI manoeuvre the ADCS controller is operating in an open-loop mode in which only the IMU is used for attitude sensing. The ADCS does not use measurements from the sun-sensors, magnetometers or EHS but simply propagates the state vector using the rate measurements from the IMU.

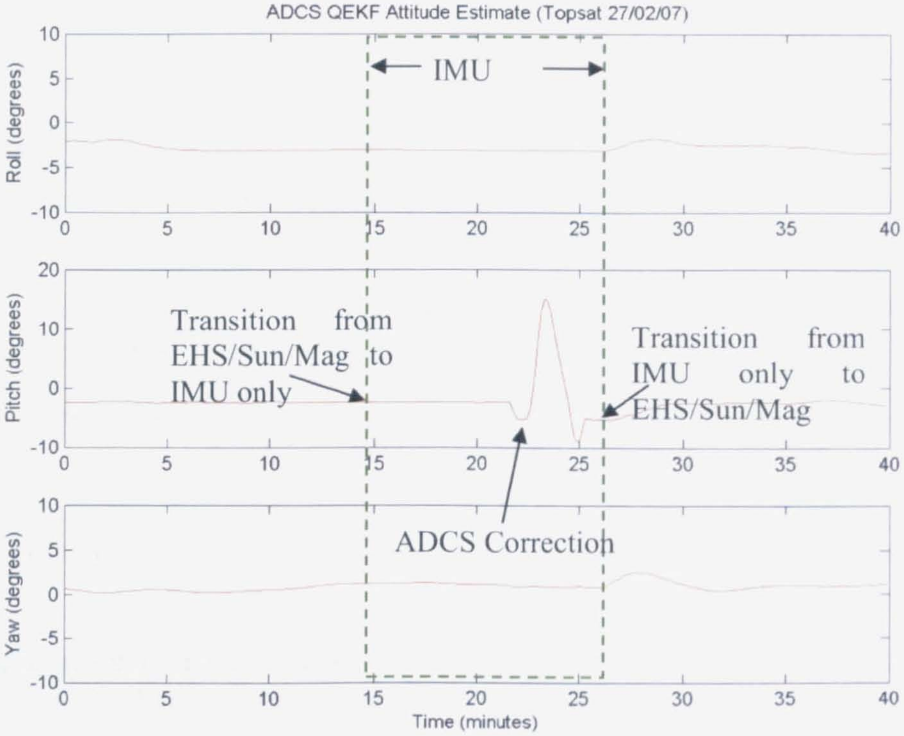

Figure 3-2 ADCS attitude showing typical TDI manoeuvre

3.1.1 ADCS reference attitude error

The ADCS is known to suffer from a number of issues which affect its accuracy. The first issue is that the orientation of the +X 2-axis sun-sensor is known to a limited accuracy and this introduces an error in the ADCS attitude solution when this sun-sensor is used. The second issue is that the momentum wheels induce vibrations in the spacecraft body which cause a jitter in the ADCS reference attitude.

During the initial experiments conducted as part of this research only one of the two EHS on Topsat was in use. The EHS known as 'DASH 2' which is mounted on the pitch axis (and hence measures roll) only worked intermittently and so was not included in the ADCS attitude filter during most of this research. Only the EHS known as 'DASH 1' which measures pitch was always operational. The ADCS attitude estimate was therefore likely to be more accurate in pitch than in roll. This was confirmed from subsequent measurement. Towards the end of this research a fix was implemented by SSTL to make use of DASH 2 when it was judged to be giving valid data, and some of the later experiments conducted as part of this research benefit from the increased accuracy in roll this provided.

The accuracy of the ADCS is monitored by the Topsat consortium by calculating the difference between the commanded ground target and the resulting image centre in the along-track and across-track directions for every image taken. This is shown by Δx and Δy in Figure 3-3.

Figure 3-3 Calculation of attitude error from imagery

Referring again to Figure 3-2 notice that at around twenty-two minutes into the experiment the satellite changes pitch by around minus three degrees. During the initial in-orbit commissioning of Topsat the AOCS engineers at SSTL estimated that the ADCS is subject to a constant rotation from the imager reference frame of:

Roll Offset (Degrees)	Pitch Offset (Degrees)	Yaw Offset (Degrees)
-0.05	-2.97	0.00 (undetermined)

Note that since this rotation was estimated via calibration with ground imagery, the yaw offset was undetermined. To correct for this offset a correction is applied to the ADCS attitude solution before each image is taken to ensure that the imager is correctly aligned with the desired target, as indicated in Figure 3-2. For the purposes of this work the GPS attitude solution is compared with the ADCS reference frame rather than the imager's reference frame since we did not have access to the imager as part of this research.

Assuming that Topsat orbits at an altitude of 686km the along and across track pointing error in degrees can be calculated from Δx and Δy using

$$\varepsilon_{along\ track} = \arctan\left(\frac{\Delta x}{686}\right)\times\frac{180}{\pi};\quad \varepsilon_{across\ track} = \arctan\left(\frac{\Delta y}{686}\right)\times\frac{180}{\pi} \qquad \textbf{3-1}$$

The along-track and across-track pointing error was calculated for all images taken during 2008. A subset of the data is shown in the tables below. From the whole dataset the mean and standard deviations for the along-track and across-track errors with and without the second horizon sensor were calculated.

Table 3-1 Subset of along and across-track errors with respect to commanded image centre (Topsat 2008 – without using DASH 2)

Image	Along-Track Error (km)	Across-Track Error (km)	Along-Track Error (Degrees)	Across-Track Error (Degrees)
2250	6.9	12.54	0.58	1.05
2251	15.97	-23.29	1.33	-1.94
2262	12.08	16.51	1.01	1.38
2274	7.7	-4.8	0.64	-0.40
2275	3.13	4.67	0.26	0.39
2278	5.39	12.92	0.45	1.08
2299	33.57	-23.1	2.80	-1.93
2307	34.8	-10.6	2.90	-0.89
2310	5.7	12.7	0.48	1.06
2311	7.6	4.7	0.63	0.39

Table 3-2 Subset of along and across-track errors with respect to commanded image centre (Topsat 2008 – after DASH 2 fix)

Image	Along-Track Error (km)	Across-Track Error (km)	Along-Track Error (Degrees)	Across-Track Error (Degrees)
2244	7.00	18.00	0.58	1.50
2248	-1.60	22.00	-0.13	1.84
2252	5.00	13.40	0.42	1.12
2260	2.94	11.62	0.25	0.97
2273	-4.48	14.28	-0.37	1.19
2272	4.85	15.50	0.41	1.29
2277	1.75	19.72	0.15	1.65
2282	-3.40	25.49	-0.28	2.13
2285	3.16	18.01	0.26	1.50
2288	7.23	15.92	0.60	1.33

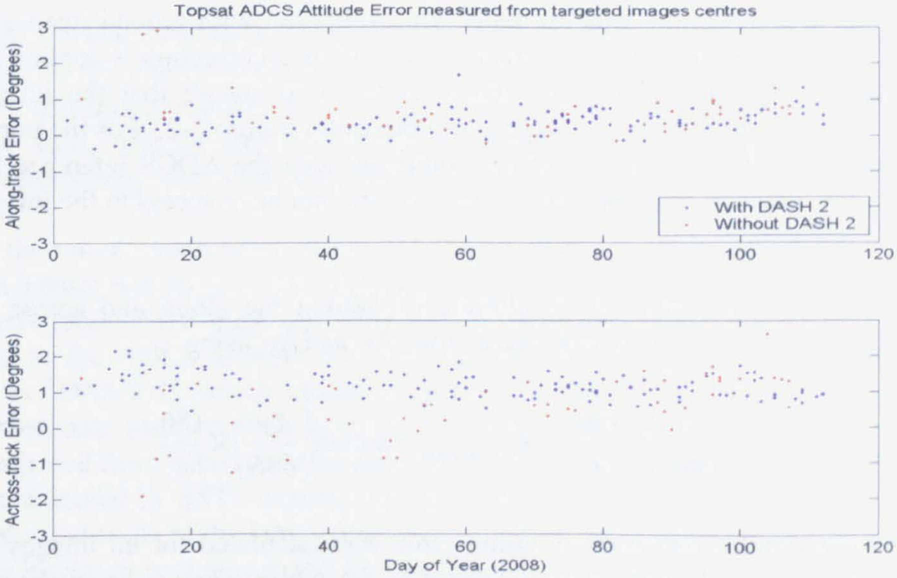

Figure 3-4 Topsat ADCS attitude error measured from targeted image centres

The mean and standard deviation of the ADCS attitude error, with and without DASH 2 are shown in the table below, with the data points plotted in Figure 3-4. The blue points show the ADCS error when both EHS were operational (with DASH 2), and the red points show the error when DASH 2 was not functioning. Note that the calculated error is the disparity between the targeted image centre and the achieved image centre after the rotational correction has been applied to the ADCS attitude.

Table 3-3 Mean and Standard deviation of ADCS pointing error derived from images

	Mean Along-Track Error (Degrees)	Std of Along-Track Error (Degrees)	Mean Across-Track Error (Degrees)	Std of Across-Track Error (Degrees)
With DASH2 (Blue)	0.38	0.30	1.19	0.34
Without DASH2 (Red)	0.60	0.51	0.53	0.89

The results in Table 3-3 show that when both EHS are working the standard deviation of the ADCS attitude error is around 0.3 degrees in each axis. This agrees with the assessment done by SSTL during in-orbit commissioning. When DASH 2 is not working the results show that the ADCS attitude uncertainty increases in both axes, but with a larger increase in the standard deviation of the across-track error.

In a number of areas of this research the ADCS is used to predict the GPS carrier phase measurements. Given the uncertainty in the ADCS it is important to estimate the resulting uncertainty in the predicted carrier phase measurements so that it can be taken into account. Assuming that the spacecraft is maintaining a nadir pointing attitude with zero yaw the along-track and across-track errors can be related to an error in the resultant predicted GPS carrier phase measurements as follows.

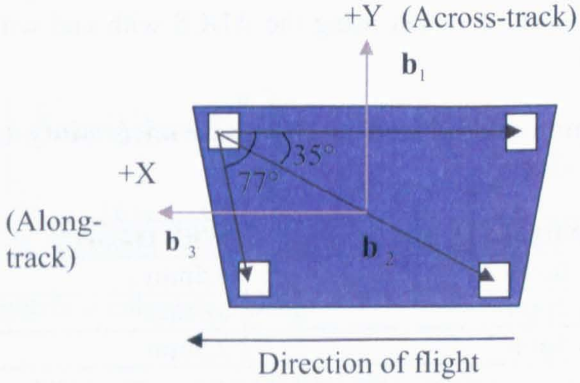

Figure 3-5 Nominal orientation of GPS baselines relative to along-track and across track

The induced error in the predicted carrier phase measurements caused by the ADCS error (having standard deviation σ_{ADCS}) can be calculated according to:

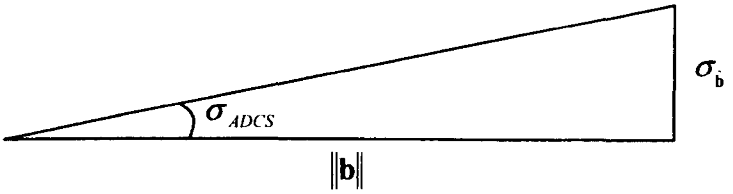

Breaking the ADCS uncertainty down in to its roll and pitch components, σ_ϕ and σ_θ, the resulting error in the predicted carrier phase measurements for baseline 1, which is nominally aligned with the along-track direction, can be calculated directly from Equation 3-2.

$$\sigma_{\dot{\mathbf{b}}_1} = \|\mathbf{b}_{1(B)}\|\sigma_\theta \qquad \textbf{3-2}$$

For baselines 2 and 3 the different orientations with respect to the along-track and across-track vectors must be taken into account. Baseline 3 lies thirteen degrees from the across-track axis. Assuming the errors in the two axes are uncorrelated the error for baseline 3 is therefore

$$\sigma_{\dot{\mathbf{b}}_3} = \|\mathbf{b}_{3(B)}\|\left(\cos^2(13^\circ)\sigma_\phi^2 + \sin^2(13^\circ)\sigma_\theta^2\right)^{1/2} \qquad \textbf{3-3}$$

Similarly, baseline 2 lies thirty-five degrees from the along-track vector and so the error for baseline 2 is given by

$$\sigma_{\dot{\mathbf{b}}_2} = \|\mathbf{b}_{2(B)}\|\left(\sin^2(35^\circ)\sigma_\phi^2 + \cos^2(35^\circ)\sigma_\theta^2\right)^{1/2} \qquad \textbf{3-4}$$

These errors can be used to estimate the error in predicted phase difference measurements calculated using the ADCS attitude for a GPS satellite located at zenith for each baseline. This apparent error when using the ADCS with and without the DASH 2 is shown in Table 3-4.

Table 3-4 Standard deviation of predicted carrier phase uncertainty due to ADCS error

Baseline	**Without DASH 2**	**With DASH 2**
1 (Length 0.677m)	6.0mm	3.5mm
2 (Length 0.713m)	8.2mm	3.9mm
3 (Length 0.423m)	6.5mm	2.5mm

The results in Table 3-4 show that when DASH 2 is not working the ADCS error may result in an increase in the standard deviation of the predicted carrier phase measurement error of up to 8.2mm. Without DASH 2 the error in the GPS-ADCS disparities due to the ADCS attitude error could exceed the expected error in the GPS carrier phase measurements, as calculated in the previous section, meaning the disparities will not be useful for determining the accuracy of the GPS measurements.

The above analysis assumes that the ADCS yaw error is negligible. An ADCS yaw error would add a further contribution to the error in the predicted GPS carrier phase difference measurements. However, the above results are useful since they show that even if both EHS are operational then the standard deviation of the ADCS attitude error will still introduce some error in to comparisons between the two systems, and therefore this error must be taken into account when drawing conclusions on the accuracy of GPS attitude determination.

3.2 Surveying the GPS antenna baselines

In this section the ADCS is used in conjunction with data logged in-orbit to estimate the GPS antenna baselines in the body-referenced frame. This is done to establish whether the baseline vectors determined from MCAD drawings are subject to any error. Any offset in the assumed baseline vectors would result in errors in any integer ambiguity resolution or attitude determination algorithms.

Since the baseline vectors in the body-referenced frame are constant a simple zero-order recursive least-squares filter was implemented to estimate them using the in-orbit data. Assuming that the errors in the ADCS described in the previous section are zero mean then the recursive least-squares filter should simply solve for any rotational offset between the GPS and ADCS body-referenced frames.

3.2.1 Method

Assuming J double-difference carrier phase measurements $\Delta\bar{r}_1[k],\ldots,\Delta\bar{r}_J[k]$ with corresponding double-difference line-of-sight vectors $\mathbf{v}_{1(O)}[k],\ldots,\mathbf{v}_{J(O)}[k]$ an estimated state vector can be calculated as

$$\hat{\mathbf{b}}[k] = \hat{\mathbf{b}}[k-1] + \mathbf{K}[k]\left(\Delta\mathbf{r}[k] - \Delta\mathbf{N}[k] - \mathbf{H}[k]\hat{\mathbf{b}}[k-1]\right) \qquad \textbf{3-5}$$

where

$$\mathbf{H}[k] = \begin{bmatrix} \left(\hat{\mathbf{A}}_{ADCS}[k]\mathbf{v}_{1(O)}[k]\right)^T \\ \vdots \\ \left(\hat{\mathbf{A}}_{ADCS}[k]\mathbf{v}_{J(O)}[k]\right)^T \end{bmatrix} \quad \Delta\mathbf{r}[k] = \begin{bmatrix} \Delta\bar{r}_1[k] \\ \vdots \\ \Delta\bar{r}_J[k] \end{bmatrix} \quad \Delta\mathbf{N}[k] = \begin{bmatrix} \Delta N_1[k] \\ \vdots \\ \Delta N_J[k] \end{bmatrix} \qquad \textbf{3-6}$$

The gain matrix is calculated using

$$\mathbf{K}[k] = \mathbf{P}[k-1]\mathbf{H}[k]^T\left(\mathbf{H}[k]\mathbf{P}[k-1]\mathbf{H}[k]^T + \mathbf{R}\right)^{-1} \qquad \textbf{3-7}$$

where

$$\mathbf{R} = 2\tilde{\sigma}_{\varphi_n}^2 \begin{bmatrix} 2 & 1 & \cdots & 1 \\ 1 & 2 & \cdots & 1 \\ \vdots & \vdots & \ddots & 1 \\ 1 & 1 & 1 & 2 \end{bmatrix} \qquad \textbf{3-8}$$

where $\tilde{\sigma}^2_{\varphi_u}$ is the assumed variance of the total measurement error in the undifferenced carrier phase measurements. The state covariance matrix for the current epoch is given by

$$\mathbf{P}[k] = (\mathbf{I} - \mathbf{K}[k]\mathbf{H}[k])\mathbf{P}[k-1] \qquad \text{3-9}$$

It was assumed that the phase measurements may relate to different satellites in each epoch and so the notation k is used to specify that the integer ambiguity correction may vary from one epoch to the next different satellites are tracked in each epoch. It is to be noted that $\tilde{\sigma}^2_{\varphi_u}$ is purely a formal value here (it can be assigned unity) in order to complete the calculation.

3.2.2 Results

The filter was applied to eight of the experiments logged on Topsat. The filter was run independently for each baseline, and the results from each experiment are shown in the table below (converted to units of metres).

Table 3-5 Baseline vectors estimated using ADCS

Date	Baseline 1 Estimate (metres)			Baseline 2 Estimate (metres)			Baseline 3 Estimate (metres)		
22/02/07	-0.6822	-0.0087	-0.0390	-0.5849	-0.4189	-0.0082	-0.0949	-0.4146	0.0198
27/02/07	-0.6761	0.0007	-0.0309	-0.5846	-0.4095	-0.0168	-0.0965	-0.4119	0.0078
01/03/07	-0.6796	-0.0147	-0.0301	-0.5780	-0.4207	0.0014	-0.0862	-0.4146	0.0246
01/05/07	-0.6729	-0.0129	-0.0216	-0.5690	-0.4267	0.0118	-0.0850	-0.4222	0.0240
09/05/07	-0.6837	-0.0157	-0.0258	-0.5785	-0.4171	0.0116	-0.0825	-0.4206	0.0290
04/07/07	-0.6813	-0.0118	-0.0279	-0.5826	-0.4207	-0.0061	-0.0933	-0.4135	0.0117
10/07/07	-0.6787	-0.0074	-0.0261	-0.5829	-0.4204	-0.0022	-0.0952	-0.4167	0.0137
03/06/08	-0.6815	0.0000	-0.0397	-0.5828	-0.4146	-0.0139	-0.0935	-0.4077	0.0039
Mean	-0.6795	-0.0088	-0.0301	-0.5804	-0.4186	-0.0028	-0.0909	-0.4152	0.0168
s.d.	0.0035	0.0063	0.0064	0.0053	0.0051	0.0107	0.0054	0.0046	0.0089

The plots show the estimate of each component of the baseline vector for the different experiments listed in Table 3-5. From Table 3-5, the mean baseline vectors (in metres) estimated using the ADCS were

$$\hat{\mathbf{b}}_{1,ADCS} = \begin{bmatrix} -0.680 \\ -0.009 \\ -0.030 \end{bmatrix} \quad \hat{\mathbf{b}}_{2,ADCS} = \begin{bmatrix} -0.580 \\ -0.419 \\ -0.003 \end{bmatrix} \quad \hat{\mathbf{b}}_{3,ADCS} = \begin{bmatrix} -0.091 \\ -0.415 \\ 0.017 \end{bmatrix}$$

The body-defined baseline vectors determined from the MCAD drawings are:

$$\breve{\mathbf{b}}_{1,MCAD} = \begin{bmatrix} -0.677 \\ 0.00 \\ 0.00 \end{bmatrix} \quad \breve{\mathbf{b}}_{2,MCAD} = \begin{bmatrix} -0.582 \\ -0.412 \\ 0.00 \end{bmatrix} \quad \breve{\mathbf{b}}_{3,MCAD} = \begin{bmatrix} -0.095 \\ -0.412 \\ 0.00 \end{bmatrix}$$

The disparity between the components of each vector estimated using the ADCS are mostly within one standard deviation of the vectors derived from the MCAD drawings. Given the level of uncertainty in the ADCS due to the problem with DASH 2 the only conclusion that can be drawn is that there is no discernable difference between the two sets of vectors, with the exception of an apparent offset in the Z component of baseline 1.

The pointing error that could result from the difference between the ADCS estimated vectors and the MCAD baseline vectors is calculated according to

$$\langle \Delta_{MCAD-ADCS} \rangle = \sin^{-1}\left(\frac{\left| \hat{\mathbf{b}}_{i,ADCS} \times \tilde{\mathbf{b}}_{i,MCAD} \right|}{\left\| \hat{\mathbf{b}}_{i,ADCS} \right\| \left\| \tilde{\mathbf{b}}_{i,MCAD} \right\|} \right) \qquad \textbf{3-10}$$

Using Equation 3-10 the potential pointing error for each baseline is as shown in Table 3-4.

Table 3-6 Baseline pointing error between ADCS estimated and MCAD derived GPS baselines

Baseline	MCAD-ADCS Baseline Pointing Error (degrees)
1	2.64
2	0.60
3	2.37

The baseline vectors estimated from the ADCS reference attitude using the recursive least-squares filter show an offset from the baseline vectors taken from the MCAD drawings. The difference could be attributed to a combination of the following factors:

- Alignment offsets in the ADCS relative to MCAD tolerances (e.g mis-aligned sun-sensors)
- Alignment offsets in the GPS antenna locations relative to MCAD tolerances (e.g. GPS antenna locations offset from MCAD drawings)
- Systematic offsets in ADCS sensors (e.g. offset in sun-sensor output)
- Systematic offsets in GPS carrier phase measurements (e.g. varying phase centre of patch antennas)

Without a third independent source of attitude information it is difficult to determine the exact cause for the offset. Therefore for the purposes of this thesis it is assumed that the offset is due to alignment offsets of the GPS antennas, and that from this point onwards the ADCS estimated GPS baselines are used to correct for any disparity.

3.3 Estimating measurement noise from GPS residuals

In this section the RMS measurement noise in the GPS carrier phase measurement is estimated using only GPS data. This is achieved by calculating residuals based on a GPS only estimate of the baseline vectors and line bias. Since the residuals are calculated purely from GPS measurements, they are not affected by any external errors such as the error in the ADCS.

3.3.1 Method

For each epoch k with at least four carrier phase difference measurements the baseline pointing and line bias for baseline i are calculated using:

$$\begin{bmatrix}\hat{\mathbf{b}}_{i(O)}[k]\\ \hat{\beta}_i[k]\end{bmatrix} = \left(\mathbf{H}[k]^T\mathbf{H}[k]\right)^{-1}\mathbf{H}^T[k]\left(\bar{\mathbf{r}}_i[k]-\mathbf{N}_i\right) \qquad \text{3-11}$$

Where

$$\mathbf{H}[k]=\begin{bmatrix}\mathbf{s}^T_{i,1(O)}[k] & 1\\ \mathbf{s}^T_{i,2(O)}[k] & 1\\ \vdots & \vdots\\ \mathbf{s}^T_{i,J(O)}[k] & 1\end{bmatrix} \qquad \bar{\mathbf{r}}_i[k]=\begin{bmatrix}\bar{r}_{i,1}[k]\\ \bar{r}_{i,2}[k]\\ \vdots\\ \bar{r}_{i,J}[k]\end{bmatrix} \qquad \mathbf{N}_i=\begin{bmatrix}N_{i,1}\\ N_{i,2}\\ \vdots\\ N_{i,3}\end{bmatrix} \qquad \text{3-12}$$

and the integer ambiguities are determined using the ADCS.

Based on the measurement model given in Equation 2-21 the fundamental residual is obtained by back substitution as

$$\omega_{i,j}[k]=\bar{r}_{i,j}[k]-N_{i,j}-\hat{\beta}_i[k]-\hat{\mathbf{b}}^T_{i(O)}[k]\mathbf{s}_{i,j(O)}[k] \qquad 1\le j\le J[k] \qquad \text{3-13}$$

From this the measurement noise variance is calculated in each epoch k according to

$$\hat{\sigma}^2_w[k]=\frac{1}{J_i[k]-4}\sum_{j=1}^{J_i[k]}\omega^2_{i,j}[k] \qquad \text{3-14}$$

where the division by $J_i[k]-4$ accounts for the number of degrees of freedom in the estimation of the variance due to estimation of the baseline vector and line bias.

An overall mean square is calculated using

$$\bar{\hat{\sigma}}^2_w=\frac{1}{K}\sum_{k=1}^{K}\hat{\sigma}^2_w[k] \qquad \text{3-15}$$

where K is the total number of epochs. Equation 3-15 then provides a meaningful mean square total measurement noise.

3.3.2 Results

The procedure described above was used to estimate the carrier phase measurement noise using in-orbit data logged on both Topsat and UoSat-12. Whilst [Purivigraipong, 2000] and [Wong, 2004] both gave estimates for the carrier phase measurement noise, the method they used was different and so the UoSat-12 data was reprocessed to provide a clearer comparison.

3.3.2.1 Topsat measurement noise

Based on our model the *measurement error* was defined as the combination of receiver noise, line bias and multipath. Line bias has been estimated and removed from the residuals so the following residual plots should provide an indication of the *measurement noise,* which was defined as the combination of receiver noise and multipath.

The residuals $\omega_{i,j}[k]$ calculated in Equation 3-13 for data logged on 27th February 2007 are plotted in Figure 3-6. The different 'tracks' represented by the different colours show the residual for a particular GPS satellite that was tracked on each baseline during the experiment. Note that the gaps in the residuals are caused by periods when the number of available measurements on that baseline was less than five, meaning that the residuals could not be calculated.

It can be seen in Figure 3-6 that the residuals do not appear consistent with a stationary stochastic process of zero mean. Assuming our model is correct, and acknowledging that the baseline vectors have been calibrated using the ADCS, any remaining errors can only be due to measurement errors in the GPS carrier phase.

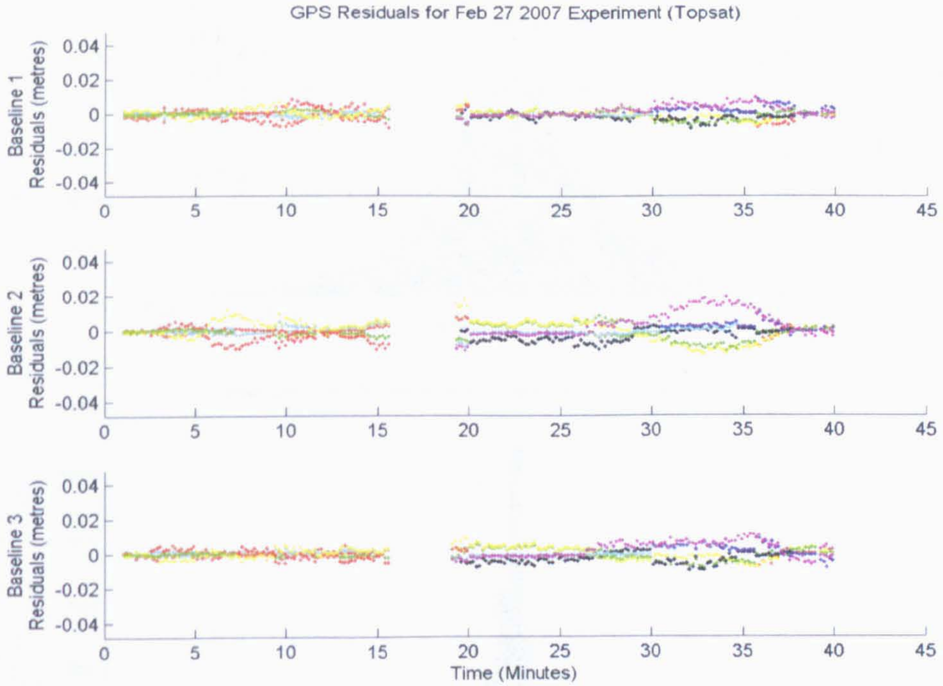

Figure 3-6 GPS residuals for 27th February 2007 Experiment (Topsat)

If the error was simply due to receiver noise then the residuals would appear to be Gaussian with zero mean, as shown in Appendix A. However, some of the residuals show a correlation with time. This is likely to indicate a spatial correlation as the GPS satellites are moving relative to the baselines on Topsat. This is strong evidence that multipath is present in the GPS carrier phase measurements and is supported by evidence from simulations as shown in Figure A-4 in Appendix A. Note that in section 2.3.2.3 the antenna phase response was included under the general term *multipath*, and so these errors could also be due to the phase response of the patch antennas changing as the incident angle of the signal changes. An increased difference in the antenna phase response for baseline 2, due to the different orientations of antennas 1 and 3, could be the cause of the increased RMS measurement noise on baseline 2.

The GPS residuals were calculated for eight experiments conducted up to June 2008. The RMS measurement noise for each experiment is shown in the table below. A histogram showing the distribution of the residuals for each baseline and all experiments is shown in Figure 3-7. Note that these residuals are scaled by a factor of $J/(J-4)$ to account for the estimation of the baseline vector and line bias in Equation 3-11.

Table 3-7 R.M.S. Measurement Noise for each experiment (Topsat)

Experiment Date	Baseline 1 (mm)	Baseline 2 (mm)	Baseline 3 (mm)
22/02/07	3.9	7.2	4.4
27/02/07	6.8	9.1	6.1
01/03/07	4.8	6.8	6.6
01/05/07	5.0	7.2	5.3
09/05/07	8.4	5.9	4.0
04/07/07	3.8	9.0	5.4
10/07/07	6.1	6.7	4.6
03/06/08	4.4	5.8	3.6
Mean Measurement noise	5.6	7.3	5.1

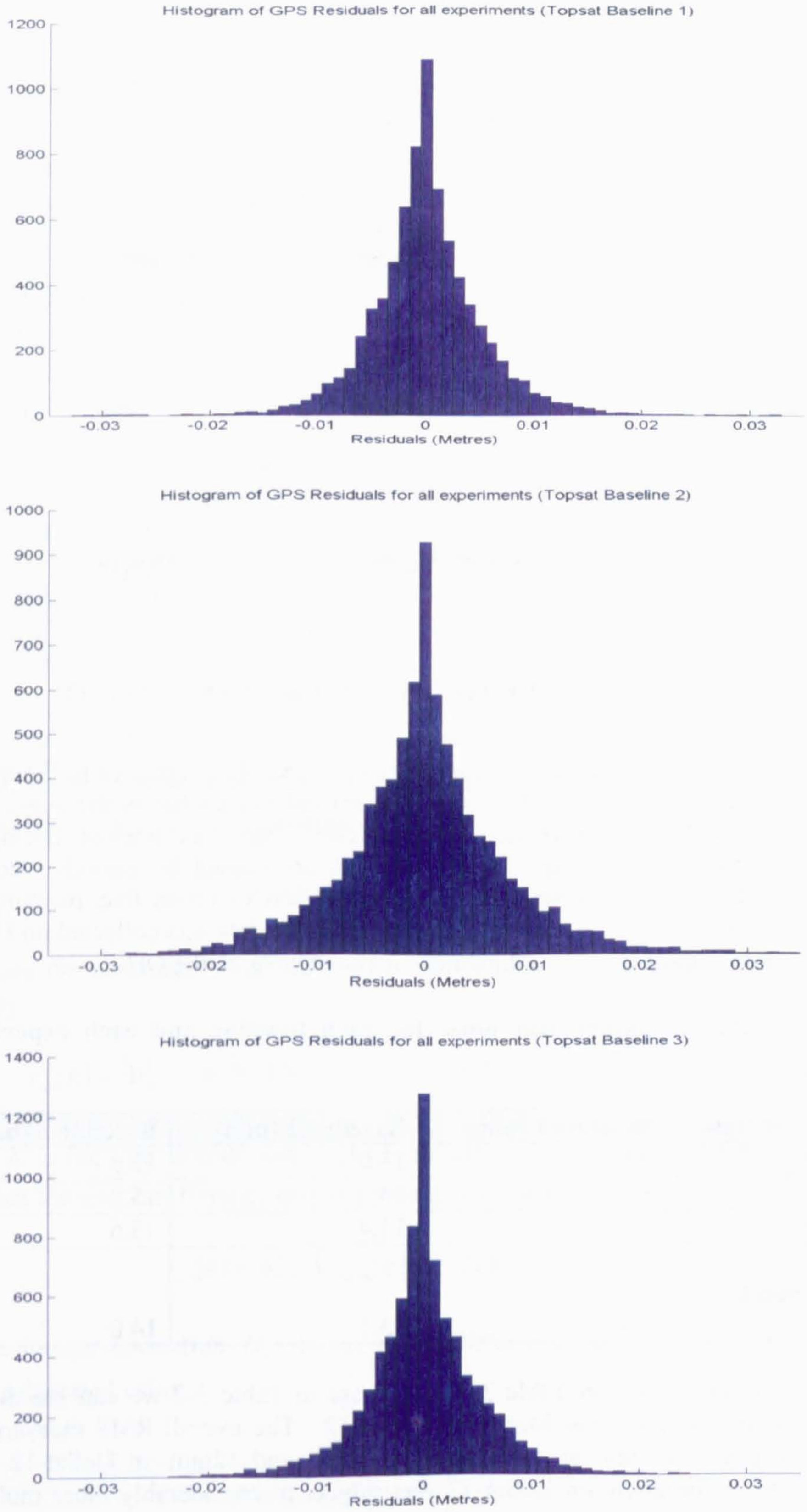

Figure 3-7 Histograms of GPS residuals for Topsat (Baselines 1,2,3 from top)

3.3.2.2 UoSat-12 measurement noise

The GPS carrier phase measurement noise on UoSat-12 is estimated using three data sets recorded on 13th, 14th and 17th January 2000.

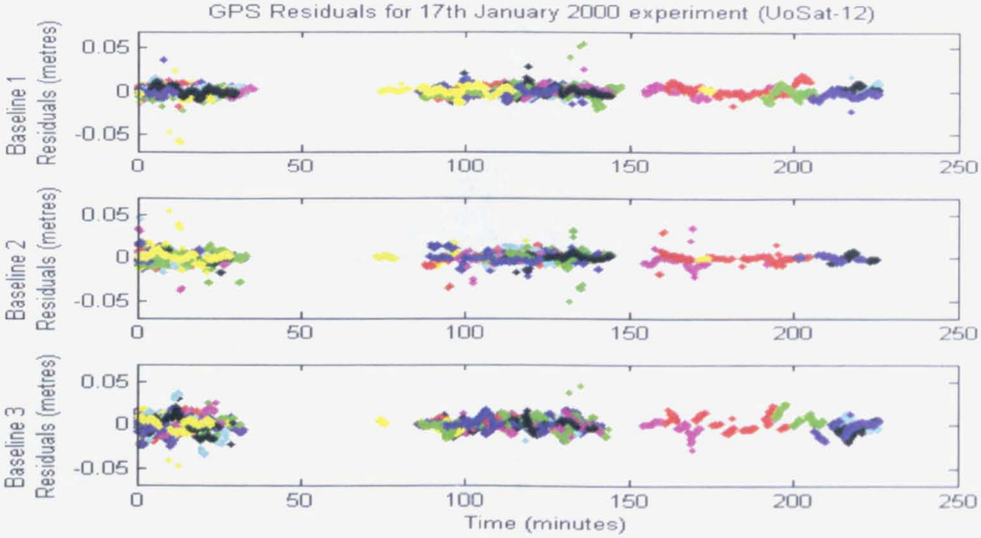

Figure 3-8 GPS residuals for 13th January 2000 experiment (UoSat-12)

The residuals for 13th January 2000 experiment on UoSat-12 are plotted in Figure 3-8. The different 'tracks' represented by the different colours visible in the above plots show the residual for a particular GPS satellite that was tracked during the experiment. Note that the gaps in the residuals are caused by periods when the number of available measurements on that baseline was less than five, meaning that the residuals could not be calculated. Also note that the data sets collected on UoSat-12 were longer since more onboard memory was available on the OBC.

Table 3-8 R.M.S. measurement noise for each baseline and each experiment (UoSat-12)

Experiment Date	Baseline 1 (mm)	Baseline 2 (mm)	Baseline 3 (mm)
13/01/00	8.1	13.0	12.5
14/01/00	8.4	14.7	15.8
17/01/00	8.6	11.4	13.6
Mean Measurement noise	8.4	13.1	14.0

By comparing the results in Table 3-8 with those in Table 3-7 we can see that the RMS measurement noise was higher on UoSat-12. The overall RMS measurement noise on Topsat is around 6mm compared with around 12mm on UoSat-12. The measurement environment on UoSat-12 was subject to considerably more multipath than Topsat due to the numerous reflectors (such as other sensors and attitude actuators) surrounding the GPS patch antennas. This can be seen in the diagram of the antenna locations on UoSat-12 provided in Figure 2-13 in section 2.6.2.1. On

Topsat the antennas have a clear field-of-view of 180° with only the –Z facet as a potential reflector, as shown in Figure 2-17 in section 2.6.2.3.

Note that during the UoSat-12 experiment there was a bug in the SGR-20 flight software which corrupted the carrier phase measurements on antenna 4. This meant that the measurements on baseline 3 were unusable, and hence this baseline was not used in [Purivigraipong, 2000]. This bug was fixed before the experiments on Topsat commenced, so the issue did not affect the Topsat results.

3.4 GPS-ADCS disparity

In this section the disparity between the carrier phase measurements predicted from the ADCS and carrier phase measurements observed by the GPS. If the ADCS reference attitude were the truth then the disparity would equal the actual error in the GPS carrier phase measurements. Since the ADCS is not an actual truth measurement it will introduce error in to the calculated disparities. The type of error observed in the calculated disparities will depend on the type of error in the ADCS.

The method used to calculate the GPS-ADCS disparity is described below.

3.4.1 Method

The assumed body referenced baseline vector $\hat{\mathbf{b}}_{i(B)}$ (estimated in section 3.2.1) is assumed to be in error relative to the true baseline vector $\mathbf{b}_{i(B)}$ due to errors in the mechanical construction and variation of the electrical phase centre of the antennas

$$\mathbf{e}_i = \hat{\mathbf{b}}_{i(B)} - \mathbf{b}_{i(B)} \tag{3-16}$$

Therefore the measured single-difference carrier phase measurement in epoch k is given by

$$\bar{r}_{i,j}[k] = \left(\mathbf{b}^T_{i(B)} + \mathbf{e}^T_i\right)\mathbf{A}[k]\mathbf{s}_{i,j(O)}[k] + N_{i,j} + \beta^*_i[k] + w_{i,j}[k] \tag{3-17}$$

where $\mathbf{A}$ is the true attitude and $\beta^*_i[k]$ is the effective line bias. The ADCS is used to predict the single-difference carrier phase according to

$$\hat{r}_{i,j}[k] = \hat{\mathbf{b}}^T_{i(B)}\hat{\mathbf{A}}_{ADCS}[k]\mathbf{s}_{i,j(O)}[k] \tag{3-18}$$

and the integer correction $N_{i,j}$ to the single-difference carrier phase measurement, $\bar{r}_{i,j}$, is calculated using

$$N_{i,j} = round\left(\bar{r}_{i,j}[k] - \hat{r}_{i,j}[k]\right) \tag{3-19}$$

It is assumed that the known attitude $\hat{\mathbf{A}}_{ADCS}$ as reported by the ADCS is in error from the true attitude $\mathbf{A}$ such that

$$\hat{\mathbf{A}}_{ADCS}[k] = \mathbf{A}[k]\left(\mathbf{I} + \mathbf{\Delta}^{\times} + \mathbf{\delta}^{\times}[k]\right) \qquad \text{3-20}$$

leading to an predicted single-difference carrier phase measurement of

$$\hat{r}_{i,j}[k] = \hat{\mathbf{b}}^{T}_{i(B)}\mathbf{A}[k]\left(\mathbf{I} + \mathbf{\Delta}^{\times} + \mathbf{\delta}^{\times}[k]\right)\mathbf{s}_{i,j(O)}[k] \qquad \text{3-21}$$

The disparity between the measured and predicted single-difference carrier phase is then given by

$$\begin{aligned}\varepsilon_{i,j}[k] &= \bar{r}_{i,j}[k] - \hat{r}_j[k] \qquad \text{3-22}\\ &= \left(\mathbf{b}^{T}_{i(B)} + \mathbf{e}^{T}_{i}\right)\mathbf{A}[k]\mathbf{s}_{i,j(O)}[k] - \mathbf{b}^{T}_{i,(B)}\mathbf{A}[k]\left(\mathbf{I} + \mathbf{\Delta}^{\times} + \mathbf{\delta}^{\times}[k]\right)\mathbf{s}_{i,j(O)}[k] + \beta^{*}_{i}[k] + w_j[k]\end{aligned}$$

leading to

$$\varepsilon_{i,j}[k] = \left\{\mathbf{e}^{T}_{i}\mathbf{A}[k] - \mathbf{b}^{T}_{i(B)}\mathbf{A}[k]\left(\mathbf{\Delta}^{\times} + \mathbf{\delta}^{\times}[k]\right)\right\}\mathbf{s}_{i,j(O)}[k] + \beta^{*}_{i}[k] + w_{i,j}[k] \qquad \text{3-23}$$

The first term in Equation 3-23 expresses all the errors in the predicted carrier phase determined using the ADCS. It incorporates an error, $\mathbf{e}$, in the knowledge of the true baseline vector $\mathbf{b}_{(B)}$; a constant rotational error, $\mathbf{\Delta}$, of the ADCS effective axes relative to the true body axes and attitude measurement noise $\mathbf{\delta}[k]$. The remaining term $w_j[k]$ defines the GPS measurement noise.

The effective line bias term $\beta^{*}_{i}[k]$ can be cancelled out by computing the epoch average

$$\bar{\varepsilon}_i[k] = \sum_{j=1}^{J_i[k]} \varepsilon_{i,j}[k] \qquad \text{3-24}$$

allowing a computed modified disparity

$$\tilde{\varepsilon}_{i,j}[k] = \varepsilon_{i,j}[k] - \bar{\varepsilon}_i[k] \qquad \text{3-25}$$

The RMS disparity over all K epochs can be calculated using

$$\sigma_{i,GPS-ADCS} = \sqrt{\frac{1}{K}\sum_{k=1}^{K}\frac{1}{J_i[k]-1}\sum_{j=1}^{J_i[k]}\left(\tilde{\varepsilon}_{i,j}[k]\right)^2} \qquad \text{3-26}$$

3.4.2 Results

Note that the ADCS estimated baseline vectors calculated in section 3.2.2 were used as the assumed body-referenced baselines in order to remove the constant rotation between the ADCS and GPS frames.

The plots in Figure 3-9 show the GPS-ADCS disparity from three of the eight experiments used in this analysis. The disparity for each of the GPS satellites has a non-zero mean and appears to be time-correlated. The RMS disparity for all satellites tracked on each baseline is shown in Table 3-9. Equation 3-23 shows that the disparity is subject to any noise and offsets in the GPS carrier phase measurements and also any errors in the ADCS reference attitude and the assumed baseline vector.

Table 3-9 R.M.S. disparity for all experiments (Topsat)

Experiment Date	Baseline 1 (mm)	Baseline 2 (mm)	Baseline 3 (mm)
22/02/07	13.4	10.3	8.8
27/02/07	15.1	14.5	9.2
01/03/07	12.6	10.5	8.7
01/05/07	12.3	10.7	8.5
09/05/07	13.6	8.8	10.5
04/07/07	11.0	9.8	5.6
10/07/07	11.0	10.3	6.2
03/06/08	8.9	6.5	5.3
R.M.S. Disparity (all dates)	12.4	10.4	8.0

Assuming that the baseline vectors estimated using the ADCS are close to the true baseline vectors, the error in the baselines $\mathbf{e}_i$ should be negligible. Equation 3-23 therefore reduces to

$$\varepsilon_{i,j}[k] = \left\{\mathbf{b}^T_{i(B)}\left(\mathbf{\Delta}^\times + \boldsymbol{\delta}^\times[k]\right)\right\}\mathbf{s}_{i,j(O)}[k] + \beta^*_i[k] + w_{i,j}[k] \qquad \text{3-27}$$

Assuming the effective line bias term has been essentially removed using the mean disparity $\bar{\varepsilon}_i[k]$ as calculated in Equation 3-24 gives

$$\tilde{\varepsilon}_{i,j}[k] = \left\{\tilde{\mathbf{b}}^T_{i(B)}\left(\mathbf{\Delta}^\times + \boldsymbol{\delta}^\times[k]\right)\right\}\mathbf{s}_{i,j(O)}[k] + w_{i,j}[k] \qquad \text{3-28}$$

Finally, assuming that the ADCS attitude uncertainty $\boldsymbol{\delta}[k]$ is uncorrelated random noise, Equation 3-28 shows that the possible causes for the correlation in the disparities are limited to measurement noise (including multipath) or a constant offset in the ADCS reference attitude.

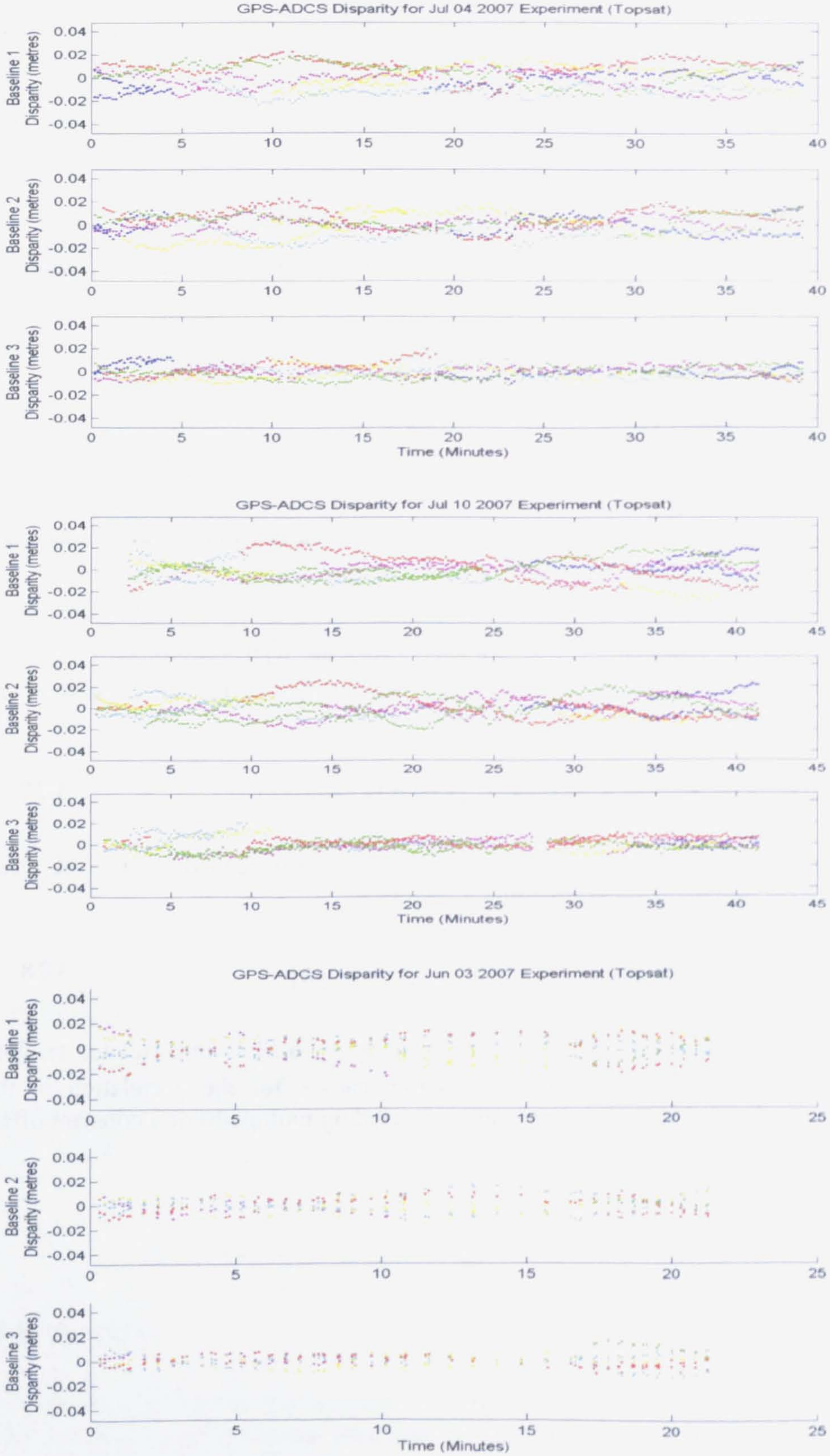

Figure 3-9 GPS-ADCS disparity from selected dates

If the time correlation in the disparities is due to reflection multipath, then according to [Reichert and Axelrad, 1999] sinusoidal fluctuations in the signal-to-noise ratio of the satellites being tracked should be evident, with the frequency of these fluctuations being dependent on the distance between the antenna and the reflector causing the multipath [Reichert and Axelrad, 1999]. However on Topsat the only possible reflector is the facet upon which the GPS patch antennas are mounted. An alternative hypothesis is that the apparent multipath effects are due to the varying phase response of the patch antennas.

Another possibility is that the ADCS reference attitude is subject to an offset. To test this conclusion the MATLAB-based simulator was used to simulate the effect of an ADCS attitude error on the GPS-ADCS disparity. The results, which are presented in Appendix A, showed that an error in the roll or pitch estimates from the ADCS would only couple into two of the three baselines, and the effect of such an error would be small. In contrast, the results showed that an ADCS yaw error had a significant effect on the GPS-ADCS disparity for all three baselines, with a 1.5 degree error causing centimetres of GPS-ADCS disparity. Therefore a likely explanation for the large GPS-ADCS disparity is an error in the ADCS yaw estimate.

Secondary evidence for this conclusion can be found from analysing the status of the ADCS during each of the experiments. It was shown in section 3.1.1 that the ADCS uncertainty increases when DASH 2 is not available. This increased uncertainty will result in an increase in the GPS-ADCS disparity. For the first seven experiments DASH 2 was not available but in early 2008 SSTL implemented a fix so that DASH 2 would be included in the ADCS attitude filter if it was determined to be functioning correctly. For the 3rd June 2008 experiment shown in Figure 3-9 the ADCS utilised both EHSs. As can be seen in Figure 3-9 correlation in the disparities has decreased, as has the RMS disparity in Table 3-9. This is particularly noticeable for baselines 2 and 3 which are affected by the ADCS across-track (nominally roll) uncertainty. The decrease in the RMS disparity for the 3rd June 2008 experiment leads to the conclusion that in the first 7 data files errors in the yaw axis in the ADCS are contributing significantly to the GPS-ADCS disparity.

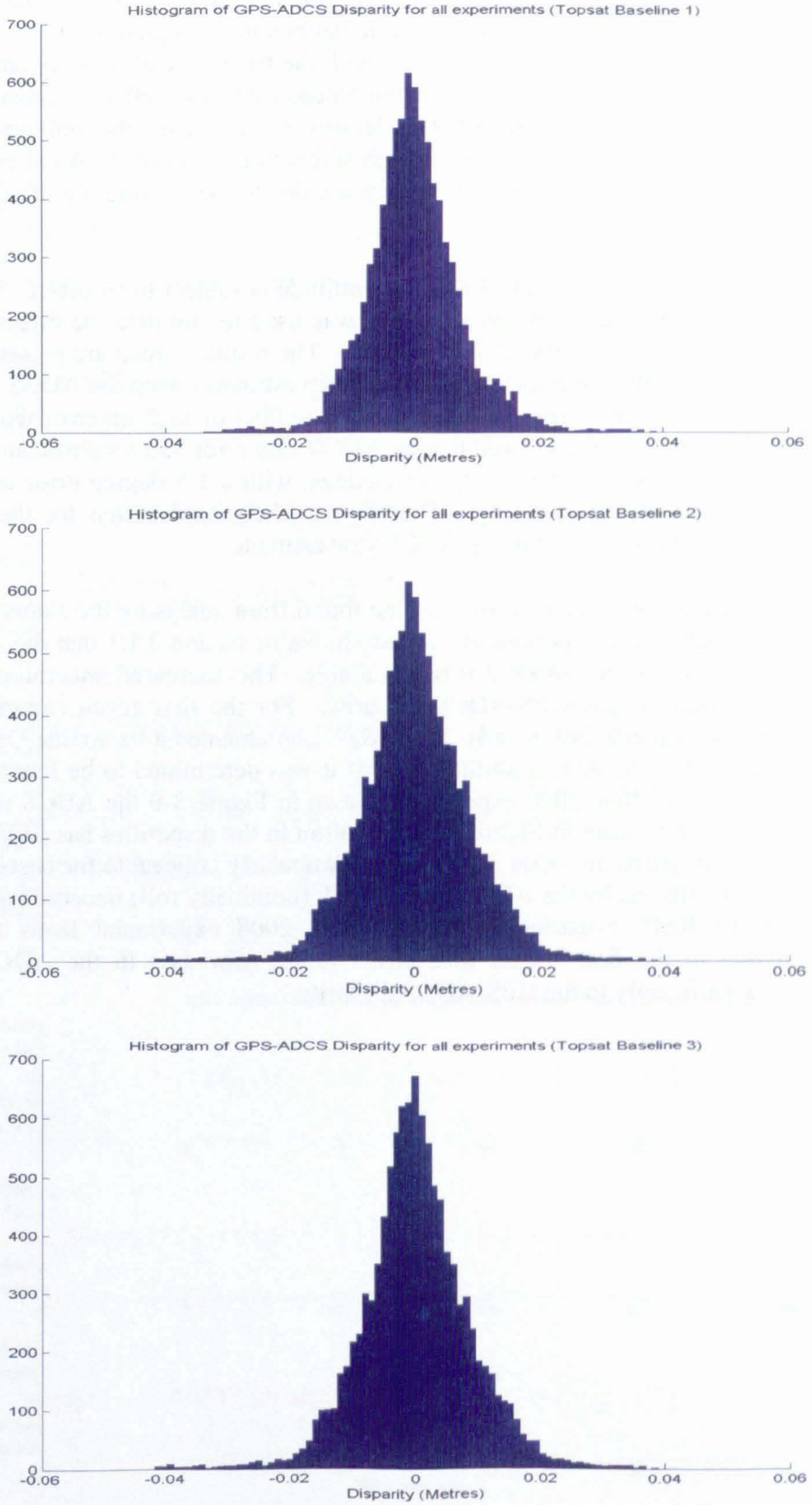

Figure 3-10 Histogram of GPS-ADCS disparity (Topsat baselines 1, 2, 3 from top)

3.5 *Multipath spatial repeatability analysis*

In the case of Topsat, multipath is assumed to be a time-invariant deterministic function of the direction of the incoming signal. For this discussion the antenna phase response is included under the term multipath. In the following sections the cross-correlation of the GPS residuals for different satellites that followed the same path through the sky relative to the spacecraft body-referenced frame is examined.

3.5.1 Cross-Correlation

The mutual correlation properties of two separate random processes $u_1[k]$ and $u_2[k]$ can be determined by calculating their *cross-correlation* using

$$R_{u_1u_2}(k,k+l)=\langle u_1[k]u_2[k+l]^T\rangle \qquad \textbf{3-29}$$

The cross-correlation of the residuals and GPS-ADCS disparity was calculated for the pair of GPS satellites consisting of PRN 6 from the data file logged on 1st March 2007 and PRN 9 logged on 22nd February 2007. The skyplot in Figure 3-11 shows the path followed by PRN 6 and PRN 9 relative to the space-facing facet of Topsat. It can be seen that the two satellites trace a similar pattern through the sky.

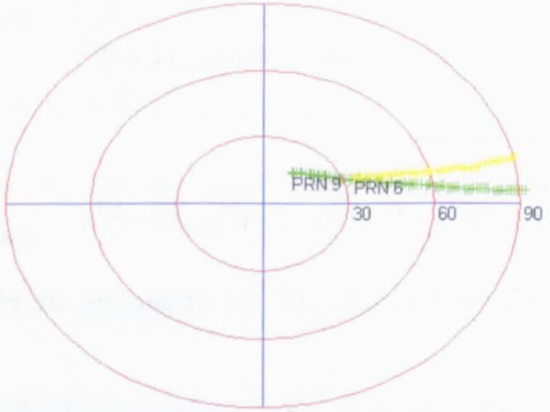

Figure 3-11 Elevation and azimuth of PRN 6 (01/03/07) and PRN 9 (22/02/07)

To measure the cross-correlation between two satellites tracked on different dates the residuals and disparities calculated for baseline 2 were aligned by referencing both processes to the elevation of the satellite at each epoch. The aligned GPS residuals and GPS-ADCS disparity for PRN 6 and PRN 9 on baseline 2 are shown in Figure 3-12. Since both satellites moved at similar relative speeds to Topsat, the elevation of each satellite changed at the same rate and so units of time can be interchanged with elevation. The residuals and the disparities show a similar pattern for a given elevation/time. The fact that there is such a high correlation between measurements taken on different dates, for the same part of the sky, is a strong indication that multipath is present in the carrier phase measurements.

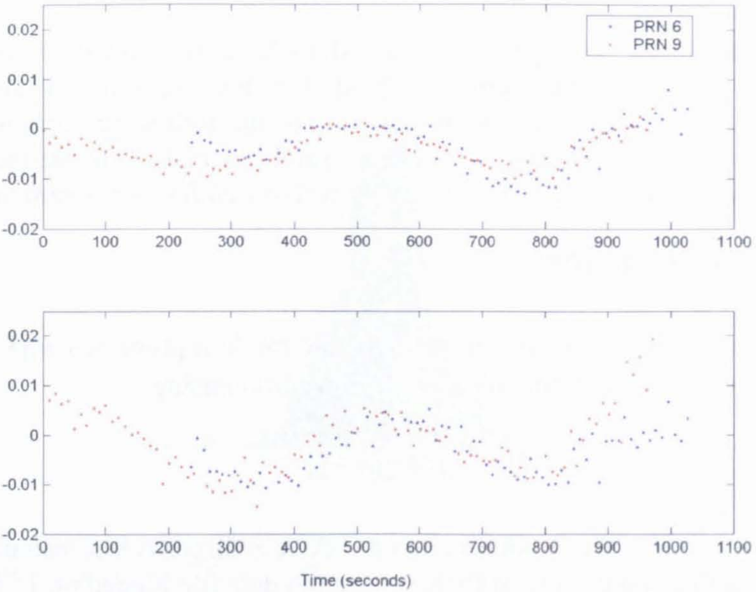

Figure 3-12 Comparison of GPS residuals and disparity of PRN 6 and 9

The cross-correlation between the residuals for PRN 6 and PRN 9 was calculated using

$$R_{PRN6 \leftrightarrow PRN9}(k,k+l) = \left\langle \omega_{PRN6}[k]\omega_{PRN9}[k+l]^T \right\rangle \tag{3-30}$$

and similarly for the disparities

$$R_{PRN6 \leftrightarrow PRN9}(k,k+l) = \left\langle \tilde{\varepsilon}_{PRN6}[k]\tilde{\varepsilon}_{PRN9}[k+l]^T \right\rangle \tag{3-31}$$

The results using both the residuals and the disparities are plotted in Figure 3-13 below.

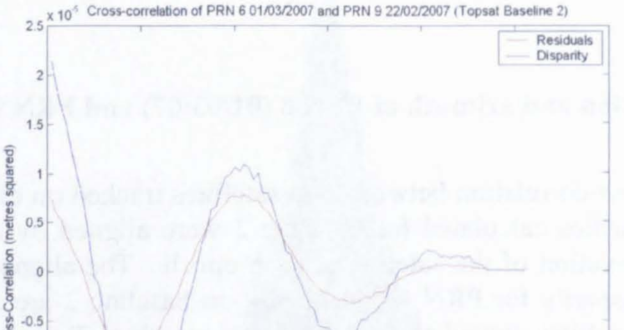

Figure 3-13 Cross-correlation of PRN 6 (01/03/2007) and PRN 9 (22/02/2007)

The cross-correlation results support the conclusion that multipath is present in the single-difference carrier phase measurements since the errors show a definite correlation between the angle of arrival of the signal and the carrier phase error. These results suggest that some way of mitigating multipath such as the method described in [Hodgart and Wong, 2006] is necessary in order to achieve the highest possible accuracy from the GPS attitude solution.

3.6 Line bias characterization

In order to use the carrier phase measurements for GPS attitude determination the line bias must either be known or eliminated using double-difference measurements. Currently there is no method for observing the line bias directly. Therefore the line-bias must be estimated which means it remains subject to corruption by error sources such as multipath and receiver noise. The line bias can be estimated using a combination of the ADCS and GPS carrier phase measurements or from GPS measurements alone. Both methods are presented and compared in the following sections.

3.6.1 Line bias estimation using ADCS

In each epoch k the ADCS reference attitude $\hat{\mathbf{A}}_{ADCS}$ is used to calculate a predicted carrier phase measurement $\hat{r}_{i,j}[k]$,

$$\hat{r}_{i,j}[k] = \hat{\mathbf{b}}_{i(B)}^T \hat{\mathbf{A}}_{ADCS} \mathbf{s}_{i,j(O)}[k] \tag{3-32}$$

The integer correction $N_{i,j}$ to the single-difference carrier phase measurement, $\bar{r}_{i,j}[k]$, is calculated using

$$N_{i,j} = round\left(\bar{r}_{i,j}[k] - \hat{r}_{i,j}[k]\right) \tag{3-33}$$

The line bias is estimated in each epoch as the mean disparity across all measurements:

$$\hat{\beta}_i[k] = \frac{1}{J_i[k]} \sum_{j=1}^{J_i} \left(\bar{r}_{i,j}[k] - N_{i,j} - \hat{r}_{i,j}[k]\right) \tag{3-34}$$

The process is repeated for each baseline.

3.6.1.1 Results

The plots in Figure 3-14 show two distinct patterns in the estimated line bias. The first is an arbitrary offset in the line bias for each baseline and each experiment. The second is a variation in the line bias over time that appears correlated from one experiment to the next.

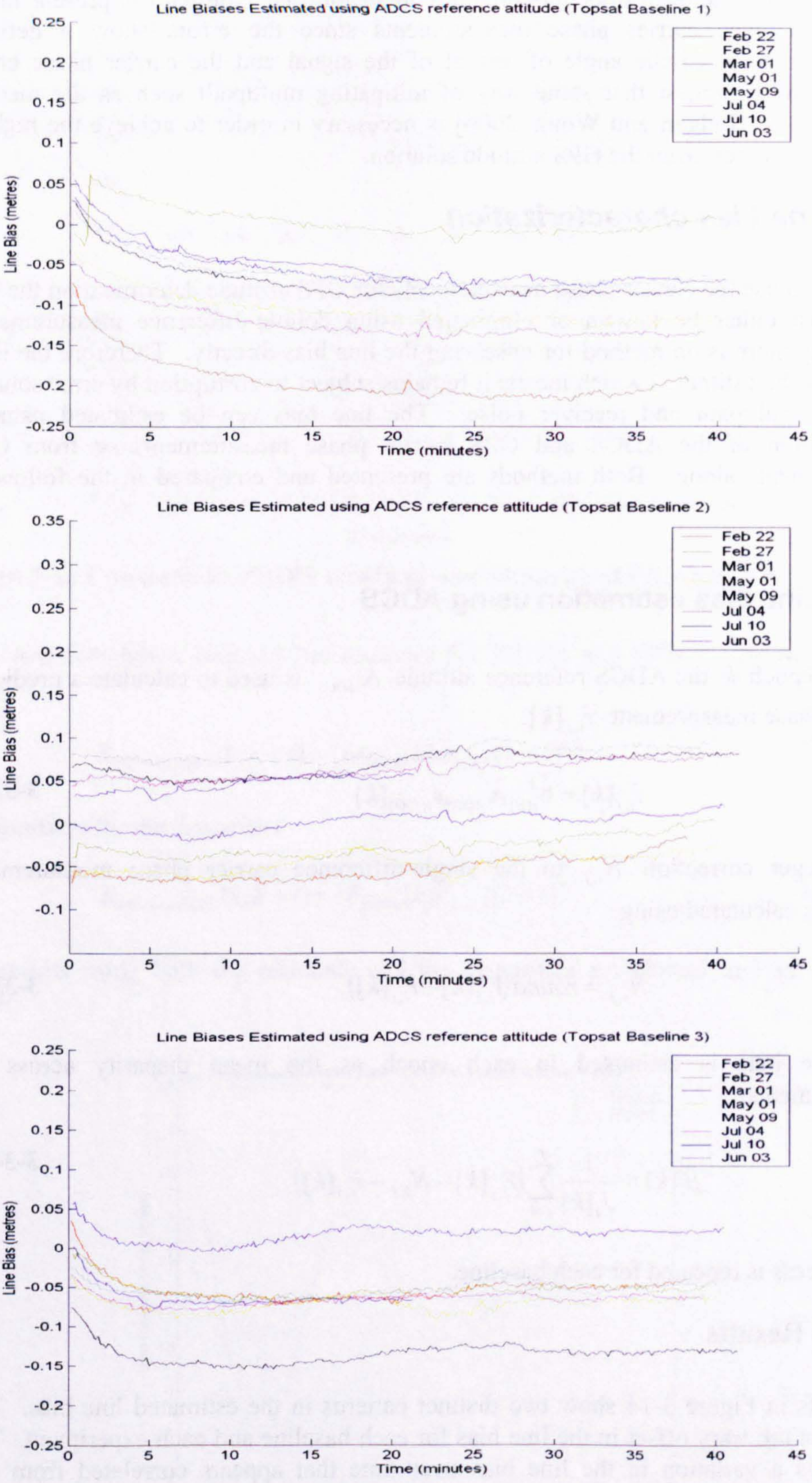

Figure 3-14 ADCS Derived Line Bias Estimates for Baseline 1, 2, 3 from top

As shown in Figure 2-17 in section 2.3.2.6 the four GPS antennas on Topsat form three baselines. Each antenna is connected to one of the four RF front-ends on the SGR-20. The connections are shown in Figure 3-15 below.

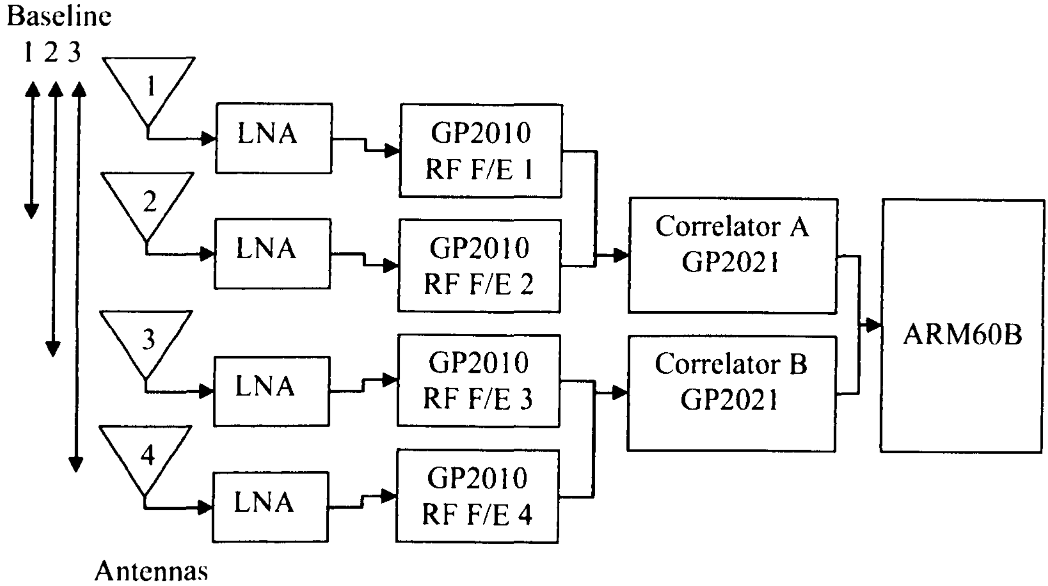

Figure 3-15 Hardware diagram showing relationship between RF Front-ends and baselines

Based on the results shown in [Morros, 1995] it is believed that the variation in line bias over time is related to the temperature of the individual RF front-ends. From Figure 3-14 it can be seen that for baselines 1 and 3 there is an initial period of around twenty minutes during which the line bias is drifting. After this initial twenty minute period the line bias settles to a more stable value. The line biases for baseline 2 do not exhibit this initial drift.

As shown in Figure 3-15 baseline 1 uses measurements from RF front-end 1 and 2; baseline 2 uses measurements from RF front-ends 1 and 3, and baseline 3 uses measurements from RF front-ends 1 and 4. In each experiment RF front-ends 1 and 3 are both turned on up to ten minutes prior to the start of the GPS attitude experiment and by the start of the experiment may have stabilised to a constant temperature. Conversely, RF front-ends 2 and 4 are not turned on until the SGR-20 configures itself for attitude determination. RF front-ends 2 and 4 will therefore be at a different operating temperature for the first twenty minutes of operation.

The SGR-20 has the ability to log both its main-board and power supply temperatures via an Analogue to Digital Board. Of the two temperature sensors the main-board temperature sensor is located nearest to the RF front-ends. The temperature of the individual RF front-ends is not recorded. Given that all four RF front-ends use identical components and are each enclosed within a metal screen-can we would expect that the change in the phase measured by each RF front-end with respect to temperature would be similar. According to the engineers at SSTL the RF front-ends are thermally isolated from the main-board of the receiver in order to reduce interference. We can therefore only assume that the RF front-ends 'self heat' when they are switched on and current is supplied to them. However, the thermal isolation means that it is unlikely that any useful model can be constructed to relate the temperature of the main-board and the change in phase measured by the individual RF front-ends.

The cause of the apparent arbitrary offset in line bias is still unknown. One possible cause is an offset in the ADCS attitude used to estimate the line bias. The error in the predicted carrier phase due to ADCS error is given by

$$\tilde{w}_{\hat{r}_{i,j}}[k] = \mathbf{b}_{i(B)}^{T}\left(\boldsymbol{\Delta}^{\times} + \boldsymbol{\delta}^{\times}[k]\right)\mathbf{s}_{i,j(O)}[k] \tag{3-35}$$

and hence the error in the line bias estimate due to ADCS error is given by:

$$\varepsilon_{\dot{\beta}_i[k],ADCS} = \frac{1}{J_i[k]}\sum_{j=1}^{J_i[k]}\left(\mathbf{b}_{i(B)}^{T}\left(\boldsymbol{\Delta}^{\times} + \boldsymbol{\delta}^{\times}[k]\right)\mathbf{s}_{i,j(O)}[k]\right) \tag{3-36}$$

The ADCS measurement noise $\boldsymbol{\delta}[k]$ will add to the RMS line bias noise, but the error in the ADCS body-referenced axes $\boldsymbol{\Delta}$ will cause an offset in the estimated line bias. Therefore the arbitrary offsets in the line bias estimates may be due to the ADCS error $\boldsymbol{\Delta}$ changing from one experiment to the next. Evidence to support this conclusion was shown in Figure 3-4 in section 3.1.1 in which it was shown that the ADCS along-track and across-track error varies with each image acquisition. To determine if this conclusion is sound, in the following section the line bias is estimated using only GPS measurements.

3.6.2 Line Bias Estimation using GPS measurements only

In section 3.3 the line bias was estimated as part of the estimation of the GPS measurement noise from the GPS residuals. The plots in Figure 3-16 show the effective line bias estimated in Equation 3-11 for each baseline during each experiment. Since the line bias estimates are based solely on GPS carrier phase measurements they are not subject to any error from the ADCS. However, as can been seen in Figure 3-16 the line bias estimates are very noisy.

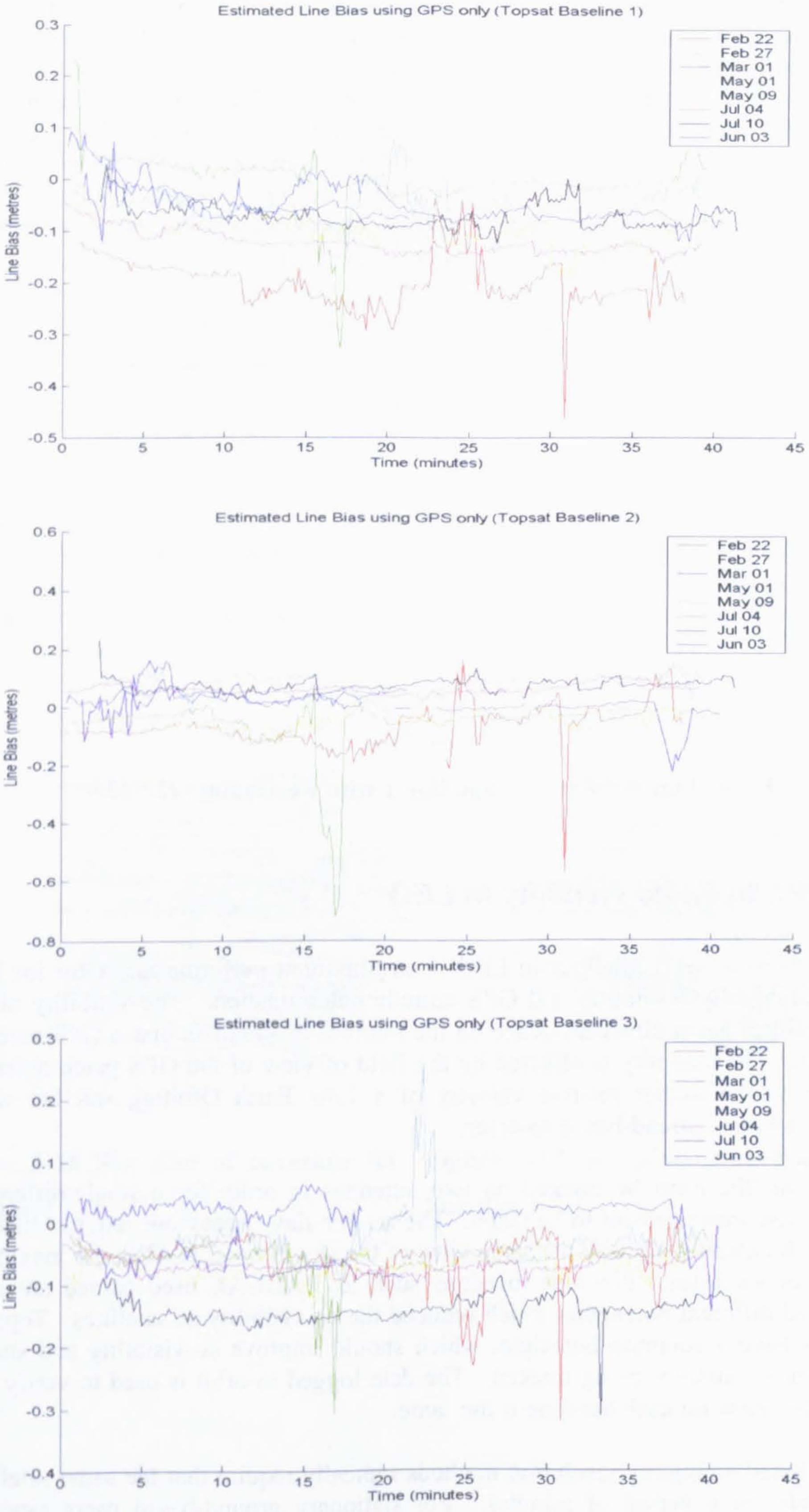

Figure 3-16 Line bias estimated using only GPS measurements

Poor observability of the line bias due to a combination of the baseline geometry on Topsat and the GPS satellite geometry results in a large dilution of precision in the line bias estimate. This lead to the poor quality of the line bias estimates. An example of the poor observability is shown in Figure 3-17 which shows the line bias estimate for baseline 1 for the 27th February 2007 experiment. The line bias uncertainty, calculated based on the dilution of precision and the RMS measurement noise estimated for that experiment, is also shown. All the large errors in the line bias estimate correspond to periods of poor dilution of precision in the line bias estimate, confirming that the cause of the errors is poor observability.

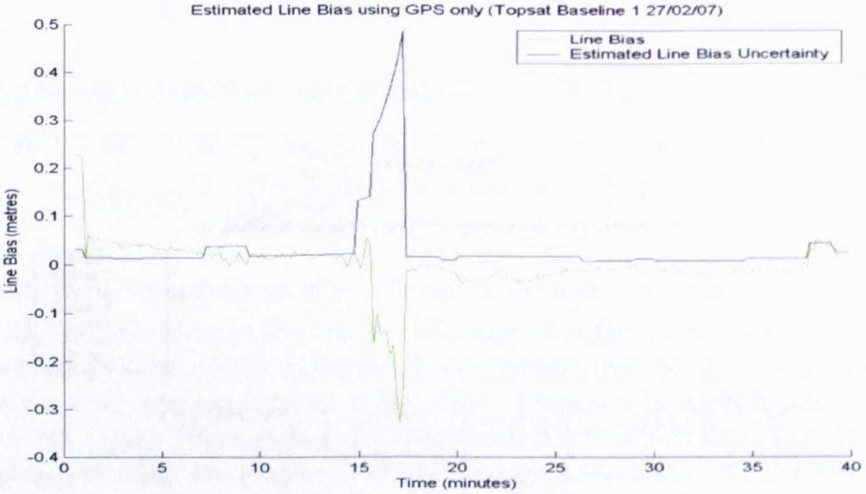

Figure 3-17 Line bias estimate for baseline 1 with uncertainty (27/02/07)

3.7 GPS satellite visibility in LEO

The visibility of GPS satellites in LEO is an important performance factor for both integer ambiguity resolution and GPS attitude determination. The visibility of the GPS satellites has a direct influence on the number of satellites that a GPS receiver can track. The visibility is affected by the field of view of the GPS patch antennas and due to the higher relative velocity of a Low Earth Orbiting satellite when compared with a ground-based receiver.

A GPS satellite must be tracked on two antennas in order for a single-difference carrier phase measurement to be taken. The master-slave behaviour requires that the GPS patch antennas all have the same view of the sky in order to track the maximum number of satellites. Previous missions such as RADCAL used canted antennas which had different boresights which reduced the co-visibility of satellites. Topsat's antennas have a common boresight, which should improve co-visibility and should lead to more satellites being tracked. The data logged in-orbit is used to verify that the field of view for each baseline is the same.

Motion-based ambiguity resolution methods typically require that the same satellites are visible for a period of minutes. For stationary ground-based users satellites typically remain in view for hours, but in Low Earth Orbit our receiver is moving at around 7.5 kilometres per second. It is therefore useful to calculate how long GPS satellites remain visible so that we can use this to guide our approach for integer ambiguity resolution.

3.7.1 Field of view for each baseline

The ADCS attitude solution was used to rotate the LOS vectors for each satellite tracked in to the body-defined coordinate system. The azimuth and elevation of each satellite were then calculated according to:

$$\begin{aligned} \text{Azimuth} &= \arctan\left(\frac{\mathbf{s}_{j,Y(B)}}{\mathbf{s}_{j,X(B)}}\right) \\ \text{Co}-\text{Elevation} &= 90-\arcsin\left(-\mathbf{s}_{j,Z(B)}\right) \end{aligned} \qquad \textbf{3-37}$$

The azimuth and co-elevation of each satellite in each epoch were then plotted to show the field of view of each baseline on Topsat. The results are shown in Figure 3-18 to Figure 3-20. Note that the direction of travel of the satellite corresponds to zero degrees in azimuth and ninety degrees in co-elevation on the plots (i.e. the left hand side of the plots).

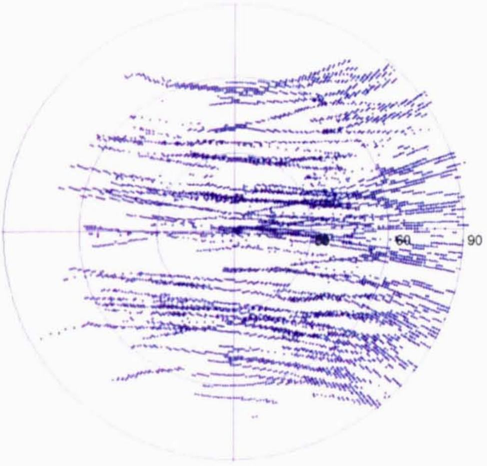

Figure 3-18 Sky plot of coverage for baseline 1

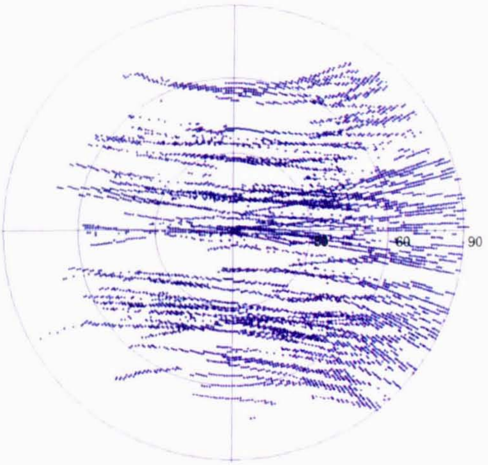

Figure 3-19 Sky plot of coverage for baseline 2

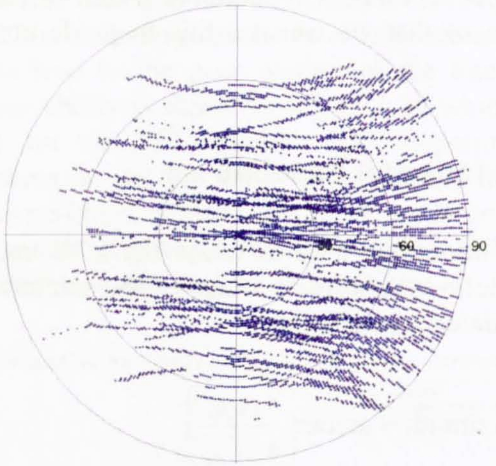

Figure 3-20 Sky plot of coverage for baseline 3

All three plots have roughly the same coverage, which is due to the unobstructed view of all four antennas and the way the SGR-20 controls the allocation of satellites to each antenna. All four antennas are co-located on the space-facing (-Z) facet of the spacecraft. There are no other sensors or obstructions on this facet, and so all baselines have roughly the same field of view.

The SGR-20 typically acquires satellites at high elevation near the centre of each plot, and then tracks each satellite until it sets (on the right hand side of each plot) and cannot be tracked any longer. This results in the pattern seen in all three plots where the plots are denser on the right hand side.

All three plots show some evidence for the SGR-20 tracking satellites below its nominal elevation mask of zero degrees. This is because it will only drop a satellite if there is another satellite which is currently not being tracked and is above the elevation mask to replace it. In the cases where a satellite is tracked below the elevation mask it is likely that there was no other visible satellite to replace the low elevation one.

3.7.2 Time in view of a GPS satellite

Using the data logged in-orbit the time in view of each GPS satellite tracked was calculated for all three baselines throughout all the experiments used in the analysis of spaceflight data. The time in view for each satellite was calculated by counting the number of epochs in which each satellite was consistently tracked. The satellites were included in the calculation as long as their elevation was greater than zero, since the SGR-20 satellite allocation routine drops any satellites with a negative elevation.

Table 3-10 Minimum, Mean and Maximum time in view for all GPS satellites

	Baseline 1	Baseline 2	Baseline 3
Minimum (s)	99	99	168
Mean (s)	838	847	858
Maximum (s)	1674	1630	1651

The results are shown in the table above. The mean time in view on all three baselines is around fourteen minutes. Across all three baselines the average minimum time is around two minutes and the average maximum time in view is around twenty-eight minutes.

3.8 Conclusions

In this chapter in-orbit data logged on the SGR-20 receiver on Topsat has been analysed in order to characterise the various error sources that effect GPS carrier phase measurements.

The ADCS which provides a reference attitude solution for this work was described and potential error sources affecting the ADCS were discussed. An estimate of the statistical properties of the ADCS error was calculated by analysing the difference between the commanded ground target and the resulting image centre in the along-track and across-track directions for every image taken. This showed that throughout most of this work the standard deviation of the along-track (pitch) and across-track (roll) error was around 0.5 and 0.9 degrees respectively. These figures were then used to show that the uncertainty in the predicted GPS carrier phase measurements due to the ADCS could be as high as 8.2 mm. The conclusion that can be drawn from this analysis is that ADCS error must be taken into account when drawing conclusions on the accuracy of GPS attitude determination.

In the second section of this chapter a recursive least-squares filter was used to 'survey' the GPS baselines. The recursive filter used the ADCS to predict the GPS carrier phase measurements. The result of this survey showed that whilst the uncertainty in the ADCS meant that there was no significant difference between the ADCS estimated baselines and the MCAD derived baseline, there was a constant rotation in pitch between the GPS and ADCS reference frames. To eliminate the potential effects of this rotation, the ADCS estimated baselines are used throughout the rest of this work.

Analysis of the GPS carrier phase residuals showed that the single-difference RMS measurement noise is around 6mm on Topsat. The results also showed that the RMS measurement noise is slightly higher on baseline 2 than baselines 1 and 3, which could be due to a greater difference in the antenna phase response, or due to more reflection multipath from the spacecraft facet. Re-analysis of the UoSat-12 data files collected during the research documented in [Purivigraipong, 2000] showed that the overall RMS measurement noise on Topsat is around half that experienced on UoSat-12.

Analysis of the disparity between the measured GPS carrier phase and the predicted GPS carrier phase calculated using the ADCS showed large variations which were non-zero mean and correlated with time. Simulation results given in Appendix A demonstrated that a small error in the ADCS yaw estimate could account for most of the disparity observed. Analysis of the cross-correlation of the GPS residuals for two satellites traversing the same part of the sky showed that some component of the error is spatially correlated and there likely to be multipath.

In section 3.6 the in-orbit data from a number of experiments was used to characterise the line bias. Estimation of the line bias using the ADCS showed that the line bias has an arbitrary offset for each baseline and for each experiment. The results also implied that the line bias varies with the temperature of the RF front-ends, but no method for verifying this assumption was available. The problem of the poor observability of the line bias when using only GPS measurements was highlighted. As a result it was decided that to simplify the problem of implementing a stand-alone GPS attitude sensor double-difference carrier phase measurements would be used for both integer ambiguity resolution and attitude tracking.

Finally the in-orbit data was used to verify that the field of view is similar for all three baselines. The sky plots in section 3.7.1 show that the field of view is similar for all three baselines on Topsat, and that it extends over most of the hemisphere. The time in view of the GPS satellites was also calculated. The results showed that the integer ambiguity algorithm must solve for the integers within two minutes, or have some method of coping with the satellites changing from one epoch to the next.

4 Robust integer ambiguity resolution

In this chapter the problem of robust integer ambiguity resolution is investigated. The basis of this work was the availability of an SGR-20 GPS receiver on the Topsat microsatellite for use in experimenting with GPS attitude determination. Having a GPS receiver in orbit provided the advantage that real data could be collected and used to analyse and validate new algorithms. However, the use of the SGR-20 also resulted in a number of constraints on the integer ambiguity resolution approach that could be considered. These constraints include:

- Only single-frequency measurements on L1 are available
- A limited number of measurements (up to six) are available on each baseline
- Co-planar baseline geometry
- Standard GPS patch antennas
- Arbitrary line bias for each baseline
- Limited available processing power and spare memory

The first part of this chapter looks at the commonly used *float solution* method for integer ambiguity resolution. The mathematics of different types of float solution are examined to demonstrate the issues with implementing such a method on the SGR-20. The alternative method of the *integer search* is then discussed. Integer search methods generally attempt an integer ambiguity solution in a single-epoch. However, as was shown by [Martin-Neira, 1995] single-epoch methods are inherently not robust. A new analysis of the reasons for the lack of robustness of single-epoch methods is shown in section 4.1.3.

The main part of this chapter describes a new robust integer ambiguity resolution algorithm suitable for implementation in real-time onboard the SGR-20. This algorithm was developed within the limitations of the SGR-20 described above. The algorithm uses an integer search process and then validation of trial solutions over multiple epochs in order to identify a unique integer ambiguity solution. The issues with validating trial solutions over multiple epochs are also discussed, and a method for tracking the double-difference integers over multiple epochs is presented.

4.1 Overview of integer ambiguity resolution

The current state of the art in terms of integer ambiguity resolution can arguably be said to be the Least-Squares Ambiguity Decorrelation Adjustment (LAMBDA) method devised by [Teunissen, 1994]. This method is popular with many GPS carrier phase users, including those in the field of geodesy (i.e. surveyors) as well as researchers investigating attitude determination on platforms such as aircraft [Buist, 2008]. The LAMBDA method is well documented in [Teunissen, 1994] and [Teunissen, 1995] and the interested reader is directed to those papers for a description of the method. Fundamentally the LAMBDA method requires *a priori* information in the form of a *float solution*, which contains a real-valued estimate of the integer ambiguities. The real valued estimates can be fixed to integers through a simple process such as rounding, or through more complex techniques such as the LAMBDA method.

4.1.1 Float solutions

Following the measurement model defined in Chapter 2, a single-difference carrier phase measurement in epoch k is defined as

$$\bar{r}_{i,j}[k] - N_{i,j} - \beta_i[k] + w_{i,j}[k] = \mathbf{s}^T_{i,j(O)}[k]\mathbf{b}_{i(O)}[k] \qquad \text{4-1}$$

Assuming that J satellites are tracked on a single baseline i, Double-differences are then formed according to the rule:

$$\begin{aligned} \Delta\bar{r}_{j-1}[k] &= \bar{r}_j[k] - \bar{r}_1[k] \\ \mathbf{v}_{j-1}[k] &= \mathbf{s}_{j(O)}[k] - \mathbf{s}_{1(O)}[k] \end{aligned} \qquad \text{4-2}$$

A set of equations can then be formed (in epoch k)

$$\Delta\bar{\mathbf{r}}[k] - \Delta\mathbf{N} - \mathbf{w}[k] = \mathbf{H}[k]\mathbf{b}_{(O)}[k] \qquad \text{4-3}$$

where $\Delta\bar{\mathbf{r}}$ is a $(J-1)\times 1$ vector containing the double-difference carrier phase-difference measurements, $\Delta\mathbf{N}$ contains the unknown double-difference integer ambiguities, $\mathbf{w}$ defines the measurement error, $\mathbf{H}$ is formed from the set of double-difference LOS vectors, $\mathbf{D}$ is a *design matrix* that indexes the integer ambiguities and $\mathbf{b}_{(O)}$ defines the unknown baseline vector.

The correct integer ambiguity solution should ideally minimise the weighted least squares cost

$$\Omega = \left(\bar{\mathbf{r}} - \mathbf{H}\mathbf{b}_{(O)} - \mathbf{D}\Delta\mathbf{N}\right)^T \mathbf{R}^{-1}\left(\bar{\mathbf{r}} - \mathbf{H}\mathbf{b}_{(O)} - \mathbf{D}\Delta\mathbf{N}\right) \qquad \text{4-4}$$

For k observations $\mathbf{R}$ has the form

$$\mathbf{R} = 2\sigma^2_{\varphi_u}\begin{bmatrix} 2 & 1 & \cdots & 1 \\ 1 & 2 & \cdots & 1 \\ \vdots & \vdots & \ddots & \vdots \\ 1 & 1 & \cdots & 2 \end{bmatrix} \qquad \text{4-5}$$

where σ_{φ_u} is the standard deviation of the undifferenced carrier phase noise. Note that in the above equation all measurements are weighted equally, however it is possible to weight individual measurements according to some measure of their quality such as the measurement's carrier-to-noise ratio (C/N_0).

Equation 4-3 contains $3+(J-1)$ unknowns relating to the baseline vector $\mathbf{b}_{(o)}$ and the integer ambiguities $\Delta\mathbf{N}$. Using just a single-epoch and single-frequency measurements on L1, then there will be $J-1$ measurements, meaning the equations are not solvable.

The equations can be made solvable by either:

- Using pseudo-range difference measurements (code phase) to allow a single-epoch float solution
- Using multiple epochs of carrier phase difference measurements

Each of these is examined below.

4.1.1.1 Combined code-phase and carrier-phase based float solution

Both the code phase (or *pseudorange*) and carrier phase measurements can be included in the float solution. Typically this requires special 'geodetic quality' receivers which are designed to provide very accurate code and carrier phase measurements. The code phase difference measurements $\Delta\rho$ are unambiguous and so can described by the equation

$$\Delta\rho[k]-\mathbf{w}_{p}[k]=\mathbf{H}[k]\mathbf{b}_{(o)}[k] \qquad \text{4-6}$$

For every satellite tracked in the current epoch k it is assumed there is both a code phase and carrier phase difference measurement

$$\begin{bmatrix} \Delta\rho_1[k] \\ \vdots \\ \Delta\rho_{J-1}[k] \\ \Delta\bar{r}_1[k] \\ \vdots \\ \Delta\bar{r}_{J-1}[k] \end{bmatrix} - \begin{bmatrix} \mathbf{0}_{J-1\times J-1} \\ \mathbf{I}_{J-1\times J-1} \end{bmatrix} \begin{bmatrix} \Delta N_1 \\ \vdots \\ \Delta N_{J-1} \end{bmatrix} + \begin{bmatrix} \mathbf{w}_{\rho}[k] \\ \mathbf{w}_{\phi}[k] \end{bmatrix} = \mathbf{H}[k]\mathbf{b}_{(o)}[k] \qquad \text{4-7}$$

Defining

$$\mathbf{r}'=\begin{bmatrix}\Delta\rho_1[k]\\ \vdots\\ \Delta\rho_{J-1}[k]\\ \Delta\bar{r}_1[k]\\ \vdots\\ \Delta\bar{r}_{J-1}[k]\end{bmatrix}\qquad \mathbf{D}=\begin{bmatrix}\mathbf{0}_{J-1xJ-1}\\ \mathbf{I}_{J-1xJ-1}\end{bmatrix} \tag{4-8}$$

Then the weighted least-squares cost can be calculated according to

$$\Omega=\left(\mathbf{r}'-\mathbf{H}\mathbf{b}_{(O)}-\mathbf{D}\mathbf{N}\right)^T\mathbf{R}^{-1}\left(\mathbf{r}'-\mathbf{H}\mathbf{b}_{(O)}-\mathbf{D}\mathbf{N}\right) \tag{4-9}$$

which allows for a single-epoch single-frequency float solution. This method is demonstrated in [Buist, 2007] and [Buist *et al*, 2008].

4.1.1.2 Simulation of a combined code and carrier phase based float solution

To determine if the combined code and carrier phase method was suitable for implementation on the SGR-20 a simulation was conducted to show the effect of code phase noise on the success rate of the LAMBDA method when using a code and carrier based float solution as described above. A MATLAB implementation of the LAMBDA method algorithm was kindly provided by Peter Joosten of Delft University, from where the method originates.

The MATLAB simulator described in Appendix A was modified to produce code phase difference measurements for each baseline. A simulation was undertaken to measure the success rate of the LAMBDA method as a function of code phase noise and carrier phase noise. Code phase noise with a zero mean Gaussian distribution and a standard deviation of between 0.01 metres and 0.5 metres was added to the code phase difference measurements. The legend in the plot specifies that carrier phase noise levels between 1mm and 16mm RMS were tested for each level of code phase noise.

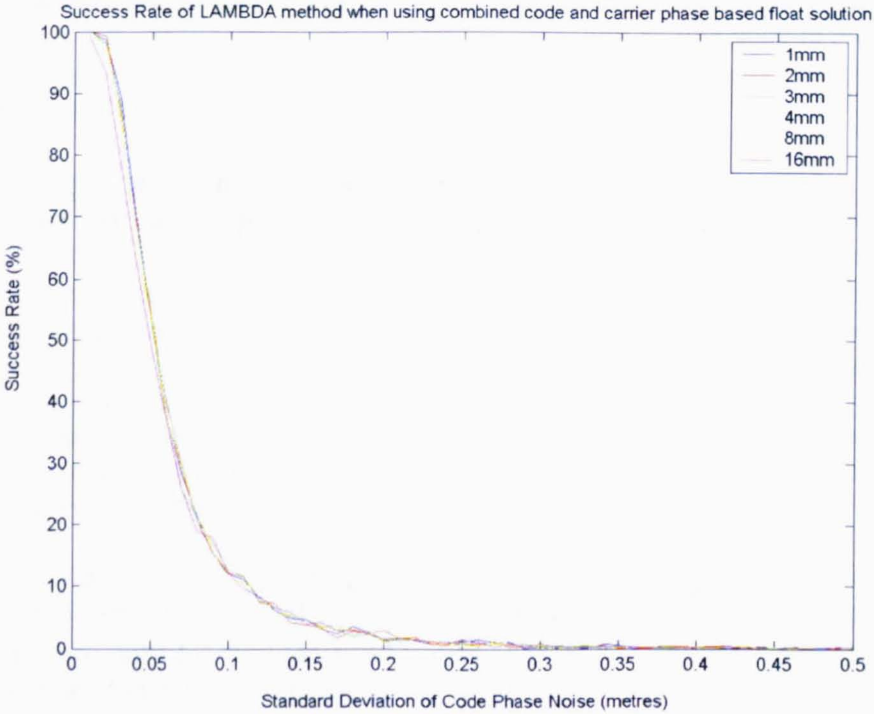

Figure 4-1 Success rate of LAMBDA method when using code and carrier phase measurements

The results show that the code phase noise is the dominant factor in terms of the success rate of the LAMBDA method. Whilst the carrier phase noise does also factor, the results in Figure 4-1 show that for the LAMBDA method to work reliably (i.e. > 95% success rate) the code phase noise must be less than two centimetres. The SGR-20 can provide carrier-smoothed pseudorange measurements with a typical RMS measurement noise of between 0.19 and 0.38m. From results above suggest that this would need to be improved upon in order for the LAMBDA method to be useful. Whilst there is a possibility of improving the tracking loops and reducing the code phase noise, achieving a code phase noise of less than two centimetres would have required a significant amount of work on improving the receiver design. Therefore it was decided that a combined code and carrier phase based float solution was not a practical solution for meeting the goals set out in this thesis.

4.1.1.3 Carrier-phase only float solution

A carrier-phase only float solution can be formed by taking measurements from two separate epochs. If J satellites are tracked continuously between two epochs k and $k+l$ then a set of equations can be formed in epoch k

$$\Delta\bar{\mathbf{r}}[k]-\Delta\mathbf{N}-\mathbf{w}[k]=\mathbf{H}[k]\mathbf{b}_{(O)}[k] \qquad \textbf{4-10}$$

and a corresponding set of equations in epoch $k+l$

$$\Delta\bar{\mathbf{r}}[k+l]-\Delta\mathbf{N}-\mathbf{w}[k+l]=\mathbf{H}[k+l]\mathbf{b}_{(O)}[k+l] \qquad \textbf{4-11}$$

Since both sets of equations relate to the same J satellites they can be combined into one larger set of equations as follows:

$$\begin{bmatrix} \Delta\bar{r}_1[k] \\ \vdots \\ \Delta\bar{r}_{J-1}[k] \\ \Delta\bar{r}_1[k+l] \\ \vdots \\ \Delta\bar{r}_{J-1}[k+l] \end{bmatrix} - \begin{bmatrix} \mathbf{I}_{J-1xJ-1} & \mathbf{0} \\ \mathbf{0} & \mathbf{I}_{J-1xJ-1} \end{bmatrix} \begin{bmatrix} \Delta N_1 \\ \vdots \\ \Delta N_{J-1} \end{bmatrix} + \begin{bmatrix} \mathbf{w}[k] \\ \mathbf{w}[k+l] \end{bmatrix} = \begin{bmatrix} \mathbf{H}_{J-1x3} & \mathbf{0} \\ \mathbf{0} & \mathbf{H}_{J-1x3} \end{bmatrix} \begin{bmatrix} \mathbf{b}_{(O)}[k] \\ \mathbf{b}_{(O)}[k+l] \end{bmatrix} \qquad \textbf{4-12}$$

Defining

$$\mathbf{r}' = \begin{bmatrix} \Delta\bar{r}_1[k] \\ \vdots \\ \Delta\bar{r}_{J-1}[k] \\ \Delta\bar{r}_1[k+l] \\ \vdots \\ \Delta\bar{r}_{J-1}[k+l] \end{bmatrix} \quad \mathbf{D} = \begin{bmatrix} \mathbf{I}_{J-1xJ-1} & \mathbf{0} \\ \mathbf{0} & \mathbf{I}_{J-1xJ-1} \end{bmatrix} \qquad \textbf{4-13}$$

$$\mathbf{H}' = \begin{bmatrix} \mathbf{H}_{J-1x3} & \mathbf{0} \\ \mathbf{0} & \mathbf{H}_{J-1x3} \end{bmatrix} \quad \mathbf{b}'_{(O)} = \begin{bmatrix} \mathbf{b}_{(O)}[k] \\ \mathbf{b}_{(O)}[k+l] \end{bmatrix}$$

then a weighted least-squares cost can be calculated according to

$$\Omega = \left(\mathbf{r}' - \mathbf{H}'\mathbf{b}'_{(O)} - \mathbf{D}\Delta\mathbf{N}\right)^T \mathbf{R}^{-1} \left(\mathbf{r}' - \mathbf{H}'\mathbf{b}'_{(O)} - \mathbf{D}\Delta\mathbf{N}\right) \qquad \textbf{4-14}$$

which is potentially solvable. The benefit of this method is that there are now only $(J-1)+6$ unknowns and $2(J-1)$ measurements. Therefore the equation is solvable if there are sufficient measurements that $2(J-1) \geq (J-1)+6$ or $J \geq 7$. This requires at least seven single-difference measurements giving six double-difference measurements. In fact, more than six double-difference measurements would be preferable so that the problem is over-determined and a least-squares solution can be calculated.

This raises the problem that six double-difference measurements require seven GPS satellites to be tracked continuously over a sufficient period for the carrier phase only float solution to converge. To ensure that the solution is not ill-conditioned it would be better to track more satellites, preferably all in view. The main aim of this research was to demonstrate real-time three-axis GPS attitude determination on a microsatellite in LEO. To solve for three-axis attitude using the SGR-20 on Topsat then the maximum number of satellites that can be tracked on a single baseline is six. Therefore it is not possible to use a float solution (and hence the LAMBDA method) and this method is not investigated any further in this thesis.

4.1.2 Integer search based methods

An alternative to the float solution method is to conduct a search for the correct integer solution that minimises a cost function.

Performing an integer search can be a computationally intensive process, since the search space can be incredibly large. For example, a one metre baseline would result in possible range of integer ambiguities of between -5 and +5, or 11 possibilities. Given J measurements this entails a total search space of 11^J trials. If for example there were six measurements, this equals a search space of 1,771,561 (over a million!) possibilities, each of which would have to be tested according to a cost function. If there are multiple baselines to solve for the computational burden obviously increases. As such the integer search process is possible given the limited number of measurements available on the SGR-20, but would still be impractical to calculate in real-time given the limited computational resources.

However, [Hatch, 1991] demonstrated that the integer ambiguity problem can be reduced to a three dimensional problem. This permits a much faster solution to be obtained, since only 11^3 or 1331 possibilities must be considered. Using the method outlined in section 4.3.2 the search space can be limited to two dimensions, thereby reducing the number of trials required to just 11^2 or 121 for a one metre baseline. Such a reduction in the number of trials required makes it practical to consider implementing the integer search algorithm onboard the SGR-20, rather than relying on external processing such as a laptop or desktop personal computer.

4.1.3 Maximum-likelihood and integer ambiguity resolution

The integer search process involves testing many trial integer ambiguity solutions in order to determine which trial is correct. Previous methods such as those presented in [Purivigraipong, 2000] and [Knight, 1994] tested each trial integer solution by calculating the least-squares cost of each solution. The assumption used in both of these methods was that the correct solution minimised the least-squares cost. [Martin-Neira, 1995] provided a complex analysis of why this assumption was incorrect. An alternative analysis, which is conceptually simpler and based on theory provided by Dr Hodgart is given below.

For a given baseline, a set of path differences $\bar{r}_1, \bar{r}_2, \ldots \bar{r}_J$ can be related to the true orbit-referenced baseline $\mathbf{b}$ according to

$$\bar{r}_j = \mathbf{s}_j^T \mathbf{b} + w_j \qquad \textbf{4-15}$$

where w_j represent independent Gaussian noise.

The joint probability distribution of a particular vector $\bar{\mathbf{r}}$ given $\mathbf{b}$ is

$$f(\bar r_1, \bar r_2, \ldots, \bar r_J | \hat{\mathbf{b}}) = \left(\frac{1}{\sqrt{2\pi\sigma_w}}\right)^J \exp\left(-\frac{(\bar r_1 - \mathbf{s}_1^T\hat{\mathbf{b}})^2}{2\sigma_w^2} - \ldots - \frac{(\bar r_J - \mathbf{s}_J^T\hat{\mathbf{b}})^2}{2\sigma_w^2}\right) \qquad \textbf{4-16}$$

then the maximum likelihood looks for the maximum value to the exponent and is equivalent to adjusting the estimate $\hat{\mathbf{b}}$ such that

$$\varepsilon_{ML}^2 = (\bar r_1 - \mathbf{s}_1^T\hat{\mathbf{b}})^2 + (\bar r_2 - \mathbf{s}_2^T\hat{\mathbf{b}})^2 + \ldots + (\bar r_J - \mathbf{s}_J^T\hat{\mathbf{b}})^2 \qquad \textbf{4-17}$$

is minimised. In this case the formal solution is the arithmetic average. Minimising the above is the same as calculating the least-squares cost

$$\Omega_{ML}(\mathbf{b}) = \sum_{j=1}^{J} (\bar r_j - \mathbf{s}_j^T\hat{\mathbf{b}})^2 \qquad \textbf{4-18}$$

Formally the mean square cost ε_{ML}^2 is the same as

$$\varepsilon_{ML}^2 = \sum_{j=1}^{J} (w_j - e)^2 \qquad \textbf{4-19}$$

where

$$e = \frac{1}{J}\sum_{j=1}^{J} w_j \qquad \textbf{4-20}$$

and the square cost solves to

$$\hat{\varepsilon}_{ML}^2 = \left(1 - \frac{1}{J}\right)\sum_{j=1}^{J} w_j^2 \qquad \textbf{4-21}$$

Therefore the expected value is

$$\langle \varepsilon_{ML}^2 \rangle = (J-1) \times \sigma_w^2 \qquad \textbf{4-22}$$

where $J-1$ are the remaining degrees of freedom.

Now returning to the simple arithmetic average, suppose all the measurements are known only when offset by some unknown integer

$$\bar r_j = \bar r_j - N_j \qquad \textbf{4-23}$$

Then the maximum likelihood method for attempting to identify the correct integer offsets is to look for trial integers $\tilde{N}_j$ as in

$$\tilde{\varepsilon}^2_{ML} = \sum_{j=1}^{J} \left(\bar{r}_j - \tilde{N}_j - \mathbf{s}_j^T \hat{\mathbf{b}}\right) \qquad \text{4-24}$$

for which the correct trial integers would tend to minimise $\tilde{\varepsilon}^2_{ML}$.

Defining a digital error

$$\delta_j = N_j - \tilde{N}_j \qquad \text{4-25}$$

then the error from Equation 4-20 becomes

$$e = \frac{1}{J} \sum_{j=1}^{J} \left(w_j + \delta_j\right) \qquad \text{4-26}$$

and the squared cost solves to

$$\hat{\varepsilon}^2_{ML} = \left(1 - \frac{1}{J}\right) \sum_{j=1}^{J} \left(w_j + \delta_j\right)^2 \qquad \text{4-27}$$

or

$$\hat{\varepsilon}^2_{ML} = \left(1 - \frac{1}{J}\right) \sum_{j=1}^{J} \left(w_j^2 + 2 w_j \delta_j + \delta_j^2\right)^2 \qquad \text{4-28}$$

The expected value on average is therefore given by

$$\left\langle \varepsilon^2_{ML} \right\rangle = (J - 1) \times \sigma_w^2 + \left(1 - \frac{1}{J}\right) \sum_{j=1}^{J} \delta_j^2 \qquad \text{4-29}$$

The above equation states that the true integer ambiguity solution minimises the *expected average* of the mean square cost. The expected average can only be estimated by taking measurements over multiple epochs. Therefore the integer ambiguity resolution algorithm must consider measurements over multiple epochs. A digital error δ_j caused by an error in the trial integers will increase the overall error.

For a single epoch (i.e. given a single set of measurements) minimising the mean square error calculated in Equation 4-27 cannot guarantee the correct trial integers are identified. This is because the cross-term $2 w_j \delta_j$ is random and may push the actual cost below that expected from measurement noise alone. Hence the cost of a given incorrect trial integer solution may result in a lower mean square cost than the true solution, when only considering a single-epoch. This demonstrates why the integer ambiguity resolution algorithm presented in [Purivigraipong, 2000] and also that of [Knight, 1994], which both compare different costs between rival integer ambiguity solutions, are not reliable.

At the start of this section it was assumed that w_j represented independent Gaussian noise. The analysis of spaceflight data in Chapter 3 demonstrated that the GPS carrier phase measurement noise is time correlated due to the presence of multipath. This adds a further difficulty to the integer ambiguity resolution problem, since it means that the expected cost of the trial integer solutions, even when averaged over multiple consecutive epochs, will also be time correlated. More precisely, multipath error may result in the actual cost of an incorrect trial solution being less than the cost of the correct solution even over multiple epochs.

4.2 Overview of robust integer ambiguity resolution algorithm

The integer ambiguity resolution algorithm presented in this section attempts to solve the integer ambiguity problem by performing an integer ambiguity search on an epoch-by-epoch basis, and then combining the results over a span of epochs in order to gain the benefits of using relative constellation motion to eliminate false solutions *whilst working within the limitations of the SGR-20 hardware.*

The new algorithm does not require any *a priori* attitude information and does not place any limits on the attitude dynamics of the platform. The only limits on the orientation of the platform are implicit from the necessity to have at least five satellites in view of all four GPS antennas.

To permit a real-time implementation for use in Low Earth Orbit, the multiple epoch validation method needs to be able to *track* the integer ambiguity solution over multiple epochs. Past experiments such as [Ward, 1996] used *a priori* attitude information to track the single-difference integer ambiguities over multiple epochs when solving for the attitude, but this method does not work if the attitude changes significantly between epochs. In this chapter a method is presented for tracking the double-difference integer ambiguities which does not limit the attitude dynamics of the platform and can be used for both robust integer ambiguity resolution over multiple epochs and for kinematic attitude estimation.

Finally, as was shown in Chapter 3, the line bias on the SGR-20 GPS receiver has an arbitrary value for each baseline at switch on. Future receiver designs may find a way to remove the arbitrary nature of the line bias, but there is currently no way to calibrate the line bias on the SGR-20 and so a double-difference approach was used to remove this nuisance parameter.

4.3 Part I - Solving for the individual baseline pointing

Part I of the algorithm solves for the unknown baseline pointing and integer ambiguities for a single baseline. Following the method first described by [Hatch, 1991] the measurements are partitioned into a *primary* and *secondary* set. To simplify the notation the subscript i denoting the baseline is dropped in this section, since only one baseline is considered.

Double-differences are formed according to the rule:

$$\Delta \bar{r}_{j-1} = \frac{1}{\lambda_{L1}}\left(\bar{r}_j - \bar{r}_1\right) \qquad \textbf{4-30}$$

$$\mathbf{v}_{j-1} = \mathbf{s}_{j(O)} - \mathbf{s}_{1(O)} \quad \text{where } 2 \le j \le J$$

Three double-difference measurements are selected and placed in the primary set. The remaining measurements are placed in the secondary set. When choosing the pivot satellite, which is $\bar{r}_1$ in the above equation, ideally a satellite with no multipath error should be chosen, since any such error will affect all the double-difference measurements. For a platform such as Topsat where the antennas have a clear field-of-view it is reasonable to assume that line of sights to GPS satellites that lie close to the boresight vector of the antennas (i.e. satellites with a high elevation) will be relatively free of multipath if the spacecraft is nominally maintaining a nadir pointing attitude. In this work it was assumed that the satellite was nominally nadir pointing and therefore $\bar{r}_1$ was selected as the highest elevation satellite in each epoch.

4.3.1 Selecting a primary set

The standard method of selecting the primary set involves finding the set that minimises the PDOP. The double-difference measurements are permuted to test all possible sets. For each possible primary set an observation matrix is formed:

$$\mathbf{H}_p = \begin{bmatrix} \mathbf{v}_{S1}^T \\ \mathbf{v}_{S2}^T \\ \mathbf{v}_{S3}^T \end{bmatrix} \qquad \textbf{4-31}$$

where $S1, S2, S3$ are one set or permutation of the double-difference measurements.

The PDOP for each set is calculated according to:

$$\text{PDOP} = \sqrt{\text{tr}\left(\left(\mathbf{H}_p^T \mathbf{R}^{-1} \mathbf{H}_p\right)^{-1}\right)} \qquad \textbf{4-32}$$

where

$$\mathbf{R} = 2\sigma_{\varphi_u}^2 \begin{bmatrix} 2 & 1 & 1 \\ 1 & 2 & 1 \\ 1 & 1 & 2 \end{bmatrix} \qquad \textbf{4-33}$$

The variance for the un-differenced carrier phase measurements σ_{φ_u} can be estimated using the measurement noise estimation technique presented in Chapter 3, since

$$\sigma_{\varphi_u} \approx \frac{\sigma_w}{\sqrt{2}} \qquad \textbf{4-34}$$

The set with the smallest PDOP is chosen as the primary set. The remaining measurements are placed in the secondary set.

4.3.2 Solving for the unknown baseline vector using the primary set

The unknown baseline vector $\mathbf{b}_{(O)}$ can be expressed as a linear combination of any two other 3-vectors providing that they are not collinear,

$$\mathbf{b}_{(O)} = \lambda_1 \mathbf{v}_1 + \lambda_2 \mathbf{v}_2 + \lambda_{12}\left(\mathbf{v}_1 \times \mathbf{v}_2\right) \qquad \textbf{4-35}$$

where $\mathbf{v}_1$ and $\mathbf{v}_2$ are known double-difference LOS vectors. Note that the third axis of the unknown baseline vector is described by the cross product of the two known double-difference LOS vectors.

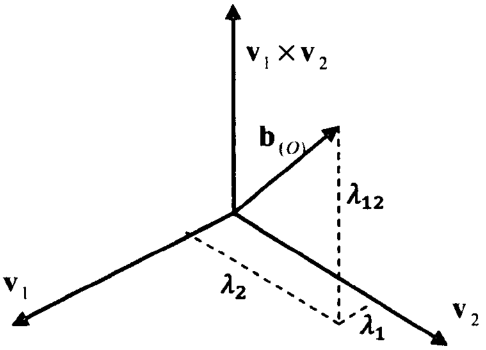

Figure 4-2 Illustration of Equation 4-35

The coefficients $\lambda_1, \lambda_2, \lambda_{12}$ can be found as follows

$$\begin{aligned} \mathbf{b}_{(O)}^T \mathbf{v}_1 &= \lambda_1 \mathbf{v}_1^T \mathbf{v}_1 + \lambda_2 \mathbf{v}_2^T \mathbf{v}_1 \\ \mathbf{b}_{(O)}^T \mathbf{v}_2 &= \lambda_1 \mathbf{v}_1^T \mathbf{v}_2 + \lambda_2 \mathbf{v}_2^T \mathbf{v}_2 \end{aligned} \qquad \textbf{4-36}$$

The projection of the unknown baseline $\mathbf{b}_{(O)}$ onto the known vector $\mathbf{v}_i$ is given by:

$$\Delta \bar{r}_i = \mathbf{b}_{(O)}^T \mathbf{v}_i \qquad \textbf{4-37}$$

which is equivalent to a *path difference*. This leads to

$$\begin{aligned} \Delta \bar{r}_1 &= \lambda_1 \mathbf{v}_1^T \mathbf{v}_1 + \lambda_2 \mathbf{v}_2^T \mathbf{v}_1 \\ \Delta \bar{r}_2 &= \lambda_1 \mathbf{v}_1^T \mathbf{v}_2 + \lambda_2 \mathbf{v}_2^T \mathbf{v}_2 \end{aligned} \qquad \textbf{4-38}$$

Defining the following variables

$$\begin{aligned} a_{11} &= \mathbf{v}_1^T \mathbf{v}_1 \\ a_{22} &= \mathbf{v}_2^T \mathbf{v}_2 \\ a_{12} &= \mathbf{v}_1^T \mathbf{v}_2 \end{aligned} \qquad \textbf{4-39}$$

leads to

$$\begin{aligned} \Delta\vec{r}_1 &= \lambda_1 a_{11} + \lambda_2 a_{12} \\ \Delta\vec{r}_2 &= \lambda_1 a_{12} + \lambda_2 a_{22} \end{aligned} \qquad \textbf{4-40}$$

and rearranging for λ_1, λ_2 gives

$$\begin{aligned} \lambda_1 &= \frac{\Delta\vec{r}_1 a_{22} - \Delta\vec{r}_2 a_{12}}{a_{11} a_{22} - a_{12}^2} \\ \lambda_2 &= \frac{\Delta\vec{r}_2 a_{11} - \Delta\vec{r}_1 a_{12}}{a_{11} a_{22} - a_{12}^2} \end{aligned} \qquad \textbf{4-41}$$

Note that $\mathbf{v}_1$ must not be collinear with $\mathbf{v}_2$ otherwise the denominator in Equation 4-41 goes to zero.

Acknowledging that the path differences $\Delta\vec{r}_1$ and $\Delta\vec{r}_2$ are offset from the measured phase differences by the unknown integer ambiguities:

$$\begin{aligned} \Delta\vec{r}_1 &= \Delta\bar{r}_1 - \Delta N_1 \\ \Delta\vec{r}_2 &= \Delta\bar{r}_2 - \Delta N_2 \end{aligned} \qquad \textbf{4-42}$$

demonstrates that the baseline pointing can be uniquely determined using just two measurements. This means that only two unknown integer ambiguities must be solved for and so the integer search space is reduced to just two dimensions.

For a given primary set, a two-dimensional integer search over ΔN_1 and ΔN_2 is performed. Trial corrected phase measurements are calculated according to:

$$\begin{aligned} \Delta\tilde{r}_1 &= \Delta\bar{r}_1 - \Delta\tilde{N}_1 \\ \Delta\tilde{r}_2 &= \Delta\bar{r}_2 - \Delta\tilde{N}_2 \end{aligned} \qquad \textbf{4-43}$$

The trial parameters $\tilde{\lambda}_1$ and $\tilde{\lambda}_2$ are calculated using

$$\begin{aligned} \tilde{\lambda}_1 &= \frac{\Delta\tilde{r}_1 a_{22} - \Delta\tilde{r}_2 a_{12}}{a_{11} a_{22} - a_{12}^2} \\ \tilde{\lambda}_2 &= \frac{\Delta\tilde{r}_2 a_{11} - \Delta\tilde{r}_1 a_{12}}{a_{11} a_{22} - a_{12}^2} \end{aligned} \qquad \textbf{4-44}$$

where a_{11}, a_{22}, a_{12} are defined in Equation 4-39. The third trial component $\tilde{\lambda}_{12}$ can be determined, and the unknown baseline vector $\mathbf{b}_{(O)}$ fully defined, by exploiting the known magnitude of $\mathbf{b}_{(B)}$ after determining $\tilde{\lambda}_1$ and $\tilde{\lambda}_2$. The component normal to the plane has a magnitude

$$\left\|\mathbf{b}_{\perp}\right\| = \sqrt{\left\|\mathbf{b}_{(B)}\right\|^2 - \tilde{\lambda}_1 \Delta\tilde{r}_1 - \tilde{\lambda}_2 \Delta\tilde{r}_2} \qquad \textbf{4-45}$$

From this the third trial parameter is given by

$$\tilde{\lambda}_{12} = \sqrt{\frac{\left\|\mathbf{b}_{(B)}\right\|^2 - \tilde{\lambda}_1 \Delta\tilde{r}_1 - \tilde{\lambda}_2 \Delta\tilde{r}_2}{a_{11}a_{22} - a_{12}^2}} \qquad \textbf{4-46}$$

leading to two trial equations for the baseline pointing:

$$\begin{aligned} \tilde{\mathbf{b}}_{(O)}^{(m)+} &= \tilde{\lambda}_1 \mathbf{v}_1 + \tilde{\lambda}_2 \mathbf{v}_2 + \left|\tilde{\lambda}_{12}\right| (\mathbf{v}_1 \times \mathbf{v}_2) \\ \tilde{\mathbf{b}}_{(O)}^{(m)-} &= \tilde{\lambda}_1 \mathbf{v}_1 + \tilde{\lambda}_2 \mathbf{v}_2 - \left|\tilde{\lambda}_{12}\right| (\mathbf{v}_1 \times \mathbf{v}_2) \end{aligned} \qquad \textbf{4-47}$$

where the superscript (m) indexes a list of M trial solutions each calculated using just two measurements. The baseline estimate in Equation 4-47 will be subject to non-linear error due to the estimation of the third trial parameter. Therefore the third trial integer ambiguity $\Delta\tilde{N}_3$ is estimated. Using the third double-difference LOS vector $\mathbf{v}_3$:

$$\Delta\tilde{r}_3 - \Delta\tilde{N}_3 \approx \mathbf{v}_3^T \tilde{\mathbf{b}}_{(O)}^{(m)+} \qquad \textbf{4-48}$$

or

$$\Delta\tilde{r}_3 - \Delta\tilde{N}_3 \approx \mathbf{v}_3^T \tilde{\mathbf{b}}_{(O)}^{(m)-} \qquad \textbf{4-49}$$

two equations can be formed

$$\begin{aligned} x_3^{(m)+} &= \mathbf{v}_3^T \tilde{\mathbf{b}}_{(O)}^{(m)+} = \tilde{\lambda}_1 \mathbf{v}_1^T \mathbf{v}_3 + \tilde{\lambda}_2 \mathbf{v}_2^T \mathbf{v}_3 + \left|\tilde{\lambda}_{12}\right| (\mathbf{v}_1 \times \mathbf{v}_2)^T \mathbf{v}_3 \\ x_3^{(m)-} &= \mathbf{v}_3^T \tilde{\mathbf{b}}_{(O)}^{(m)-} = \tilde{\lambda}_1 \mathbf{v}_1^T \mathbf{v}_3 + \tilde{\lambda}_2 \mathbf{v}_2^T \mathbf{v}_3 - \left|\tilde{\lambda}_{12}\right| (\mathbf{v}_1 \times \mathbf{v}_2)^T \mathbf{v}_3 \end{aligned} \qquad \textbf{4-50}$$

which each give a real valued estimate for $\Delta\tilde{N}_3$. Both estimates can be rounded to provide an integer estimate for $\Delta\tilde{N}_3$:

$$\begin{aligned} \Delta\tilde{N}_3^+ &= \mathrm{round}\left(\Delta\tilde{r}_3 - x_3^{(m)+}\right) \\ \Delta\tilde{N}_3^- &= \mathrm{round}\left(\Delta\tilde{r}_3 - x_3^{(m)-}\right) \end{aligned} \qquad \textbf{4-51}$$

Initial testing found that measurement errors can result in neither of the above integer estimates providing the correct estimate for ΔN_3. A simple method for correcting this problem is to estimate two further possible values for $\Delta\tilde{N}_3$ according to:

$$\begin{aligned} \Delta\tilde{N}_3^{++} &= \Delta\tilde{N}_3^{+} + \operatorname{sign}\left(x_3^{(m)+} - \Delta\tilde{N}_3^{+}\right) \\ \Delta\tilde{N}_3^{--} &= \Delta\tilde{N}_3^{-} + \operatorname{sign}\left(x_3^{(m)-} - \Delta\tilde{N}_3^{-}\right) \end{aligned} \tag{4-52}$$

Of these four integer ambiguity estimates it is highly likely that at least two are duplicates and so to save on processing later any duplicate estimates are eliminated at this stage. It is also possible that value inside the radicand in Equation 4-46 is negative which would result in a non-real estimate for $\tilde{\lambda}_{12}$. In such cases $\tilde{\lambda}_{12}$ is set to zero and only two trial third integers are estimated:

$$\begin{aligned} \Delta\tilde{N}_3^{+} &= \operatorname{round}\left(\Delta\bar{r}_3 - x_3^{(m)+}\right) \\ \Delta\tilde{N}_3^{++} &= \Delta\tilde{N}_3^{+} + \operatorname{sign}\left(x_3^{(m)+} - \Delta\tilde{N}_3^{+}\right) \end{aligned} \tag{4-53}$$

Finally, up to four updated estimates for the trial baseline vector are calculated, depending on the number of unique estimates for ΔN_3

$$\tilde{\mathbf{b}}_{(O)}^{(m)\pm} = \mathbf{H}_p^{-1}\left(\Delta\bar{\mathbf{r}}_p - \Delta\tilde{\mathbf{N}}_p\right) \tag{4-54}$$

where

$$\mathbf{H}_p = \begin{bmatrix} \mathbf{v}_1^T \\ \mathbf{v}_2^T \\ \mathbf{v}_3^T \end{bmatrix} \quad \bar{\mathbf{r}}_p = \begin{bmatrix} \Delta\bar{r}_1 \\ \Delta\bar{r}_2 \\ \Delta\bar{r}_3 \end{bmatrix} \quad \Delta\tilde{\mathbf{N}}_p = \begin{bmatrix} \Delta\tilde{N}_1 \\ \Delta\tilde{N}_2 \\ \Delta\tilde{N}_3^{*} \end{bmatrix} \tag{4-55}$$

and $\Delta\tilde{N}_3^{*}$ is one of the up to four possibilities generated above. Note that $\mathbf{H}_p$ is the same for every trial solution and so its inverse can be precalculated and stored for use in the integer search.

The result of the integer search is a list of trial baseline vectors and their associated integer ambiguity vectors which is assumed to contain the correct solution, but there is currently no way of identifying it.

4.3.2.1 Integer Ambiguity Search Range

For each dimension of the integer search space the minimum and maximum integer ambiguity values that bound the search space can be calculated. Ideally these bounds should be as small as possible in order that the search can be performed quickly. However, the correct solution must always lie within the integer search space otherwise the search is invalid.

Reasonable bounds for each dimension of the search can be calculated based on the measurements and geometry of each epoch of measurements as follows. Each carrier phase difference measurement $\Delta\bar{r}_j$ and its accompanying LOS vector $\mathbf{v}_j$ are related via

$$\Delta\bar{r}_j - \Delta N_j + w_j = \mathbf{v}_j^T \mathbf{b}_{(O)} \qquad \textbf{4-56}$$

which can be rearranged to give

$$\Delta N_j = \mathrm{round}\left(\Delta\bar{r}_j - \mathbf{v}_j^T \mathbf{b}_{(O)} + w_j\right) \qquad \textbf{4-57}$$

The true baseline vector $\mathbf{b}_{(O)}$ (in units of cycles) is unknown, but its magnitude $\left\|\mathbf{b}_{(B)}\right\|$ is known since it is the same in both body-referenced and orbit-referenced coordinates. Depending on the relative pointing of the LOS vector and the true baseline vector, the scalar product of the two vectors may lie anywhere in the range $-\left\|\mathbf{v}_j\right\|\left\|\mathbf{b}_{(B)}\right\|$ to $\left\|\mathbf{v}_j\right\|\left\|\mathbf{b}_{(B)}\right\|$.

The integer search bounds for ΔN_j can therefore be defined as

$$\begin{aligned} \Delta N_{j,\min} &= \mathrm{round}\left(\Delta\bar{r}_j - \left\|\mathbf{v}_j\right\|\left\|\mathbf{b}_{(B)}\right\| + w_j\right) \\ \Delta N_{j,\max} &= \mathrm{round}\left(\Delta\bar{r}_j + \left\|\mathbf{v}_j\right\|\left\|\mathbf{b}_{(B)}\right\| + w_j\right) \end{aligned} \qquad \textbf{4-58}$$

Note that the bounds in Equation 4-58 must account for the unknown measurement noise w_j in the carrier phase difference measurements. A simple method is to increase the search space by one in each direction, leading to the bounds

$$\begin{aligned} \Delta N_{j,\min} &= \mathrm{round}\left(\Delta\bar{r}_j - \left\|\mathbf{v}_j\right\|\left\|\mathbf{b}_{(B)}\right\|\right) - 1 \\ \Delta N_{j,\max} &= \mathrm{round}\left(\Delta\bar{r}_j + \left\|\mathbf{v}_j\right\|\left\|\mathbf{b}_{(B)}\right\|\right) + 1 \end{aligned} \qquad \textbf{4-59}$$

These search bounds can be calculated for each of the available measurements in each epoch. The bounds can also be used to check the integers calculated for the secondary set of measurements to ensure that they lie within the permitted range. Any trial solutions which result in an integer lying outside these bounds can then be excluded from the list of possible solutions.

4.3.3 Eliminating unlikely trial baseline vectors

The integer search process produces a list of trial baseline vectors and their associated trial integer ambiguities based on the three measurements in the primary set. The resulting list can contain hundreds of potential solutions depending on the length of the baseline, and so we require a method for eliminating unlikely solutions.

For each trial solution the integer ambiguities for the secondary set can be calculated using each of the M trial baseline vectors calculated using the primary set. A real valued estimate for the jth integer ambiguity is given by:

$$x_j^{(m)} = \Delta\tilde{r}_j - \mathbf{v}_j^T \tilde{\mathbf{b}}_{(O)}^{(m)} \qquad j = 3,4 \text{ etc} \tag{4-60}$$

This can be rounded to give the integer ambiguity for the jth measurement in the secondary set:

$$\Delta\tilde{N}_j = \text{round}\left(x_j^{(m)}\right) \tag{4-61}$$

A potential method for eliminating unlikely solutions would be to calculate the least-squares cost using all the available measurements for the baseline

$$\Omega = \left(\Delta\bar{\mathbf{r}} - \Delta\tilde{\mathbf{N}}^{(m)} - \mathbf{H}\tilde{\mathbf{b}}_{(O)}^{(m)}\right)^T \mathbf{R}^{-1} \left(\Delta\bar{\mathbf{r}} - \Delta\tilde{\mathbf{N}}^{(m)} - \mathbf{H}\tilde{\mathbf{b}}_{(O)}^{(m)}\right) \tag{4-62}$$

It is well known that the χ_n^2 distribution is the distribution of the sum of squares of n independent Gaussian random variables. Assuming that the measurement error w_j is an independent Gaussian random variable then the weighted least-squares cost Ω will satisfy a χ^2 distribution with $J-3$ degrees of freedom.

The cumulative chi-squared distribution is defined as

$$F_n(z^2) = \int_0^{z^2} \chi_n^2(\xi)d\xi \tag{4-63}$$

This represents the probability that the value of the χ_n^2 random variable is less than z^2. From the cumulative distribution it is possible to calculate a threshold t^2 above which it is highly unlikely that the weighted least-squares cost Ω will fall.

$$t^2 = z^2\sigma_w^2 = F_n^{-1}(\alpha)\sigma_w^2 \tag{4-64}$$

where α is the desired probability that if the weighted least-squares cost exceeds this threshold it is unlikely to be the correct solution.

The weighted least-squares cost Ω for each trial baseline vector can be evaluated using the threshold t^2 to determine if the trial baseline vector is likely to be the correct solution. If

$$\Omega < t^2 \tag{4-65}$$

then the solution can admitted to the list of possible solutions. If the above condition is not met then the trial solution can be discarded.

The problem with this method is that it requires the calculation of Ω for the entire list of M trials. For real-time operation the processing requirements need to be kept to a minimum. A faster method is to calculate the individual residuals for each of the measurements in the secondary set and compare this residual against an expected variance.

Using each of the M trial baseline vectors calculated using the primary set, a real valued estimate for the jth integer ambiguity in the secondary set can be calculated:

$$\tilde{x}_j^{(m)} = \Delta\bar{r}_j - \mathbf{v}_j^T\tilde{\mathbf{b}}_{(O)}^{(m)} \qquad j = 3,4 \text{ etc} \tag{4-66}$$

This can be rounded to give the integer ambiguity for the jth measurement in the secondary set:

$$\Delta\tilde{N}_j^{(m)} = \text{round}\left(\tilde{x}_j^{(m)}\right) \tag{4-67}$$

And the residual for the jth measurement is then calculated as

$$d_j^2 = \left(\tilde{x}_j^{(m)} - \Delta\tilde{N}_j^{(m)}\right)^2 \tag{4-68}$$

Since the residual is a function of the trial baseline pointing the variance for the residual calculated in Equation 4-68 must be determined. The following derivation for the variance of a double-difference measurement in the secondary set, relative to the baseline estimate calculated using only the primary set, follows the method shown in [Kee et al, 2007].

The true integer is given by

$$\Delta N_j = \text{round}\left(\Delta r_j - \mathbf{v}_j^T\mathbf{b}_O\right) \tag{4-69}$$

where Δr_j is the true double-difference phase.

Given that

$$\tilde{\mathbf{b}}_{(O)}^{(m)} = \mathbf{H}_p^{-1}\left[\Delta\bar{\mathbf{r}}_p - \Delta\tilde{\mathbf{N}}_p^{(m)}\right] \tag{4-70}$$

Equation 4-66 can be expanded as follows

$$\tilde{x}_j = \Delta\bar{r}_j - \mathbf{v}_j^T\mathbf{H}_p^{-1}\left[\Delta\bar{\mathbf{r}}_p - \Delta\tilde{\mathbf{N}}_p^{(m)}\right] \tag{4-71}$$

Then the residual d_j is calculated as

$$d_j = \Delta\bar{r}_j - \mathbf{v}_j^T\mathbf{H}_p^{-1}\left[\Delta\bar{\mathbf{r}}_p - \Delta\tilde{\mathbf{N}}_p^{(m)}\right] - \Delta r_j - \mathbf{v}_j^T\mathbf{b}_{(O)} \tag{4-72}$$

and noting that the true baseline vector is given by

$$\mathbf{b}_{(O)} = \mathbf{H}_p^{-1}\left[\Delta\mathbf{r}_p - \Delta\mathbf{N}_p\right] \tag{4-73}$$

leads to

$$d_j = \Delta\bar{r}_j - \mathbf{v}_j^T \mathbf{H}_p^{-1}\left[\Delta\bar{\mathbf{r}}_p - \Delta\widetilde{\mathbf{N}}_p^{(m)}\right] - \Delta r_j - \mathbf{v}_j^T \mathbf{H}_p^{-1}\left[\Delta\mathbf{r}_p - \Delta\mathbf{N}_p\right] \qquad \text{4-74}$$

For the correct trial integers the residual reduces to

$$d_j = \left(\Delta\bar{r}_j - \Delta r_j\right) - \mathbf{v}_j^T \mathbf{H}_p^{-1}\left(\Delta\bar{\mathbf{r}}_p - \Delta\mathbf{r}_p\right) \qquad \text{4-75}$$

The variance of Equation 4-75 is given by

$$\sigma_{d_j}^2 = E\left\{d_j d_j^T\right\} \qquad \text{4-76}$$

$$\begin{aligned} E\left\{d_j d_j^T\right\} = E\Big\{\Big(\left(\Delta\bar{r}_j - \Delta r_j\right) - \mathbf{v}_j^T \mathbf{H}_p^{-1}\left(\Delta\bar{\mathbf{r}}_p - \Delta\mathbf{r}_p\right)\Big)\ldots \\ \Big(\left(\Delta\bar{r}_j - \Delta r_j\right) - \mathbf{v}_j^T \mathbf{H}_p^{-1}\left(\Delta\bar{\mathbf{r}}_p - \Delta\mathbf{r}_p\right)\Big)^T\Big\} \end{aligned} \qquad \text{4-77}$$

leading to

$$\begin{aligned} E\left\{d_j d_j^T\right\} = E\left\{\left(\Delta\bar{r}_j - \Delta r_j\right)\left(\Delta\bar{r}_j - \Delta r_j\right)^T\right\}\ldots \\ - 2E\left\{\mathbf{v}_j^T \mathbf{H}_p^{-1}\left(\Delta\bar{\mathbf{r}}_j - \Delta\mathbf{r}_j\right)\left(\Delta\bar{r}_j - \Delta r_j\right)\right\}\ldots \\ + E\left\{\mathbf{v}_j^T \mathbf{H}_p^{-1}\left(\Delta\bar{\mathbf{r}}_p - \Delta\mathbf{r}_p\right)\left(\Delta\bar{\mathbf{r}}_p - \Delta\mathbf{r}_p\right)^T \mathbf{H}_p^{-T}\mathbf{v}_j\right\}\Big] \end{aligned} \qquad \text{4-78}$$

then acknowledging that

$$\mathbf{R} = E\left\{\left(\Delta\bar{\mathbf{r}}_p - \Delta\mathbf{r}_p\right)\left(\Delta\bar{\mathbf{r}}_p - \Delta\mathbf{r}_p\right)^T\right\} \qquad \text{4-79}$$

$$\sigma_{dd(i,j)} = E\left\{\left(\Delta\bar{r}_j - \Delta r_j\right)\left(\Delta\bar{r}_j - \Delta r_j\right)^T\right\} \qquad \text{4-80}$$

$$\begin{bmatrix} \sigma_{dd(1,j)}^2 \\ \sigma_{dd(2,j)}^2 \\ \sigma_{dd(3,j)}^2 \end{bmatrix} = E\left\{\mathbf{v}_j^T \mathbf{H}_p^{-1}\left(\Delta\bar{\mathbf{r}}_j - \Delta\mathbf{r}_j\right)\left(\Delta\bar{r}_j - \Delta r_j\right)\right\} \qquad \text{4-81}$$

Equation 4-79 can be simplified to give

$$\sigma_{d_j}^2 = R_{i,i} - 2\mathbf{v}_j^T \mathbf{H}_p^{-1}\begin{pmatrix} R_{1,j} \\ R_{2,j} \\ R_{3,j} \end{pmatrix} + \mathbf{v}_j^T \mathbf{H}_p^{-1}\mathbf{R}_p \mathbf{H}_p^{-T}\mathbf{v}_j \qquad \text{4-82}$$

where $R_{i,i}$ is the respective diagonal element of the covariance matrix $\mathbf{R}_{j-1}$ defined as

$$\mathbf{R}_{J-1} = 2\sigma_{\varphi_u}^2 \begin{bmatrix} 2 & 1 & \cdots & 1 \\ 1 & 2 & \cdots & 1 \\ \vdots & \vdots & \ddots & 1 \\ 1 & 1 & 1 & 2 \end{bmatrix}_{(J-1)\times(J-1)} \qquad \textbf{4-83}$$

The residual calculated in Equation 4-68 has a single degree of freedom, rather than the $J-3$ degrees of freedom for the weighted least-squares cost Ω. For a single degree of freedom the cumulative chi-squared distribution reduces to a simple confidence interval test for a single random variable. A confidence interval can be defined within which the residual d_j for the correct solution will lie to a given probability α.

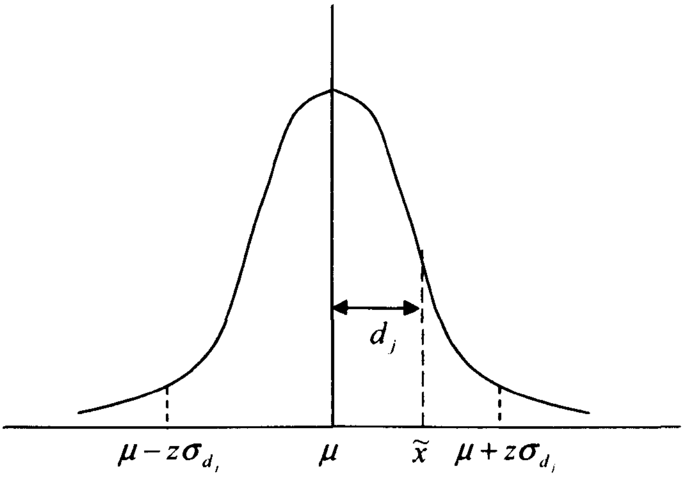

For example, if α=95%, then $z = 1.96$ and by checking that the residual d_j lies within

$$-1.96\sigma_{d_j} \le d_j \le 1.96\sigma_{d_j} \qquad \textbf{4-84}$$

or equivalently

$$d_j^2 < 3.84\sigma_{d_j}^2 \qquad \textbf{4-85}$$

there is a 95% probability that the residual d_j fits the assumed noise distribution and hence provides an indication that the trial baseline vector is a likely solution.

Each residual calculated using the secondary set can be tested against the threshold as in Equation 4-85. If either of the (up to two) residuals for the measurements in the secondary set lie within the confidence interval the trial baseline vector is added to the list of likely solutions. This is repeated for each trial baseline vector generated by the integer search, resulting in a list containing only the likely solutions according to the above test.

4.3.4 Updating the trial baseline pointing solutions

For each trial baseline pointing solution the estimate of the baseline pointing is updated using the measurements from the secondary set.

The updated baseline estimate is calculated as

$$\tilde{\mathbf{b}}^{(m)}_{(O)} = \mathbf{P}\left[\Delta\bar{\mathbf{r}}_{J-1} - \tilde{\mathbf{N}}^{(m)}_{J-1}\right] \qquad \text{4-86}$$

where

$$\mathbf{P} = \left(\mathbf{H}^T_{J-1}\mathbf{R}^{-1}_{J-1}\mathbf{H}_{J-1}\right)^{-1}\mathbf{H}^T_{J-1}\mathbf{R}^{-1}_{J-1}$$

$$\mathbf{H}_{J-1} = \begin{bmatrix} \mathbf{v}^T_1 \\ \mathbf{v}^T_2 \\ \vdots \\ \mathbf{v}^T_{J-1} \end{bmatrix} \quad \Delta\bar{\mathbf{r}}_{J-1} = \begin{bmatrix} \Delta\bar{r}_1 \\ \Delta\bar{r}_2 \\ \vdots \\ \Delta\bar{r}_{J-1} \end{bmatrix} \quad \tilde{\mathbf{N}}^{(m)}_{J-1} = \begin{bmatrix} \Delta\tilde{N}^{(m)}_1 \\ \Delta\tilde{N}^{(m)}_2 \\ \vdots \\ \Delta\tilde{N}^{(m)}_{J-1} \end{bmatrix} \qquad \text{4-87}$$

and the weighting matrix $\mathbf{R}_{J-1}$ is defined in Equation 4-83.

Note that $\mathbf{P}$ is a function of the geometry which is the same for trials and so $\mathbf{P}$ can be precalculated at the beginning of the algorithm.

4.3.5 Constraining the list size through baseline length check

The longer the list generated in Part I, the longer the entire algorithm requires for completion. A simple method for constraining the list size whilst ensuring the correct solution is in the list is to compare the length of the weighted least squares baseline estimates calculated in Equation 4-86 with the known length of the baseline.

$$\varepsilon^2_{\|\tilde{\mathbf{b}}\|} = \left(\left\|\tilde{\mathbf{b}}^{(m)}_{(O)}\right\| - \left\|\mathbf{b}_{(B)}\right\|\right)^2 \qquad \text{4-88}$$

The variance of the error in the trial baseline length $\varepsilon_{\|\tilde{\mathbf{b}}\|}$ is given by

$$\sigma^2_{\|\tilde{\mathbf{b}}\|} = \operatorname{tr}\left(\frac{\mathbf{b}^T_{(O)}}{\left\|\mathbf{b}_{(O)}\right\|}\left(\mathbf{H}^T\mathbf{R}^{-1}\mathbf{H}\right)^{-1}\frac{\mathbf{b}_{(O)}}{\left\|\mathbf{b}_{(O)}\right\|}\right) \qquad \text{4-89}$$

which can be approximated by

$$\sigma^2_{\|\tilde{\mathbf{b}}\|} = \operatorname{tr}\left(\frac{\tilde{\mathbf{b}}^{(m)T}_{(O)}}{\left\|\tilde{\mathbf{b}}^{(m)}_{(O)}\right\|}\left(\mathbf{H}^T\mathbf{R}^{-1}\mathbf{H}\right)^{-1}\frac{\tilde{\mathbf{b}}^{(m)}_{(O)}}{\left\|\tilde{\mathbf{b}}^{(m)}_{(O)}\right\|}\right) \qquad \text{4-90}$$

The error in the length of each trial baseline vector can then be tested against a threshold in a similar manner to the residuals of the secondary set as described above. A threshold t^2 can be defined above which it is highly unlikely that the error in the correct baseline will fall.

$$t^2 < z^2\sigma^2_{\|\tilde{\mathbf{b}}\|} \qquad \textbf{4-91}$$

where $z^2 = F_n^{-1}(\alpha)$ and $n = (J-2)$ since the baseline length is estimated. To reduce the amount of required processing the threshold can be precalculated using the known length of the baseline as follows

$$\sigma^2_{\|\tilde{\mathbf{b}}\|} = \left\|\mathbf{b}_{i(B)}\right\|^2 \mathrm{trace}\left(\left(\mathbf{H}^T\mathbf{R}^{-1}\mathbf{H}\right)^{-1}\right) \qquad \textbf{4-92}$$

If the condition is met then the trial solution is permitted, otherwise it is removed from the list.

4.3.6 Overview of Part I algorithm

The figure below gives an overview of Part I of the algorithm.

1. *Calculate double-differences for phase measurements and LOS vectors (Equation* 4-30*)*
2. *Select measurements for primary set based on minimum PDOP (Section 4.3.1)*
3. *Pre-compute variances and thresholds (Equations* 4-82 *and* 4-92*)*
4. *Calculate permitted bounds of integer search and secondary set (Equation* 4-59*)*
5. *Perform 2D integer search (section 4.3.2)*
6. *For each potential set of trial integers (there may be up to four),*
    a. *Calculate the trial baseline pointing (direct solution) (Equation* 4-54*)*
    b. *For each measurement in the secondary set*
        i. *Predict the integer ambiguity (Equation* 4-67*)*
        ii. *Calculate the residual (Equation* 4-68*)*
        iii. *Use pre-computed threshold to test goodness of fit (Equation* 4-85*)*
    c. *Update the baseline estimate with secondary set measurements using least-squares (Equation* 4-86*)*
    d. *Calculate norm of trial baseline vector (Equation* 4-88*) and check against threshold*
    e. *If trial solution passes thresholds in 6.b.iii and 6.d then add to list*

Figure 4-3 Overview of Part I algorithm

The whole process described above is repeated for each baseline, resulting in a list of trial solutions for each. As was shown in section 4.1.3 it is likely that there are many possible solutions in the list, and choosing one solution over the others based on a relative comparison (such as their least-squares cost) is not reliable. Therefore it is necessary to use additional information to identify the correct solution.

4.4 Part II – Constructing trial baseline pairs

In this part of the algorithm a pair of trial baseline pointing solutions is used to calculate a *virtual phase measurement* by projecting one baseline onto the other. This allows the method of testing against a threshold (as used in Part I) to be used to assess whether or not the two trial baseline vectors match the known relative geometry of the body-referenced baselines to some confidence interval.

A *virtual phase measurement* is calculated by projecting the trial solution for baseline 1, $\tilde{\mathbf{b}}_{1(O)}$, onto the trial solution for baseline 2, $\tilde{\mathbf{b}}_{2(O)}$:

$$r_{virtual(O)} = \tilde{\mathbf{b}}_{1(O)}^{T}\tilde{\mathbf{b}}_{2(O)} \qquad \textbf{4-93}$$

A similar equation can be formed based on the body-referenced baselines $\mathbf{b}_{1(B)}$ and $\mathbf{b}_{2(B)}$,

$$r_{virtual(B)} = \mathbf{b}_{1(B)}^{T}\mathbf{b}_{2(B)} \qquad \textbf{4-94}$$

from which a residual $d_{virtual}^{2}$ can be calculated according to:

$$d_{virtual}^{2} = \left(r_{virtual(O)} - r_{virtual(B)}\right)^{2} \qquad \textbf{4-95}$$

A confidence interval can be defined to test whether the virtual phase measurement residual lies within the assumed noise distribution and therefore shows that the trial pair of pointing solutions is a likely solution.

4.4.1 Establishing the distance threshold for the virtual phase measurements

The covariance for the error in the *true* trial baseline vector estimate $\tilde{\mathbf{b}}_{(O)}$ is given by

$$\sigma_{\mathbf{b}_{(O)}}^{2} = \left(\mathbf{H}^{T}\mathbf{R}^{-1}\mathbf{H}\right)^{-1} \qquad \textbf{4-96}$$

Using the covariance propagation law, the expected variance for a single trial baseline estimate projected onto a second *known* baseline vector is given by

$$\sigma_{\mathbf{b}_{h(O)}^{T}\mathbf{b}_{i(O)}}^{2} = \mathbf{b}_{i(O)}^{T}\left(\mathbf{H}_{h}^{T}\mathbf{R}^{-1}\mathbf{H}_{h}\right)^{-1}\mathbf{b}_{i(O)} \qquad \textbf{4-97}$$

Therefore, as shown in [Brown, 1992], the expected total variance of the virtual phase measurement is given by

$$\sigma_{d_{virtual}}^{2} = \mathbf{b}_{h(O)}^{T}\left(\mathbf{H}_{i}^{T}\mathbf{R}^{-1}\mathbf{H}_{i}\right)^{-1}\mathbf{b}_{h(O)} + \mathbf{b}_{i(O)}^{T}\left(\mathbf{H}_{h}^{T}\mathbf{R}^{-1}\mathbf{H}_{h}\right)^{-1}\mathbf{b}_{i(O)} \qquad \textbf{4-98}$$

where $\mathbf{H}_i$ is the observation matrix of double-difference LOS vectors for the satellites tracked on baseline i. Since the true baseline vectors in orbit-referenced coordinates are unknown there is no way of solving Equation 4-98 directly. An approximation to Equation 4-98 can be calculated using the estimated baseline vectors, as suggested in [Quinn, 1993]:

$$\sigma^2_{d_{virtual}} = \tilde{\mathbf{b}}^T_{h(O)}\left(\mathbf{H}_i^T\mathbf{R}^{-1}\mathbf{H}_i\right)^{-1}\tilde{\mathbf{b}}_{h(O)} + \tilde{\mathbf{b}}^T_{i(O)}\left(\mathbf{H}_h^T\mathbf{R}^{-1}\mathbf{H}_h\right)^{-1}\tilde{\mathbf{b}}_{i(O)} \qquad \textbf{4-99}$$

but this would require recalculating the threshold for each trial solution, of which there may be many. [Kee *et al*, 2003] suggests an alternative method is to set an upper-bound using an approximation to Equation 4-98 based on the major axis of the error ellipse. The covariance of the baseline estimate given in Equation 4-97 can be geometrically described as an m-dimensional ellipsoid, where m is three due to the re-projection onto the second *known* baseline. The dimensions of the ellipsoid along each axis represent the variance of baseline pointing estimate along that axis. The axes and dimensions of the ellipsoid can be calculated by performing eigenvalue decomposition on Equation 4-97. The eigenvectors then describe the axes of the ellipsoid, and the eigenvalues define the variance along each axis. Due to the correlation of the double-difference measurements, one of the eigenvalues is typically much larger than the other two, and an upper bound on the variance of the baseline estimate can be defined by using the maximum eigenvalue:

$$\sigma^2_{\mathbf{b}_{upper}} = \left\|\mathbf{b}_{i(B)}\right\|^2 \max\left\{\mathrm{eig}\left(\left(\mathbf{H}^T\mathbf{R}^{-1}\mathbf{H}\right)^{-1}\right)\right\} \qquad \textbf{4-100}$$

Calculating the eigenvalue decomposition is computationally expensive so therefore to reduce processor loading we use an approximation to Equation 4-100. By assuming that one eigenvalue is much larger than the others, and knowing that the trace of a matrix is the sum of the eigenvalues of the matrix, gives:

$$\sigma^2_{\mathbf{b}_{upper}} = \left\|\mathbf{b}_{i(B)}\right\|^2 \mathrm{trace}\left(\left(\mathbf{H}^T\mathbf{R}^{-1}\mathbf{H}\right)^{-1}\right) \qquad \textbf{4-101}$$

which negates the need to perform the eigenvalue decomposition. This then allows Equation 4-98 to be simplified to

$$\sigma^2_{d_{virtual}} = \left\|\mathbf{b}_{h(B)}\right\|^2 \mathrm{trace}\left(\left(\mathbf{H}_i^T\mathbf{R}^{-1}\mathbf{H}_i\right)^{-1}\right) + \left\|\mathbf{b}_{i(B)}\right\|^2 \mathrm{trace}\left(\left(\mathbf{H}_h^T\mathbf{R}^{-1}\mathbf{H}_h\right)^{-1}\right) \qquad \textbf{4-102}$$

and if assuming that both baselines are tracking the same satellites (which is generally the case due to the receiver software) then

$$\sigma^2_{d_{virtual}} = \left(\left\|\mathbf{b}_{h(B)}\right\|^2 + \left\|\mathbf{b}_{i(B)}\right\|^2\right)\mathrm{trace}\left(\left(\mathbf{H}^T\mathbf{R}^{-1}\mathbf{H}\right)^{-1}\right) \qquad \textbf{4-103}$$

This approximation to the variance is sub-optimal since it does not represent the true variance of the virtual phase measurement. A Monte-Carlo style simulation was run to compare the different approximations to the variance. The true variance given in Equation 4-99, and the eigenvalue and trace approximations to the true variance were all calculated for each epoch. A histogram of the virtual phase measurement residuals from Equation 4-95 is shown in Figure 4-4. The blue vertical line gives the value of the true standard deviation calculated by taking the square root of the mean variance from Equation 4-99. Similarly the red line gives the standard deviation calculated using the eigenvalue approximation, and the green line the trace approximation. For the true variance calculation, sixty-eight percent of the residuals lie within one standard deviation of the mean. For the eigenvalue approximation this rises to seventy-seven percent, and for the trace approximation the figure is eighty-eight percent.

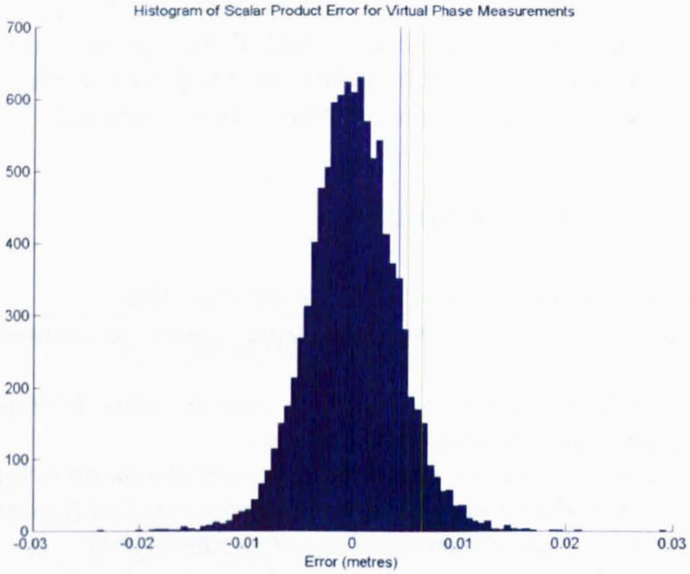

Figure 4-4 Histogram of virtual phase measurement residuals

The results of simulation show that both the eigenvalue and trace approximations are sub-optimal and will allow a larger percentage of unlikely solutions to pass the threshold. However, both approximations are computationally simpler and can be pre-calculated. The pre-computed variance can be used to test to all trial pairs in that epoch. This results in a saving in computational power when compared to Equation 4-99 as used in [Quinn, 1993]. The eigenvalue method used in [Kee *et al,* 2003] would require more computation time than the trace method, whilst still being suboptimal. Given the limited computational resources of the SGR-20 the trace method was chosen for a real-time implementation onboard the SGR-20.

4.4.2 Confidence interval

If the true variance for Part II was known a confidence interval could be established which would ensure that a chosen percentage of correct solutions lie within the confidence interval. The variance in Part II is an approximation of the true variance and so only an approximation to the confidence interval can be calculated.

$$t^2 \approx z^2\sigma^2_{d_{virtual}} \qquad \textbf{4-104}$$

This approximation will typically result in a higher number of trial baseline pairs being placed in the list for Part II, meaning that Part III and Part IV of the algorithm will have more trial solutions to test.

4.4.3 Eliminating unlikely trial baseline pairs

For each trial baseline pair the virtual phase measurement technique is used to test the relative geometry of the pair against the known geometry of the body-referenced baselines. If the virtual phase measurement residual for a given trial baseline pair is less than the calculated threshold then the trial pair is placed in the list for Part II. Any solutions not meeting the geometry constraint can be discarded.

4.4.4 Overview of Part II algorithm

The figure below gives an overview of Part II of the algorithm.

```
1. Precalculate the threshold for the virtual phase measurement (Equation 4-103)
2. Precalculate the projection of baseline 'a' onto baseline 'b' (Equation 4-94)
3. For each pair-wise combination of baselines
    a. Calculate the virtual phase measurement (Equation 4-93)
    b. Calculate the virtual phase measurement residual (Equation 4-95)
    c. Use precalculated threshold to test goodness of fit
        i. If residual lies within threshold, place in list
        ii. If not do not add to output list (remove pair from solution)
    d. Repeat from step 1
```

Figure 4-5 Overview of Part II algorithm

Since Part II only uses two of the three available lists from Part I, it is run for each of the three combinations of two baselines. This has the advantage of reducing the overall computation by requiring [MxN] + [NxP] + [MxP] combinations, rather than [MxNxP], which will always be larger.

4.5 Part III – Using the third baseline and solving for attitude

It is likely that there are multiple solutions that met the geometry constraints in Part II. To reduce the number of solutions further, additional tests can be conducted by using the extra information available in the measurements and relative geometry of the third baseline.

4.5.1 Estimating the pointing of the third baseline

Firstly, each pair of trial baseline pointing vectors, $\tilde{\mathbf{b}}^{(l)}_{1(O)}$ and $\tilde{\mathbf{b}}^{(l)}_{2(O)}$, passed from Part II are used to estimate the attitude. For each trial pair of solutions the TRIAD method (see section 2.3.3.2) is used to directly estimate a trial attitude matrix $\tilde{\mathbf{A}}^{(l)}$. The trial estimated attitude $\tilde{\mathbf{A}}^{(l)}$ can then be used to calculate the unknown integer ambiguities for the third baseline using:

$$\Delta\tilde{N}_{3,j}^{(l)} = \text{round}\left(\Delta\bar{r}_{3,j} - \mathbf{b}_{3(B)}^{T}\tilde{\mathbf{A}}^{(l)}\mathbf{v}_{3,j}\right) \tag{4-105}$$

where the subscript '3' denotes the third (as yet unused) baseline. Solving for the integer ambiguities in this way allows the third baseline to be solved directly without resorting to the two-dimensional integer search as was required in Part I. Given a primary set of measurements $\Delta\bar{r}_1, \Delta\bar{r}_2, \Delta\bar{r}_3$ for the third baseline and their corresponding trial integer ambiguities from Equation 4-105 the pointing of the third baseline is given by

$$\tilde{\mathbf{b}}_{3(O)}^{(l)} = \mathbf{P}_p\left[\Delta\bar{\mathbf{r}}_p - \Delta\tilde{\mathbf{N}}_p^{(l)}\right] \tag{4-106}$$

where

$$\mathbf{P}_p = \left(\mathbf{H}_p^T\mathbf{R}_p^{-1}\mathbf{H}_p\right)^{-1}\mathbf{H}_p^T \tag{4-107}$$

and

$$\mathbf{H}_p = \begin{bmatrix} \mathbf{v}_{1(O)}^T \\ \mathbf{v}_{2(O)}^T \\ \mathbf{v}_{3(O)}^T \end{bmatrix} \quad \Delta\bar{\mathbf{r}}_p = \begin{bmatrix} \Delta\bar{r}_1 \\ \Delta\bar{r}_2 \\ \Delta\bar{r}_3 \end{bmatrix} \quad \mathbf{R}_p = 2\sigma_{\phi_u}^2\begin{bmatrix} 2 & 1 & 1 \\ 1 & 2 & 1 \\ 1 & 1 & 2 \end{bmatrix} \tag{4-108}$$

Since **P** is only a function of the satellite geometry it can be precalculated and used for all the trial solutions in the list.

The trial baseline vector $\tilde{\mathbf{b}}_{3(O)}^{(l)}$ is calculated for each trial solution contained in the list from Part II. Note that when selecting the measurements for the primary set the same method as described in section 4.3.1 is used.

4.5.2 Eliminating unlikely trial baseline triplets

Using the third trial baseline vector estimated above, the procedure from Part I is repeated (see section 4.3.3). For each measurement in the secondary set a residual d_j is calculated. This residual is tested to see whether it lies within a calculated confidence interval. If either of the residuals of the (up to two) measurements in the secondary set lie within the confidence interval then the trial triplet is deemed likely and added to a list of likely trial triplets for Part III. Trial triplets for which neither of the residuals for the measurements in the secondary set met the calculated threshold are discarded.

4.5.2.1 Updating the trial baseline pointing solution

Given the list of trial triplets an improved estimate $\tilde{\mathbf{b}}^{(l)}_{3(O)}$ can be calculated using all the measurements for the third baseline

$$\tilde{\mathbf{b}}^{(l)}_{3(O)} = \mathbf{P}_{J-1}\left[\Delta\bar{\mathbf{r}}_{J-1} - \Delta\mathbf{N}^{(l)}_{J-1}\right] \qquad \textbf{4-109}$$

where

$$\mathbf{P}_{J-1} = \left(\mathbf{H}^{T}_{J-1}\mathbf{R}^{-1}_{J-1}\mathbf{H}_{J-1}\right)^{-1}\mathbf{H}^{T}_{J-1}\mathbf{R}^{-1}_{J-1} \qquad \textbf{4-110}$$

Again $\mathbf{P}_{J-1}$ can be precalculated since it is constant for a given geometry and number of satellites.

4.5.2.2 Relative geometry tests

In Part II the relative geometry of the trial baseline pairs was compared with the known relative geometry of the baselines in body-referenced coordinates. In Part III the trial third baseline vector is compared with each of the two trial baselines from Part II using the same method. Since the baseline vector for the third baseline was estimated a new variance and distance threshold must be calculated.

First, a virtual phase measurement is calculated

$$r_{virtual(O)} = \tilde{\mathbf{b}}^{T}_{i(O)}\tilde{\mathbf{b}}_{3(O)} \qquad i = 1,2 \qquad \textbf{4-111}$$

A similar equation is formed based for the body-referenced baselines

$$r_{virtual(B)} = \mathbf{b}^{T}_{i(B)}\mathbf{b}_{3(B)} \qquad \textbf{4-112}$$

from which a residual $d^2_{virtual}$ can be calculated according to:

$$d^2_{virtual} = \left(r_{virtual(O)} - r_{virtual(B)}\right)^2 \qquad \textbf{4-113}$$

The variance for the residual in Equation 4-113 is given by

$$\sigma^2_{d_{virtual}} = \mathbf{b}^{T}_{i(O)}\left(\mathbf{H}^{T}_{3}\mathbf{R}^{-1}\mathbf{H}_{3}\right)^{-1}\mathbf{b}_{i(O)} + \mathbf{b}^{T}_{3(O)}\left(\mathbf{H}^{T}_{i}\mathbf{R}^{-1}\mathbf{H}_{i}\right)^{-1}\mathbf{b}_{3(O)} \qquad \textbf{4-114}$$

which again because the true baseline vectors are unknown, must be approximated using:

$$\sigma^2_{d_{virtual}} \approx \left(\left\|\mathbf{b}_{i(B)}\right\|^2 + \left\|\mathbf{b}_{3(B)}\right\|^2\right)\mathrm{trace}\left(\left(\mathbf{H}^{T}\mathbf{R}^{-1}\mathbf{H}\ \right)^{-1}\right) \qquad \textbf{4-115}$$

assuming that the same satellites are tracked on each baseline.

The assumed variance in Equation 4-115 can be used to define a confidence interval as in section 4.4.2. This confidence interval can be used to test whether the relative geometry of the trial triplet matches that of the body-referenced baseline vectors to a given confidence interval as was done in section 4.4.3. If the relative geometry matches then the trial triplet is allowed to remain in the list, otherwise it is discarded.

4.5.3 Attitude residuals test

By this point in the algorithm it is assumed that only a handful of solutions remain i.e. fewer than five. So far the attitude has only been estimated using the TRIAD algorithm which only uses information from two of the baselines. A better attitude estimate can be calculated using the double-difference attitude point solution described in section 2.3.3.4. This algorithm calculates a non-linear least-squares estimate of the attitude using information from all three baselines. The *a priori* attitude solution required to initialise the algorithm is available from the TRIAD estimate of the attitude used to calculate the pointing of the third baseline. The attitude estimate for each trial triplet in the list is therefore updated using the double-difference point solution algorithm. For minimal addition computational cost the normalised attitude residuals can be calculated as follows:

$$\Omega = \left(\Delta\mathbf{r}_i[k] - \mathbf{H}^T[k]\hat{\mathbf{x}}[k]\right)^T \mathbf{R}'^{-1} \left(\Delta\mathbf{r}_i[k] - \mathbf{H}^T[k]\hat{\mathbf{x}}[k]\right) \qquad \textbf{4-116}$$

The residuals vector $\mathbf{z}$ is already calculated as part of the double-difference point solution algorithm

$$\mathbf{z}[k] = \begin{bmatrix} \vdots \\ \Delta\bar{r}_{i,j}[k] - 2\left(\hat{\mathbf{A}}[k]\mathbf{v}_{i,j}[k]\right)^T \mathbf{B}^\times[k]\hat{\mathbf{x}}[k] \\ \vdots \end{bmatrix} = \begin{bmatrix} \vdots \\ \Delta\bar{r}_{i,j}[k] - \Delta\hat{r}_{i,j}[k] \\ \vdots \end{bmatrix} \qquad \textbf{4-117}$$

and therefore the normalised sum of squares can be easily calculated as

$$\Omega = \mathbf{z}^T \mathbf{R}'^{-1}\mathbf{z} \qquad \textbf{4-118}$$

where **R'** is defined in Equation 2-65.

Assuming that the measurement error w_j is an independent Gaussian random variable then the weighted least-squares cost Ω will satisfy a χ^2 distribution with $3(J-1)-3$ degrees of freedom. This assumes $(J-1)$ measurements on three baselines are used to estimate three parameters (roll, pitch and yaw).

The cumulative chi-squared distribution is defined as

$$F_n(z^2) = \int_0^{z^2} \chi_n^2(\xi)d\xi \qquad \textbf{4-119}$$

This represents the probability that the value of the χ_n^2 random variable is less than z^2. From the cumulative distribution it is possible to calculate a threshold t^2 above which it is highly unlikely that the weighted least-squares cost Ω will fall.

$$t^2 = z^2\sigma_w^2 = F_n^{-1}(\alpha)\sigma_w^2 \qquad \textbf{4-120}$$

where α is the desired probability that if the weighted least-squares cost exceeds this threshold it is unlikely to be the correct solution. Since the sum of squared residuals is normalised this reduces to

$$t^2 = z^2 = F_n^{-1}(\alpha) \qquad \textbf{4-121}$$

The weighted least-squares cost Ω for the attitude solution calculated using each trial triplet can be evaluated using the threshold t^2 to determine if the trial is likely to be the correct solution. If

$$\Omega < t^2 \qquad \textbf{4-122}$$

then the solution can admitted to the list of possible solutions. If the above condition is not met then the trial solution can be discarded. The values of t^2 for different degrees of freedom and different confidence intervals are commonly referenced from look-up tables due to the asymmetric nature of the chi-squared distribution. An example table of these *critical values* is given in Appendix F. For example, the probability of Ω exceeding 26.217 with 12 degrees of freedom is one percent. This can be verified by calculating the mean or expectation of Ω over many epochs, which should tend to the number of degrees of freedom (i.e. 12 for the above example). For the purposes of this algorithm the 0.001 (or 0.1%) critical values were used. Since the number of measurements used in the attitude solution can vary, it was necessary to store the critical values in a look-up table so that the correct value could be used depending on the number of satellites tracked.

The main advantage of using a chi-squared test on the attitude residuals is that the sum of squares of the attitude residuals collates all the geometric constraints in to a single value, Ω. This means the chi-squared test is more effective at eliminating false solutions than some of the other tests used in the algorithm. For example, the geometry tests described in section 4.5.2.2 only check the relative geometry between pairs of baselines, and hence do not fully constrain the baselines to lie in the correct geometry i.e. it is possible that two pairs of baselines meet the relative geometry checks, but the three baselines are not coplanar. The disadvantage of using the chi-squared test is that it is computationally expensive to calculate the least-squares attitude solution for many trials. That is why the test is left until the end of Part III of the algorithm, so that the faster pre-calculated threshold tests should have eliminated as many false trials as possible. Using the attitude residuals to eliminate more false solutions should mean that fewer solutions have to be compared in the next epoch, meaning a multi-epoch solution is found more rapidly.

4.5.4 Removing duplicate trial triplets

Since Part III is run on each of three lists generated by Part II, there will be three separate lists of trial baseline triplets at this point. Each list will typically contain fewer than five solutions.

To create the final list, the three lists from Part III must be combined and any duplicate solutions dealt with. Firstly the three lists are concatenated in to one larger list. The integer ambiguity vector for each trial solution is then compared with all the other integer ambiguity vectors in the list to find identical integer ambiguity solutions. Matching solutions are combined by taking the mean of each baseline vector and the mean attitude solution.

4.5.5 Overview of Part III algorithm

The following figure gives an overview of Part III of the algorithm.

1. *Calculate double-differences for phase measurements and LOS of third baseline*
2. *Select primary set based on minimum PDOP (as section 4.3.1)*
3. *Pre-compute variances and thresholds (Equations* 4-82 *and* 4-92 *and* 4-103*)*
4. *Calculate permitted bounds of integers for all measurements (Equation* 4-59*)*
5. *For each trial pair-wise solution from Part II*
    - a. *Use TRIAD to estimate the attitude matrix (section* 2.3.3.2)
    - b. *Predict integers for third baseline directly from attitude matrix (Equation* 4-105*)*
    - c. *Calculate direct solution for third baseline using measurements from primary set (Equation* 4-106*)*
    - d. *Test remaining measurements using threshold (as section* 4.3.3)
        - i. *If either residual meets threshold add triplet to list for Part III*
    - e. *Update baseline estimate based on all measurements (Equation* 4-109*)*
    - f. *Compare relative geometry of third baseline with other two baselines using method from Part II (section 4.4)*
        - i. *Remove trial triplet from list if relative geometry does not match to given confidence interval*
    - g. *Update attitude estimate using double-difference point solution method (section 2.3.3.4)*
    - h. *Test sum of squared attitude residuals using chi-squared threshold (section 4.5.3)*
        - i. *If the sum of squared residuals exceeds the chi-squared threshold remove the solution from the list.*

Figure 4-6 Overview of Part III algorithm

4.6 *Part IV - Extension to multiple epochs*

Typically there are multiple solutions remaining in the list from Part III and it is necessary to use the measurements from subsequent epochs to try and find a unique solution.

The use of accumulated carrier phase measurements means that as long as a satellite is tracked continuously its integer ambiguity will remain constant. It is assumed that the PRNs of the satellites tracked between consecutive epochs are maintained in a look-up table so it can quickly be established which satellites are common to the epoch in which Part III was last run (epoch $k-1$) and the next consecutive epoch k which may be at some arbitrary time t in the future.

Taking each baseline i where $i = 1,2,3$ in turn, it is assumed that J satellites are tracked on this baseline and all satellites are common to both epochs. If it were the case that a satellite had set and a new one was being tracked in its place, using the trial integer ambiguity vectors from Part III is more complex. This problem is discussed in section 4.6.2.

Note that there must be at least five satellites common to both epochs in order that four double-difference measurements can be formed and the measurements in the secondary set can be used to test the goodness of fit of the trial baseline vectors.

4.6.1 Eliminating false solutions using a new epoch of measurements

If the same satellites are tracked in epoch k as were tracked in epoch $k-1$ the double-difference integer tracking process (defined in section 4.6.3) will have calculated all the required integers. However as long as at least four satellites are common between both epochs a primary set can be formed using the common measurements.

Using the list of trial solutions from Part III, each trial integer ambiguity vector $\Delta\tilde{\mathbf{N}}_{i,p}^{(l)}$ is taken in turn and the primary set of measurements is used to directly estimate each baseline vector according to

$$\tilde{\mathbf{b}}_{i(O)}[k] = \mathbf{P}\left[\Delta\bar{\mathbf{r}}_{i,p}[k] - \Delta\tilde{\mathbf{N}}_{i,p}[k-1]\right] \qquad \textbf{4-123}$$

where $\Delta\tilde{\mathbf{N}}_{i,P}[k-1]$ is calculated using the double-difference integer tracking process described in section 4.6.3 and

$$\mathbf{P} = \left(\mathbf{H}^T[k]\mathbf{R}^{-1}\mathbf{H}[k]\right)^{-1} \qquad \textbf{4-124}$$

As with Part III there is no need for the integer search process since the integer ambiguities are assumed to be common across both epochs. Also, since **P** is the same for each trial solution (for a given baseline) it only needs to be calculated once and then can be used for all the trial solutions in the list. The trial baseline vector can then be used to estimate the integer ambiguities for the secondary set according to

$$\Delta\widetilde{N}_{i,j,s}[k] = \text{round}\left(\Delta\bar{r}_{i,j}[k] - \widetilde{\mathbf{b}}^{T}_{i(O)}[k]\mathbf{v}_{i,j}[k]\right) \qquad \textbf{4-125}$$

The secondary set can in turn be used to test the goodness of fit of the trial baseline vector using the method described in section 4.5.2. Having eliminated any trial solutions for which none of the measurements in the secondary set met the thresholds, an improved estimate $\widetilde{\mathbf{b}}_{i(O)}$ is calculated for each trial baseline vector

$$\widetilde{\mathbf{b}}_{i(O)}[k] = \left(\mathbf{H}^{T}[k]\mathbf{R}^{-1}\mathbf{H}[k]\right)^{-1}\mathbf{H}^{T}[k]\mathbf{R}^{-1}\left[\Delta\bar{\mathbf{r}}_{i}[k] - \Delta\widetilde{\mathbf{N}}_{i}[k]\right] \qquad \textbf{4-126}$$

This process is repeated for all three baselines. The improved estimates $\widetilde{\mathbf{b}}_{1(O)}$, $\widetilde{\mathbf{b}}_{2(O)}$ and $\widetilde{\mathbf{b}}_{3(O)}$ are used to calculate virtual phase measurements using the method shown in Part III (see section 4.5). If the relative geometry of the updated baseline vectors matches that of the known baseline geometry to the calculated confidence interval then the trial triplet is allowed to remain in the list, otherwise it is discarded.

Finally, the attitude solution for each remaining trial solution is updated using the double-difference point solution algorithm described in section 2.3.3.4. As in Part III, the normalised sum of squares of the attitude residuals is tested using a chi-squared test. A 0.1% confidence interval is used to try and eliminate any remaining false solutions.

This process is repeated over multiple epochs until a single solution remains. As will be shown in the next chapter, it is necessary to consider a minimum number of epochs before allowing the correct solution to be used to initialise the attitude tracking algorithm.

4.6.2 Tracking the double-difference integer ambiguities across multiple epochs

In Low Earth Orbit the GPS satellites rise and set much more quickly than they do for most ground users. As was shown in Chapter 3 the minimum time that a GPS satellite is in view for the SGR-20 on Topsat is around two minutes. This raises the problem that one or more satellites may have set since the previous epoch and potentially new satellites have been acquired in their place. This will result in some of the integer ambiguities calculated in Part III becoming outdated, and new measurements appearing for which the integer ambiguities must be solved.

This is a particular problem when using double-difference measurements since it is possible that the pivot satellite has set since the last epoch, meaning that all the double-difference ambiguities are invalid. One solution to this problem, presented in [Ward, 1996], is to use the attitude estimate from the previous epoch to calculate the double-difference ambiguities in the current epoch. However, for this to work, the attitude must remain reasonably constant between the two epochs, placing dynamic limits on the performance of the integer ambiguity resolution process.

If a baseline vector, $\mathbf{b}_{i(O)}$, is known in orbit-referenced coordinates, any of the $J-1$ double-difference integer ambiguities for that baseline can be calculated using

$$\Delta N_{i,j} = \mathrm{round}\left(\Delta\bar{r}_{i,j} - \mathbf{v}_{i,j(O)}^{T}\mathbf{b}_{i(O)}\right) \qquad \textbf{4-127}$$

The maximum permissible change in baseline pointing before the estimated integer ambiguity changes depends on the level of measurement noise expected in the carrier phase difference measurements. Assuming the measurement noise (including multipath) never exceeds quarter of a cycle, then the total angular change between the LOS vector $\mathbf{v}_{i,j}$ and the baseline vector $\mathbf{b}_{i(O)}$ from one epoch to the next must not exceed quarter of a cycle, or there is the possibility of the wrong integer being estimated by Equation 4-127.

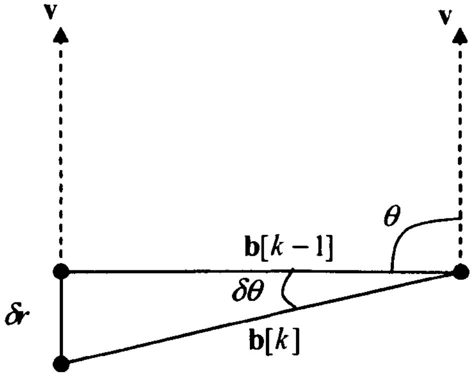

Figure 4-7 Effect of change in attitude on phase measurement

If from one epoch to the next the attitude changes by an angle $\delta\theta$, for small angles the resulting change in the accumulated phase difference measurement δr is

$$\delta r = \left\|\mathbf{b}_{i(O)}\right\| \delta\theta \sin\theta \qquad \textbf{4-128}$$

which can be rearranged to give

$$\delta\theta = \frac{\delta r}{\left\|\mathbf{b}_{i(O)}\right\| \sin\theta} \qquad \textbf{4-129}$$

which gives the change in attitude for a given change in the accumulated carrier phase difference. Note that Equation 4-129 shows that the maximum permissible change in attitude is inversely proportional to the baseline length. For baseline 1 on Topsat the attitude can change by around 4 degrees before we calculate the wrong integer. For baseline 2 the figure is 3.8 degrees, and for baseline 3 it is 6.4 degrees. Note that this is the maximum permissible change *between epochs* and so if measurements are taken every ten seconds the maximum permissible rate of change will be 0.4 degrees per second for baseline 1 etc. On agile microsatellites like Topsat, and potential future agile SSTL microsatellites this could be an issue, and so either the integer ambiguity resolution algorithm would have to run at a higher rate, or a method for tracking the integers over larger time spans is required.

4.6.3 Double-difference integer tracking

In order to be able to track the double-difference integer ambiguities over multiple epochs (without estimating them using an *a priori* attitude estimate) the algorithm must be able to cope with the rising and setting of satellites, including the *pivot* satellite. In this work double-differences are formed according to the rule

$$\begin{aligned} \Delta\bar{r}_{j-1} &= \bar{r}_j - \bar{r}_1 \\ \mathbf{v}_{j-1} &= \mathbf{s}_j - \mathbf{s}_1 \\ \Delta N_{i,j-1} &= N_{i,j} - N_{i,1} \end{aligned} \qquad \textbf{4-130}$$

where $2 \leq j \leq J$. The pivot satellite is the first satellite, which is differenced from all the others.

Three distinct scenarios must be considered with regards to rising and setting satellites:

1. The pivot satellite sets and a new pivot is chosen.
2. The satellite geometry changes so another satellite is the optimal pivot.
3. A non-pivot satellite sets and another satellite is acquired in its place, but is not chosen to be the pivot.

Scenario three is the simplest to deal with, since this measurement can just be placed in the secondary set in the current epoch. Four of the measurements from satellites which were common between both epochs (assuming there are at least four) can then be used to form the primary set in Part IV. The primary set can then be used to estimate the baseline vector, which in turn can be used to estimate the double-difference integer ambiguities relating to the satellites which have just risen. This way no *a priori* information is needed, and all measurements can be used to validate the trial solutions passed in the list from Part III.

If the pivot satellite sets it must be exchanged for another. Therefore scenarios one and two are both handled in the same way. For each baseline the trial integer ambiguity vector $\Delta\tilde{N}_i^{(l)}$ (one vector from the list of L trial solutions) was calculated in Part III using the previous epoch of data. This vector contains:

$$\Delta\tilde{\mathbf{N}}_i^{(l)}[k-1]=\begin{bmatrix}\Delta\tilde{N}_{i,1}^{(l)}\\ \Delta\tilde{N}_{i,2}^{(l)}\\ \vdots\\ \Delta\tilde{N}_{i,J-1}^{(l)}\end{bmatrix}=\begin{bmatrix}\tilde{N}_{i,2}^{(l)}-\tilde{N}_{i,1}^{(l)}\\ \tilde{N}_{i,3}^{(l)}-\tilde{N}_{i,1}^{(l)}\\ \vdots\\ \tilde{N}_{i,J}^{(l)}-\tilde{N}_{i,1}^{(l)}\end{bmatrix} \qquad \textbf{4-131}$$

The pivot satellite can be changed from $\tilde{N}_{i,1}^{(l)}$ to say $\tilde{N}_{i,3}^{(l)}$ by simply subtracting $\Delta\tilde{N}_{i,2}^{(l)}$ from all the other double-difference integer ambiguities:

$$\Delta\tilde{\mathbf{N}}_i^{(l)}[k]=\begin{bmatrix}\Delta\tilde{N}_{i,1}^{(l)}-\Delta\tilde{N}_{i,2}^{(l)}\\ -\Delta\tilde{N}_{i,2}^{(l)}\\ \vdots\\ \Delta\tilde{N}_{i,J-1}^{(l)}-\Delta\tilde{N}_{i,2}^{(l)}\end{bmatrix}=\begin{bmatrix}\tilde{N}_{i,2}^{(l)}-\tilde{N}_{i,1}^{(l)}-\tilde{N}_{i,3}^{(l)}+\tilde{N}_{i,1}^{(l)}\\ -\left(\tilde{N}_{i,3}^{(l)}-\tilde{N}_{i,1}^{(l)}\right)\\ \vdots\\ \tilde{N}_{i,J}^{(l)}-\tilde{N}_{i,1}^{(l)}-\tilde{N}_{i,3}^{(l)}+\tilde{N}_{i,1}^{(l)}\end{bmatrix}=\begin{bmatrix}\tilde{N}_{i,2}^{(l)}-\tilde{N}_{i,3}^{(l)}\\ \tilde{N}_{i,1}^{(l)}-\tilde{N}_{i,3}^{(l)}\\ \vdots\\ \tilde{N}_{i,J}^{(l)}-\tilde{N}_{i,3}^{(l)}\end{bmatrix} \qquad \textbf{4-132}$$

Note that $\Delta\tilde{N}_{i,2}^{(l)}$ simply undergoes a change of sign to reflect the new pivot.

This technique can be applied between any two epochs in which there are at least four common satellites. This allows the double-difference integer ambiguities to be tracked without resorting to using *a priori* attitude information. The technique can be used both during the integer ambiguity resolution process and whilst tracking the attitude. This means that there is no dynamic limit on the spacecraft's attitude imposed by the integer ambiguity resolution algorithm or the attitude tracking algorithm.

4.6.4 Overview of Part IV algorithm

The following figure gives an overview of Part IV of the algorithm.

1. *For each baseline*
    - a. *Use integer tracking technique in section 4.6.3 to update integer ambiguities.*
    - b. *Calculate double-differences for phase measurements and LOS vectors for measurements common to both epochs (Equation* 4-30*)*
    - c. *Select primary set based on best PDOP (or using common satellites if required)(section 4.3.1)*
    - d. *Pre-compute variances and thresholds (Equations* 4-82 *and* 4-92 *and* 4-103*)*
    - e. *Calculate direct solution for baseline vector using primary set (Equation* 4-123*)*
    - f. *Estimate integers for newly risen satellites using direct solution for baseline vector (Equation* 4-125*)*
    - g. *Calculate residuals for measurements in secondary set (as section* 4.5.2)
    - h. *Test remaining measurements using threshold*
        - ii. *If no residuals meet the threshold, remove the solution from the list*

        i. *Update baseline estimate based on all measurements (Equation* 4-126*)*
2. *Compare relative geometry of all three baselines using method from Part III. (section 4.4)*
    a. *If relative geometry does not match to given confidence interval then remove from list*
3. *Update attitude estimate using double-difference point solution method (section 2.3.3.4)*
4. *Calculate weighted sum of square attitude residuals and test using chi-squared (section 4.5.3)*
    a. *Eliminate solutions that exceed the chi-squared threshold.*

Figure 4-8 Overview of Part IV algorithm

If there were sufficient satellites to run Part IV on the current epoch then the list of trial solutions from Part III will have been updated with the trial baseline vectors for the current epoch and their corresponding integer ambiguity vectors. There may now be a unique solution at this epoch. If there is still no unique solution then Part IV is repeated on the next epoch to see if that produces a unique solution. This process would continue until a unique solution was found or all solutions were invalidated. It is envisaged that it would only require a period of tens of seconds for the algorithm to reach a conclusion due to the faster relative motion of the constellation when operating in Low Earth Orbit. This will be examined in the next chapter.

Note that due to the requirement for five satellites to be common between epochs it may not have been possible to run Part IV of the algorithm. Alternatively, Part IV may invalidate all the solutions in the list from Part III and report 'No Solution'. In either case it would be necessary to start again from Part I at the next epoch.
An overview of the entire algorithm is given in Figure 4-9 below.

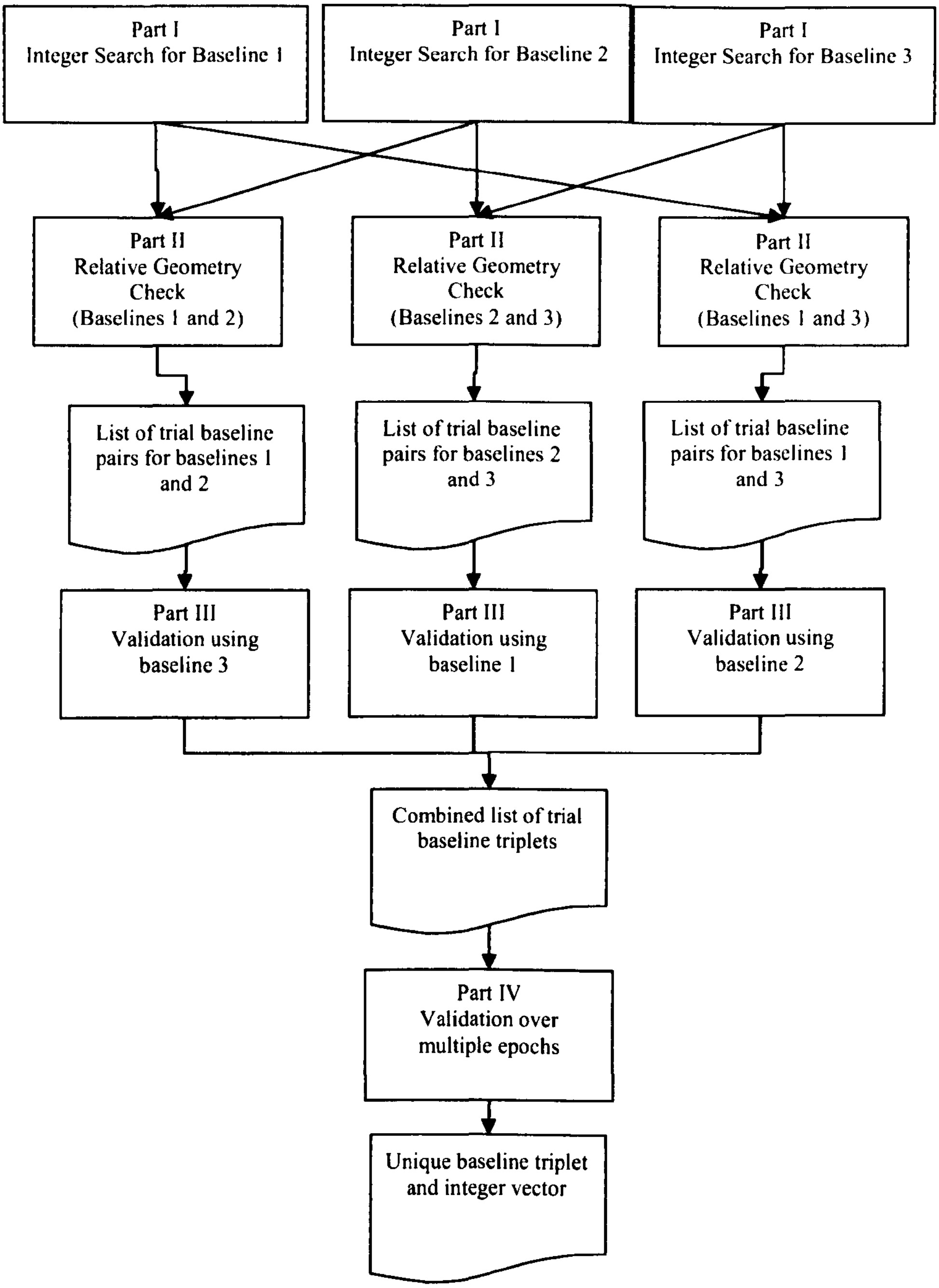

Figure 4-9 Overview of the robust integer ambiguity resolution algorithm

4.6.5 Conclusions

In this chapter an overview of the different methods for integer ambiguity was given. It was shown that the LAMBDA method is not practical on the SGR-20 due to our requirement to provide a stand-alone three-axis attitude solution. The LAMBDA method requires a float solution to be calculated as described in section 4.1.1. On the SGR-20 there are insufficient measurements to calculate a carrier-phase only float solution cannot be calculated. The simulation results in section 4.1.1.2 demonstrated that a combined code-and-carrier based float solution would be unreliable due to the code phase noise of the tracking loops in the SGR-20.

To allow the aim of demonstrating real-time stand-alone GPS attitude on a microsatellite a new algorithm for robust integer ambiguity resolution was presented. The algorithm uses measurements from multiple epochs to provide a reliable solution that is suitable for implementation onboard the SGR-20 GPS receiver. Many authors have hinted at an extension of their method to multiple epochs [Purivigraipong, 2000], [Knight, 1994], [Martin-Neira *et al*, 1995] but few, if any, have actually published how this was accomplished.

This new algorithm also differs from the current state of the art, such as the LAMBDA method [Teunissen, 1995] and the method presented in [Kee *et al*, 2007], in that it solves the integer ambiguity problem with fewer measurements. Many modern techniques, mostly aimed at the field of surveying, assume geodetic quality receivers that consistently track up to twelve satellites over long periods. In developing this new algorithm it was assumed that only up to six satellites are tracked in any one epoch, and that due to the high-dynamic environment the satellites may change over the course of a few minutes.

The other main differences between this new algorithm and past work such as [Brown, 1992], [Kee, 2003] and [Kee, 2007] are:

- The algorithm is designed for use on a GPS receiver in LEO, and presents a method for coping with the rapidly changing satellite geometry experienced in LEO.
- The algorithm uses a number of approximations to simplify the implementation and reduce the computational complexity to allow it to run in real-time onboard the SGR-20 as will be demonstrated in a Chapter 7.
- The algorithm provides a method for using measurements from multiple epochs to eliminate false integer ambiguity solutions, with the aim of identifying a single unique solution.
- The multi-epoch component of the algorithm uses epoch-by-epoch tests, rather than a moving average of the residuals as in [Kee, 2007], in order to reduce the effect of multipath on the success rate of the algorithm.

The performance of the new algorithm is tested in the next chapter.

5 Simulation and testing of robust IAR algorithm

This chapter describes the testing of the performance of the new IAR algorithm using both simulated and real GPS measurement data. Firstly the performance of the new IAR algorithm was tested using data from the MATLAB based simulator. By using the simulator the true values of the integer ambiguities were known, and important performance factors such as the measurement error characteristics, the number of satellites tracked and the satellite geometry could be controlled directly. The performance of each stage of the algorithm is analysed in terms of the percentage of epochs in which the correct solution passes the statistical checks and is placed in the list of likely solutions. The size of the list generated by each stage of the algorithm is also analysed to determine the suitability of the algorithm for real-time implementation.

It will be shown that by running the new IAR algorithm over multiple epochs a success rate of nearly one hundred percent can be achieved using only single-frequency measurements on L1.

As a further test of the performance of the algorithm real data logged in-orbit on the Topsat microsatellite was post-processed in MATLAB and input into the new IAR algorithm. This allows the real-world performance the new IAR algorithm on actual data from a satellite in Low Earth Orbit to be demonstrated.

5.1 IAR algorithm testing using simulated GPS measurements

The MATLAB based simulator described in Appendix A was used to generate realistic GPS measurement data at one second intervals. At each epoch the position of each satellite in the GPS constellation and the position of the user platform - in this case a simulated microsatellite - are recalculated. A 'Highest Elevation' satellite selection algorithm is used to determine which satellites are tracked by the simulated GPS receiver.

In order to thoroughly test the performance of the new algorithm a Monte-Carlo style simulation was conducted. A uniformly distributed random selection of one thousand different start times or *epochs* was chosen from one full day of constellation motion. The simulation was started at each of the one thousand epochs, with the GPS constellation and simulated microsatellite position propagated to the selected time. By selecting a randomly distributed set of epochs the aim was to randomise the constellation geometry for each run, resulting in a more realistic range of geometries and dilution of precision than would be achieved by running the simulation for one thousand consecutive epochs. The aim was to ensure the IAR algorithm was tested under realistic constellation geometries.

To allow proper testing of the multi-epoch component of the new algorithm the simulation was run for as many consecutive epochs following the starting epoch as were required for the algorithm to find a unique solution. An interval of ten seconds was used between each consecutive epoch in order to allow for some constellation motion to have occurred. In each epoch the GPS constellation geometry and simulated microsatellite position were updated to provide realistic motion to test the performance of the new algorithm. Once a unique solution was found, the simulation was restarted at the next random epoch in the set of one thousand epochs.

The Monte-Carlo style simulation was repeated twelve times, using different configurations as shown in Table 5-1. In the first five simulations the IAR algorithm was provided with simulated GPS measurements from five GPS satellites on each baseline. In each simulation the RMS double-difference measurement noise was set at the values between 2mm and 10mm as specified in the table. This was done to examine the effect of receiver noise on the IAR algorithm. The same process was repeated for simulations 6 through 10, but the IAR algorithm was provided with simulated GPS measurements from six GPS satellites on each baseline. The simulated measurement noise for the first ten simulations was zero mean Gaussian noise (i.e. no multipath). The attitude of the spacecraft remains nadir pointing throughout. All simulations used the same random selection of start epochs and hence experienced the same GPS constellation geometry.

For real data the measurement noise is a combination of receiver noise and a multipath error, since the receiver noise is determined by the GPS signal conditions, dynamics and receiver design, whilst the multipath error is a function of the incident signal direction relative to the structure of the spacecraft. Therefore two further simulations numbered 11 and 12 were conducted using the multipath simulation method described in Appendix A.5 to test the effect of multipath on the IAR algorithm. Dynamic effects on receiver tracking loops are not simulated.

Table 5-1 Simulation configurations

Simulation No.	**No. of Epochs**	**Number of satellites tracked**	**Double-Difference RMS Measurement Noise (mm)**	**Multipath**
1	1000	5	2	No
2	1000	5	4	No
3	1000	5	6	No
4	1000	5	8	No
5	1000	5	10	No
6	1000	6	2	No
7	1000	6	4	No
8	1000	6	6	No
9	1000	6	8	No
10	1000	6	10	No
11	1000	5	8.5	Yes
12	1000	6	8.5	Yes

5.2 *Performance of the IAR algorithm in the presence of measurement noise*

In this section the performance of Parts I to IV of the algorithm is analysed to determine the percentage of epochs in which the correct solution is present in the list of possible solutions output by each part of the algorithm. The performance of the algorithm under the simulated conditions specified for scenarios 1 to 10 in Table 5-1 is analysed in order to determine the effect of constellation geometry, measurement noise and the number of satellites tracked on the performance of the algorithm.

When quantifying the performance of the algorithm there are two main aspects to consider: the percentage of epochs in which the correct solution is present in the list output by each part of the algorithm and the size of the list output by each part of the algorithm. Both these factors are important since we wish to find the correct solution over a short a time as possible.

5.2.1 Performance in Part I

In Part I of the algorithm the initial integer search is conducted using the primary set of measurements and potential trial solutions are tested for their likelihood based on their goodness of fit with the measurements in the secondary set. The percentage of epochs in which the correct solution is in the list of trial solutions generated by Part I for each baseline when tracking five or six satellites is shown in the tables below. Note that the RMS noise level relates to the double-difference measurement noise, which is nominally $\sqrt{2}$ larger than the single-difference measurement noise.

Table 5-2 Percentage of correct solutions in lists from Part I when tracking five satellites

RMS Noise Level	Baseline 1 (%)	Baseline 2 (%)	Baseline 3 (%)
2mm	100.00	100.00	100.00
4mm	100.00	100.00	100.00
6mm	99.90	100.00	99.90
8mm	100.00	99.81	99.62
10mm	99.72	99.44	99.06

Table 5-3 Percentage of correct solutions in list for each baseline from Part I when tracking six satellites

RMS Noise Level	Baseline 1 (%)	Baseline 2 (%)	Baseline 3 (%)
2mm	100.00	100.00	100.00
4mm	100.00	100.00	100.00
6mm	100.00	100.00	100.00
8mm	99.90	100.00	100.00
10mm	100.00	100.00	99.90

The results show that when tracking six satellites Part I of the new algorithm identifies the correct solution in over 99.9 percent of epochs for all levels of measurement noise tested. When only tracking five satellites there is a slight decrease in performance, but the correct solution is still identified in over 99.0 percent of epochs. The level of measurement noise simulated does not have a significant effect on the percentage of correct solutions. This result was expected since all the thresholds used in the algorithm to try and eliminate false solutions are a function of the measurement noise, and so should work effectively at each of the noise levels simulated.

Detailed analysis of the small percentage of epochs in which the correct solution was not identified highlighted two different causes for the failure cases. The main cause of failures was the residual d_i for the measurements in the secondary set not meeting the variance threshold, which occurred in around 0.3% of the total runs of Part I when tracking five satellites. Since the threshold was set at $3\sigma_{d_i}$, this is result is to be expected since the three sigma threshold should encompass the correct solution in 99.7% of the epochs. The remaining cause of around 0.1% of failure cases was the correct trial solution not meeting the baseline length threshold, which again given the $3\sigma_{\|\tilde{\mathbf{b}}\|}$ confidence interval, is an acceptable result. At all levels of receiver noise tested there were no issues with method of using the baseline length constraint to reduce the search space to two dimensions, and this technique always resulted in the correct integers being identified for the primary set.

5.2.1.1 Number of trial solutions generated by Part I

Since the algorithm must run in real time on the SGR-20 the number of potential solutions output by Part I of the algorithm is of particular interest. If ensuring that the correct solution is in the list output by Part I required that the list be exhaustive, there is a chance that the limited available memory and spare processing power on the SGR-20 would not be sufficient to host the new algorithm onboard the receiver.

As part of the simulation the size of list output by Part I for each baseline, in each epoch and for each level of simulated noise was recorded. The mean and standard deviation of the list size for each baseline for each level of receiver noise tested is given in Table 5-4 through Table 5-7.

Table 5-4 Mean list sizes for Part I vs Measurement Noise when tracking five satellites

RMS Noise Level	**Baseline 1**	**Baseline 2**	**Baseline 3**
2mm	1.68	1.72	1.23
4mm	3.75	3.91	2.03
6mm	7.02	7.82	3.39
8mm	11.77	13.02	5.20
10mm	18.00	19.89	7.60

Table 5-5 Standard deviation of list sizes for Part I vs Measurement Noise when tracking five satellites

RMS Noise Level	Baseline 1	Baseline 2	Baseline 3
2mm	0.87	0.93	0.46
4mm	1.78	1.80	0.99
6mm	2.74	2.92	1.55
8mm	4.08	4.14	2.18
10mm	5.94	6.17	2.89

Table 5-6 Mean list sizes for Part I vs Measurement Noise when tracking six satellites

RMS Noise Level	Baseline 1	Baseline 2	Baseline 3
2mm	2.44	2.58	1.56
4mm	6.51	7.12	3.12
6mm	12.82	14.31	5.71
8mm	21.48	23.81	8.98
10mm	31.75	35.30	13.04

Table 5-7 Standard deviation of list sizes for Part I vs Measurement Noise when tracking six satellites

RMS Noise Level	Baseline 1	Baseline 2	Baseline 3
2mm	1.24	1.28	0.79
4mm	2.45	2.65	1.44
6mm	3.92	4.30	2.22
8mm	5.76	6.64	3.00
10mm	7.90	8.80	3.90

These results also show that the mean list size output by Part I is proportional to the level of measurement noise. The main factor in determining the list size is how many trial solutions pass the baseline length test described in section 4.3.5. The threshold calculated is proportional to the expected measurement noise variance and this results in the number of trial solutions in the list also being proportional to the expected noise variance.

The results also show that the mean list size for Part I is proportional to the baseline length. Baseline 2, which is the longest baseline, has the largest mean list size for each level of measurement noise whereas baseline 3, which is the shortest baseline, has the lowest mean list size at each noise level. This is again a result of the baseline length check which uses the estimated variance calculated in Equation 4-92 to determine the threshold. This means that the threshold is a function of the baseline length. Therefore shorter baselines will have a lower threshold and result in fewer trial solutions being output by Part I. The other interesting point to note is that the mean list sizes for each level of noise are lower in the five satellite simulation than the six satellite simulation. This shows that Part I of the IAR algorithm is generating fewer trial solutions when five satellites are tracked. The list sizes given six satellites are still reasonably small, and should not pose a problem for real-time implementation.

5.2.2 Performance in Part II

In Part II of the algorithm the lists of trial solutions for each baseline generated by Part I are combined to form trial baseline pairs. The trial pairs are then tested for their likelihood using the known relative geometry of the baselines. The percentage of epochs in which the correct solution is in the list generated by Part II when tracking five or six satellites is shown below.

Table 5-8 Percentage of correct solutions in list for each trial pair of baselines from Part II when tracking five satellites

RMS Noise Level	Baseline 1+2	Baseline 2+3	Baseline 3+1
2mm	100.00	100.00	100.00
4mm	100.00	100.00	100.00
6mm	99.90	99.90	99.81
8mm	99.81	99.43	99.62
10mm	99.15	98.59	98.78

Table 5-9 Percentage of correct solutions in list for each trial pair of baselines from Part II when tracking six satellites

RMS Noise Level	Baseline 1+2	Baseline 2+3	Baseline 3+1
2mm	100.00	100.00	100.00
4mm	100.00	100.00	100.00
6mm	100.00	100.00	100.00
8mm	99.90	100.00	99.90
10mm	100.00	99.90	99.90

The success rates in Part II are the product of the success rates in Part I for each combination of baselines. For example, when tracking six satellites with 8mm of simulated noise the success rates for baselines 1 and 2 in Part I were 99.9% and 100.0% respectively. The product of these two success rates is 99.9% which is the success rate achieved for the combination of baselines 1 and 2 as shown in Table 5-9 above. The same result applies to the other figures in the table. This demonstrates that as long as the correct solution is identified in Part I, it will always pass the geometry checks in Part II and therefore be output in the list from Part II. It should be noted that if the true variance (as defined in section 4.4.1) was used to define the threshold used in Part II then we would expect 0.3% of correct solutions to be rejected. However, the confidence interval calculated in Part II used an approximation which over estimated the variance, which means the correct solution is more likely to lie within the calculated confidence interval. Note that the success rate when only tracking five satellites drops to 98.6% for 10mm of simulated noise due to the reduced success rate of Part I when tracking five satellites.

5.2.2.1 Number of trial solutions output by Part II

The number of solutions output by Part II is a function of the number of solutions in each list from Part I and the number of trial pairs that pass the geometry test. The aim of Part II is to reduce the number of trial solutions by comparing the relative geometry of the trial baseline pairs with the known relative geometry. Unlikely trial pairs will not match the relative geometry and so will be removed from the list. The number of solutions in the list in Part II should therefore be fewer than the product of the two lists from Part I. By examining the size of the lists output by Part II compared with the size of the lists serving as input to Part II (the lists from Part I) we can determine if Part II has any benefit in terms of rejecting false solutions.

Table 5-10 Mean list sizes for Part II vs Measurement Noise when tracking five satellites

RMS Noise Level	Baselines 1 + 2	Baselines 2 + 3	Baselines 3 + 1
2mm	1.10	1.08	1.07
4mm	2.31	1.89	1.90
6mm	8.32	5.45	5.26
8mm	26.82	16.12	16.20
10mm	73.00	41.46	43.41

Table 5-11 Standard deviation of list sizes for Part II vs Measurement Noise when tracking five satellites

RMS Noise Level	Baselines 1 + 2	Baselines 2 + 3	Baselines 3 + 1
2mm	0.39	0.30	0.27
4mm	1.86	1.36	1.32
6mm	6.77	4.71	4.11
8mm	20.79	13.54	13.86
10mm	54.92	32.27	36.30

Table 5-12 Mean list sizes for Part II vs Measurement Noise when tracking six satellites

RMS Noise Level	Baselines 1 + 2	Baselines 2 + 3	Baselines 3 + 1
2mm	1.21	1.16	1.16
4mm	4.07	2.97	2.69
6mm	17.75	11.12	10.22
8mm	61.15	35.20	33.42
10mm	158.34	88.18	87.05

Table 5-13 Standard deviation of list sizes for Part II vs Measurement Noise when tracking six satellites

RMS Noise Level	Baselines 1 + 2	Baselines 2 + 3	Baselines 3 + 1
2mm	0.55	0.45	0.47
4mm	3.17	2.21	2.00
6mm	12.59	8.18	7.95
8mm	41.33	26.40	27.47
10mm	99.95	58.61	66.37

The mean and standard deviation of the list sizes for each trial pair of baselines when tracking five satellites and six satellites are shown in Table 5-10 through Table 5-13. These results show Part II significantly reduces the number of trial solutions whilst – as shown in the previous section – not resulting in the loss of any of the correct solutions. For example, when tracking six satellites with 10mm of noise the mean number of trial pairs of baselines resulting from the combination of the lists from Part I for baselines 1 and 2 should on average result in approximately $32 \times 35 = 1120$ possible trial baseline pairs. However, the mean size of the list output by Part II for the combination of baselines 1 and 2 when tracking six satellites with 10mm of noise is only around 158, which is around 14 percent of the total trial baseline pairs that would be tested. This shows that Part II is beneficial since it greatly reduces the number of trial solutions that must be tested in Part III.

The results also show that the mean number of trial solutions output by Part II increases as the measurement noise increases. This is because the threshold used to eliminate false solutions in Part II is based on estimated variance for the virtual phase measurements (calculated in Equation 4-103). Therefore the threshold value will increase with the square of the measurement noise, which results in more trials lying within the confidence interval defined by the threshold.

5.2.3 Performance in Part III

Part III of the algorithm is run three times, once for each potential ordering of the baselines i.e. 1-2-3, 2-3-1 and 3-1-2. The results from each of the individual runs of Part III are then concatenated into a single 'final' list and any duplicate solutions removed as described in Chapter 4.

The performance of the algorithm in Part III is given in Table 5-14 and Table 5-15. The results are shown for each parallel run of Part III as shown in Figure 4-9 in Chapter 4, and also for the final concatenated list where the solutions from the three Part III lists are combined.

Table 5-14 Percentage of correct solutions in lists from Part III when tracking five satellites

RMS Noise Level	Baselines 1,2,3	Baselines 2,3,1	Baselines 3,1,2	Final List
2mm	100.00	100.00	100.00	100.00
4mm	100.00	99.90	100.00	100.00
6mm	99.71	99.42	99.52	100.00
8mm	98.66	98.19	98.66	100.00
10mm	97.74	96.15	96.71	100.00

Table 5-15 Percentage of correct solutions in lists from Part III when tracking six satellites

RMS Noise Level	Baselines 1,2,3	Baselines 2,3,1	Baselines 3,1,2	Final List
2mm	99.20	99.40	99.80	100.00
4mm	99.80	99.20	99.60	100.00
6mm	99.10	99.50	99.40	100.00
8mm	99.60	99.31	99.60	100.00
10mm	99.41	98.81	98.81	100.00

By taking the three lists of trial baseline pairs from Part II and incorporating the extra information from the third baseline using three separate runs of Part III we potentially save many processing loops since we only have to process $(M \times N)+(N \times P)+(P \times M)$ trial solutions rather than $M \times N \times P$. The results show that this method also adds some additional reliability, since if the correct solution is not identified in the list from one pair of baselines, it may still be in the lists from the other two pairs of baselines. Therefore the correct solution can still be passed to Part IV in the final list. This is particularly apparent when only tracking five satellites, where the correct solution may only be present in the individual lists from Part III in 96% of epochs, but by combining the lists the final list always contains the correct solution for the levels of measurement noise tested.

Note that even when tracking six satellites there is a small percentage of epochs in which the correct solution is not identified in one or more of the parallel runs of Part III. However, since the correct solution is always identified in at least one of the lists from Part III, the correct solution is always present in the final list for all levels of noise simulated. It is important that the correct solution is in the final list output by the single-epoch stage of the algorithm so that the correct solution is passed to Part IV and can be uniquely identified over multiple epochs.

5.2.3.1 Number of trial solutions output by Part III

The mean size of the lists output by each run of Part III (for each combination of baselines) and also the final list created by concatenating the output from each run of Part III are shown in Table 5-16 and Table 5-18 for when tracking five and six satellites respectively.

Table 5-16 Mean list sizes for Part III vs Measurement Noise when tracking five satellites

RMS Noise Level	Baselines 1,2,3	Baselines 2,3,1	Baselines 3,1,2	Final List
2mm	1.00	1.00	1.00	1.00
4mm	1.01	1.01	1.01	1.01
6mm	1.05	1.05	1.05	1.06
8mm	1.17	1.14	1.13	1.24
10mm	1.48	1.51	1.63	2.14

Table 5-17 Standard deviation of list sizes for Part III vs Measurement Noise when tracking five satellites

RMS Noise Level	Baselines 1,2,3	Baselines 2,3,1	Baselines 3,1,2	Final List
2mm	0.03	0.03	0.03	0.03
4mm	0.12	0.13	0.12	0.12
6mm	0.25	0.24	0.24	0.28
8mm	0.72	0.64	0.46	1.18
10mm	2.31	2.09	3.37	5.69

Table 5-18 Mean list sizes for Part III vs Measurement Noise when tracking six satellites

RMS Noise Level	Baselines 1,2,3	Baselines 2,3,1	Baselines 3,1,2	Final List
2mm	0.99	0.99	1.00	1.00
4mm	1.00	0.99	1.00	1.00
6mm	1.00	1.00	1.00	1.01
8mm	1.02	1.02	1.01	1.04
10mm	1.17	1.15	1.13	1.37

Table 5-19 Standard deviation of list sizes for Part III vs Measurement Noise when tracking six satellites

RMS Noise Level	Baselines 1,2,3	Baselines 2,3,1	Baselines 3,1,2	Final List
2mm	0.09	0.08	0.04	0.00
4mm	0.04	0.09	0.06	0.03
6mm	0.13	0.11	0.09	0.14
8mm	0.18	0.20	0.13	0.33
10mm	1.83	1.19	1.11	2.69

These results show that Part III of the new IAR algorithm is successfully reducing the number of trial solutions from the potential 160 solutions passed in from Part II down to just a handful of solutions in the final list created by combining the three runs of Part III. Again there is a correlation between the measurement noise variance and the mean list sizes due to the various thresholds in Part III all being a function of the assumed measurement noise variance.

The mean number of trial solutions in the final list is larger when only five satellites are tracked, as is the standard deviation of the list sizes. The results show that having more measurements means the algorithm is more likely to find a unique solution in a single epoch, since the mean list size is around one for all levels of measurement noise when tracking six satellites. The standard deviation of the list sizes when tracking six satellites is also close to zero, which shows that generally for levels of measurement noise up to 8mm, the algorithm is generating a unique solution in a single epoch. This is examined further in the next section.

5.2.3.2 Single-epoch success rate

Many integer ambiguity algorithms in the literature attempt a solution using a single-epoch of data. It was shown in section 4.1.3 that single-epoch methods are unlikely to be robust and multi-epoch methods are preferable. However, it is still interesting to validate the theory by examining the single-epoch success rate.

The *single-epoch success rate* of the IAR algorithm is defined as the percentage of epochs in which Part III of the IAR algorithm outputs a single answer, and this answer is correct when compared with the truth integer ambiguity solution provided by the simulation. It is also possible that the algorithm will fail to find any solution i.e. reject the correct solution. Alternatively it is possible that the algorithm could identify a unique solution which is incorrect. This would constitute a Type I error or *false positive.*

Table 5-20 Single-epoch performance when tracking five and six satellites

	Five Satellites			Six Satellites		
RMS Noise Level	Correct Solution (%)	Incorrect Solution (Type I error) (%)	No Solution (%)	Correct Solution (%)	Incorrect Solution (Type I error) (%)	No Solution (%)
2mm	99.9	0.0	0.1	100.0	0.0	0.0
4mm	98.4	0.0	1.6	99.9	0.0	0.1
6mm	94.5	0.5	5.0	99.3	0.0	0.7
8mm	86.7	0.6	12.7	98.5	0.3	1.2
10mm	78.3	1.4	20.2	95.7	0.5	3.8

The simulation results show that a high success rate can be achieved at very low levels of measurement noise. However, the algorithm will not reliably identify the correct solution in a single epoch for levels of measurement noise above 4mm when tracking five satellites. The analysis in Chapter 3 showed that the single-difference RMS measurement noise on Topsat was 6mm. This equates to $\sqrt{2} \times 6 = 8.5$mm of double-difference measurement noise. The results in Table 5-20 therefore show that the new IAR algorithm cannot guarantee the correct solution is identified using only a single-epoch of data in realistic measurement environments.

It would be unsatisfactory to initialise the attitude tracking algorithm given the above results since a false or mimic solution would result in the attitude estimate being incorrect. If this attitude solution was used as part of the ADCS attitude solution it could lead to divergence of the ADCS attitude filter and possible tumbling the spacecraft. Obviously in a real-world situation a combination of attitude sensors would be used to guard against such problems, but we are aiming to achieve a robust stand-alone GPS attitude sensor. Therefore the trial solutions output by Part III of the algorithm must be validated using data from multiple epochs to ensure that a success rate of one hundred percent is achieved.

5.2.4 Performance in Part IV

The single-epoch results in the previous section demonstrated that if the time span over which the list of trial solutions is monitored is too short the errors in the trial solutions will result in a mean square cost that resembles Equation 4-27, which is subject to the digital error. If the list of trial solutions is monitored over a longer period the mean square costs will approach the expected cost given in Equation 4-28 and hence be a better indication of the likelihood of the trial solution(s) being correct. Note that in this algorithm the mean square cost is not calculated explicitly, but testing the trial solutions against the various thresholds provides the same end result, since the trial solution that meets all the thresholds is by definition the maximum likelihood solution.

The number of epochs required to ensure the new IAR algorithm correctly rejected all false solutions was initially unknown. Therefore simulation scenarios 1 through 10 (as detailed in Table 5-1) were re-run with the new IAR algorithm configured to run for a different minimum number of epochs in each re-run. The algorithm was tested with a range of minimum epochs from two to nine. As each epoch is ten seconds in length, the algorithm was run for minimum periods of between twenty and ninety seconds from each starting epoch.

5.2.4.1 Multi-epoch success rate

The multi-epoch performance of the new IAR algorithm when tracking five and six satellites for minimums of two, three, six and nine epochs are shown in the tables below.

Table 5-21 Multi-epoch performance of IAR algorithm, minimum two epochs

	Five Satellites			Six Satellites		
RMS Noise Level	Correct Solution (%)	Incorrect Solution (Type I error) (%)	No Solution (%)	Correct Solution (%)	Incorrect Solution (Type I error) (%)	No Solution (%)
2mm	99.6	0.0	0.4	99.6	0.0	0.4
4mm	99.6	0.0	0.4	99.7	0.0	0.3
6mm	98.8	0.0	1.2	99.5	0.0	0.5
8mm	98.4	0.0	1.6	99.3	0.0	0.7
10mm	96.3	0.5	3.3	99.0	0.0	1.0

Table 5-22 Multi-epoch performance of IAR algorithm, minimum three epochs

	Five Satellites			Six Satellites		
RMS Noise Level	Correct Solution (%)	Incorrect Solution (Type I error) (%)	No Solution (%)	Correct Solution (%)	Incorrect Solution (Type I error) (%)	No Solution (%)
2mm	100.0	0.0	0.0	99.5	0.0	0.5
4mm	99.4	0.0	0.6	99.7	0.0	0.3
6mm	99.4	0.0	0.6	99.6	0.0	0.4
8mm	98.6	0.0	1.4	99.5	0.0	0.5
10mm	96.7	0.3	3.0	99.0	0.0	1.0

Table 5-23 Multi-epoch performance of IAR algorithm, minimum six epochs

	Five Satellites			Six Satellites		
RMS Noise Level	Correct Solution (%)	Incorrect Solution (Type I error) (%)	No Solution (%)	Correct Solution (%)	Incorrect Solution (Type I error) (%)	No Solution (%)
2mm	98.8	0.0	1.2	98.8	0.0	1.2
4mm	97.5	0.0	2.5	98.7	0.0	1.3
6mm	97.2	0.0	2.8	98.7	0.0	1.3
8mm	95.9	0.0	4.1	98.3	0.0	1.7
10mm	93.5	0.0	6.5	98.2	0.0	1.8

Table 5-24 Multi-epoch performance of IAR algorithm, minimum nine epochs

	Five Satellites			Six Satellites		
RMS Noise Level	Correct Solution (%)	Incorrect Solution (Type I error) (%)	No Solution (%)	Correct Solution (%)	Incorrect Solution (Type I error) (%)	No Solution (%)
2mm	96.3	0.0	3.7	97.5	0.0	2.5
4mm	95.9	0.0	4.1	97.9	0.0	2.1
6mm	93.8	0.0	6.2	97.6	0.0	2.4
8mm	93.1	0.0	6.9	97.3	0.0	2.7
10mm	91.8	0.1	8.1	97.1	0.0	2.9

The results in the tables above show the percentage of epochs in which either a correct solution, an incorrect solution or no solution was reported by the IAR algorithm for different levels of measurement noise.

Each of the tables shows the results when tracking either five or six satellites on each baseline. If the measurement noise was the only factor affecting the performance of the IAR algorithm we would expect that the performance should be the same when tracking five or six satellites. Also since the various threshold tests used in the algorithm are based on an assumed noise variance, the performance should be the same for all levels of measurement noise simulated. The above results show consistent performance for the different levels of noise when tracking six satellites. However, the performance varies when only tracking five satellites. This is because when tracking five satellites the performance is also affected by a number of other factors such as the geometry of the satellites tracked, the number of satellites that are common from one epoch to the next and the successful estimation of the integers for newly risen satellites.

The geometry of the satellites tracked affects the performance of the algorithm as all the precalculated thresholds are a function of the satellite geometry. For example, Parts I, III and IV of the algorithm use the primary set of measurements (consisting of three double-difference measurements) to calculate residuals for the measurements in the secondary set. These residuals are tested using a threshold (such as the one in Equation 4-82). The estimated variance of the residuals is directly proportional to the PDOP of the primary set. When tracking six satellites there are generally five or more satellites common between consecutive epochs and so we can choose the satellites to form a primary set with the least PDOP and hence a lower threshold. This will in turn result in smaller list sizes and the algorithm finding the correct solution more quickly. However, when only five satellites are tracked there will be more epochs in which only four satellites are common between consecutive epochs. The PDOP of the primary set is then limited to the PDOP of these four satellites, which could be large. This would result in higher thresholds, larger list sizes and more time being required to find the solution. A similar effect will occur with the other threshold tests used throughout the algorithm, since all the thresholds are a function of the satellite geometry.

When tracking five satellites if there are only four satellites in common between consecutive epochs the double-difference integer tracking method described in section 4.6.3 can only be used to form the primary set in the new epoch. If a new satellite has risen then integer ambiguity of this satellite has to be estimated using the updated baseline vectors calculated using Equation 4-123. Due to poor geometry and noise in the carrier phase measurements this process can sometimes result in the incorrect integer ambiguity. During the testing of the algorithm it was found that when calculating the residuals using Equation 4-125, it is quick and simple to also calculate the residuals for ± 1 integers. By choosing the smallest residual of the three and using the corresponding integer value we can account for most of the effects of poor geometry. The same technique was applied in Parts I and III to maximise the performance of the algorithm.

When tracking six satellites the results show that by using Part IV of the algorithm over just two epochs, or twenty seconds, there are no epochs in which an invalid solution or no solution is output. As the minimum number of epochs considered increases there is a slight decrease in the success rate of the algorithm and a corresponding increase in the percentage of epochs in which 'No solution' is reported. The reason for this is that the statistical tests define a confidence interval within which the correct solution will tend to a given probability. In these simulations a three-sigma confidence interval was used for the baseline, residuals and geometry checks in Part IV. This means that any one of these tests will reject the correct solution in 0.3% of epochs. For the chi-squared test on the attitude residuals the critical values used result in the correct solution being rejected in 0.1% of epochs. The combined chance of any of these tests rejecting the correct solution accumulates as more epochs are considered. This accounts for the decrease in the percentage of correct solutions and corresponding increase in no solution as shown in the results above.

5.2.4.2 Number of trial solutions

The number of trial solutions that Part IV of the algorithm must process is the number of trial solutions output by Part III in the first epoch. In subsequent epochs the number of trials solutions is the number output by Part IV in the previous epoch. As shown in section 5.2.3.1 Part III of the algorithm outputs an average of between 1.37 and 2.14 solutions depending on the number of satellites tracked (obviously the actual number of trial solutions must be an integer). This means that Part IV only requires a few epochs in order to eliminate the remaining false solutions, as was demonstrated in the previous section.

5.2.5 Effect of multipath on IAR performance

To understand the effect of multipath on the new IAR algorithm two further scenarios were simulated (scenarios 11 and 12 in Table 5-1). Multipath was simulated using the method described in Appendix A. The level of multipath and receiver noise was configured to represent the level of measurement noise observed on Topsat. In Chapter 3 the *single-difference* measurement noise was estimated as 6mm. This equates to $\sqrt{2}\times 6\text{mm} = 8.5\text{mm}$ of double-difference measurement noise.

Scenarios 11 and 12 were repeated eight times. In each re-run of the simulation Part IV of the algorithm was required to run for a minimum number of epochs between two and nine. This was done to examine the effect of the time-correlated nature of multipath on the multi-epoch success rate of the IAR algorithm.

The results of the multipath simulations are shown in Table 5-25. The results are classified in the same way as in section 5.2.4.1.

Table 5-25 Multi-epoch performance of IAR algorithm in presence of multipath, for different number of minimum epochs

	Five Satellites			Six Satellites		
Min Epochs	Correct Solution (%)	Incorrect Solution (Type I error) (%)	No Solution (%)	Correct Solution (%)	Incorrect Solution (Type I error) (%)	No Solution (%)
2	97.3	0.4	2.3	98.3	0.0	1.7
3	96.8	0.8	2.4	97.9	0.0	2.1
4	95.1	0.7	4.3	96.1	0.0	3.9
5	95.7	0.4	3.9	94.7	0.0	5.3
6	94.0	0.2	5.8	94.3	0.0	5.7
7	92.4	0.5	7.1	91.6	0.0	8.4
8	91.7	0.1	8.2	92.1	0.0	7.9
9	92.5	0.2	7.3	90.7	0.0	9.3

5.2.5.1 Effect of multipath on Parts I to III of IAR algorithm

The residuals, baseline and relative geometry tests used in Parts I to III of the algorithm assume the measurement noise is zero mean random noise with a Gaussian distribution. When multipath is present this is not the case. An example histogram of the measurement errors for one baseline is shown in Figure 5-1. The plot shows the histogram of the measurement errors simulated that are the combination of multipath and receiver noise. Overlaid on this plot is a noise distribution for the equivalent receiver noise only measurement errors (i.e. zero mean random error with a Gaussian distribution).

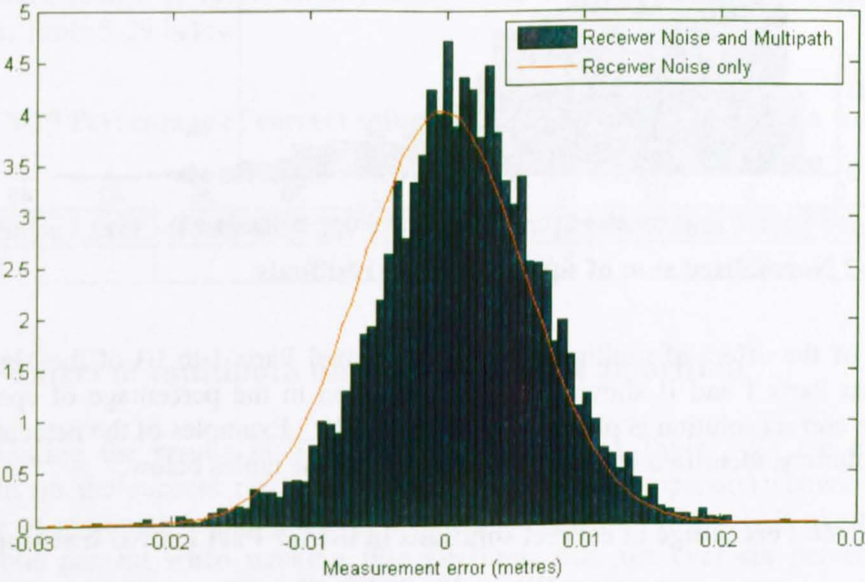

Figure 5-1 Comparison of measurement error distribution for multipath simulation and receiver noise only simulation

From the above plot it can be seen that multipath results in the measurement noise distribution having a non-zero mean. Whilst the multipath error is unlikely to result in significant errors in the trial baseline or attitude solutions (assuming good geometry) the non-zero mean will result in an increase in the percentage of correct solutions rejected by the various threshold tests in all four parts of the algorithm. This effect will be minimal for a single-epoch of data, but the likelihood of rejection will increase with the number of epochs tested. This results in a reduction in success rate as observed in Table 5-25.

The chi-squared test on the attitude residuals used in Part III (and Part IV) is also affected by multipath. By definition the chi-squared test assumes the measurement errors are zero mean normal random variables. Since multipath makes the measurement errors non-zero mean (as shown in Figure 5-1) this assumption is invalidated. Analysis of the simulation results shows that multipath causes a larger percentage of the normalised sum of squared errors to lie above the critical value used to define the chi-squared threshold. As a result the chi-squared test will reject a larger percentage of correct solutions.

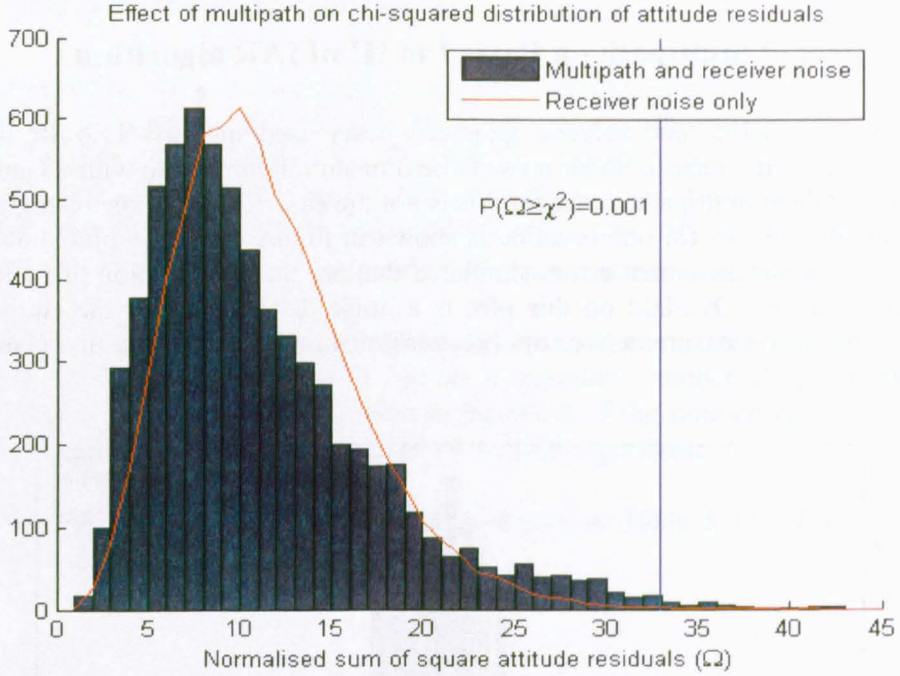

Figure 5-2 Normalised sum of square attitude residuals

Analysis of the effect of multipath on the individual Parts I to III of the algorithm shows that Parts I and II show negligible reduction in the percentage of epochs in which the correct solution is placed in their output list. Examples of the percentage of correct solutions identified in each part are shown in the tables below.

Table 5-26 Percentage of correct solutions in list for Part I when tracking six satellites with multipath

RMS Noise Level	Baseline 1	Baseline 2	Baseline 3
8.5mm	100.0	100.0	99.9

Table 5-27 Percentage of correct solutions in list for Part II when tracking six satellites with multipath

RMS Noise Level	Baseline 1+2	Baseline 2+3	Baseline 3+1
8.5mm	100.0	99.9	99.9

However, in Part III of the algorithm the effect of multipath would be considerable if it were not for the added check of testing the residuals for ±1 integers for the measurements on the third baseline. Table 5-28 shows the percentage of correct solutions in the lists output by the separate runs of Part III when we do not check the adjacent integers. Without the additional check the success rate drops to less than forty percent for the 3,1,2 baseline order (i.e. when baselines 3 and 1 are used to predict the integers for baseline 2). This loss of performance is due to the way the integers are estimated for the third baseline in Part III. In Part III the TRIAD algorithm is used to estimate the attitude from the two baseline vectors passed in from Part II. This attitude estimate is used in Equation 4-105 to estimate the integers for the third baseline. The problem with this approach is that the trial baseline vectors which are estimated in Part I can be particularly poor in the presence of multipath. Whilst the correct integer ambiguities are contained in the list from Part I, the trial baseline vector that is calculated from the correct ambiguities can be in error. This results in a poor attitude estimate from the TRIAD algorithm, and incorrect integer estimates for the third baseline.

Table 5-28 Percentage of correct solutions in lists from Part III when tracking six satellites (without checking ±1 integer)

RMS Noise Level	Baselines 1,2,3	Baselines 2,3,1	Baselines 3,1,2	Final List
8.5mm	52.9	41.8	35.8	100.0

By checking ±1 integers for the third baseline this problem is eradicated and the performance returns to levels close to that of the receiver noise only simulation, as shown in Table 5-29 below.

Table 5-29 Percentage of correct solutions in lists from Part III when tracking six satellites (with checking ±1 integer)

RMS Noise Level	Baselines 1,2,3	Baselines 2,3,1	Baselines 3,1,2	Final List
8.5mm	99.8	99.8	99.7	100.0

5.2.5.2 Effect of multipath on Part IV of IAR algorithm

By comparing the results in Table 5-25 with those in Table 5-23 the effect of multipath on the success rate can be quantified. The comparison shows that the presence of multipath causes a decrease in the success rate of the IAR algorithm of around one percent when tracking five satellites, and just over six percent when tracking six satellites. The results show that as with the receiver noise only simulation (see section 5.2.4.1) the success rate decreases as the minimum number of epochs tested increases, but multipath makes the reduction more pronounced.

The results in Table 5-25 show that the success rate does not decrease linearly as the minimum number of epochs tested increases. The most likely explanation for this is that the simulated error is a combination of receiver noise and multipath and in some epochs the random receiver noise will sum with the multipath error to such an extent that the correct trial solution is rejected by one of the statistical tests in Part IV.

As in Parts I to III the multipath error will cause the statistical tests in Part IV to reject the correct solution slightly more often. Since Part IV is run anew on each consecutive epoch the chance of Part IV rejecting the correct solution increases linearly with the number of epochs tested. Detailed analysis of the simulation results showed that for the nine epoch case, the correct integer solution was rejected by the chi-squared test on the attitude residuals in Part IV in 0.75% of the simulated epochs. For the receiver noise only case this figure was 0.1% as expected given the critical values used. If the chi-squared test rejects the correct solution in 0.75% of epochs on average, then in the above simulation (where 1000 runs were tested over nine consecutive epochs) it will reject $8 \times 0.75 = 6\%$ of the correct solutions. This agrees with the reduction in performance observed in the nine epoch case when comparing the receiver noise only and multipath simulations. Using a larger confidence interval in Part IV could mitigate the effect of multipath to some extent, although it would increase the likelihood of false solutions.

Finally, the results in Table 5-25 show that when only tracking five satellites the presence of multipath can sometimes result in Part IV finding a unique solution that is incorrect. This happens when the correct solution was rejected by the chi-squared test whilst an incorrect solution passed the test. This problem does not occur when tracking six satellites and hence this problem could also be mitigated when more measurements are available on a future GNSS attitude receiver.

5.3 Performance on In-orbit Data

In the following sections the performance of the IAR algorithm is analysed by post-processing data logged in-orbit on Topsat. The IAR algorithm was run for every epoch in which at least five satellites were available. Part IV was configured to validate the trial solutions for at least sixty seconds before declaring a unique solution to be valid. A period of sixty seconds was chosen based on the results from the previous section which showed that the new IAR algorithm could provide a reliable result when tracking six satellites, albeit with a small chance of a false solution when only tracking five satellites. By analysing the performance over six epochs (rather than just two) the effect that the number of satellites tracked on Topsat from one epoch to the next on the performance of the IAR algorithm can be examined.

Once the IAR algorithm had completed the multi-epoch testing using Part IV it was started anew on the next epoch, so that every epoch with sufficient satellites was tested to see if the algorithm could find a unique solution starting with that epoch.

The analysis divided the data in the in-orbit log files into three categories:

- Epochs in which at least five satellites were tracked on each baseline (i.e. the IAR algorithm could be started)
- Epochs in which five satellites were tracked on each baseline

- Epochs in which six satellites were tracked on each baseline

Obviously the first category encompasses all the epochs in the latter two categories. However, by analysing the epochs separately in this way a comparison can be made between the results based on real data and the results from simulation presented above.

5.3.1 Overview of in-orbit data and performance of SGR-20

Table 5-30 gives an overview of the data collected during each of the seven data logging experiments on Topsat in 2007. For each experiment the GPS measurements were logged at a rate of 0.1Hz. This resulted in an average of around 230 epochs of data per experiment. This number varies from experiment to experiment depending on how long the SGR-20 took to obtain a position fix and switch to its attitude determination configuration. Table 5-30 also shows the percentage of epochs in which at least five satellites were tracked on all three baselines and the percentage of epochs in which five or six satellites were tracked on all three baselines. The percentage of epochs with at least five satellites demonstrates how many epochs the new IAR algorithm could be used out of the total number of epochs logged. The percentage of epochs with five or six satellites demonstrates how many epochs were used in the comparison with the simulated results presented above.

Table 5-30 Overview of in-orbit data

Experiment	Total Number of Epochs	Number of epochs with at least five measurements per baseline	Number of epochs with five measurements per baseline	Number of epochs with six measurements per baseline
22/02/07	225	191 (84.9%)	64 (28.4%)	108 (48.0%)
27/02/07	238	208 (87.4%)	86 (36.1%)	99 (41.6%)
01/03/07	217	131 (60.4%)	21 (9.7%)	7 (3.2%)
01/05/07	236	192 (81.4%)	65 (27.5%)	83 (35.2%)
09/05/07	234	115 (49.1%)	11 (4.7%)	54 (23.1%)
04/07/07	228	194 (85.1%)	20 (8.8%)	53 (23.2%)
10/07/07	249	195 (78.3%)	69 (27.7%)	85 (34.1%)

For most of the experiments the percentage of useable epochs was over 75%. Two of the experiments resulted in fewer useable epochs. This was due to an issue with the satellite acquisition and tracking algorithms on the SGR-20 which require further improvements to get the best performance.

Table 5-31 shows the percentage of epochs which were useful for Part IV of the algorithm. For the Part IV of the algorithm to run successfully, the rule is enforced that the SGR-20 must maintain lock on at least five satellites over a period of at least sixty seconds. If the number of satellites tracked drops below five on any baseline then Part IV of the algorithm will not be able to proceed and will report 'No solution'. The IAR algorithm will then have to wait until at least five measurements are available before starting again.

Table 5-31 Percentage of epochs useful for multi-epoch integer ambiguity resolution

Experiment	Number of epochs with at least five measurements per baseline	Number of epochs with five measurements per baseline	Number of starting epochs with six measurements per baseline
22/02/07	181 (80.4%)	62 (27.6%)	99 (44.0%)
27/02/07	195 (81.9%)	76 (31.9%)	95 (39.9%)
01/03/07	122 (56.2%)	20 (9.2%)	6 (2.8%)
01/05/07	182 (77.1%)	59 (25.0%)	78 (33.1%)
09/05/07	105 (44.9%)	3 (1.3%)	53 (22.7%)
04/07/07	193 (84.6%)	19 (8.3%)	52 (22.8%)
10/07/07	188 (75.5%)	62 (24.9%)	84 (33.7%)

The first column in Table 5-31 shows the number of epochs in which *at least five* satellites were tracked on each baseline and *at least five* satellites were tracked in subsequent epochs. This allowed Part IV of the algorithm to be run for at least sixty seconds. The second column shows the number of epochs in which *exactly five* satellites were tracked on each baseline, and *at least five* satellites were tracked in subsequent epochs so that Part IV of the algorithm could run for at least sixty seconds. The third column shows the same, but with *six satellites* in the initial epoch.

The first column is the most useful in terms of judging the overall performance of the new IAR algorithm since it shows the number of epochs in which the new IAR algorithm could be started and would result in a correct solution within a few epochs.

For most of the experiments the percentage of useful epochs is over seventy percent. This suggests that for real-time operations the SGR-20 would be able to run the IAR algorithm successfully. However, during the 9th May 2007 experiment only forty-five percent of epochs with at least five measurements per baseline were suitable for the multi-epoch to validate the trial solutions over a period of sixty seconds or more. Again, this suggests that more work needs to be done on the satellite acquisition and tracking algorithms on the SGR-20 in order to get the best performance out of the integer ambiguity resolution algorithm. This problem would likely be removed on a future receiver since more channels would be available for tracking.

5.3.2 In-orbit integer ambiguity success rates

The results in Table 5-32, Table 5-33 and Table 5-34 list the percentage of epochs in which the new IAR algorithm outputs the correct solution, an incorrect solution or no solution. The three tables show the performance for those epochs in which at least five satellites, five satellites and six satellites were tracked, respectively.

The *success rate* is defined as the percentage of epochs in which the algorithm outputs a unique solution, and this solution was the correct solution. Since the following results show that the algorithm never outputs an incorrect solution the success rate is the same as the percentage of correct solutions.

The results in Table 5-33 and Table 5-34 correspond to the bar charts in Figure 5-4 and Figure 5-5 respectively. The results in the tables and figures allow a direct comparison with the results from simulation presented in section 5.2. The mean success rate across the seven experiments tested is 98.2% when tracking both five and six satellites. The results of the receiver noise only simulation in section 5.2 showed that the success rate was 97.2% when tracking five satellites and 98.7% when tracking six satellites. Given that only a few hundred epochs of in-orbit data were tested it is reasonable to assume that there is negligible difference between the in-orbit results and those achieved in the receiver noise only simulations. Comparison of the in-orbit success rate with the success rate achieved in the multipath simulations in section 5.2 shows that the IAR algorithm performed better on the in-orbit data. Since the level of multipath on Topsat is unknown, the multipath simulation results may not be representative and it is not possible to draw a definite conclusions from the two results.

Table 5-32 Multi-epoch performance when tracking at least five satellites based on in-orbit data

Experiment	Correct Solution (%)	Incorrect Solution (%)	No Solution (%)
22/02/07	97.2	0.0	2.8
27/02/07	97.9	0.0	2.1
01/03/07	96.7	0.0	3.3
01/05/07	96.7	0.0	3.3
09/05/07	98.1	0.0	1.9
04/07/07	100.0	0.0	0.0
10/07/07	97.9	0.0	2.1

Table 5-33 Multi-epoch performance when tracking five satellites based on in-orbit data

Experiment	Correct Solution (%)	Incorrect Solution (%)	No Solution (%)
22/02/07	100.0	0.0	0.0
27/02/07	97.4	0.0	2.6
01/03/07	100.0	0.0	0.0
01/05/07	96.6	0.0	3.4
09/05/07	100.0	0.0	0.0
04/07/07	100.0	0.0	0.0
10/07/07	93.5	0.0	6.5

Table 5-34 Multi-epoch performance when tracking six satellites based on in-orbit data

Experiment	Correct Solution (%)	Incorrect Solution (%)	No Solution (%)
22/02/07	94.9	0.0	5.1
27/02/07	97.9	0.0	2.1
01/03/07	100.0	0.0	0.0
01/05/07	94.9	0.0	5.1
09/05/07	100.0	0.0	0.0
04/07/07	100.0	0.0	0.0
10/07/07	100.0	0.0	0.0

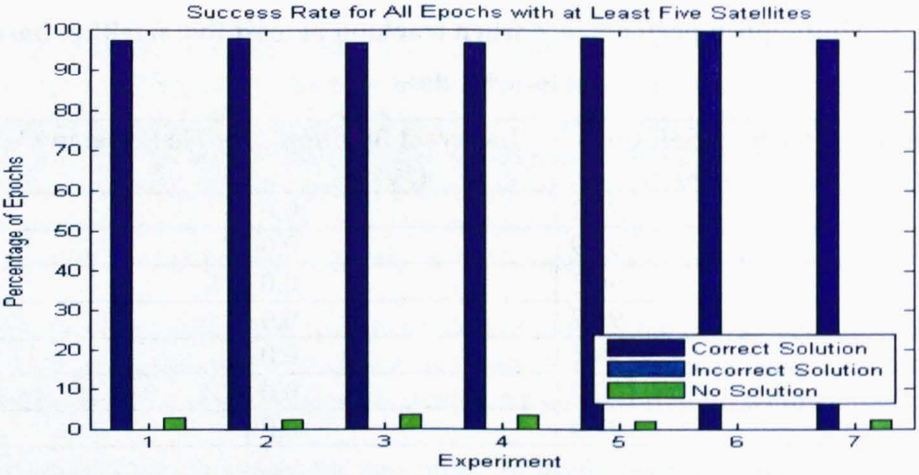

Figure 5-3 Multi-epoch success rate when tracking at least five satellites using in-orbit data

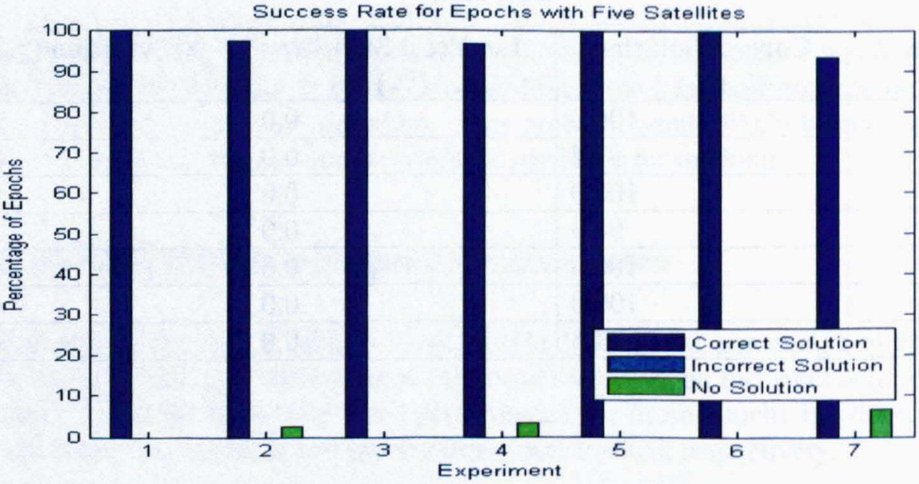

Figure 5-4 Multi-epoch success rate when tracking five satellites using in-orbit data

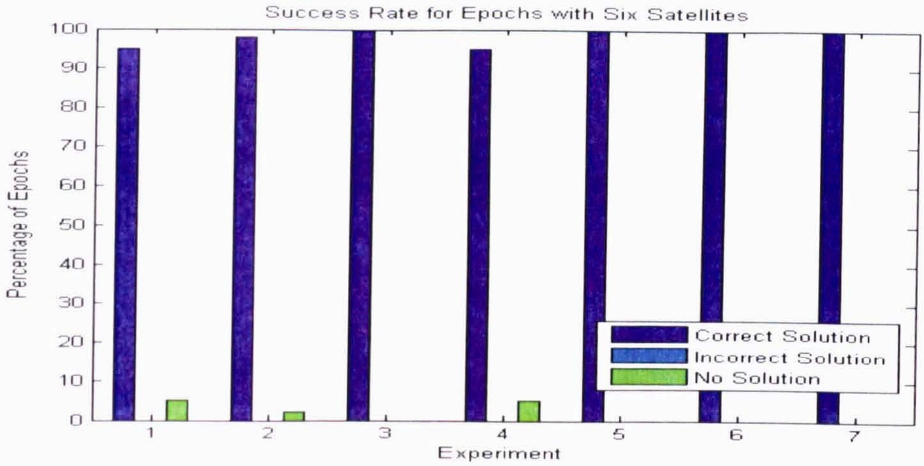

Figure 5-5 Multi-epoch success rate when tracking at six satellites using in-orbit data

5.3.3 Case Studies of IAR performance on specific GPS attitude experiments

In the following sections, three particular GPS attitude experiments conducted on Topsat are studied in more detail to analyse the performance of the IAR algorithm when it is operating on real data.

5.3.3.1 22nd February 2007 Experiment

In this section the performance of the IAR algorithm during the 22nd February 2007 experiment in discussed. This experiment was chosen as an example since it was the first example of the typical GPS attitude experiment carried out on Topsat for this research. It includes a TDI=2.2 imaging manoeuvre (see section 3.1) in which the spacecraft is commanded to off-point in pitch by around twenty degrees.

As shown in Table 5-30 and Table 5-31 there were 225 epochs of data collected during this experiment, of which 181 epochs have sufficient measurements for the IAR algorithm to run successfully. The results in Table 5-32 show that the IAR algorithm identified the correct integer ambiguities in 97.2 percent of useable epochs, and reported no solution in the remaining 2.8 percent. In no epochs was an incorrect solution chosen.

An example plot showing the number of satellites tracked on each baseline during the 22nd February 2007 experiment is shown in Figure 5-8 below. Note that on baseline 1 the number of satellites tracked drops to three at around 22 minutes into the experiment. This coincides with the TDI manoeuvre, and resulted from antenna 2 losing lock on a number of satellites due to the off-pointing in pitch (see Figure 5-6 below).

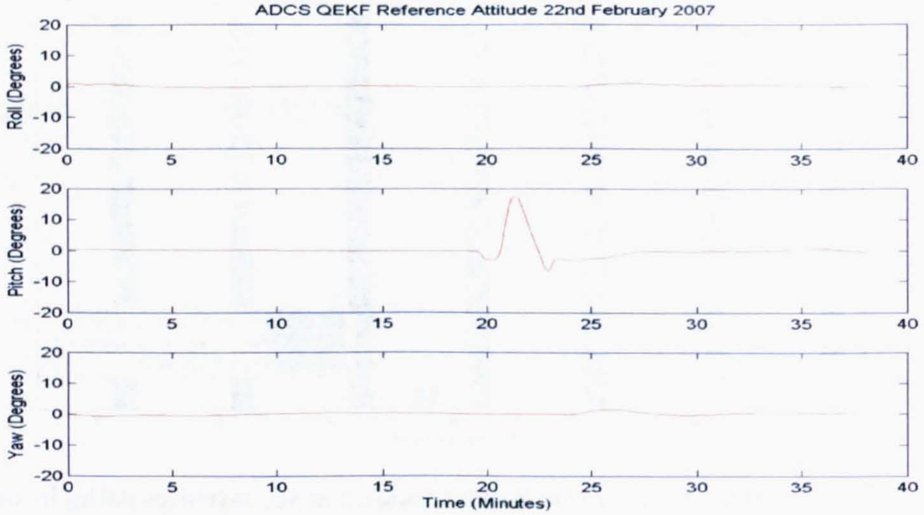

Figure 5-6 ADCS QEKF Reference Attitude 22nd February 2007

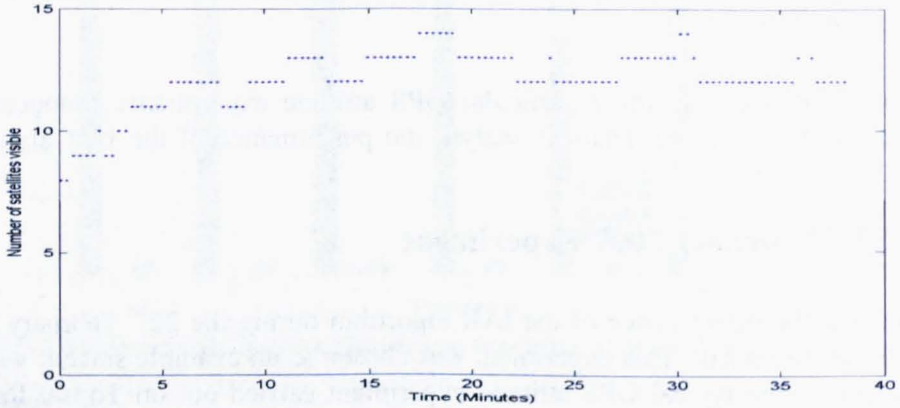

Figure 5-7 Number of satellites visible during 22nd February 2007 experiment

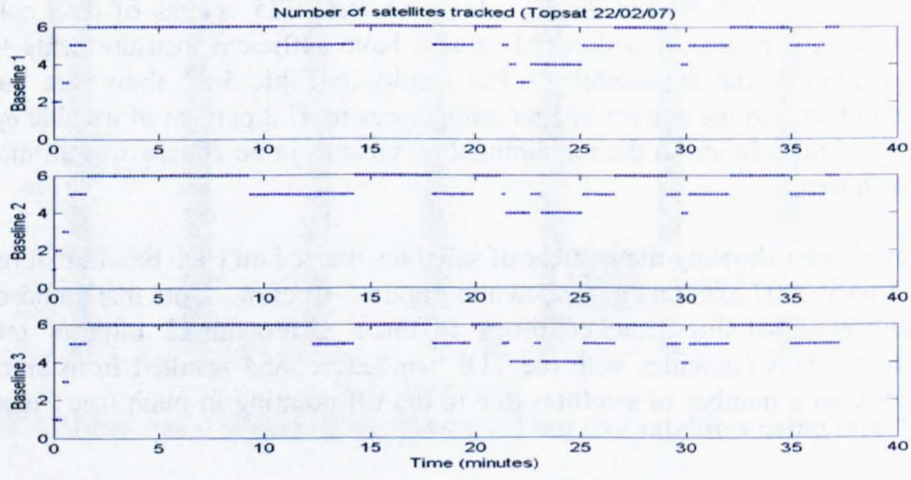

Figure 5-8 Number of satellites tracked on each baseline during 22nd February 2007 experiment

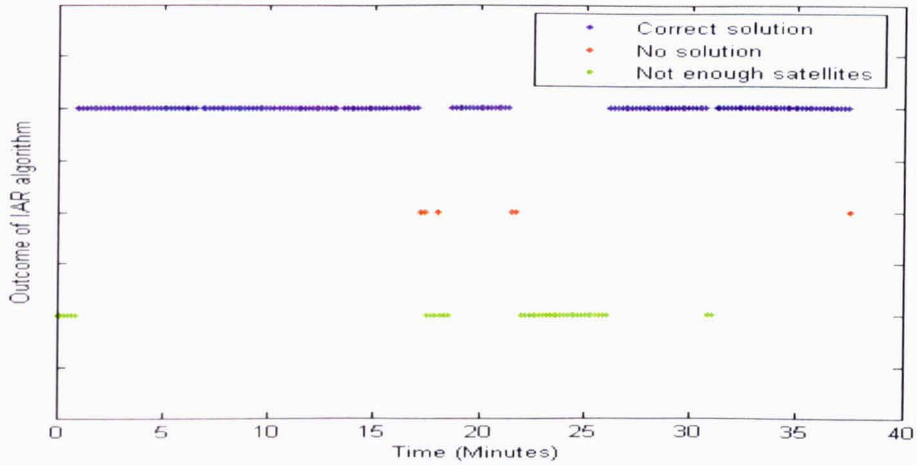

Figure 5-9 Outcome of IAR algorithm vs time during 22nd February 2007 experiment

The plot in Figure 5-9 shows the outcome of the IAR algorithm for each epoch during the experiment. The blue dots show the epochs in which the IAR algorithm outputted a correct solution. The red dots show the epochs in which it outputted no solution. The green dots show when there were too few satellites for the algorithm to complete successfully. Since there were no incorrect solutions there are none shown in the plot. Comparing Figure 5-9 with the number of satellites tracked in Figure 5-8 shows that for the first minute after the experiment started the SGR-20 hadn't acquired at least five satellites on each baseline, and so the IAR algorithm could not start. About 70 seconds into the experiment the receiver was tracking five satellites on each baseline. There was then a period of around 16 minutes during which the IAR algorithm could run successfully in each epoch. At around 21 minutes into the experiment, which coincides with the peak of the TDI pitch manoeuvre, the SGR-20 is only tracking three satellites on baseline 1 and hence the IAR algorithm cannot run. During much of the period from around 21 minutes to 25 minutes there are fewer than five satellites tracked on each baseline, meaning that the IAR algorithm could not be run on these epochs. Comparison of the number of satellites tracked in Figure 5-8 with the number of satellites above the elevation mask shown in Figure 5-7 indicates that the SGR-20 could have performed better in terms of maintaining six satellites on each baseline. However, the satellite selection algorithm in the SGR-20 assumes the satellite is always nadir pointing, which was not the case during the TDI manoeuvre at around 22 minutes.

Figure 5-10 shows the GPS residuals for each baseline throughout the experiment. There are a number of periods, particularly on baseline 2, which show time-correlation in the residuals. This demonstrates that multipath was present in the measurements at that time. A comparison of the outcome of the IAR algorithm in Figure 5-9 with the GPS residuals in Figure 5-10 shows that there is no obvious correlation between the presence of multipath and the IAR algorithm failing to find a solution.

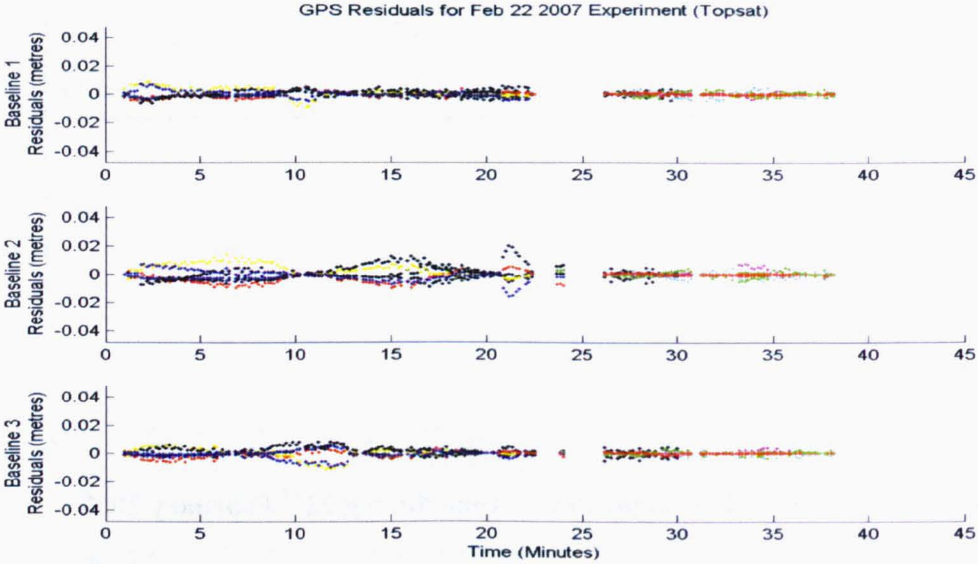

Figure 5-10 GPS residuals during 22nd February 2007 experiment

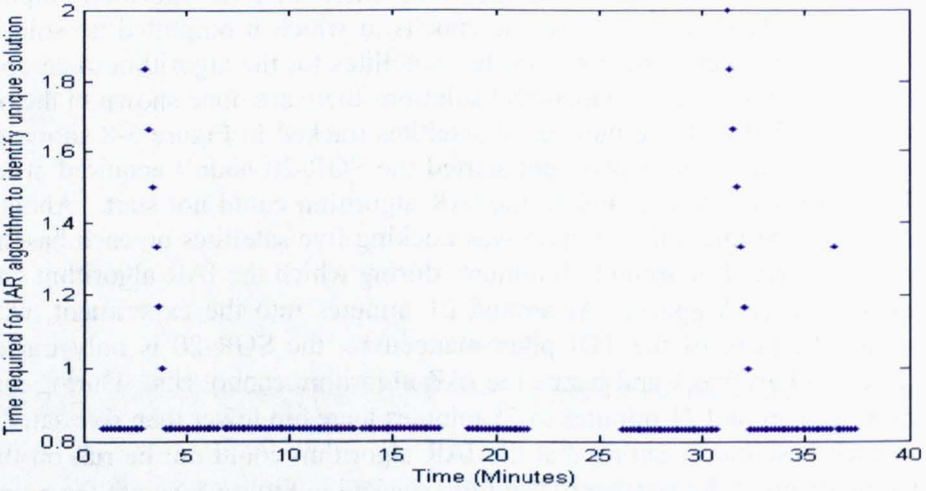

Figure 5-11 Time required for unique solution for each epoch of 22nd February 2007 experiment

Figure 5-11 shows the time required for a unique solution to be found for each epoch in which the IAR algorithm was run. Figure 5-11 shows that in the majority of cases the IAR algorithm has identified a unique solution within sixty seconds. There are thirteen epochs in which the algorithm takes longer to find a unique solution. Figure 5-10 shows that there was multipath present on baseline 2 for much of the first twenty minutes of the experiment, but this appears to have no significant effect on the time taken to resolve the integer ambiguities. In both periods where the IAR algorithm required more than sixty seconds to find the solution, Part IV of the algorithm was testing two different solutions to see which one was correct. This demonstrates how difficult it can be to eliminate false solutions, since sometimes they can fit the measurements as well or better than the true solution. Only by comparing over sufficient epochs can the algorithm successfully eliminate such false solutions.

5.3.3.2 1st May 2007 Experiment

The main purpose of this experiment was to determine if the new IAR algorithm could successfully solve for the integer ambiguities during large angle manoeuvres. In this experiment Topsat was commanded to perform a thirty degree off-pointing in roll as well as the standard TDI=2.2 pitch manoeuvre (see section 3.1). The ADCS QEKF attitude solution for this experiment is shown in Figure 5-12 below.

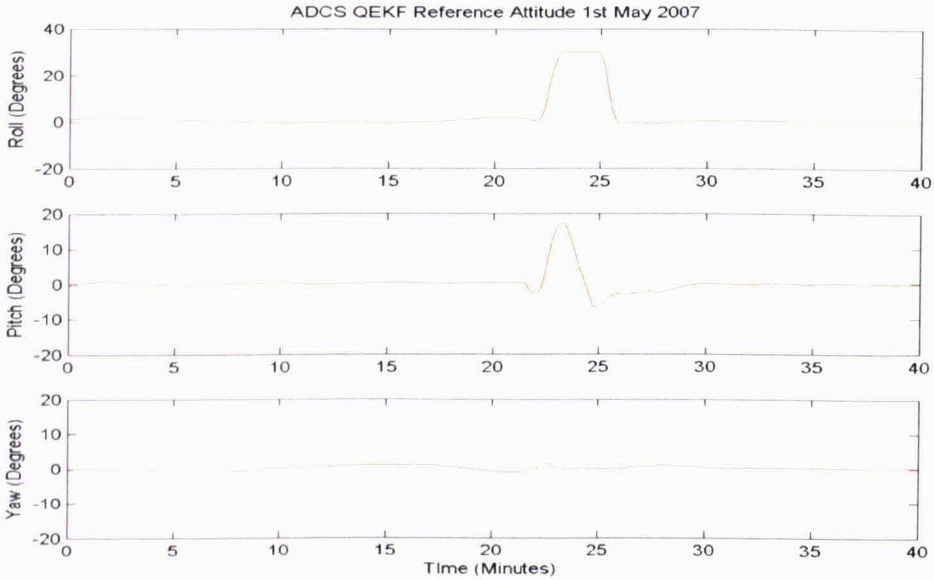

Figure 5-12 ADCS QEKF reference attitude 1st May 2007

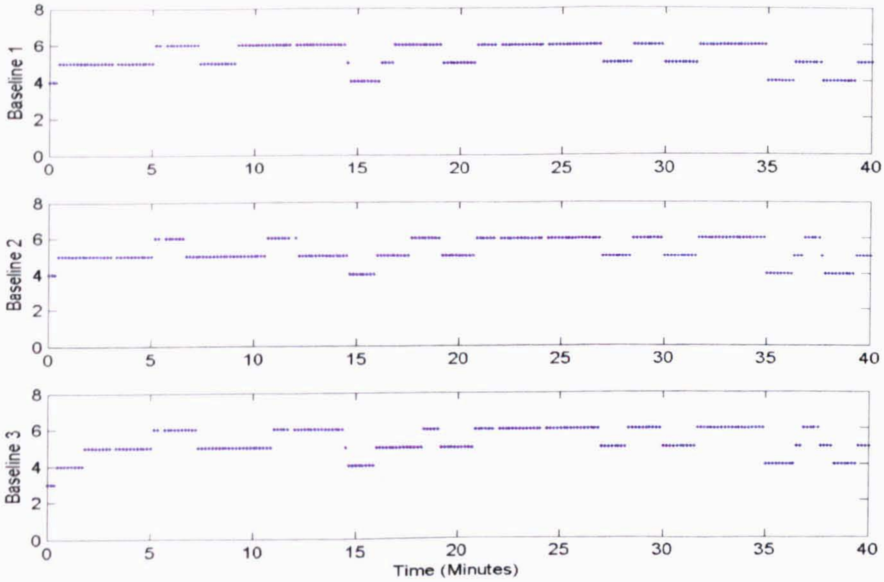

Figure 5-13 Number of satellites tracked on each baseline 1st May 2007

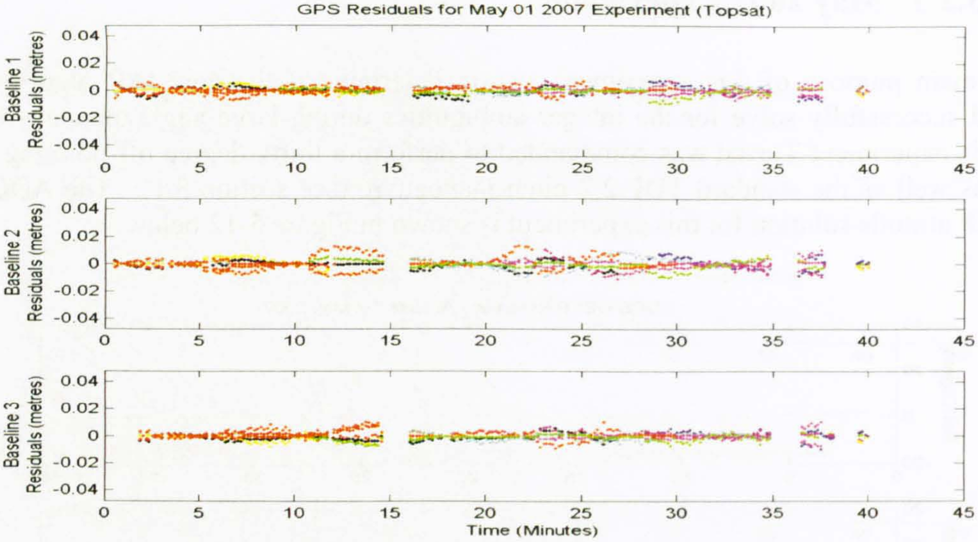

Figure 5-14 GPS residuals during 1st May 2007 experiment

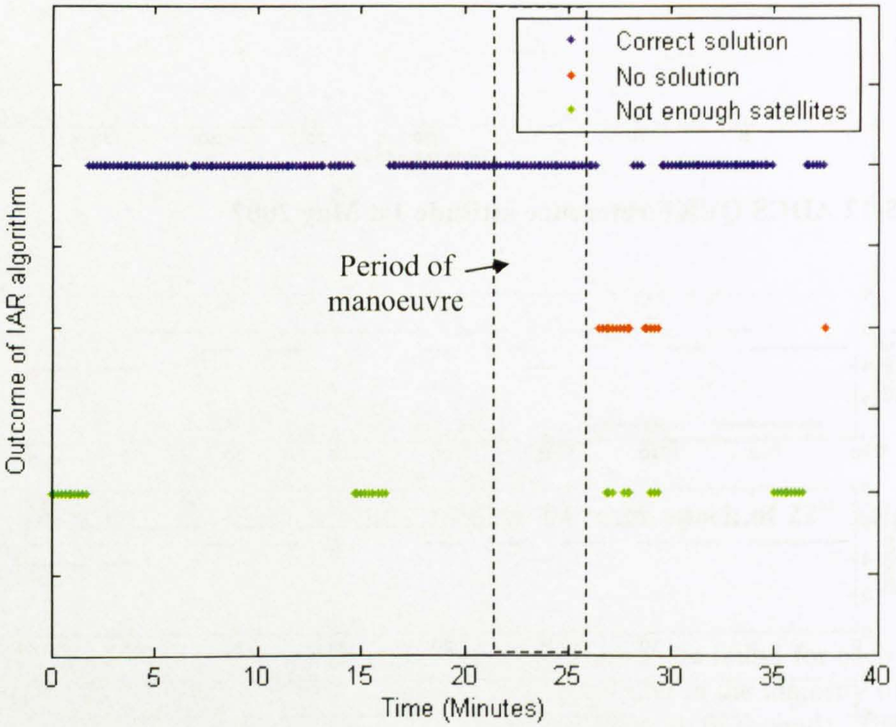

Figure 5-15 Outcome of IAR algorithm vs time during 1st May 2007 experiment

The plots in Figure 5-13 show that six satellites were tracked on all three baselines during the period of the large angle manoeuvres. Therefore the IAR algorithm had sufficient measurements to perform its sixty second validation of the trial solutions during the manoeuvres. The GPS residuals shown in Figure 5-14 show that there was minimal multipath on all three baselines, even during the manoeuvres. Figure 5-15 shows the outcome of the IAR algorithm in each of the 182 epochs in which sufficient measurements were available for the new IAR algorithm to find and validate the correct solution.

These results demonstrate that the new IAR algorithm can successfully initialise the integer ambiguities during large angle manoeuvres. Importantly this initialisation is totally stand-alone since the IAR algorithm has no *a priori* knowledge of the attitude of the spacecraft.

5.3.3.3 4th July 2007 Experiment

This experiment is another example where Topsat conducted a TDI=2.2 imaging manoeuvre (see section 3.1) which involves a twenty degree pitch manoeuvre. For this experiment the elevation mask of the SGR-20 was increased to ten degrees, whereas in all the previous in-orbit data logging experiments it had been zero. The reason for the change in elevation mask was to see if this would reduce the level of multipath observed in the GPS carrier phase measurements. The RMS measurement noise given in Table 4-7 in Chapter 3 showed that there was no observable benefit to the increased elevation mask in terms of reducing the multipath. This is also demonstrated by comparing the GPS residuals shown in Figure 5-16 with the residuals for the experiments discussed above. There is no appreciable difference in the amount of time-correlation observed in the residuals.

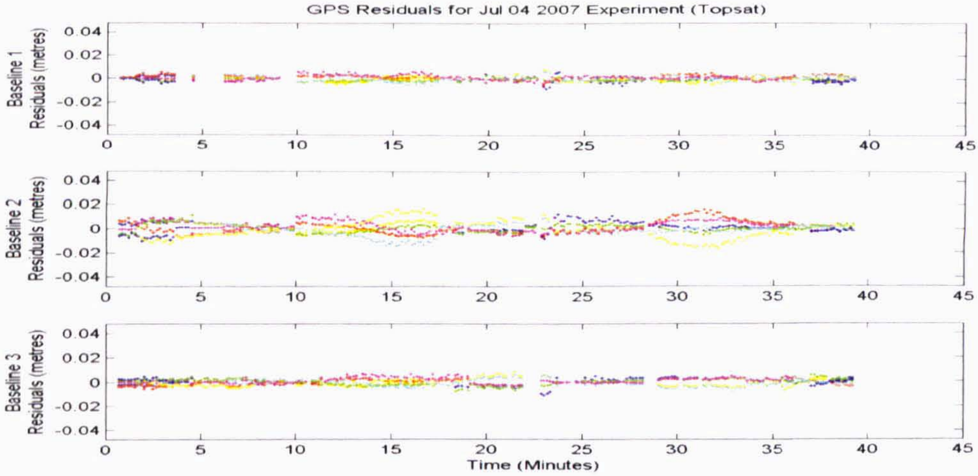

Figure 5-16 GPS Residuals for July 4th 2007 Experiment (Topsat)

However, a secondary benefit of increasing the elevation mask was that it forced the SGR-20 to swap satellites more often. This is because when a satellite that was being tracked dropped below the elevation mask it was swapped out for one above the elevation mask. As can be seen from Table 5-31 this appears to have resulted in a slightly higher percentage of epochs being suitable for running the multi-epoch component of the IAR algorithm. Also, one hundred percent of the epochs in which five or six satellites were tracked on all three baselines were suitable for running Part IV of the algorithm. This makes the 4th July 2007 experiment a good example for comparison with the simulated results.

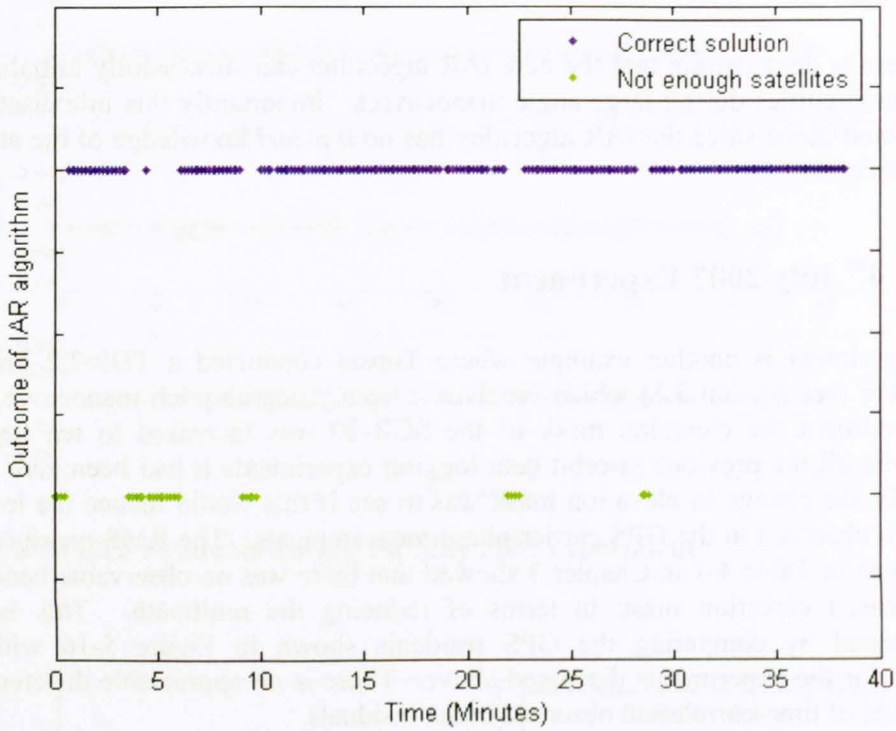

Figure 5-17 Outcome of IAR algorithm vs Time during 4th July 2007 experiment

The results in Table 5-33 and Table 5-34 show that the new IAR algorithm achieved a success rate of one hundred percent when tracking both five and six satellites on all three baselines. This is also reflected in the plot in Figure 5-17, which shows that the IAR algorithm calculated the correct integer ambiguity solution in every epoch in which there were sufficient measurements. This shows that new IAR algorithm can achieve a success rate of close to one hundred percent given the level of RMS measurement noise on Topsat, as long as there are sufficient satellites for the algorithm to run.

5.4 Conclusions

The performance of the new IAR algorithm presented in Chapter 4 has been tested using both simulated data and real data logged on a microsatellite in orbit.

A Monte-Carlo style simulation was used to test the performance of the new IAR algorithm under varying GPS constellation geometries and for a number of levels of RMS receiver noise. RMS measurement noise levels between 2mm and 10mm were tested. The receiver noise only simulation results demonstrated that the algorithm provides the correct solution in close to one hundred percent of epochs when tracking six satellites and over ninety percent if tracking five satellites. The simulation results showed that the success rate decreases as the number of epochs tested by Part IV increases. This is because the likelihood of the various statistical checks rejecting the correct solution increases with the number of epochs tested.

The performance of the algorithm was analysed in terms of the percentage of epochs in which each Parts I to IV identified the correct solution. The results showed that Parts I and II identified the solution in almost one hundred percent of epochs. Part III's performance was slightly poorer, particularly when only tracking five satellites. However, by running Part III for each pairing of baselines used in Part II and combining the lists in to a single final list the correct solution is always passed to Part IV of the algorithm. For Part IV of the algorithm it was observed that when tracking only five satellites there is a greater likelihood that there will be fewer than four satellites in common between epochs. This results in decreased performance in Part IV, since it relies on using the double-difference integer tracking method to calculate the integers in each epoch. This method cannot work if there are less than four satellites in common between epochs. However, when six satellites are tracked this is less of an issue and Part IV can achieve a higher success rate.

Analysis of the list sizes of output by each part of the algorithm showed that the algorithm effectively constrains the integer search problem so that it is practical to calculate a solution in real-time. As was discussed in Chapter 4, the potential number of trial solutions can be over one million for a one metre baseline, but by intelligently using the constraints available the new algorithm can reduce this to a single solution in only a few epochs. Whilst it is possible that the algorithm can identify a unique solution in a single-epoch, the simulation results showed that this solution is not guaranteed to be the correct solution. However, when tracking six satellites the algorithm can typically find a unique solution using only twenty seconds of data. This may be improved upon on future receivers when more channels are available for tracking satellites.

The simulation results showed that the mean list size increased as the RMS measurement noise increased. This was to be expected since all the statistical thresholds are a function of the assumed noise variance. Therefore, the size of the confidence interval defined by each threshold increases with the square of the measurement noise. This leads to the conclusion that when using this algorithm it is beneficial to reduce the RMS measurement noise since this will result in smaller list sizes. This will result in lower computational loading since the algorithm will have fewer false solutions to eliminate. It was also observed that the mean list size was higher when tracking six satellites. This is due to Part I permitting trial solutions where either of the measurements in the secondary set lies within the confidence interval. For a future receiver which could potentially track more than six satellites it would be even more beneficial to reduce the RMS measurement noise in order that the computational loading could be reduced.

The small size of the lists output by the single-epoch component (Parts I to III) of the new IAR algorithm demonstrates that the algorithm is suitable for implementation onboard the SGR-20. The results show that the receiver code will not have to store a large list of potential solutions to test over multiple epochs, and also that the correct solution should be found quickly by Part IV of the algorithm since there are few false solutions to eliminate.

The effect of multipath on the performance of the new IAR algorithm was studied in section 5.2.5. A 'multipath map' based on measurements of an SSTL GPS patch antenna in an anechoic chamber was used to simulate measurement errors with the same RMS as was calculated for Topsat in Chapter 3. This simulation showed that the simulated multipath error produced measurement errors having non-zero mean. This caused a slight increase in the percentage of correct solutions that did not meet the statistical thresholds and an increased the likelihood of each of the thresholds rejecting the correct solution. The simulated multipath error also led to the attitude residuals having a skewed distribution. This caused a slight increase in the percentage of correct solutions which failed the chi-squared tests in Part III and Part IV.

During testing it was discovered that multipath error can result in poor baseline pointing and attitude estimates. When these estimates are used to estimate the integer ambiguities for measurements in the secondary set (or for newly risen satellites) it is possible that the integer is calculated incorrectly. It was found that by simply checking the residuals, the algorithm could easily account for multipath error and ensure that the correct integer is calculated. After this improvement, analysis of the success rates of each part of the algorithm showed that the algorithm is robust in the presence of multipath, since all parts achieve close to one hundred percent success rate.

Real data logged on the Topsat microsatellite in-orbit was used to demonstrate the real-life performance of the new IAR algorithm. It was shown that the new IAR algorithm can resolve the integer ambiguities with a one hundred percent success rate, even with the constraints imposed by the SGR-20 hardware such as poor satellite allocation and tracking performance. The results show that further work is required on the tracking algorithms of the SGR-20 in order to get the best performance out of the integer ambiguity resolution algorithm.

To the best of our knowledge this is the first demonstration of integer ambiguity resolution on a satellite during a large angle manoeuvre. All previous GPS attitude experiments on spacecraft relied on *a priori* knowledge of the spacecraft's attitude, or imposed constraints on the attitude of the spacecraft during integer ambiguity resolution to limit the integer ambiguity search space so that it could be searched within a practical time span. The new algorithm presented in this work requires no constraints on the attitude of the platform, and can even initialise during large angle manoeuvres.

6 Attitude determination from GPS measurements

In this chapter the issues surrounding tracking the attitude of the spacecraft using GPS measurements are examined. Firstly, a brief study on some of the factors which affect the performance of GPS attitude is undertaken.

The first performance factor studied is the baseline geometry of the platform. The baseline geometry of the platform is a major factor in the achievable attitude performance. For example, co-planar baseline geometries like that found on Topsat increase the attitude uncertainty in the direction perpendicular to the antenna plane. The length of the baselines also affects the achievable accuracy, since the achievable accuracy is directly proportional to the baseline length. To examine the effect of the baseline geometry on Topsat a numerical simulation comparing different baseline geometries is performed and the expected GPS attitude accuracy given the baseline geometry on Topsat is calculated. The actual attitude accuracy achieved on Topsat is examined in Chapter 7. The simulation is also used to calculate the attitude accuracy achievable on a future GNSS attitude receiver that can track all GPS satellites in view.

The second performance factor studied is the use of ADCS information to estimate and remove the line bias. In [Purivigraipong, 2000] it was suggested that the ADCS could be used to estimate the line bias. The use of the ADCS to estimate the line bias and the effect this has on the RMS disparity and RMS error of the GPS solution is examined.

The third performance factor studied is the effect of different elevation masks on the number of satellites visible. When configuring a GPS receiver it is common to set an elevation mask to try and remove low elevation satellites that are more likely to contain atmospheric errors and multipath.

Finally data logged in-orbit was post-processed in MATLAB and used to analyse the performance of the double-difference Attitude Point Solution algorithm. The GPS attitude solution is compared with the Quaternion Extended Kalman Filtered attitude solution provided by the ADCS on Topsat. Data from three in-orbit experiments are used to analyse the performance of the SGR-20 as an attitude sensor for micro-satellites by examining the ability of the SGR-20 to track large angle manoeuvres, the ADOP throughout each experiment and the achievable pointing accuracy.

Throughout this chapter it is assumed that the algorithm from Chapter 4 has successfully solved for the integer ambiguities.

6.1 Study on GPS attitude performance issues

In this section the MATLAB based simulator is used to analyse the performance factors of GPS attitude determination on a microsatellite.

6.1.1 Baseline geometry

The concept of Attitude Dilution of Precision (ADOP) was defined in Chapter 2. The derivation in Chapter 2 allows the effect of baseline geometry on the ADOP to be calculated. From Equation 2-69 it can be seen that the ADOP is a function of the baseline geometry and Equation 2-73 shows that the accuracy of the attitude estimate increases as the baseline length increases.

As shown in [Purivigraipong, 2000], assuming triple orthonormal baselines, the covariance matrix $\hat{\mathbf{H}}^T\mathbf{W}^{-1}\hat{\mathbf{H}}$ used to calculate the ADOP in Equation 2-70 can be written as

$$\hat{\mathbf{H}}^T\mathbf{W}^{-1}\hat{\mathbf{H}} = \sum_{j-1}^{n}\left(\mathbf{v}^{\times}_{i,j(O)}\right)^T \hat{\mathbf{A}}^T\mathbf{B}\mathbf{W}^{-1}\mathbf{B}^T\hat{\mathbf{A}}\left(\mathbf{v}^{\times}_{i,j(O)}\right) \qquad \textbf{6-1}$$

where $\mathbf{B} = \begin{bmatrix}\mathbf{b}_{1B} & \mathbf{b}_{2B} & \mathbf{b}_{3B}\end{bmatrix}$. For triple orthonormal baselines $\mathbf{B}\mathbf{W}^{-1}\mathbf{B}^T = b_0^2\mathbf{I}\mathbf{W}^{-1}$ where b_0 is the effective baseline length. For such a baseline configuration the ADOP would then simply be a function of the selected LOS vectors

$$\mathrm{ADOP} = \sqrt{tr\left(\sum_{j=1}^{n}\left(\mathbf{v}^{\times}_{i,j(O)}\right)^T\mathbf{W}^{-1}\left(\mathbf{v}^{\times}_{i,j(O)}\right)\right)^{-1}} \qquad \textbf{6-2}$$

However, on Topsat the baselines are coplanar and have varying lengths. To determine the effect of the baseline geometry on the ADOP a numerical simulation was conducted. The MATLAB based simulator described in Appendix A was used to simulate the location of twenty-four GPS satellites and the Topsat satellite in LEO at ten second intervals over a period of twenty-four hours. The attitude of the spacecraft was assumed nadir-pointing throughout. A 'Highest Elevation' algorithm was used to select six satellites in each epoch and Equation 2-70 was used to compute the ADOP.

The ADOP was calculated for triple orthonormal baselines with a length of both 1m and 0.607m (the effective baseline length on Topsat). The ADOP was also calculated for the specific baseline geometry of Topsat. As can be seen from the results in Figure 6-1 - where the blue plot and green plot are coincident - the ADOP is independent of the baseline length. However, it must be remembered that the achievable pointing accuracy is affected by the baseline length as shown in Equation 2-73.

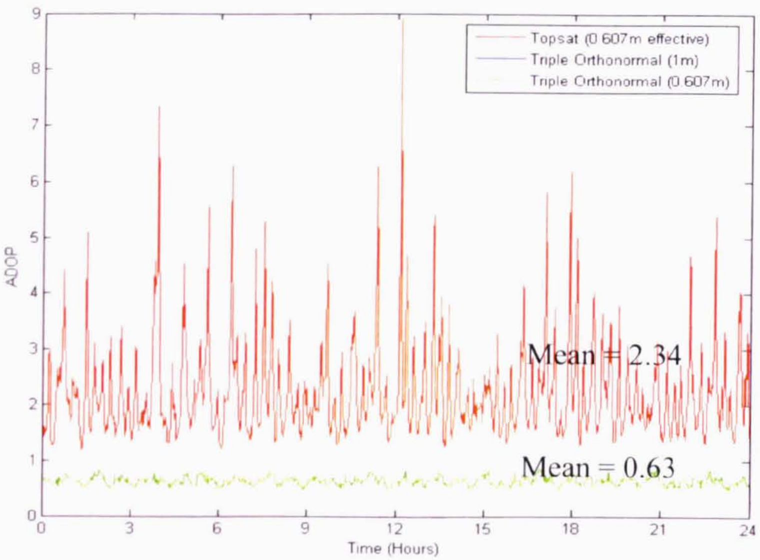

Figure 6-1 Simulated results of ADOP for Triple Orthonormal and Topsat baseline geometries

The above plot shows that the mean ADOP for the coplanar baseline geometry on Topsat is nearly four times the ADOP for triple orthonormal baselines. This shows that the coplanar baseline geometry will result in greater uncertainty in the GPS attitude estimate. The ADOP was then split into roll, pitch and yaw components as shown in Equation 2-72. The dilution of precision in each axis, assuming the spacecraft is nadir pointing, is shown in Table 6-1.

Table 6-1 Simulated ADOP split into roll, pitch and yaw components

Baseline Geometry	Mean Roll DOP	Mean Pitch DOP	Mean Yaw DOP
Triple Orthonormal (1m baselines)	0.65	0.70	0.52
Triple Orthonormal (0.607m baselines)	0.65	0.70	0.52
Topsat (0.607m effective baseline)	3.29	2.26	0.79

Once the ADOP is split into roll, pitch and yaw components we can observe that the coplanar baseline geometry increases the dilution of precision in the roll and pitch axes much more than it does in the yaw axis. This is logical since all three baselines are perpendicular to the yaw axis when the spacecraft is nadir pointing, and so all three baselines have good observability of yaw.

The mean measurement noise across all experiments analysed in Chapter 3 was used to estimate the expected accuracy of the GPS attitude solution on Topsat. Based on Table 3-7 the average single-difference RMS measurement noise across all baselines is 5.9mm. This equates to a double-difference measurement noise of 8.5mm. Using an effective baseline length of 0.6043 metres and a double-difference RMS measurement noise of 8.5mm the expected attitude error for Topsat will be:

$$\sigma_{\mathrm{GPS}}^2 = \mathrm{ADOP}\frac{\sigma_{\mathrm{w}}^2}{b_0} \tag{6-3}$$

which assuming an average ADOP of 2.34 (calculated from Table 6-1) gives an RMS attitude error of 1.89 degrees.

Finally, it is worthy of note that even though Topsat has a shorter effective baseline length than UoSat-12 (0.6m vs 0.65m) it could theoretically achieve a higher pointing accuracy because the measurement noise is lower (as shown in Chapter 3). The decrease in measurement noise is because the antennas on Topsat have an uncluttered view of the GPS constellation, whereas on UoSat-12 the antennas were surrounded by multiple other sensors which caused significant multipath, as demonstrated in [Wong, 2004].

6.1.1.1 ADOP for future GNSS attitude receiver

The accuracy of the GPS attitude solution on Topsat is limited by the coplanar baseline geometry and the ability of the SGR-20 to only track six satellites on each antenna when in its attitude configuration. Whilst it is likely that future small satellites employing GPS attitude sensors also use coplanar baselines due to their practicality, a future GNSS attitude receiver may be able to track up to twelve satellites on each antenna. To demonstrate the potential benefits of tracking all satellites in view a further numerical simulation was conducted. The results of this simulation are used to calculate the expected accuracy of the GPS attitude solution for a future GNSS attitude receiver. Again twenty-four satellites were simulated over a twenty-four hour period. The spacecraft remained nadir pointing throughout and an elevation mask of zero degrees was assumed.

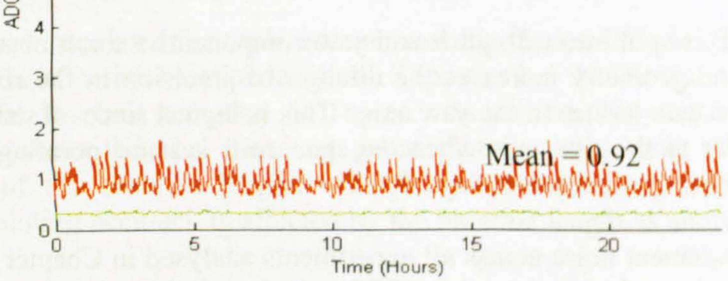

Figure 6-2 Simulated ADOP for future GNSS receiver tracking all GPS satellites in view

The mean ADOP for the Topsat baseline geometry when tracking all satellites in view is 0.92. As expected, increasing the number of satellites decreases the ADOP. Again the ADOP can be split in to roll, pitch and yaw components. The dilution of precision in each axis, assuming the spacecraft is nadir pointing, is shown in Table 6-2.

Table 6-2 Simulated ADOP split into roll, pitch and yaw components

Baseline Geometry	Mean Roll DOP	Mean Pitch DOP	Mean Yaw DOP
Triple Orthonormal (1m baselines)	0.33	0.32	0.34
Triple Orthonormal (0.607m baselines)	0.33	0.32	0.34
Topsat (0.607m effective baseline)	1.29	0.85	0.48

Using an effective baseline length of 0.6043 metres and a double-difference RMS measurement noise of 8.5mm the expected attitude error for a future GNSS attitude receiver tracking all GPS satellite in view and with the same baseline geometry as Topsat is 0.74 degrees. Performing the same calculation for the yaw alone indicates that the expected accuracy of the yaw estimate would be 0.39 degrees. This would make it comparable to the EHS's used on Topsat, which have an assumed accuracy of 0.3 degrees.

6.1.2 Effect of using ADCS attitude to estimate line bias on GPS-ADCS disparity

In Chapter 3 the GPS-ADCS disparity was derived as

$$\varepsilon_{i,j}[k] = \left\{\mathbf{e}_i^T \mathbf{A}[k] - \breve{\mathbf{b}}_{i(B)}^T \mathbf{A}[k]\left(\mathbf{\Delta}^\times + \boldsymbol{\delta}^\times[k]\right)\right\}\mathbf{s}_{i,j(O)}[k] + \beta_i^*[k] + w_{i,j}[k] \qquad \textbf{6-4}$$

In [Purivigraipong, 2000] the ADCS was used to estimate both the GPS integer ambiguities and the unknown line bias. The line bias is estimated as the mean disparity across all measurements on each baseline:

$$\hat{\beta}_i^*[k] = \frac{1}{J_i[k]}\sum_{j=1}^{J_i} \varepsilon_{i,j}[k] \qquad \textbf{6-5}$$

which from Equation 6-4 follows that

$$\hat{\beta}_i^*[k] = \frac{1}{J_i[k]}\sum_{j=1}^{J_i}\left(\left\{\mathbf{e}_i^T \overline{\mathbf{A}}[k] - \breve{\mathbf{b}}_{i(B)}^T\left(\mathbf{\Delta}^\times + \boldsymbol{\delta}^\times[k]\right)\right\}\mathbf{s}_{i,j(O)}[k] + \beta_i^*[k] + w_{i,j}[k]\right) \qquad \textbf{6-6}$$

which is actually the mean GPS-ADCS disparity. If the mean GPS-ADCS disparity is then used to 'correct' the GPS carrier phase measurements, we are essentially left with the ADCS attitude solution plus some noise from the GPS measurements. The integer ambiguities have zero variance (since they are a constant) and so do not affect the variance of the GPS-ADCS disparity.

The following simulation is used to demonstrate the effect of using the ADCS attitude solution to estimate the line bias and then correcting the GPS measurements using the ADCS estimated line bias. In this simulation the GPS accumulated carrier phase measurements are subject to an RMS measurement noise of 5.2mm and the ADCS attitude is free of errors. Two versions of the sLSE algorithm are used to estimate the attitude from the GPS measurements. The first version is a stand-alone version that estimates the line bias as part of the algorithm. The second version takes the ADCS line bias estimate as an input and uses this to correct the GPS measurements. The state vector in the second algorithm is therefore reduced in size since the line bias is not estimated.

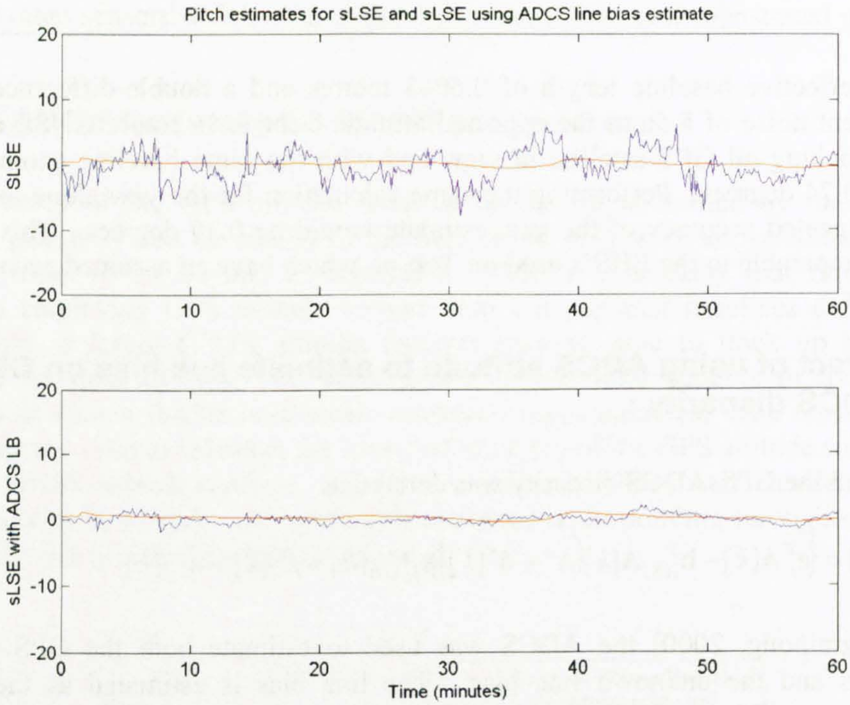

Figure 6-3 Comparison of pitch estimated by standard sLSE and sLSE using ADCS line bias estimate (estimated line bias in blue, true line-bias in red)

The results of this simulation are shown in Figure 6-3 and Table 6-3. It can be seen from these results that the stand-alone sLSE algorithm calculates an attitude estimate with a total RMS error of 4.1 degrees. The sLSE algorithm that is aided by the ADCS line bias estimate achieves an apparent total RMS error of 1.14 degrees, since as explained above the ADCS line bias estimate is actually an estimate of the mean disparity between the GPS and ADCS attitude solutions.

Table 6-3 Difference in RMS attitude error between stand-alone and aided sLSE algorithms

Algorithm	RMS Roll Error (deg)	RMS Pitch Error (deg)	RMS Yaw Error (deg)
sLSE (Stand-alone)	3.30	2.40	0.50
sLSE (ADCS Line Bias)	0.84	0.62	0.46

This leads to the problem that by using the ADCS to estimate the line bias any systematic offsets in the ADCS attitude solution will be imposed on the GPS attitude estimate, thereby removing the benefit of having a stand-alone three axis attitude sensor. This is demonstrated by the following simulation results, in which a constant offset of three degrees was added to the ADCS pitch.

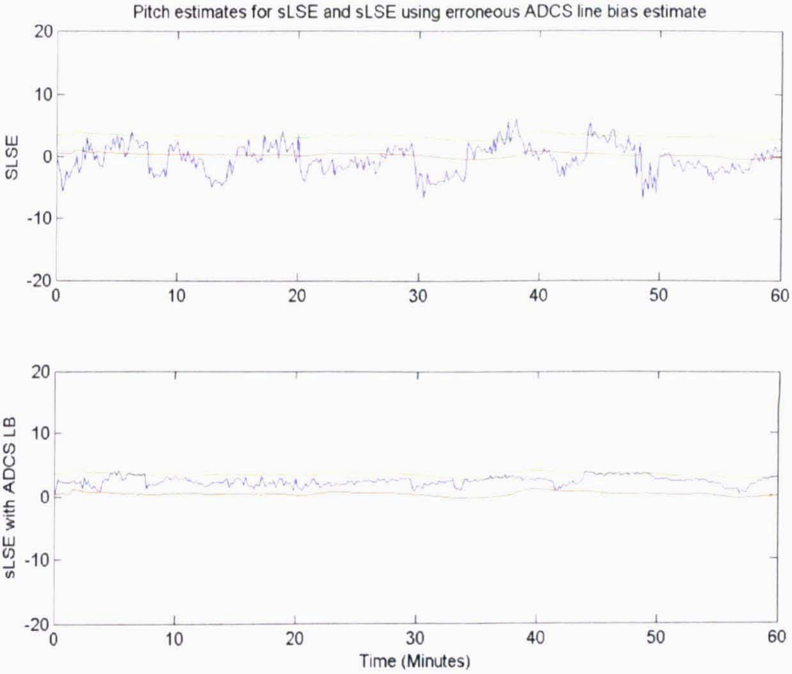

Figure 6-4 Comparison of pitch estimated by standard sLSE and sLSE using erroneous ADCS line bias estimate (estimated line bias in blue, true line-bias in red, erroneous line bias in yellow)

Table 6-4 Difference in RMS attitude disparity between stand-alone and aided sLSE algorithms (3° offset added to ADCS pitch)

Algorithm	RMS Roll Error (deg)	RMS Pitch Error (deg)	RMS Yaw Error (deg)
sLSE (Stand-alone)	3.74	4.10	0.50
sLSE (ADCS Line Bias)	0.85	1.05	0.46

As can be seen from the results in Table 6-4 and Figure 6-4 the simulated ADCS error results in an increase of three degrees in the RMS pitch disparity between the stand-alone GPS attitude estimate and the ADCS attitude as expected. However, for the GPS attitude estimate that utilises the ADCS line bias the increase in disparity is much less, with no change at all for roll and yaw, and only a 0.43 degree increase in pitch even though the true disparity has increased by three degrees. This demonstrates that using the ADCS to estimate line bias results in an overly optimistic estimate of the accuracy of the GPS attitude solution, which is affected by any systematic offsets present in the ADCS attitude estimate.

6.1.3 Effect of elevation mask on number of visible satellites

The SGR-20 uses its current position and knowledge of the GPS satellite positions to calculate which satellites are above the elevation mask in each epoch. These satellites are deemed 'visible' and can be assigned to idle channels by the channel allocation algorithm.

In order to determine the relationship between the elevation mask and the number of satellites visible a simulation was conducted in which a full day of constellation and simulated satellite motion was generated. The simulation assumed that there were twenty-four satellites in the GPS constellation. The simulation calculated the number of satellites visible above elevation masks ranging from -25 degrees (Earth Tangent) up to 30 degrees. The satellite visibility was calculated every minute for twenty-four hours of motion. The results from the simulation are presented in Figure 6-5.

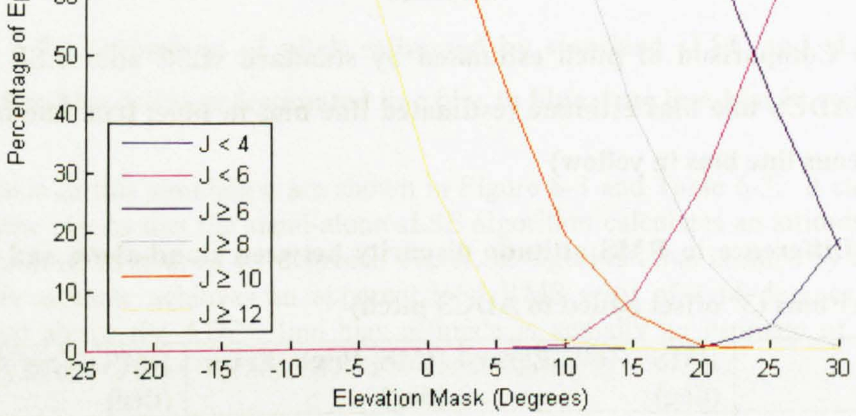

Figure 6-5 Effect of elevation mask on number of visible satellites

The plots in Figure 6-5 show the percentage of epochs in which fewer than four, fewer than six and at least six, eight, ten and twelve satellites were visible over the whole day (which is around fourteen orbits).

The elevation mask on the SGR-20 has a default value of zero degrees. For an elevation mask of zero degrees there are at least eight satellites visible all of the time and at least ten satellites visible in around eighty-five percent of epochs. If the elevation mask is set to ten degrees there should still be at least six satellites visible in every epoch. For elevation masks greater than ten degrees the percentage of epochs in which fewer than six satellites are visible begins to increase. For most of the experiments conducted on the SGR-20 on Topsat the elevation mask was left at its default value of zero degrees. The SGR-20 assigns six channels per antenna when in its attitude configuration and so the plots in Figure 6-5 show that the receiver should be able to track six satellites at all times, on all three baselines, assuming the spacecraft remains nadir pointing.

Many GPS users set the elevation mask to a value of five degrees or more in order to eliminate multipath caused by the GPS signals reflecting off surrounding structures. In the case of a microsatellite the only surrounding structure is that of the spacecraft itself. In the case of Topsat there are no potential reflectors within the 180 degree field-of-view of the GPS patch antennas, with the possible exception of the -Z facet. However, on UoSat-12 the GPS patch antennas were surrounded by other sensors and actuators which resulted in both a reduced field-of-view and significant multipath at each antenna. It is possible that setting the elevation mask to a value of at least fifteen degrees would have reduced the likelihood of multipath on UoSat-12, but the results of the visibility simulation above show that this would also result in the percentage of epochs in which at least six satellites are visible dropping to around ninety percent. This would have an impact on both the integer ambiguity resolution success rate and the achievable attitude accuracy as shown in previous sections.

6.2 Attitude estimation results from in-orbit data

The following section demonstrates GPS attitude determination using integrated carrier phase measurements and LOS vectors logged in-orbit.

In the following sections the integer ambiguity resolution algorithm described in Chapter 4 is used to calculate the integer ambiguities and an initial attitude estimate. The double-difference point solution algorithm described in Chapter 2 is then used to calculate the attitude in each epoch where there are sufficient measurements. By using a double-difference attitude estimator the problem of having to estimate the line bias is removed. As was shown in Chapter 3 there are some circumstances in which the line bias is poorly observed, resulting in a large error in the line bias estimates. This can make implementing look-up tables for the single-difference integer ambiguities difficult, since errors in the line bias estimate can lead to errors in calculating the integers for newly risen satellites. In this section the double-difference integers are 'tracked' using the method described in section 4.6.3. By using this method no limits are imposed on the permissible change in attitude between two epochs, which was a limitation of the method shown in [Ward, 1996].

6.2.1 Overview of experiment procedure

All the GPS attitude experiments on Topsat were conducted with the help of the ground operations team at SSTL. For each experiment the new SGR-20 flight code was copied into the RAM of the SGR-20 and executed. The earlier experiments involved new SGR-20 flight software capable of outputting integrated carrier phase measurements, but no real-time algorithms. From around March 2008 the flight software was updated to permit real-time in-orbit GPS attitude determination using a preliminary version of the new integer ambiguity resolution algorithm which did not contain the multi-epoch validation part of the algorithm. Once the new flight software has booted, the OBC commands the SGR-20 to output specified packets at set rates and configures the antennas and channels to permit carrier phase difference measurements to be taken. For the later real-time code the IAR and attitude algorithms were run automatically once enough measurements were available. The operation of the real-time code is detailed in the next chapter.

The SGR-20 would then output integrated carrier phase differences, LOS vectors and the PVT solution for the duration of the experiment. The data from the SGR-20 was logged in the SBPP format in the GPS binary file on the OBC. At midnight each day the GPS binary file was zipped and scheduled for download on the next available pass over the ground-station at SSTL.

6.2.2 Post-processing the SGR-20 log files for attitude determination

Once downloaded the GPS binary is processed in SGR-PC which converts the SBPP packet data into human-readable ASCII. A number of MATLAB scripts are used to extract the carrier phase difference measurements, LOS vectors and PVT solution from the relevant ASCII files.

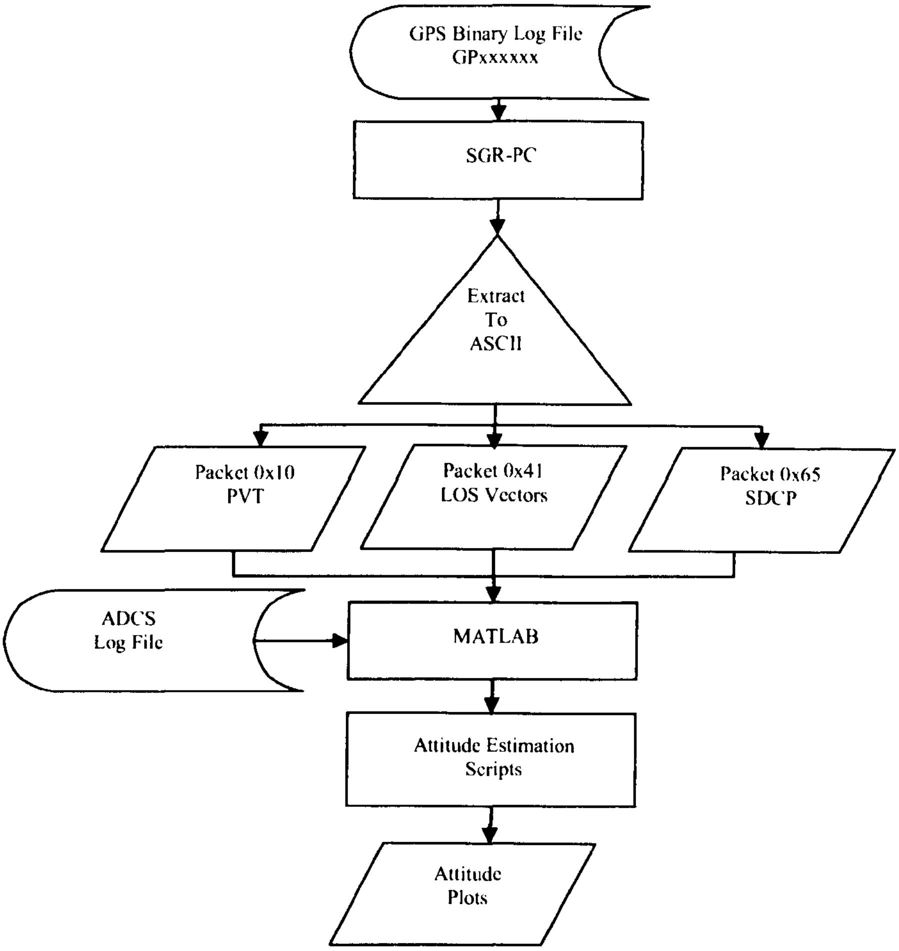

Figure 6-6 Overview of post-processing process

The SBPP packets used for attitude determination all contain timestamps to state when the data they contain was measured, but the data in the different packets is not latched to the carrier phase measurements, so the LOS vectors and PVT solution generally have different timestamps which must be aligned with the carrier phase measurements. The alignment of the timestamps is performed by taking the timestamp of each set of carrier phase difference measurements in Packet 0x65 and interpolating the LOS vectors and PVT solution to this time using MATLAB's built-in spline interpolation function. Once the data is synchronised the PVT solution is used to determine the transformation matrix to rotate the LOS vectors from WGS-84 to the orbit-referenced frame. This transformation is detailed in Appendix C.

For each epoch the data is used to form four matrices – the **r** matrix containing the carrier phase difference measurements, the **s** matrix containing the orbit-referenced LOS vectors; a matrix containing the SNR at each antenna and a matrix which stores which satellites were tracked in that epoch. These matrices are then used as inputs to the attitude estimation script which uses the double-difference attitude point solution described in section 2.3.3.4 to estimate the attitude.

The estimated attitude is compared with the ADCS QEKF reference attitude to calculate an attitude disparity, and the expected RMS attitude error in terms of roll, pitch and yaw is calculated using the method presented in section 2.3.4. Note that the noise covariance matrix **R** used to calculate the ADOP is based on a different σ_w for each baseline and the values of σ_w used in the remaining sections of this chapter were the RMS measurement noise estimates for each baseline for the respective experiments as were calculated in Chapter 3.

6.2.3 Experiment 1 – 27th February 2007

In this in-orbit experiment Topsat was commanded to perform a standard TDI = 2.2 imaging manoeuvre (see section 3.1), although no image was taken. This manoeuvre included a twenty degree pitch to align the imager with the target before Topsat was directly overhead, and then a slew in the pitch axis as Topsat passed over the target. Roll and yaw were both commanded to zero degrees. Whilst both EHS were functional during this experiment, the EHS measuring roll (known as DASH2) was not configured to be included in the ADCS attitude solution due an intermittent fault.

The results from this experiment are shown in Figure 6-7 to Figure 6-10 below. Figure 6-7 shows the GPS double-difference attitude solution is blue with the ADCS attitude solution shown in red for comparison. It is important to remember that the GPS attitude solution is a point solution, whereas the ADCS uses a Quaternion Extended Kalman filter to smooth the attitude estimate.

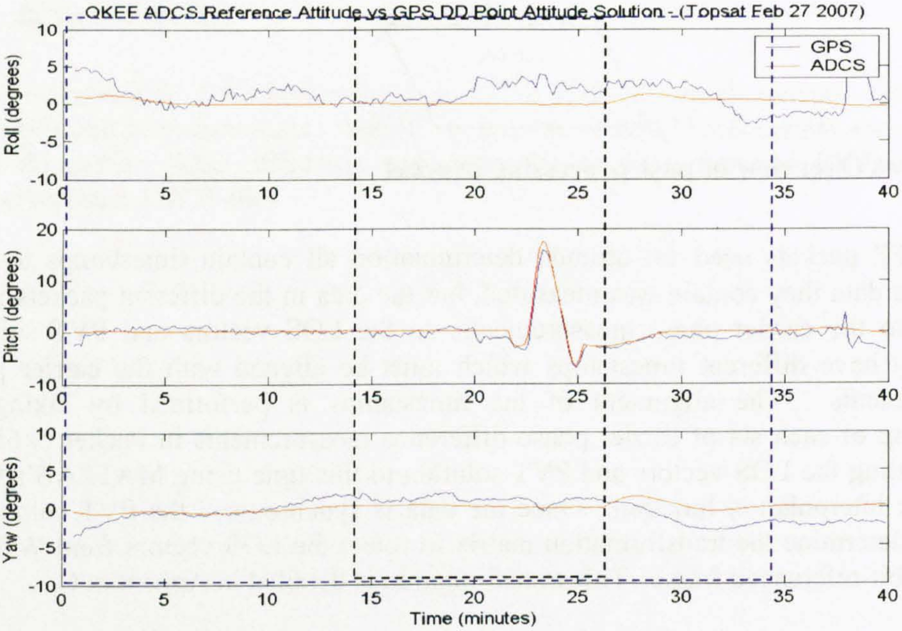

Figure 6-7 GPS double-difference attitude solution 27th February 2007

In the above plot the blue dashed box indicates when the pitch EHS was included in the ADCS attitude solution. The black-dashed box indicates when the ADCS was relying on the IMU to propagate the attitude solution, and the absolute measurements from the other attitude sensors were not used.

Figure 6-8 shows the attitude disparity, calculated by subtracting the ADCS attitude from the GPS attitude in each epoch. If the ADCS attitude was determined to be accurate enough this disparity could be used to judge the error in the GPS attitude solution. However, as discussed in Chapter 3, the ADCS may also suffer from systematic offsets and this must be acknowledged when making comparisons between the two attitude solutions. The black dashed lines indicate the 1 sigma expected GPS attitude accuracy based on the RMS measurement noise given in Table 3-7 and calculated according to the method presented in section 2.3.4.1.

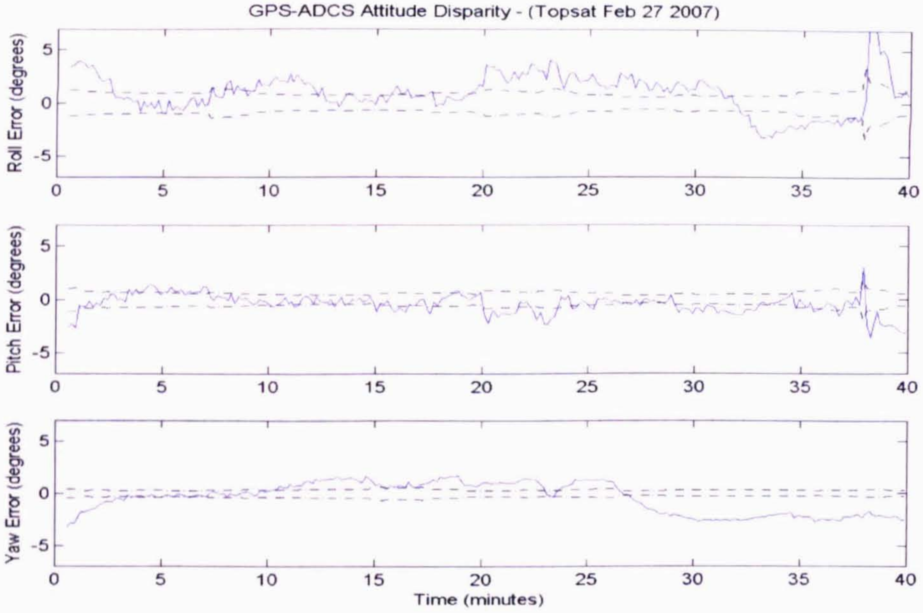

Figure 6-8 GPS-ADCS attitude disparity 27th February 2007

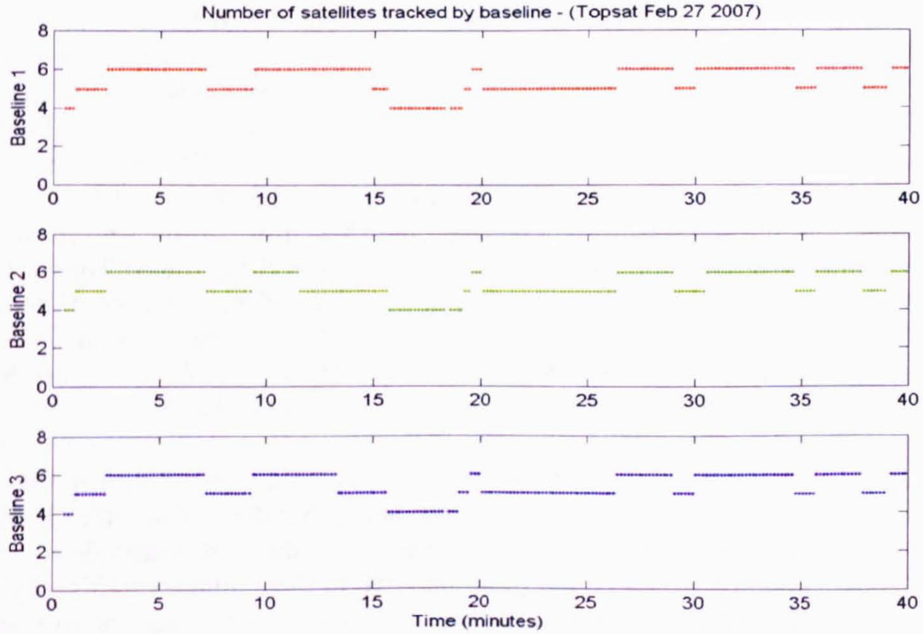

Figure 6-9 Number of satellites tracked on each baseline 27th February 2007

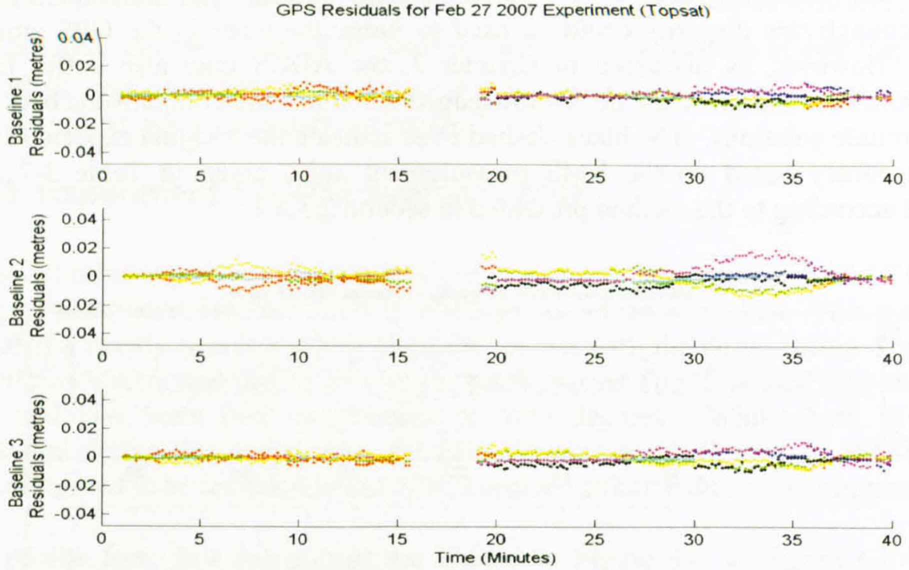

Figure 6-10 GPS residuals for 27th February 2007

The first point to note is that the GPS solution appears to initially disagree with the ADCS QEKF attitude solution by around five degrees in both roll and yaw. Over a period of just under five minutes the GPS solution appears to converge on the ADCS solution. It is unlikely that this is actually a GPS attitude error, since such an error suggests that there is some sort of warm-up process going on in the SGR-20. Whilst this may be true if we were using single-difference measurements (since we suspect the line bias is related to the temperature of the RF-front ends), we are using double-difference measurements to calculate the GPS attitude solution so any oscillator errors would be common to each satellite and so cancel out.

Most of the GPS attitude experiments on Topsat were scheduled to begin as the satellite moved from eclipse to the sun-lit region. Topsat has three sun-sensors mounted on the –Y facet, aligned in the +X, -Z and -X directions. As the spacecraft comes out of eclipse the sun-sensor aligned with the -X direction is the first to observe the Sun and produce measurements. Discussion with the ADCS engineers at SSTL indicated that the -X sun-sensor suffered from a mis-alignment which results in a discontinuity in the sun-sensor data between the -X sensor and the -Z sensor. Sun-sensor azimuth and elevation data is recorded in the ADCS log file on Topsat. Figure 6-11 shows the sun-sensor data for the first five minutes of the experiment. As can be seen from the plot there is a step of nearly five degrees at around 1.3 minutes into the experiment. Analysis of the ADCS log files shows that this coincides with the sun-sensor data switching from the -X sun-sensor to the –Z sun-sensor.

It is therefore assumed the apparent 'warm-up' effect is due to an error in the ADCS when using data from the –X sun-sensor. It is likely that the discontinuity in the sun-sensor data is smoothed out by the QEKF, resulting in the ADCS attitude converging on the correct solution over a period of around two to three minutes. This may be the cause of the GPS-ADCS disparity in Figure 6-8 converging to zero at five minutes into the experiment.

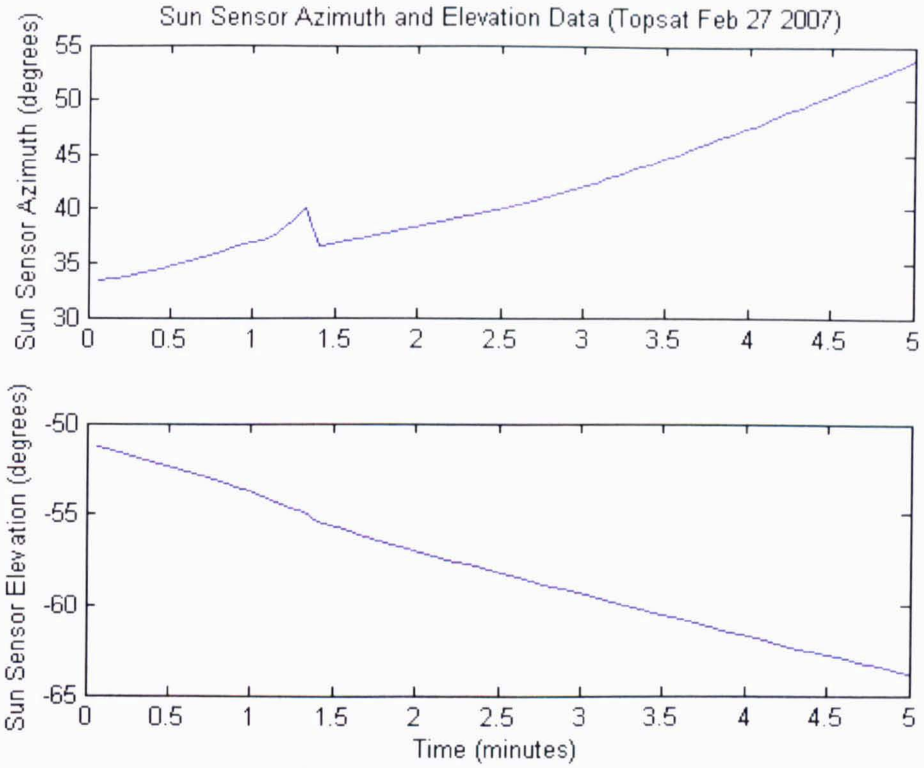

Figure 6-11 Sun-sensor Azimuth and Elevation data during first five minutes of experiment

Figure 6-8 shows a disparity in yaw between the GPS and ADCS attitude solution with a bias that changes sign at a number of points during the experiment. Yaw is the best axis in terms of GPS since all three baselines are coplanar on the –Z facet where the Z axis is the yaw axis. This is reflected in the tight error bounds on the yaw axis shown in Figure 6-8. At just after twenty-six minutes into the experiment the IMU is turned off and the QEKF attitude solution reverts to a combination of sun-sensors, magnetometers and the pitch EHS. At exactly this time there is an apparent control response, which is most obvious in the yaw axis, but also visible in the roll axis, which shows that the QEKF is moving to a new steady-state. The GPS yaw output undergoes a similar change in value as the ADCS yaw, but arrives at a yaw value around three degrees offset from the ADCS solution – an offset which is maintained for the rest of the experiment. From Figure 6-8 it can be seen that the GPS-ADCS pitch-disparity lies within the 1-sigma bounds (of around 1 degree) for most of the experiment, but the roll and yaw disparities do not generally lie within their respective 1-sigma bounds. The ADCS pitch estimate should have been the most accurate axis (since it is measured by DASH 1 which was functional) during this experiment. Since this axis demonstrates good agreement with the GPS pitch estimate, which lies within the estimated 1-sigma bounds, it is reasonable to assume that the GPS yaw estimate, whose 1-sigma bounds for suggest an uncertainty in yaw of around 0.3 degrees, may in fact be correct and it is the ADCS yaw estimate that is in error during this period.

Table 6-5 Attitude disparity for 27/02/07 experiment

Roll Disparity (degrees)	Pitch Disparity (degrees)	Yaw Disparity (degrees)
2.10	1.01	1.52

The RMS GPS-ADCS disparity shows that the GPS pitch estimate is in agreement with the ADCS pitch estimate, and this is reflected in the GPS-ADCS pitch disparity having close to zero mean and generally lying within the 1-sigma bounds in Figure 6-8. The GPS residuals shown in Figure 6-10 show that there is little multipath on baseline 1 (which nominally measures pitch), but baseline 2 appears to suffer from multipath throughout the experiment, with the worst error occurring between thirty and thirty-seven minutes into the experiment. This multipath error may be contributing to the increased disparity in roll during this period, or it may be due to the ADCS error in yaw coupling into the roll estimate.

From the first epoch in which GPS integrated carrier phase measurements are available it takes the SGR-20 around 2.5 minutes to acquire and allocate six satellites on all three baselines. This highlights a potential issue with the IAR algorithm in that we cannot attempt integer ambiguity resolution until at least five satellites are tracked on each baseline and preferably should wait until six satellites are tracked on each baseline. Therefore in the real-time implementation it would be wise to only start the IAR algorithm when six satellites are available on each baseline, and if not then wait.

The number of satellites tracked varies between four and six throughout the experiment. This shows that the SGR-20 successfully maintains its position fix whilst in attitude determination mode. For this experiment the elevation mask was set to zero degrees (with respect to local horizontal) and therefore it is a slight concern that in some cases the SGR-20 only tracks four satellites for a period of up to five minutes. By examining the GPS Status packet (packet 0x30) it is possible to see how many satellites the receiver calculated were visible at each epoch.

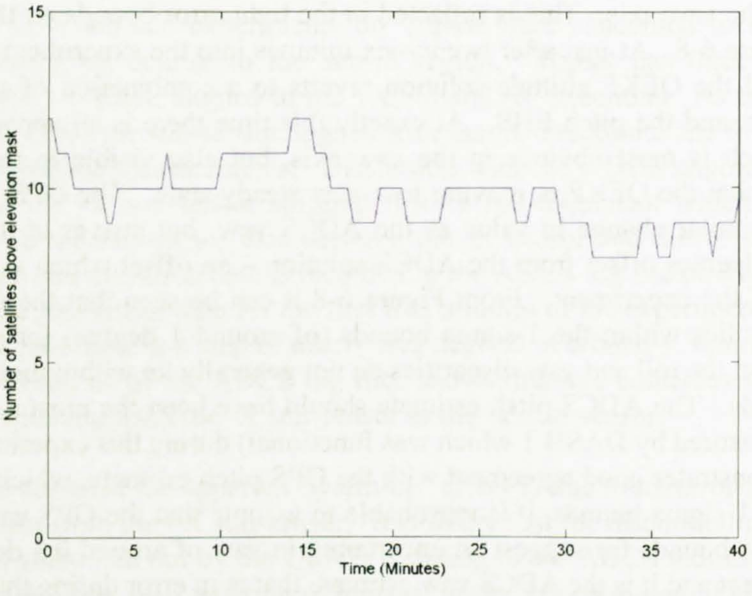

Figure 6-12 Number of satellites above elevation mask throughout 27th February 2007 experiment

The plot in Figure 6-12 shows the number of satellites above the elevation mask was at least eight throughout the experiment. This indicates that the satellite acquisition code on the SGR-20 is not operating as efficiently as it might, since there are many periods where the number of satellites tracked on each baseline drops below six. Judging from Figure 6-12 and the numerical simulation in section 6.1.3 there should have been no problem maintaining six satellites on each baseline. Analysis of the GPS log file indicates that the problem was caused by the master antenna successfully maintaining lock on six satellites for much of the experiment, but the slave antennas losing satellites mostly as they set out of view of the slave antennas. The SGR-20 code is supposed to monitor when a satellite is lost from a slave antenna and if other satellites are in view it should force the acquisition of a new satellite on the master antenna. This in turn should result in the new satellite being assigned to the now idle slave channels, thereby increasing the number of measurements on each baseline back towards six. These results suggest this code is not functioning as intended and needs to be improved to get the best performance.

From Figure 6-9 we can see that all three baselines do not track the same number of satellites throughout. The number of satellites tracked follows a similar pattern on all three baselines but there are occasions when one baseline appears to lose a satellite a minute or two before the others. In some cases, such as at around twenty minutes into the experiment, there appears to be a correlation between a change in the number of satellites tracked and a step in the GPS-ADCS disparity. This is likely due to multipath error on particular satellites which are either being added to or removed from the GPS attitude calculations, resulting in a changing bias due to multipath error in the GPS attitude solution.

6.2.4 Experiment 2 – 1st May 2007

In this experiment Topsat conducted a TDI = 2.2 pitch manoeuvre (see section 3.1) with a thirty degree off-pointing in roll. Again only the pitch EHS is functional. It is important to note that even when functional the EHS could not track the thirty degree off-pointing in roll since it has a field of view of +/- 2.5 degrees and therefore the ADCS attitude solution has to rely solely on measurements from the IMU to propagate the most recent absolute attitude measurement throughout this manoeuvre. A comparison of the GPS double-difference point attitude solution and the ADCS QEKF attitude solution is given in Figure 6-13 below.

Figure 6-13 shows that the GPS attitude solution successfully tracked both the large angle pitch manoeuvre and the large off-pointing in roll. Figure 6-14 shows the GPS-ADCS disparity. There is a variation in the disparity between the GPS and ADCS attitude solutions throughout the experiment, with the variation in roll having the largest peak-to-peak amplitude. As with the 27th February 2007 experiment the GPS-ADCS disparity at the beginning of the experiment suggests a possible warm-up effect in the GPS attitude solution. As discussed in the previous section, since double-difference measurements are used any warm-up effects in the SGR-20 should cancel out.

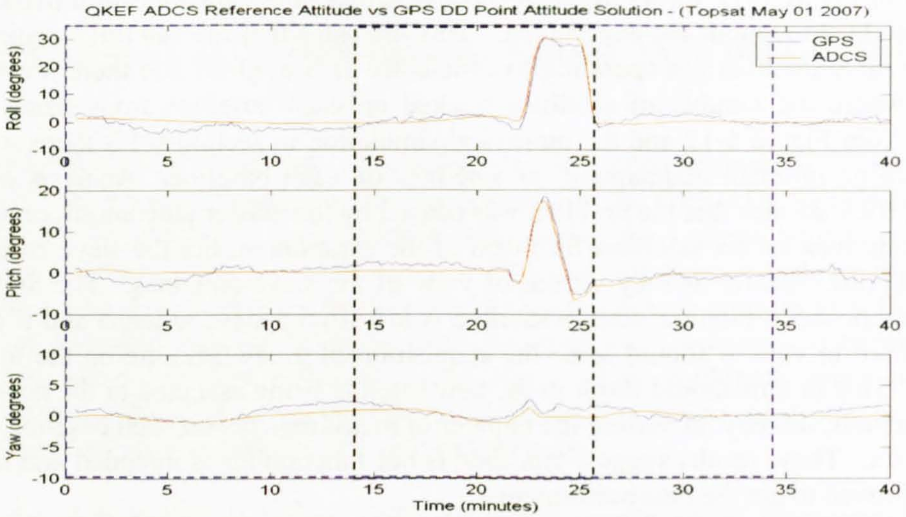

Figure 6-13 GPS double-difference attitude 1st May 2007

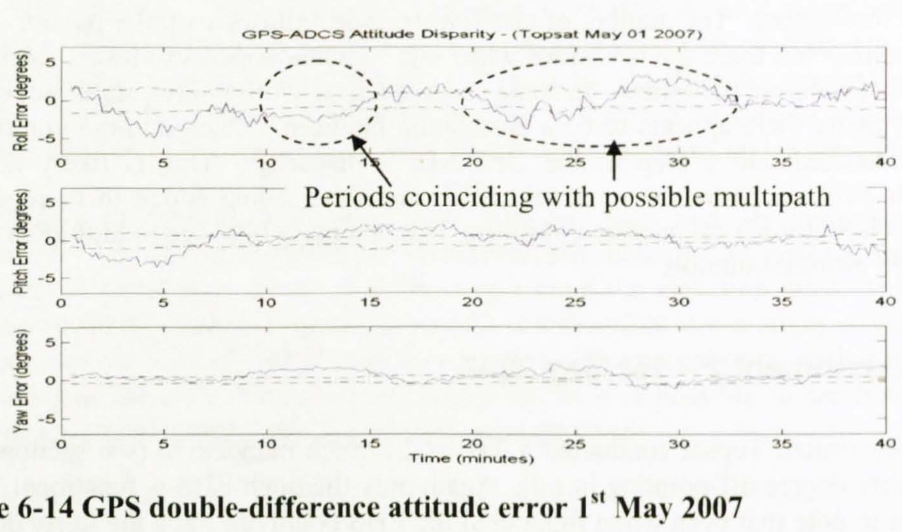

Figure 6-14 GPS double-difference attitude error 1st May 2007

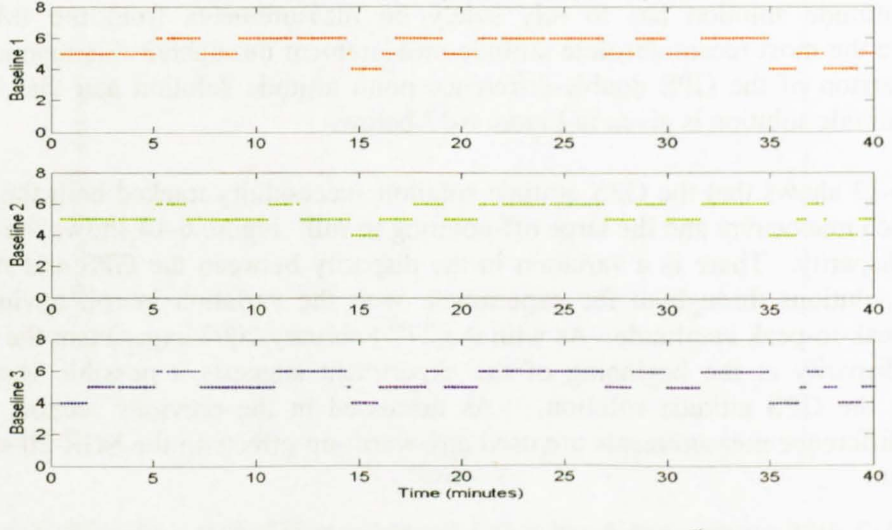

Figure 6-15 Number of satellites tracked on each baseline 1st May 2007

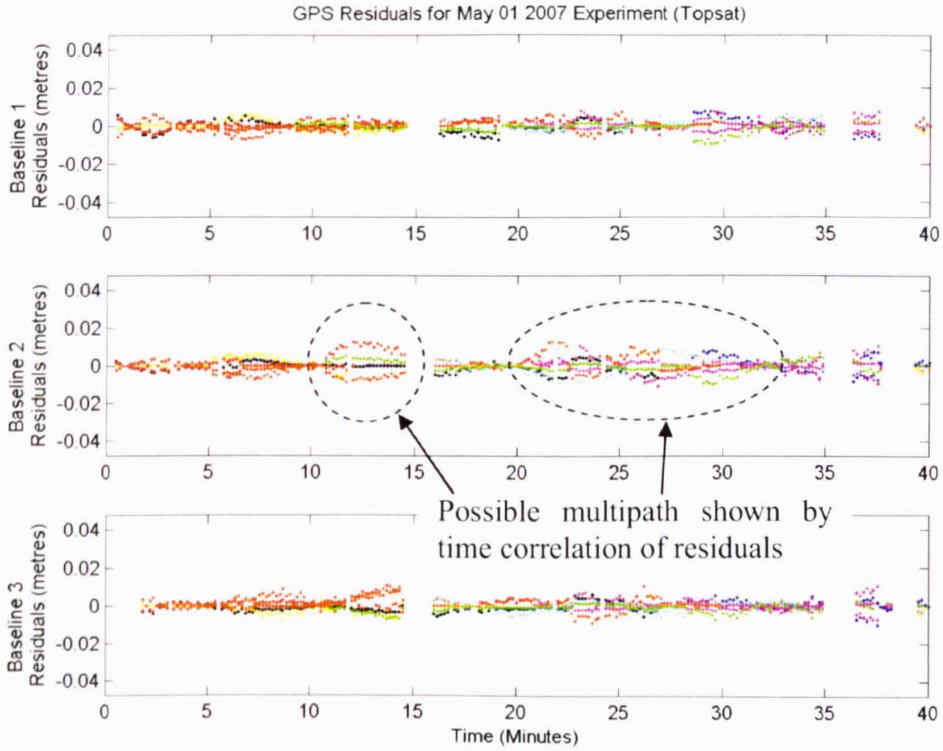

Possible multipath shown by time correlation of residuals

Figure 6-16 GPS residuals for May 1st 2007 Experiment

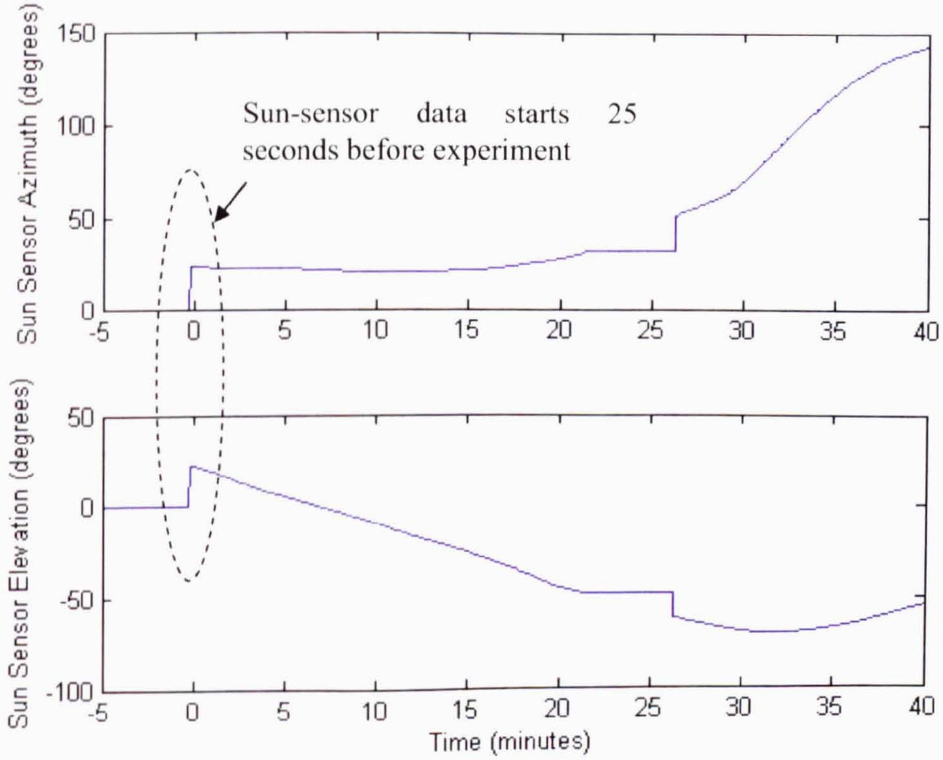

Sun-sensor data starts 25 seconds before experiment

Figure 6-17 Sun-sensor Azimuth and Elevation data, with start of data highlighted

As was the case with the 27th February 2007 experiment, in this experiment the GPS attitude experiment was also commanded to start as Topsat moved from eclipse into the sun-lit region. Analysis of the ADCS log file showed that the sun-sensors only began taking measurements about twenty-five seconds before the GPS attitude experiment started. This was due to the -X sun-sensor not having LOS with the Sun until this time. This means that the ADCS would have been estimating the attitude solely based on magnetometer measurements. The GPS-ADCS disparity within the first five to eight minutes of the experiment may therefore be due to the ADCS attitude converging on a more accurate solution as the sun-sensor data becomes available. The possible misalignment of the –X sun-sensor (which is the first to provide data) may also have contributed to the GPS-ADCS disparity by causing an error in the ADCS attitude.

The roll disparity between the GPS and ADCS varies by more than five degrees at various points during the experiment. Whilst the time correlation of the GPS residuals in Figure 6-16 suggests possible multipath error on baseline 2 the same periods for baseline 3 show minimal multipath error. Also, the self-consistency of the roll disparity over short periods appears to lie within the 1 sigma bounds in Figure 6-14. This suggests that the variations in the roll disparity may be due to systematic errors in the ADCS roll estimate. As mentioned previously the EHS that measures roll ('DASH2') was not used by the ADCS during this experiment, and so the ADCS QEKF attitude solution was mainly relying on sun-sensor measurements to estimate roll. Figure 6-18 shows the raw sun-sensor elevation data from the ADCS log file during the GPS attitude experiment. The sun-sensors have two axes, which each provide two analogue voltage signals known as A and B. The raw sun-sensor elevation data is the ratio A/A+B for one of the two axes. The data from both axes is normally calibrated using a polynomial to obtain the sun angle.

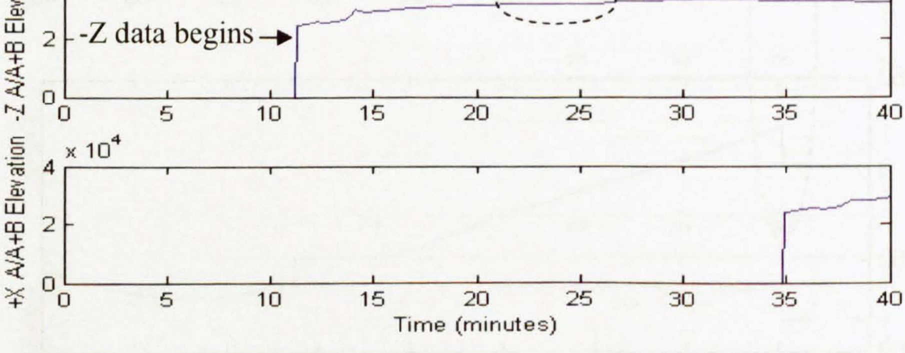

Figure 6-18 Raw sun-sensor elevation data 1st May 2007

The main point to note from Figure 6-18 is the cross-over between the data from each sun-sensor. The point at which the –Z sun-sensor begins producing data coincides with the GPS-ADCS disparity reducing from minus two degrees to zero degrees. Also the point at which the –X sun-sensor stops producing data coincides with the GPS-ADCS disparity reducing from three degrees to zero degrees. It is therefore possible that the sun-sensors are causing the increased disparity in roll rather than multipath errors in the GPS measurements.

Table 6-6 RMS GPS-ADCS disparity 1st May 2007

Roll Disparity (degrees)	Pitch Disparity (degrees)	Yaw Disparity (degrees)
1.89	1.35	0.87

6.2.5 Experiment 3 - 4th July 2007

This experiment provides another example of Topsat performing a TDI=2.2 imaging manoeuvre (see section 3.1). Both EHS were functional but again because of the intermittent fault on DASH2 it was not included in the ADCS attitude solution. A comparison of the GPS double-difference attitude solution with the ADCS QEKF attitude solution is shown in Figure 6-19. Again the blue dashed lines indicate when the EHS was used in the ADCS, and the black dashed box indicates when the ADCS attitude solution was propagated using the IMU (i.e. no absolute attitude measurements were used by the ADCS).

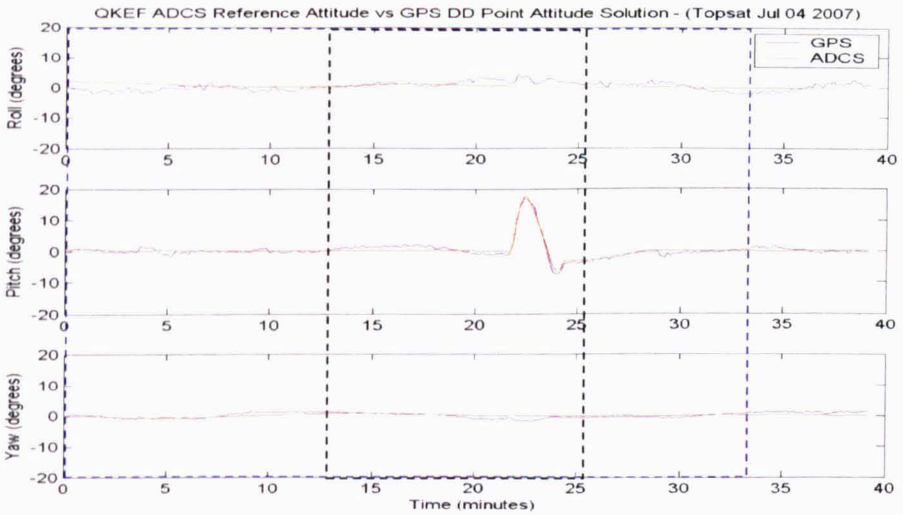

Figure 6-19 GPS double-difference attitude solution 4th July 2007

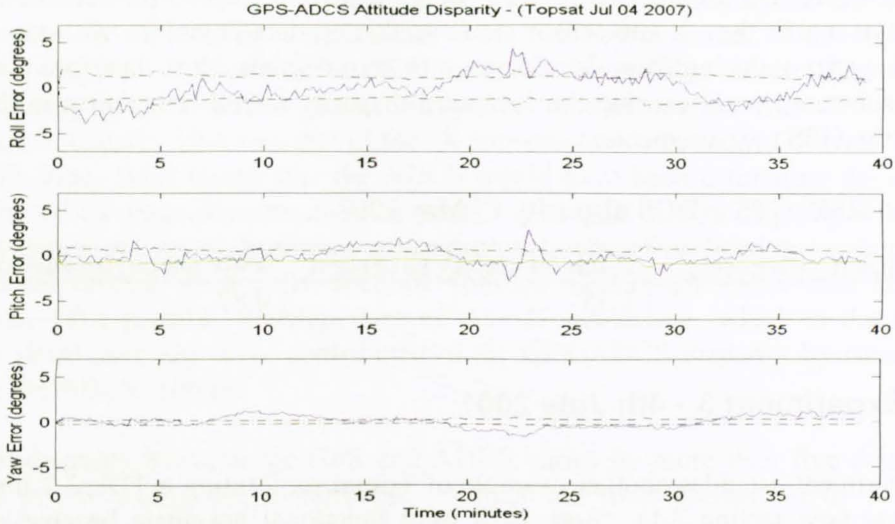

Figure 6-20 GPS-ADCS attitude disparity 4th July 2007

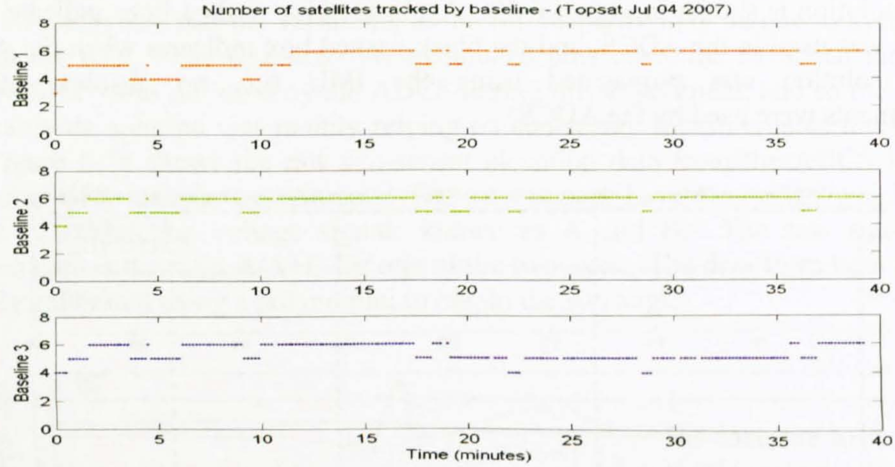

Figure 6-21 Number of satellites tracked on each baseline 4th July 2007

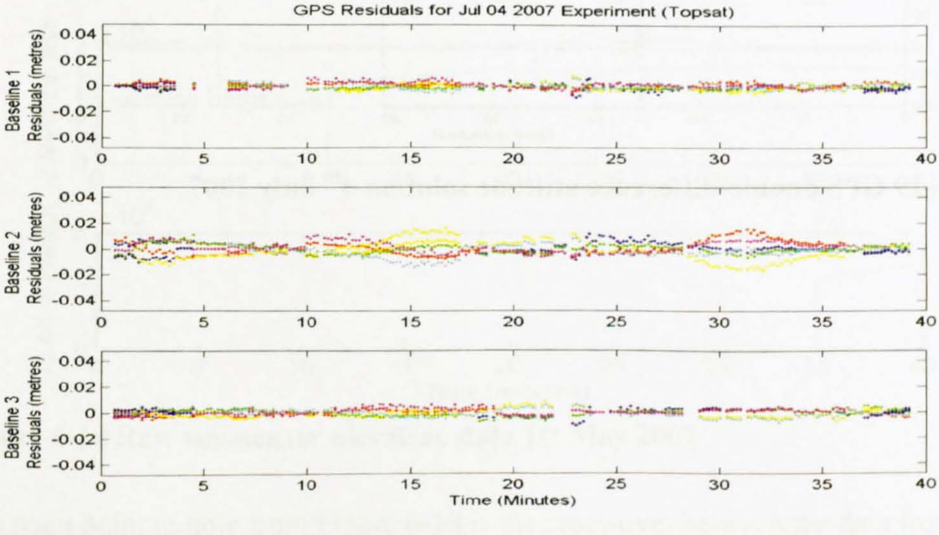

Figure 6-22 GPS residuals for July 4th 2007

Table 6-7 RMS GPS-ADCS disparity 4th July 2007

Roll Disparity (degrees)	Pitch Disparity (degrees)	Yaw Disparity (degrees)
1.54	0.79	0.65

The GPS-ADCS roll disparity is similar in magnitude to that observed in the 27th February and 1st May experiments. The roll disparity reduces from around minus four degrees to zero degrees over the first five minutes of the experiment. Again Table 4-7 in Chapter 3 shows that all three experiments had a similar level of measurement noise on baseline 3 which nominally measures roll, so it is unlikely that the GPS measurements the cause of the disparity. This effect is again likely due to the sun-sensors only producing data around two minutes before the experiment began, and the ADCS attitude solution changing as the sun-sensor data becomes available.

The GPS attitude solution performs well throughout this experiment, with the RMS GPS-ADCS disparity being sub-degree in both the pitch and yaw axes. For this experiment the GPS elevation mask was increased from zero degrees (as used in the previous experiments) to ten degrees. Judging from the RMS measurement noise for each baseline given in Table 4-7 in Chapter 3 this resulted in a decrease in the RMS measurement noise on baseline 1, which may account for the decrease in pitch disparity shown in Table 6-7.

The change in elevation mask does not appear to have had any significant effect on the RMS measurement noise of baselines 2 and 3. The original intention behind increasing the elevation mask was to attempt to remove some of the multipath error which it was assumed would be more common on lower elevation satellites. The evidence for this having any effect is inconclusive, since the decrease in GPS-ADCS disparity could be due to the changed elevation mask or due to decreased systematic error in the ADCS attitude solution. To properly determine if there was any benefit (with respect to reducing multipath) in changing the elevation mask it would be necessary to log many hours worth of data at each elevation mask setting in order to get good sky coverage at each setting and hence enough data for a proper comparison.

6.3 Conclusions

In this chapter a study on a number of GPS attitude performance factors was presented. The concept of ADOP was used to demonstrate the effect that the coplanar baseline geometry on Topsat has on the achievable attitude accuracy. A numerical simulation was used to compare the coplanar baseline geometry of Topsat with the ideal case of triple orthonormal baselines. The results of this simulation showed that the ADOP increased by almost a factor of four when coplanar baselines are used. From this a conclusion could be made that future platforms carrying a GPS attitude sensor should use triple orthonormal baselines. However, there are practicality issues with implementing triple orthonormal baselines on a small satellite, as it would require one of the patch antennas to be mounted on a boom above the facet. This boom would add extra mass, and would potentially shadow the other patch antennas causing signal outages and multipath. Implementing coplanar baselines is simpler, since all patch antennas can be mounted on the same facet.

The study of ADOP also highlighted that one of the factors limiting the accuracy of the GPS attitude solution on Topsat is that the SGR-20 can only track up to six satellites on each baseline when in its attitude configuration. A future GNSS attitude receiver should be able to track all satellites in view. To determine the effect this would have on the accuracy of the attitude estimate from such a receiver the numerical simulation of ADOP was re-run assuming up to twelve satellites could be tracked on each baseline. The results of this simulation showed that a future GNSS attitude receiver, even with coplanar baselines, could achieve an overall attitude accuracy of 0.74 degrees, with the yaw estimate accurate to 0.39 degrees. This is assuming the same level of measurement noise as Topsat, without any form of multipath mitigation, i.e. with no extra effort required. This would be achievable using only the GPS constellation, and could be improved further if more channels and more GNSS satellites are available.

The second performance factor studied was the problem using the ADCS attitude to estimate line bias. It was demonstrated that by using the ADCS to estimate the line bias it is actually the mean GPS-ADCS disparity that is being calculated and this results in both an overly optimistic assessment of the performance of the GPS attitude solution and can also hide potential systematic errors in the ADCS attitude solution, thereby removing much of the benefit of GPS as a stand-alone three-axis attitude sensor.

The third performance factor studied was the effect of using an elevation mask to remove low elevation satellites. A numerical simulation was used to demonstrate that an elevation mask of twenty degrees or less should result in one hundred percent availability of the GPS attitude solution. However, a lower elevation mask would be preferable in order to provide a more accurate attitude solution.

In the second half of the chapter in-orbit data logged on Topsat was used to study the performance of the double-difference attitude point solution algorithm. Data sets from three experiments were chosen as examples. All data sets included large off-pointings in pitch, with the 1st May experiment also incorporating a thirty degree off-point in roll. The post-processed results showed that the attitude point solution algorithm could successfully track the attitude throughout these large angle manoeuvres.

The post-processed GPS attitude solution was compared with the ADCS reference attitude for each experiment. The GPS and ADCS typically agreed to around two degrees, but as was discussed in Chapter 3, it is difficult to determine whether the GPS attitude solution is actually in error by comparing it with the ADCS since the ADCS may be subject to systematic offsets. An example of this is the apparent 'warm-up' effect seen at the start of each experiment. In the first five minutes of each experiment the GPS-ADCS disparity tends to decrease from around five degrees to less than one degree. Analysis of the ADCS log files suggests that this is an ADCS issue caused by the fact that each experiment started just as the satellite moved from eclipse into sunlight, which meant that the ADCS was previously using magnetometer data to propagate the attitude solution resulting in greater attitude error. A misalignment of the –X sun-sensor which is typically in use during the first five minutes of each experiment may also have contributed to the disparity.

Post-processing the in-orbit data demonstrated that the SGR-20 can sometimes struggle to track more than four satellites on each baseline whilst in its attitude configuration. Analysis of the data packets from the SGR-20 showed that there were typically at least eight satellites in view throughout the experiment, and therefore the low number of satellites tracked was attributed to issues with the satellite allocation routines on the SGR-20. Further improvements to the SGR-20 flight software should result in improved satellite allocation and hence improved attitude accuracy and availability.

7 Real-time in-orbit GPS attitude determination

This chapter describes the demonstration of real-time GPS attitude determination using the SGR-20 on the Topsat microsatellite in Low Earth Orbit.

Firstly, details of modifications made to the SGR-20 flight software to support real-time GPS attitude determination are provided. The method used for testing and verification of this new flight software is described. This testing included development of a hardware-in-the-loop simulation using MATLAB and outdoor testing using a mock satellite to verify the real-time operation of the modified receiver code.

Finally, the results from a number of in-orbit experiments demonstrating real-time stand-alone GPS attitude determination are given. The real-time GPS attitude solution is compared with the ADCS to provide an indication of the accuracy. These results are analysed to determine possible performance issues with the real-time implementation and to look at the various external factors affecting the GPS attitude solution.

7.1 Overview of SGR-20 software

The SGR-20 is based on the GEC Plessey 'GPS Architect' board, albeit highly modified to provide simultaneous measurements from four antennas for GPS attitude determination. The SGR-20 flight software operates under a task-switching operating system to provide a concurrent structure of operations which lends itself to the requirements of GPS signal processing and software.

The task-switched operating system consists of interrupt and task driven routines and only one task can be active at any time. The main interrupt is provided by one of the GP2021 correlators and is serviced by an Interrupt Service Routine which accumulates data from the correlators and closes the signal tracking loops. An overview of the task structure that forms the basis for the SGR-20 code can be found in [Zarlink, 1998].

7.2 Software modifications

This section describes the work undertaken to implement the algorithms described in Chapters 2 and 4 in the flight software of the SGR-20 GPS receiver. This allowed the code to be tested using live measurements both on the ground and in-orbit. The implementation was conducted in a number of stages, starting with porting the MATLAB algorithms to C and finishing with an experimental version of flight software suitable for in-orbit testing.

7.2.1 Porting of MATLAB algorithms to C

The first stage involved porting the integer ambiguity resolution and double-difference point solution attitude tracking MATLAB algorithms into C; the language used for the SGR-20 flight software.
The engineering model SGR-20 used for development during this research does not have any dedicated debug interface. The only method of observing how the software functions in real time is the data output in the SBPP packets. Therefore to allow debugging, the C functions used to construct the new flight software were compiled as a dynamic-link-library using the MATLAB MEX compiler so that they could be called from MATLAB. The algorithms were tested by using the MATLAB based simulator (see Appendix A) to input the same data in to both the original MATLAB scripts and the new C based versions of the same algorithms. The performance of the C based algorithms was confirmed by directly comparing the results of the new algorithms with their MATLAB equivalents to ensure they were identical.

Testing the ported C code in this way minimised the time spent debugging coding errors such as memory leaks and uninitialized variables. By running the code via the MEX wrapper, test data from the MATLAB based simulator could be fed into the C code and an inline debugger could be used to step through the code to detect any errors or memory leaks.

7.2.2 Modification of SGR-20 flight software

Once debugged using MATLAB the C code was integrated into the SGR-20 flight software. Additional commands were added to allow for configuration and control of the attitude determination functions and new SBPP packets were defined to display the output. These changes are described in more detail in Appendix E. As part of the implementation of the real-time GPS attitude determination algorithms changes were made to the following files:

- **TakeMeas.c** – New structures used to store accumulated carrier phase data. Changes made to initialisation and clearing of structures to improve measurements.
- **Display.c** – added packets 0x65 and 0x66 to permit logging of raw GPS accumulated carrier phase measurements and output of the status of the attitude determination algorithms, respectively.
- **Attitude.c** – Implemented new code to construct data structures for input to integer ambiguity resolution and attitude tracking algorithms. Implemented real time code for integer ambiguity resolution and attitude tracking.
- **Allocate.c** – Made changes to allocation of satellites to slave channels to improve number of available measurements on each baseline.

7.2.2.1 Attitude Software Design

The main effort in the implementation of the real-time attitude determination code involved the changes made to Attitude.c which contains all code for the attitude task. This task contains the significant functions for collating the measurements as well as the integer ambiguity resolution and the attitude tracking algorithms.
The first part of the attitude determination code is a function called 'merge_attitude_variables'. This function is called once a second from the attitude task and is used to collate the accumulated carrier phase difference measurements and LOS vectors for each baseline into a single data structure. This data structure also contains information on which satellites are currently being tracked. The function loops through all channels that are currently tracking a satellite and calculates accumulated carrier phase differences for each satellite common to both antennas on each baseline.

It then checks if a LOS vector is available for each satellite. This relies upon the broadcast ephemeris having been downloaded and the SGR-20 having calculated a recent position estimate. If the LOS vector is available it is rotated into the orbit-referenced frame, using the procedure described in Appendix C, and stored in the data structure. This process is repeated every second. If in any one epoch there are six satellites tracked on all three baselines the integer ambiguity resolution algorithm is started. The minimum requirement of six satellites was hard-coded in order to make the real-time implementation as robust as possible. This simplified the debugging and analysis of the results.

The integer ambiguity resolution algorithm implemented in the SGR-20 flight software differs slightly from the algorithm described in Chapter 4. Due to the amount of time required to implement the new flight software only Parts I to III of the integer ambiguity resolution algorithm were implemented. This meant that the integer ambiguity resolution algorithm is only considering a single epoch of data.

When the integer ambiguity resolution algorithm identifies a unique solution it sets a flag to indicate that the attitude tracking algorithm can begin. The integer ambiguity resolution algorithm provides an initial attitude estimate. This is used to initialise the attitude tracking code based on the double-difference point solution algorithm described in section 2.3.3.4. In the current implementation the attitude tracking code will run continuously unless there are fewer than four measurements available on any baseline for a given epoch, in which case a flag is set that tells the receiver to run the integer ambiguity resolution algorithm again when possible. An overview of the overall attitude determination algorithm is shown in Figure 7-1 below.

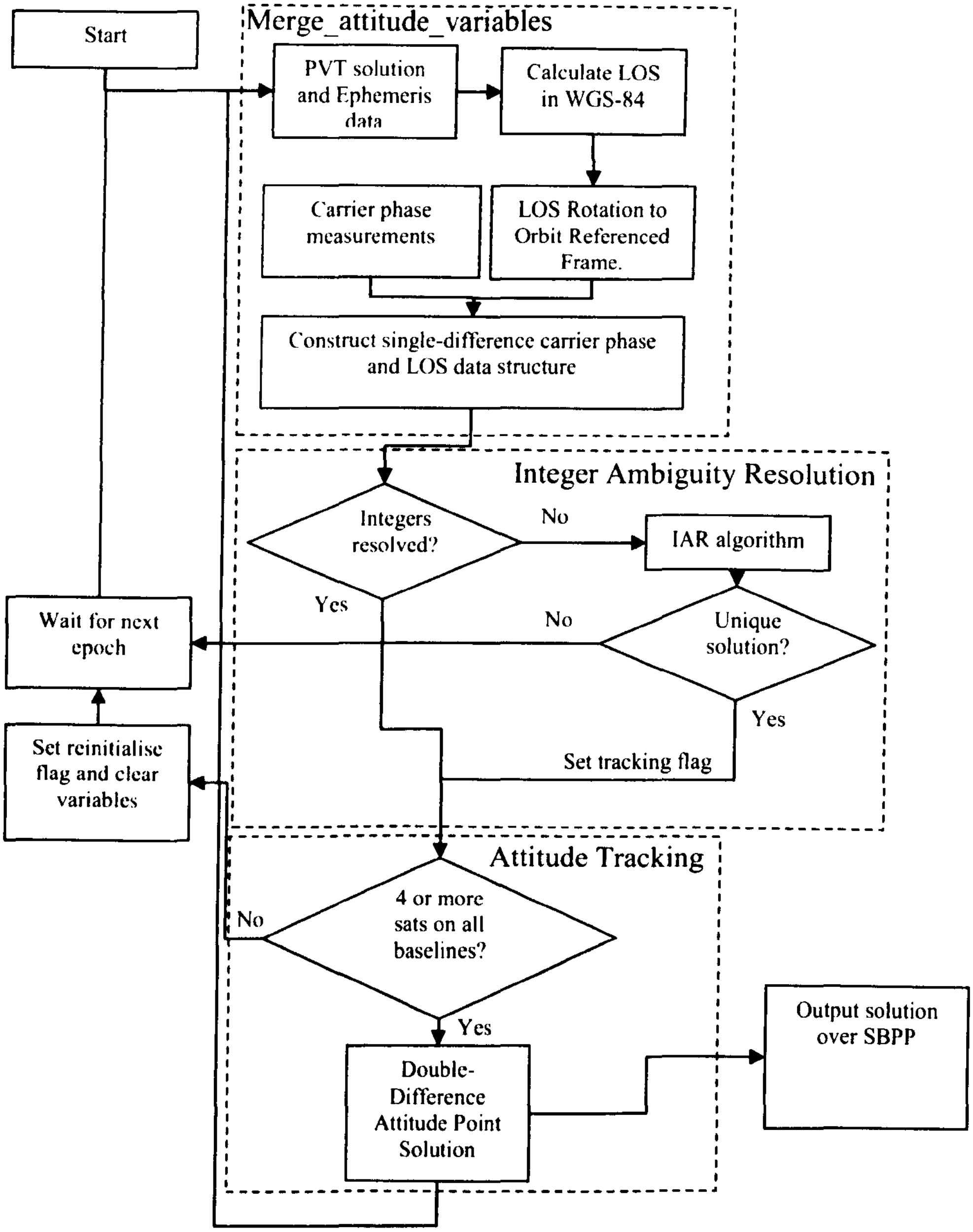

Figure 7-1 Overview of GPS attitude determination algorithm

7.2.3 Hardware-in-the-loop simulation

Since the author did not have access to a four RF-port GPS simulator MATLAB was used, running on a host PC, to generate simulated test data that was passed to the SGR-20 via the RS-232 port for processing. The SGR-20 code was modified to process this test data in the same way it would process real measurements. It would then output the results back to the host PC for validation in MATLAB. This effectively provided a 'hardware-in-the-loop' simulation by using the modified software running in real-time onboard the SGR-20 to produce a simulated 'stand-alone' GPS attitude solution. The hardware-in-the-loop simulation also permitted the playback of data logged in orbit on the SGR-20.

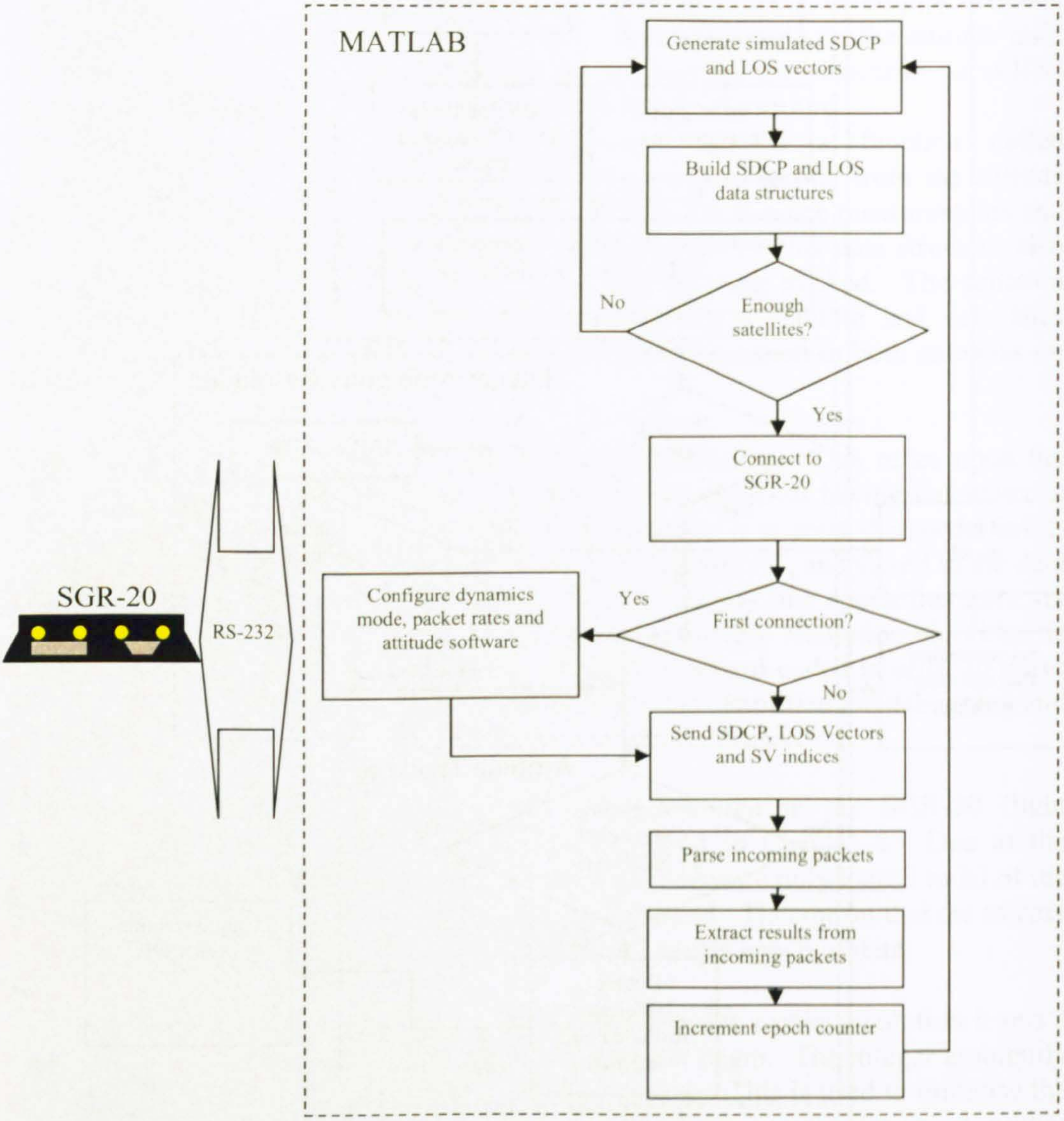

Figure 7-2 Overview of Hardware-in-the-loop test using simulated data

The hardware-in-the-loop simulation runs in real-time, with the simulator sending a new set of data every ten seconds, and the receiver calculating and returning the answer, generally within five seconds.

The returned data contains both the estimated integer ambiguities (double-difference only) and the estimated attitude solution (roll, pitch and yaw). The returned data is compared with the truth solution generated by the simulation, and is used to establish the performance of the integer ambiguity resolution algorithm and the accuracy of the attitude solution.

As part of the testing, the hardware-in-the-loop simulation was used to simulate carrier phase measurements subject to 6mm RMS measurement noise on each baseline. An example plot showing the results of the simulation is shown in Figure

7-3. The blue lines show the GPS attitude estimated by the SGR-20. The red lines show the simulation truth attitude based on the ADCS attitude data logged on Topsat from 27th February 2007. The results of this simulation demonstrated that the new algorithms implemented in the modified receiver code were operating correctly.

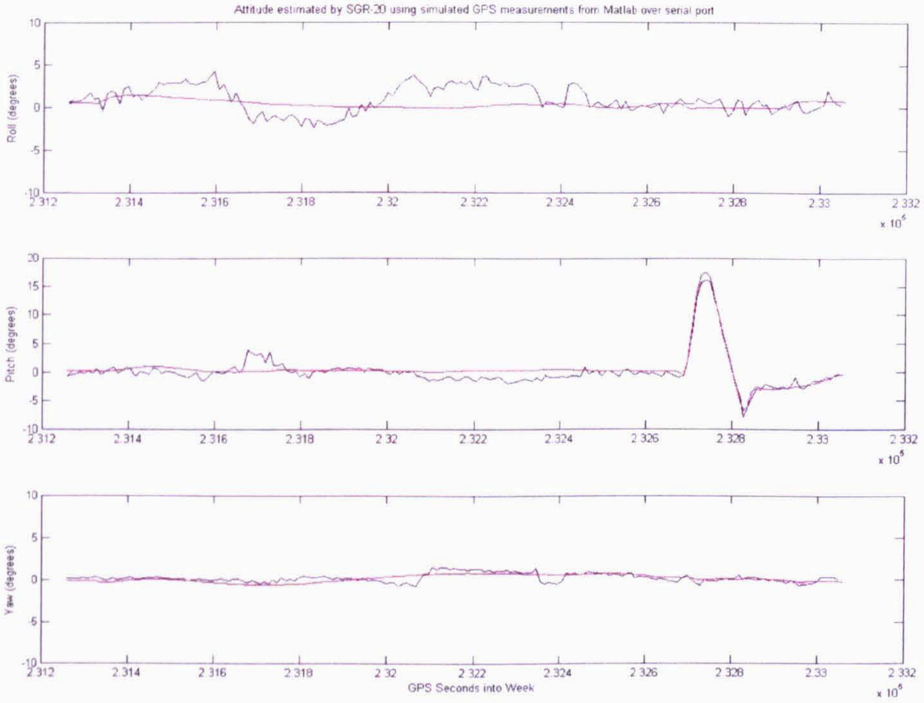

Figure 7-3 Hardware-in-the-loop simulation results (simulated data)

7.2.4 Post-processing of in-orbit data onboard the SGR-20

As an extension to the hardware-in-the-loop simulation, a second set of MATLAB scripts was written to enable 'play-back' of the real SGR-20 data logged during the various experiments conducted in 2007 (see Appendix D). The logged data is read in from a number of ASCII files, formatted into an SBPP packet and sent to the SGR-20. The receiver waits until there are six satellites on each baseline and then uses the integer ambiguity resolution algorithm to solve the integer ambiguities. Once these integer ambiguities are known the receiver initialises the attitude tracking algorithm and begins tracking the attitude. The results of each operation are used to construct Packet 0x66 (the attitude results packet) which is output to the personal computer. The MATLAB script then parses the SBPP data and extracts the necessary information from the packets.

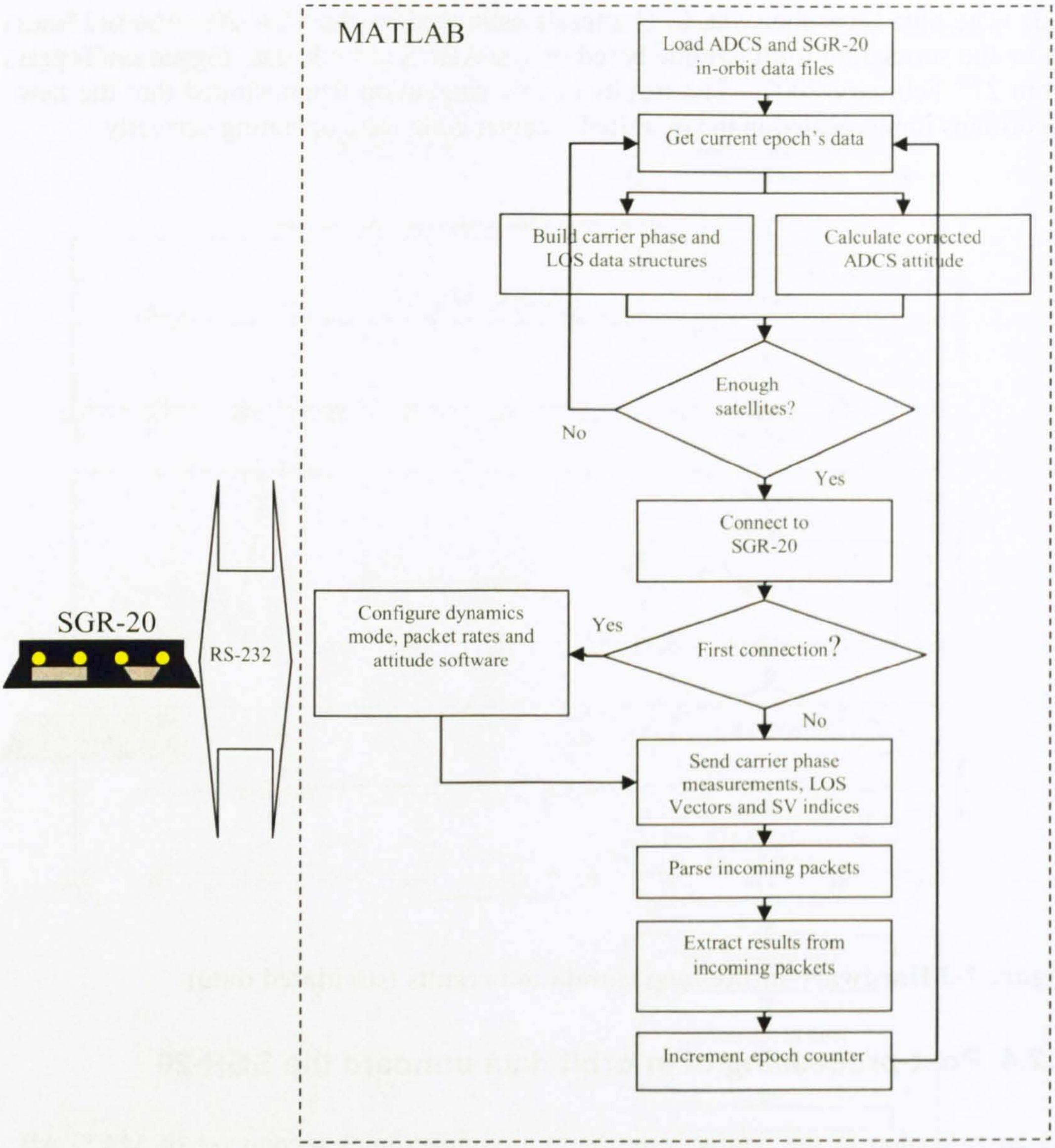

Figure 7-4 Overview of Hardware-in-the-loop test using data from orbit

To validate the onboard implementation measurement data logged on the SGR-20 on Topsat on 22nd February 2007 was played back through the receiver using the hardware-in-the-loop method. The resulting GPS attitude solution calculated by the SGR-20 is shown in Figure 7-5. The results of this test demonstrate that the SGR-20 can successfully initialise the integer ambiguity solution, and track the attitude solution. This is achieved even given the number of available measurements and the satellite geometry experienced on the Topsat receiver in orbit. The use of the hardware-in-the-loop method indicated that the new flight software was almost ready to start real-time testing in orbit. The limitation of the hardware-in-the-loop method was that the sections of code that took the real-time phase differences and LOS vectors could not be tested to ensure that the data was being fed into the onboard algorithms correctly. To mitigate this risk, a final outdoor test using a mock-up of a satellite was required to thoroughly test the new software. This is described in the next section.

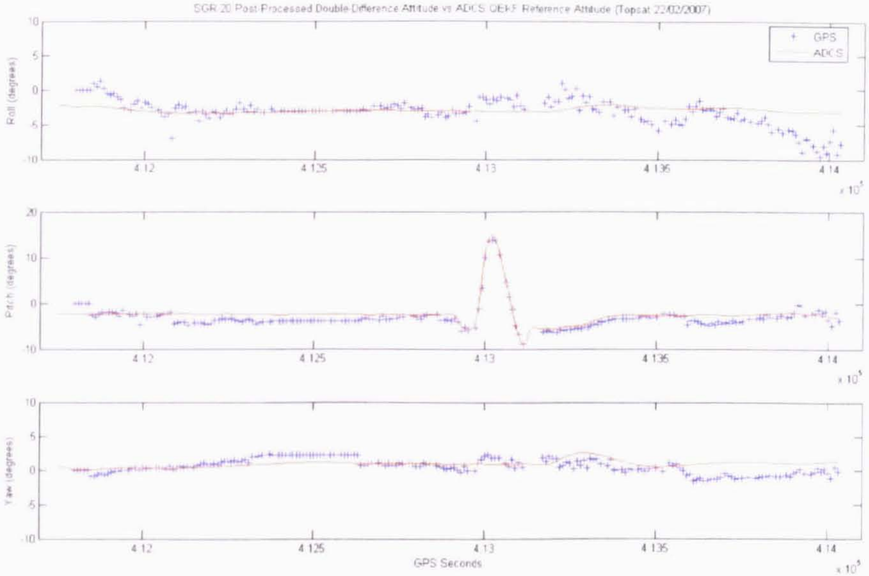

Figure 7-5 Hardware-in-the-loop simulation results (post-processed real data)

7.2.5 Outdoor testing using a mock-up satellite

The final stage of pre-flight testing involved the use of live signals via a mock satellite facet mounted on a tripod. This platform was constructed, by the author, to test the new flight software using real-time measurements onboard the SGR-20. The construction of the mock-up satellite was necessary because a suitable RF signal simulator that could simulate four separate antennas was not available. To properly test the new flight software it was necessary to ensure that the code fed real measurements from the four patch antennas on the satellite mock-up to the attitude determination algorithms. This test also demonstrated that the algorithms could use real measurements to successfully calculate an integer ambiguity solution and to track the attitude.

Figure 7-6 Testing GPS attitude code using a mock-up satellite facet

The test setup did not provide an accurate reference attitude. A rough alignment with magnetic north was achieved using a compass and by ensuring the facet was level using a spirit level. As an accurate reference was not available the attitude error could not be calculated, but correct operation of the modified flight code, successful integer ambiguity resolution and attitude estimation were demonstrated using this setup. The results of this test were used to gain confidence in the operation of the modified flight code before it was uploaded to a satellite.

Figure 7-7 Close-up of mock-up facet showing four GPS L1 patch antennas

7.2.5.1 Results of mock-satellite test

A significant area of concern for the real-time operation of the integer ambiguity resolution code on the SGR-20 centred around the spare processing available when the receiver is tracking satellites on all of its twenty-four channels. Testing using the mock-up satellite allowed the SGR-20 processor to be loaded as it would be when operating in orbit. In the current standard flight software tracking satellites on all twenty-four channels leaves around 6-7% spare processing. This can be seen in Figure 7-8 between around 8 minutes and 10 minutes when the receiver had just switched to 'Mode 2' - which is a user configurable mode in this case configured for attitude determination.

Once the integer ambiguity resolution algorithm had started the spare processing dropped to zero for a period of 20-30 seconds, until the algorithm reported a solution. At this point the algorithm began tracking the attitude and from this point onwards the spare processing oscillated around the 2% mark. Through experience with using the SGR-20 it is known that the onboard software can handle short periods during which the spare processing is around zero, particularly if the lower priority tasks are the ones using the processor. The priorities assigned to each task will ensure that the higher priority tasks such as taking measurements and calculating the navigation solution are still completed. The overall effect will be that it takes longer for the SGR-20 to complete the integer ambiguity resolution algorithm.

A second area for concern was whether the SGR-20 would have sufficient spare memory to be able to run the new integer ambiguity resolution code. Due to the limited tools available to debug and inspect the real time operation of the SGR-20 the only way to test this was again using real signals outdoors via the tripod setup. A special debug packet was used to log the number of bytes allocated on the heap throughout the integer ambiguity resolution and attitude tracking code. An example plot is shown in Figure 7-9. The results of this test showed that the new algorithms ran successfully alongside the existing code and there were no issues with insufficient memory being available to run the integer ambiguity resolution or attitude tracking algorithms.

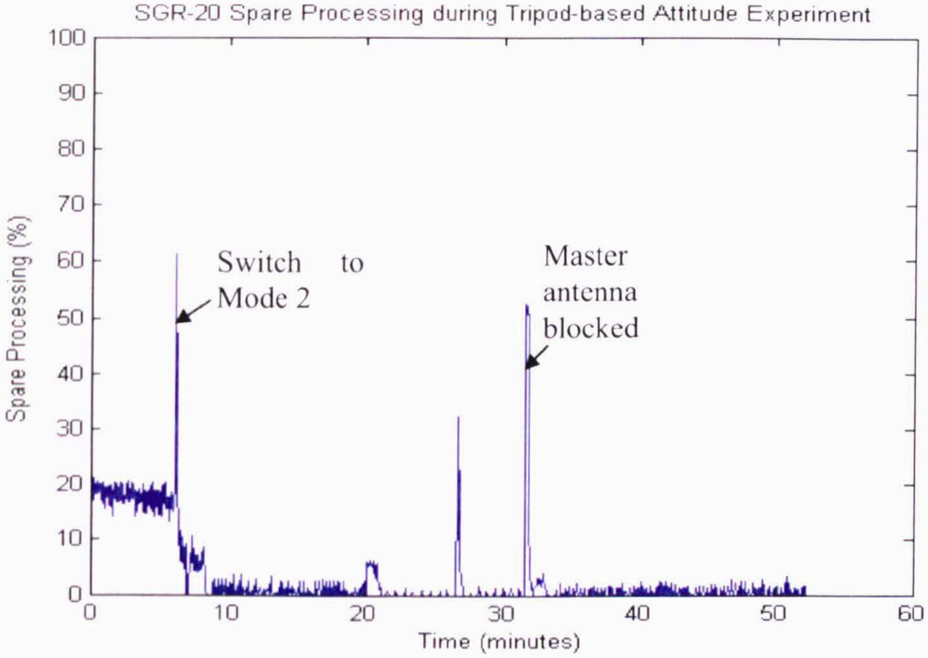

Figure 7-8 Spare processing of SGR-20 during tripod experiment

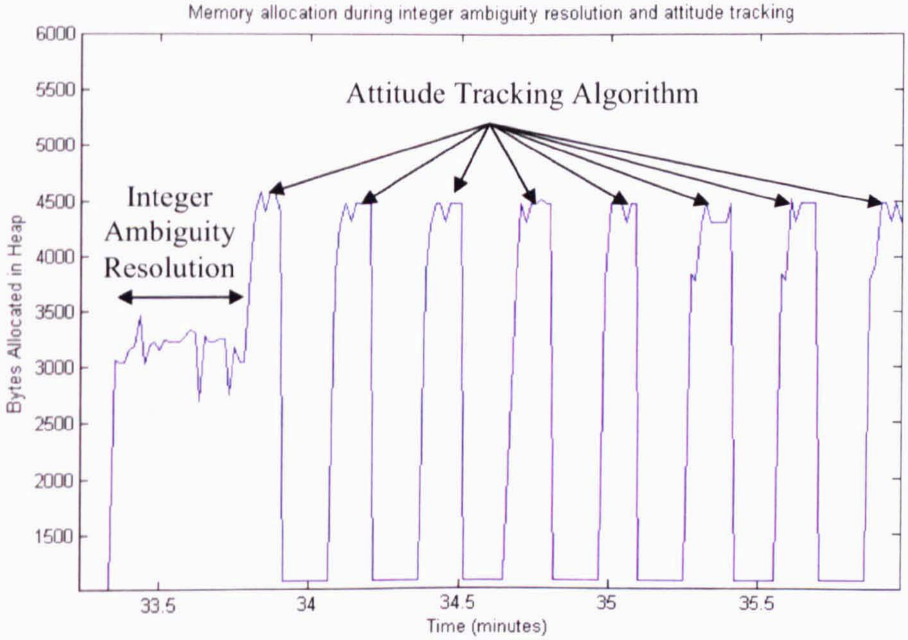

Figure 7-9 Memory allocation onboard the SGR-20 during tripod experiment

7.3 Real-time in-orbit experiments

In this section the results of stand-alone GPS attitude determination on the Topsat microsatellite are presented. A series of experiments were conducted starting in the summer of 2008 in order to analyse the performance of the SGR-20 as an attitude sensor on a microsatellite. The main aim of these experiments was to demonstrate robust integer ambiguity resolution and attitude tracking based on the new algorithms developed as part of this research.

7.3.1 Overview of experiments conducted

The Topsat microsatellite is a technology demonstration satellite built for the UK Ministry of Defence by SSTL as part of a consortium led by Qinetiq. It was originally intended as a one year mission, but later became an operational imaging satellite used by companies such as InfoTerra and DMCII to provide commercial imagery to paying customers. This meant that the GPS attitude experiments could not interfere with nominal operations and so there was a limit to the types of manoeuvres and length of experiments that could be conducted. This is in contrast to the UoSAT-12 experiments conducted in [Purivigraipong, 2000] since UoSAT-12 was a technology demonstration mission over which SSTL had full control.

To minimise the impact on nominal operations all the real time GPS attitude experiments conducted involved either a standard TDI manoeuvre (as described in Chapter 3) or the satellite remained nadir pointing throughout. Since the SBPP log file generated by the SGR-20 resides on the OBC there was also a limit to the length of the experiment due to the size of the data file generated by the experiment. The OBC on Topsat only has around 19 megabytes of RAM which is used to store all the log files for every system on the spacecraft. All these files are downloaded to the ground-station at SSTL on a daily basis, which also imposes a limit on the size of the GPS log file since it must be downloaded quickly enough to not interfere with the download of the other log files.

By default, on power-on the SGR-20 will copy its standard flight software from its onboard Flash memory into SRAM and then boot the flight software from SRAM. In order to use the modified flight software, after power on the SGR-20 is placed in to its boot-loader mode and the OBC loads the modified code directly to the SGR-20s SRAM via the CAN interface. Once uploaded the receiver is commanded to boot directly from SRAM, therefore temporarily replacing the standard flight code with the experimental software. When the SGR-20 has started executing the experimental software the OBC configures the receiver using a command file. This ensures that the receiver is configured for attitude determination, once it has established a position fix and downloaded sufficient GPS almanacs. An example command file is shown in the figure below.

```
23 2 16        %Packet 10
23 3 10        %Set rate to 0.1Hz
23 2 65        %Packet 41
23 3 10        %Set rate to 0.1Hz
23 2 101       %Packet 65
23 3 10        %Set rate to 0.1Hz
23 2 102       %Packet 66
23 3 10        %Set rate to 0.1Hz
23 21 6        %Assign 6 channels to Antenna 1
23 21 262      %Assign 6 channels to Antenna 2
23 21 518      %Assign 6 channels to Antenna 3
23 21 774      %Assign 6 channels to Antenna 4
23 21 1025     %Set Antenna 1 to Master
23 21 1282     %Set Antenna 2 to Slave
23 21 1538     %Set Antenna 3 to Slave
23 21 1794     %Set Antenna 4 to Slave
23 21 2050     %Apply changes to Mode 2
23 22 213      %Execute Antenna Config Command
23 21 10       %Set Elevation Mask to 10 degrees
23 22 167      %Execute Elevation Mask Command
23 21 1        %Set Mode 1
23 22 182      %Execute Antenna Allocation Mode Command (ensures all data sent)
```

Figure 7-10 Example command file used to configure SGR-20 on Topsat for attitude determination

Once the experiment is complete the SGR-20 is powered down. This removes the experimental software from memory, and on the next power on the receiver will copy its standard flight software from FLASH memory and return to nominal operations.

Once operating the SGR-20 outputs integrated carrier phase differences (Packet 0x65), LOS vectors (Packet 0x41) and the PVT solution (Packet 0x10) as well as the results of the real time GPS attitude algorithms (Packet 0x66) for the duration of the experiment. The data from the SGR-20 is logged in the SBPP format in the GPS binary file on the OBC. At midnight each day the GPS binary file is zipped and scheduled for download on the next available pass over the ground-station at SSTL. Once downloaded the GPS binary is processed in SGR-PC which parses the SBPP packet data and displays it via the various windows implemented by the author for visualising the data from the SGR-20. Details of these forms are given in Appendix E.

7.4 Experimental results

At the time of writing fifteen real time GPS attitude experiments have been conducted on Topsat. The following section summarises the results of these experiments and presents a more detailed analysis of a selection of the experiments which have demonstrated various performance factors relating to the operation of the SGR-20 as an attitude sensor.

7.4.1 Data file GP080500 (5th August 2008)

This was the first successful real time operation of the modified SGR-20 flight software on Topsat. This experiment began at around 21:58 on 5th August 2008 (GPS Week 1412, GPS Seconds 251909.0) and ran for 40 minutes. The ground-track of Topsat during the experiment is shown in Figure 7-11. Note that the yellow disc denotes the position of the Sun and the shaded area represents the umbra (at ground level) for the last epoch of the experiment.

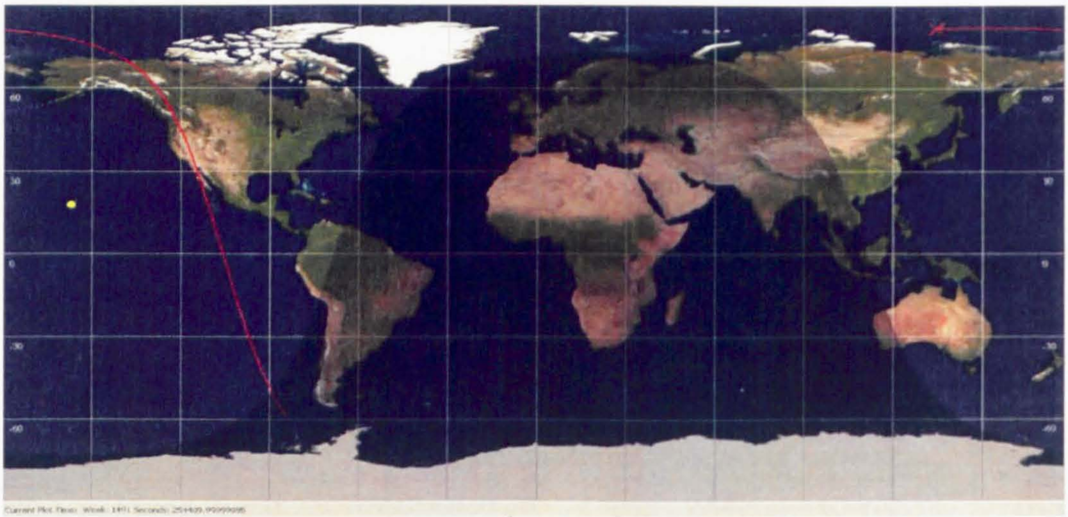

Figure 7-11 Ground-track of Topsat 5th August 2008

The nominal mode of operation of the receiver involves an initial 'Cold search' using all twenty-four channels in order to acquire at least four satellites and calculate an initial position, velocity and time (PVT) solution. A typical Time-To-First-Fix for the SGR-20 is around three-hundred seconds. Once the PVT solution is being generated the receiver waits until at least twenty GPS almanacs have been downloaded before switching to the commanded attitude configuration.

For these initial experiments the modified flight software only permitted integer ambiguity resolution to start once six satellites were assigned to all three baselines, to ensure a robust solution. For this experiment it took around seven minutes for the SGR-20 to have downloaded sufficient almanacs to switch the attitude configuration and a further five minutes for the receiver to assign six satellites to all three baselines (as can be seen in Figure 7-12).

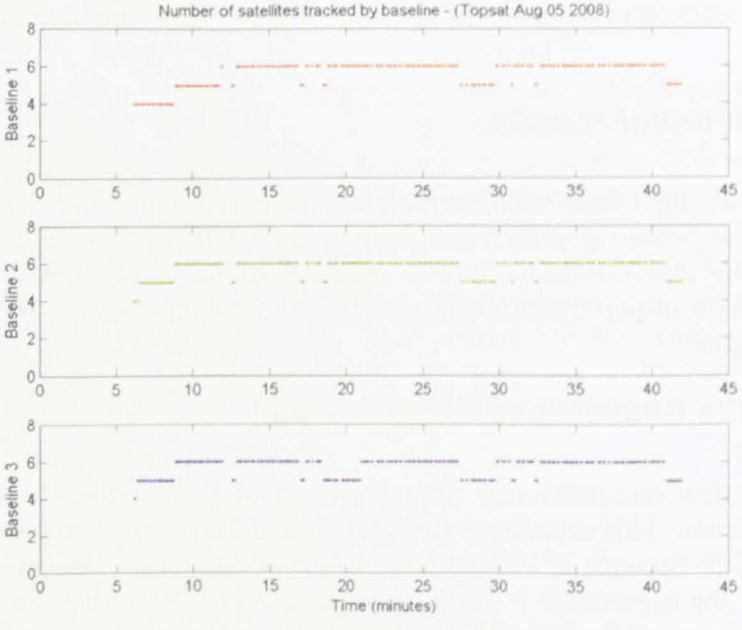

Figure 7-12 Number of satellites tracked 5th August 2008

It then took the SGR-20 less than ten seconds to solve for the integer ambiguities and initialise the attitude tracking algorithm. Note that Packet 0x66, which outputs the status of the attitude initialisation and tracking algorithms, was only logged at ten second intervals so the initialisation may only have taken one or two seconds.

From this point onwards the SGR-20 tracks the attitude solution using the double-difference point solution algorithm. The attitude estimation results are shown in Figure 7-13 below. The blue plot is the post-processed GPS double-difference point solution. This was calculated by post-processing the data logged in-orbit using the same MATLAB scripts used in Chapter 6 to demonstrate the estimation of attitude from GPS measurements. The post-processed plot is provided to allow a comparison with the real-time onboard double-difference GPS attitude solution shown in green. The ADCS Quaternion Extended Kalman Filtered (QEKF) reference attitude solution is shown in red.

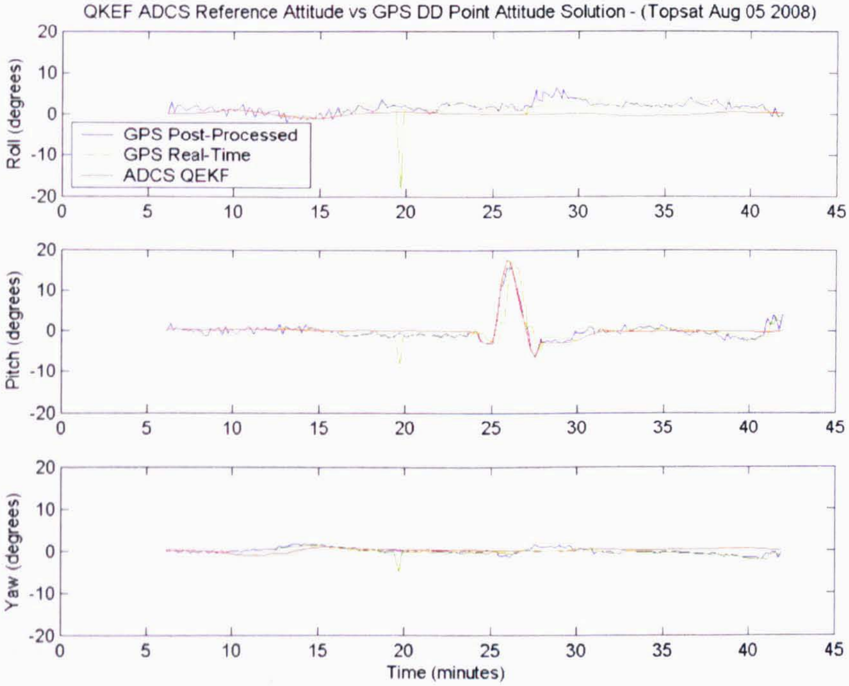

Figure 7-13 Real time GPS attitude point solution 5th August 2008

As can be seen from the above figure the real-time attitude solution from the SGR-20 reliably tracks the attitude of Topsat throughout the experiment, including during the large angle pitch manoeuvre. During this manoeuvre the pitch varies by more than twenty degrees. The plot shows that the real-time GPS attitude solution exhibited a constant offset in time relative to both the post-processed GPS attitude solution and the ADCS QEKF attitude. This offset was caused by the wrong timestamp being output in Packet 0x66. This was fixed in the next iteration of the flight software.

The above plot highlighted a number of other issues with the experimental receiver code. There was an issue with the iteration of the double-difference point solution attitude estimator (see section 2.3.3.4) which was enforcing too small a threshold resulting in an occasional spike in the attitude estimate. There was also an issue with the update rate of the attitude algorithms that sometimes resulted in the receiver not outputting packet 0x66 as demonstrated by the lack of points in the GPS attitude estimate around the TDI manoeuvre. This is examined further in the next section.

7.4.2 Data file GP081400 (14th August 2008)

In order to minimise the load on the SGR-20's processor the first few experiments were conducted with the attitude code only being run every ten seconds. Due to the large angle pitch manoeuvre conducted during the TDI operation this was quickly realised to be too slow since the attitude could change by a number of degrees between consecutive measurements epochs. The results for the experiment conducted on 14th August 2008 demonstrate this issue aptly.

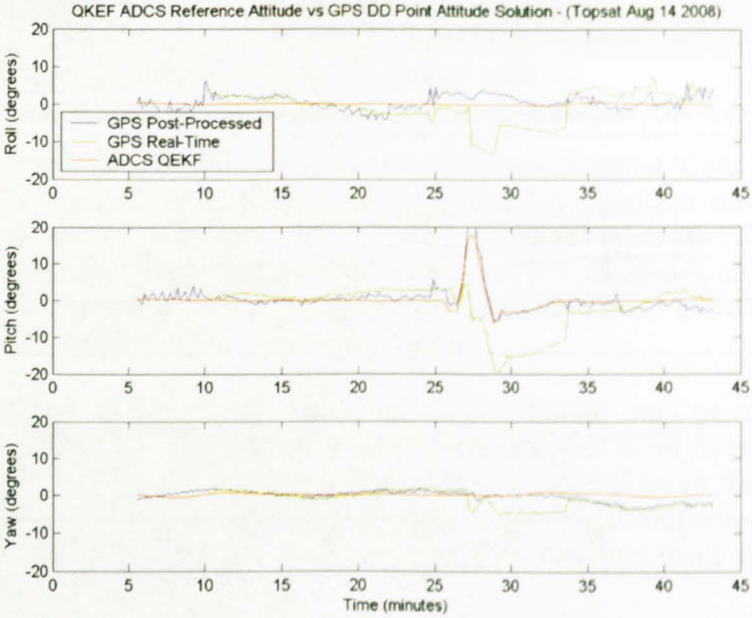

Figure 7-14 Real time GPS attitude point solution 14th August 2008

Whilst the receiver correctly initialised the integer ambiguities and tracked the attitude for around sixteen minutes, as soon as the attitude rate increased (during the TDI manoeuvre) the real-time double-difference point solution algorithm incorrectly estimated the integer ambiguities for the current epoch. This was because the attitude had changed by more than four degrees since the previous measurement epoch. To prevent this problem from happening again the update rate of the attitude algorithms was increased to 1Hz given that the attitude of Topsat is not expected to change by more than 0.5 degrees per second. Note that using the double-difference integer tracking algorithm presented in Chapter 4 would mitigate this problem.

7.4.3 Data file GP121500 (15th December 2008)

Another issue highlighted by the in-orbit testing was that it can take the SGR-20 several minutes to assign six satellites to all three baselines, which due to the imposed limitation on the experimental code can mean that the first attitude solution is not generated for many minutes.

The real-time experiment conducted on 15th December 2008 demonstrated this issue when one of the slave channels on antenna three (forming part of baseline two) failed to acquire PRN 26 until over thirteen minutes after the other two slave antennas had successfully acquired it. This is not a problem with the attitude code, but rather the signal acquisition and tracking code on the SGR-20, and as such it was outside the scope of this PhD to try and fix this problem. If this problem is addressed in a later update to the standard SGR-20 flight software then the robustness of the attitude code should not be affected in this way.

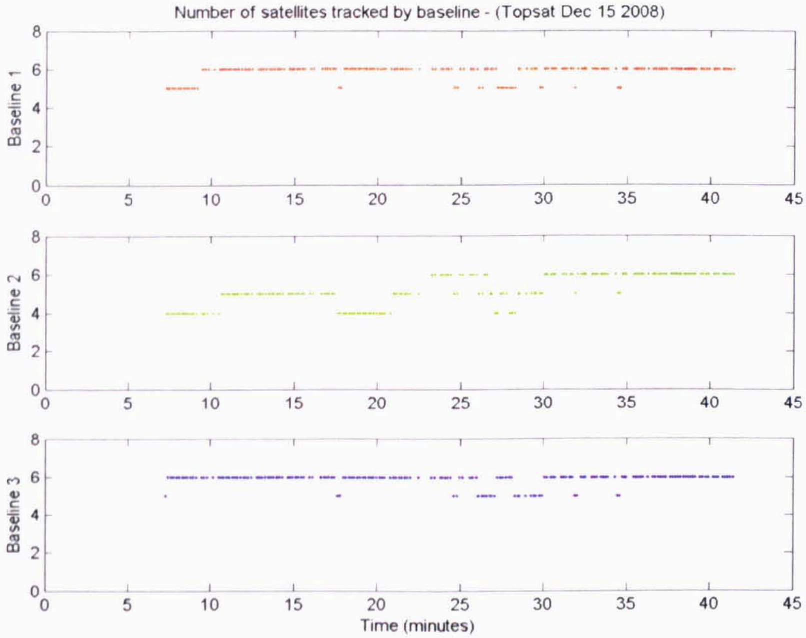

Figure 7-15 Number of satellites tracked 15th December 2008

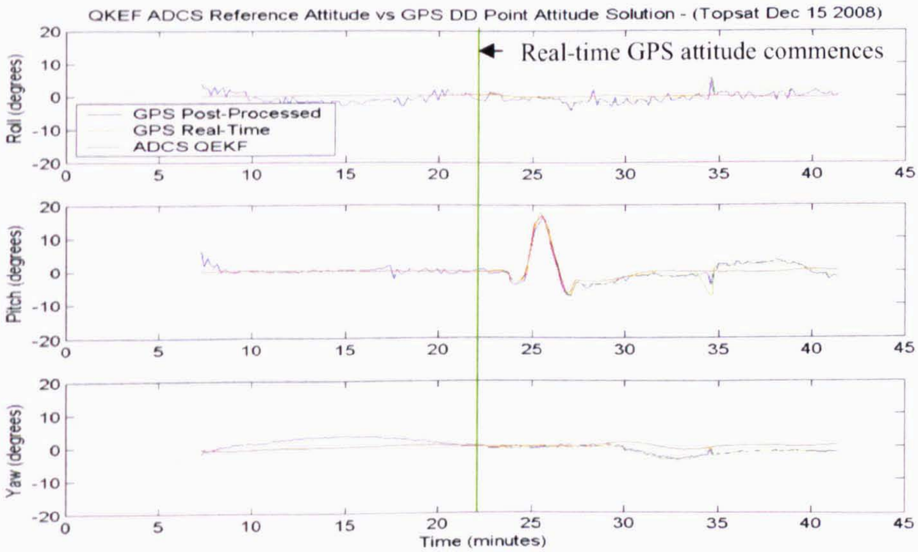

Figure 7-16 Real time GPS attitude point solution 15th December 2008

Once baseline two had finally acquired all six satellites assigned to it, the integer ambiguity resolution algorithm was started. Again, because of the 0.1Hz logging of Packet 0x66, it is not possible to determine how long the integer ambiguity algorithm took to find a solution. However, it did initialise the attitude tracking algorithm successfully. The attitude was then tracked successfully for the remaining twenty minutes of the experiment. This can be seen in Figure 7-16 in which the real-time GPS attitude estimate shown in green does not begin until 23 minutes in to the experiment. The blue plot again shows the post-processed GPS attitude estimate calculated in MATLAB from the raw data logged during the experiment.

The post-processed GPS attitude estimate began as soon as there were four satellites on each baseline, and demonstrates what the real-time GPS attitude solution would have been if not for the problems with satellite acquisition and tracking. Note that the real-time and post-processed GPS attitude estimates are in good agreement for the period that they coincide, and both track the pitch manoeuvre successfully.

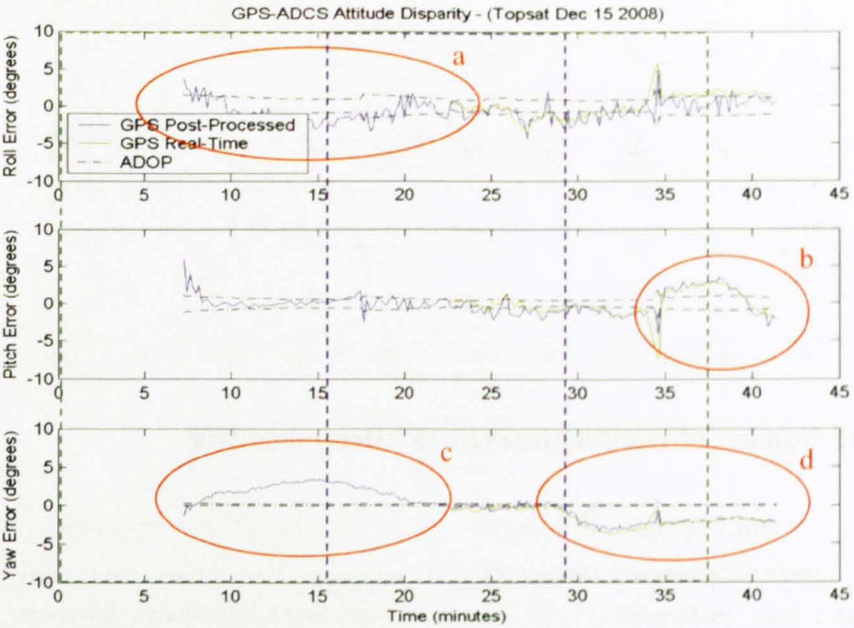

Figure 7-17 GPS-ADCS Attitude Disparity 15th December 2008

The GPS-ADCS disparity is shown in Figure 7-17. The green plot shows the disparity between the real-time GPS attitude estimate and the ADCS estimate. The blue plot shows the disparity between the post-processed GPS attitude estimate and the ADCS estimate. The Attitude Dilution of Precision (ADOP) is calculated as part of the post-processed GPS attitude estimate. The ADOP was used to define the expected GPS attitude accuracy in each epoch, using the method described in section 2.3.4.1. The expected GPS attitude accuracy is shown by the black dashed error bars which give the $\pm 1\sigma_a$ uncertainty in the GPS attitude estimate, where $a = \phi, \theta, \psi$.

The RMS disparity between the real-time GPS attitude estimate and the ADCS estimate is shown in Table 7-1. All three axes agree to within two degrees RMS. However, as can be seen from Figure 7-16 there are number of periods in which the

GPS real-time and post-processed attitude solutions are self-consistent but in disagreement with the ADCS attitude estimate. Since there is no external reference to validate either estimate, there is no scope for determining which estimate is closer to the true attitude.

Table 7-1 RMS GPS-ADCS disparity 15th December 2008

Roll Disparity (degrees)	Pitch Disparity (degrees)	Yaw Disparity (degrees)
1.64	1.72	1.91

The mean expected (or theoretical) attitude error calculated from the ADOP is shown in Table 7-2. This suggests that on average the GPS attitude estimate should be accurate to within 1.53 degrees in roll, 1.05 degrees in pitch and 0.42 degrees in yaw. The RMS disparity between the GPS and ADCS exceeds these values for all three axes. Two potential reasons for the increased disparity are multipath in the GPS carrier phase measurements or errors in the ADCS.

Table 7-2 Expected accuracy of GPS real-time point solution 15th December 2008

Roll (degrees)	Pitch (degrees)	Yaw (degrees)
1.53	1.05	0.42

Multipath present in any particular epoch will result in an error in the GPS attitude solution which will cause a disparity with the ADCS attitude. To determine if multipath was present in the GPS carrier phase measurements the GPS carrier phase residuals for this experiment were calculated as shown in Figure 7-18. The time-correlation of the residuals on baseline two shows that there was multipath on this baseline throughout most of the experiment. This may explain the increased disparity in roll and yaw highlighted by events 'a' and 'c' in Figure 7-17. Baselines one and three show minimal time-correlation except towards the end of the experiment (from around 35 minutes) at which point there is an increase in the variance of the residuals which coincides with an increase in the disparity in both the roll and pitch axes (event 'b' in Figure 7-17).

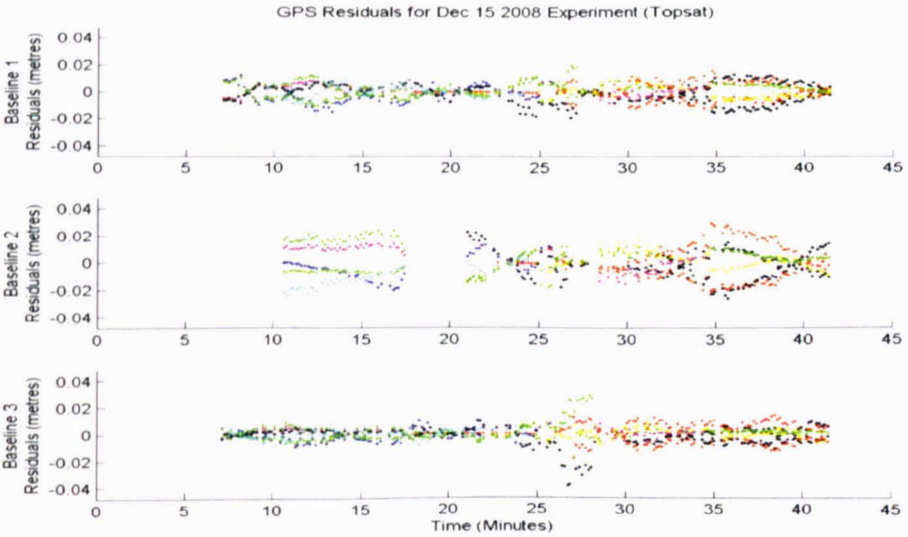

Figure 7-18 GPS residuals 15th December 2008

Alternatively errors in the ADCS attitude estimate will also result in disparity between the GPS and ADCS attitude solutions. For example, event 'd' in Figure 7-17 coincides with the switching off of the IMU. This resulted in the ADCS attitude estimate being updated using the Earth Horizon Sensors, Sun-sensors and magnetometers. This appears to have resulted in a response from the attitude controller on the spacecraft which adjusted the attitude of the spacecraft. The GPS receiver which shows close to two degrees of rotation in yaw whilst the ADCS attitude estimate simply oscillates around zero degrees. The fact that the GPS attitude estimate appears self-consistent during this 'event' suggests that event 'c' is also due to an error in the ADCS, however it is uncertain what caused this event.

7.4.4 Data file GP010600 (6th January 2009)

This experiment demonstrates the nominal performance of the SGR-20 as a GPS attitude sensor. There were no issues relating to satellite acquisition and tracking, and the update rate of the attitude code was set to 1Hz. The experiment started at 19:00 on 6th January 2009 and ran for forty minutes. The ground track of Topsat during this experiment is shown in Figure 7-19 below.

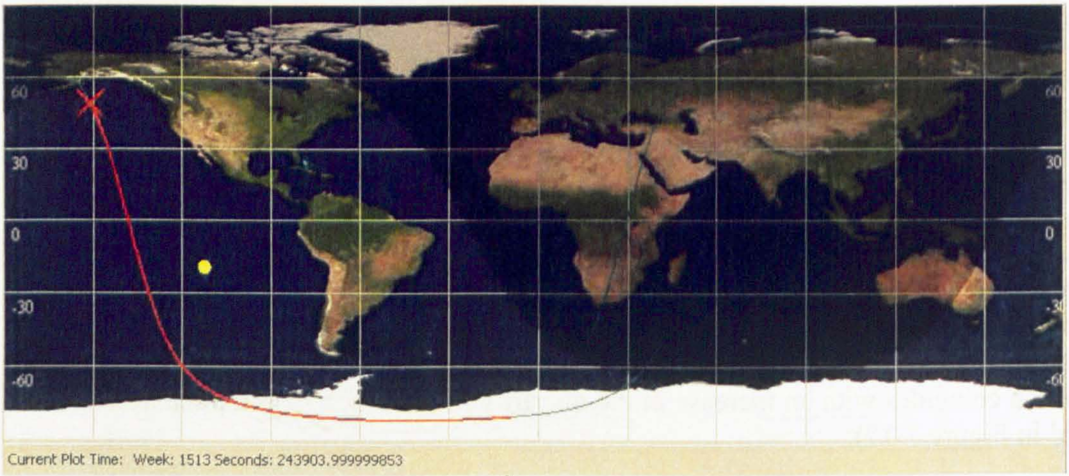

Figure 7-19 Ground track of Topsat 6th January 2009

The SGR-20 achieved a TTFF of 282 seconds and switched to the attitude configuration after a further four minutes. All three baselines quickly acquired five satellites. However, it took around ten minutes for all baselines to acquire six satellites and the integer ambiguity resolution algorithm to be run. The integer ambiguity algorithm calculated the correct integer ambiguity solution and initialised the attitude tracking algorithm successfully. The resulting GPS attitude point solution is shown blue in Figure 7-21 below. The ADCS attitude solution is shown in red for comparison.

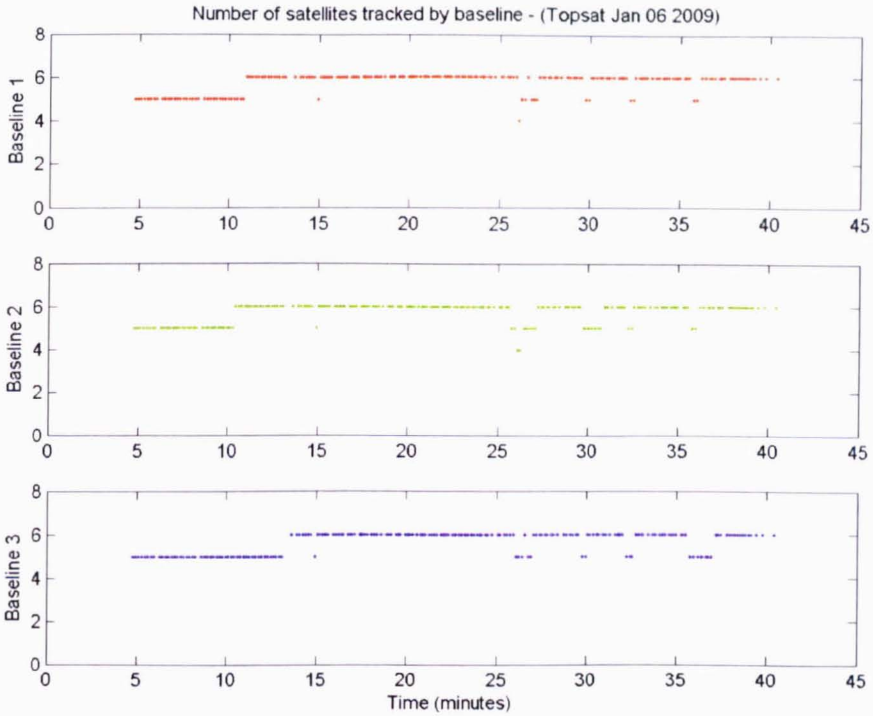

Figure 7-20 Number of satellites tracked 6th January 2009

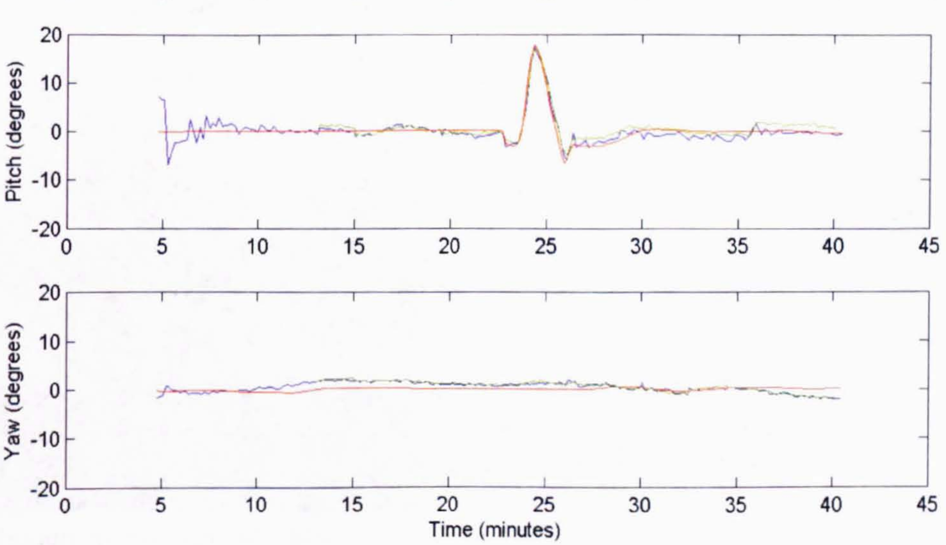

Figure 7-21 Real time GPS attitude point solution 6th January 2009

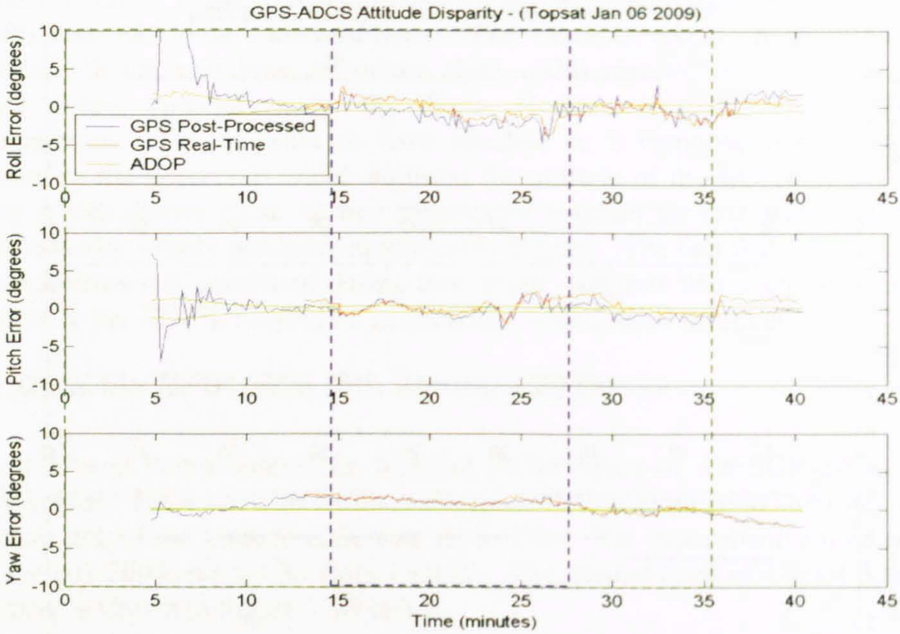

Figure 7-22 GPS-ADCS attitude disparity 6th January 2009

The RMS disparity between the real-time GPS attitude solution (shown in green in the above plot) and the ADCS is given in Table 7-3. The RMS disparity is just over one degree in each axis. The expected accuracy of the GPS attitude solution calculated from the ADOP (see Table 7-4) suggests that the SGR-20 is calculating an attitude solution with an RMS error of less than one degree in all axes.

Table 7-3 RMS GPS-ADCS attitude disparity 6th January 2009

Roll Disparity (degrees)	Pitch Disparity (degrees)	Yaw Disparity (degrees)
1.25	1.07	1.22

Table 7-4 Expected accuracy of GPS attitude solution 6th January 2009

Expected Accuracy		
Roll (degrees)	Pitch (degrees)	Yaw (degrees)
0.91	0.61	0.26

The yaw axis shows the largest discrepancy between the expected error and the calculated disparity. The yaw axis is observed by all three baselines on Topsat since the baselines are co-planar on the –Z facet which is nominally aligned with the yaw plane. Therefore the yaw measurement from the SGR-20 is expected to be the most accurate as was demonstrated in Chapter 6.

There is evidence in the disparity plot in Figure 7-22 to suggest an error in the ADCS yaw estimate is contributing to the disparity. This is particularly the case at around thirty-six minutes into the experiment when the EHS are switched off. The ADCS from this point was only using sun-sensors and magnetometers and it was from this point that the disparity between GPS and ADCS started to increase in magnitude. Note also that the yaw disparity was reasonably constant during the period the IMU was switched on, as highlighted by the blue box. However, the disparity changes when the ADCS switches back to the EHS/Sun sensor/Magnetometer combination. This suggests the IMU is not measuring any change in yaw during this time, but may have been propagating a yaw error which disappeared when absolute attitude measurements were available again.

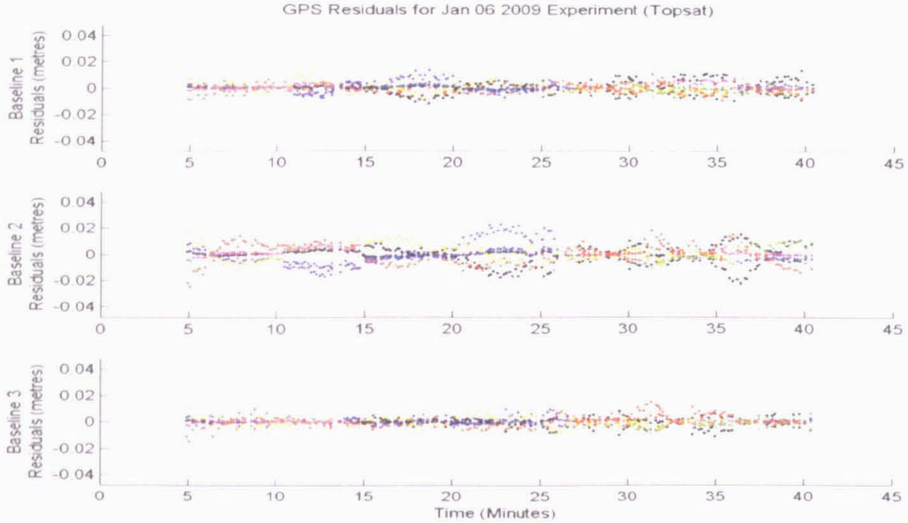

Figure 7-23 GPS Phase Residuals 6th January 2009

The result of this experiment is a positive demonstration that the SGR-20 is capable of calculating an independent three-axis attitude solution with an error of around one degree.

7.4.5 Data file GP012200 (22nd January 2009)

For this experiment Topsat was commanded to remain nadir pointing. The ADCS used a combination of EHS, Sun-Sensors and Magnetometers. Both EHS were operating for the first ten minutes but the IMU was not used. The GPS elevation mask was reduced from ten degrees (as used in the previous experiments) to five degrees.

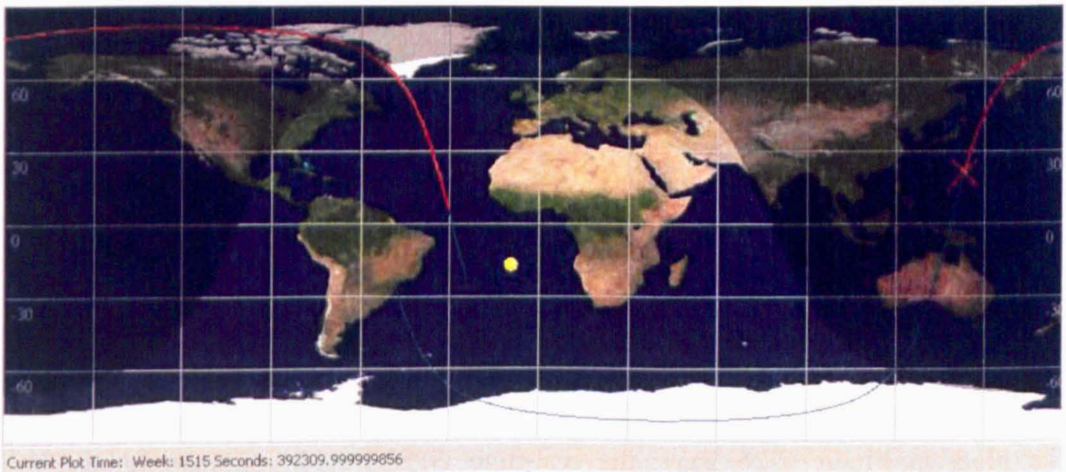

Current Plot Time: Week: 1515 Seconds: 392309.999999856

Figure 7-24 Ground track of Topsat 22nd January 2009

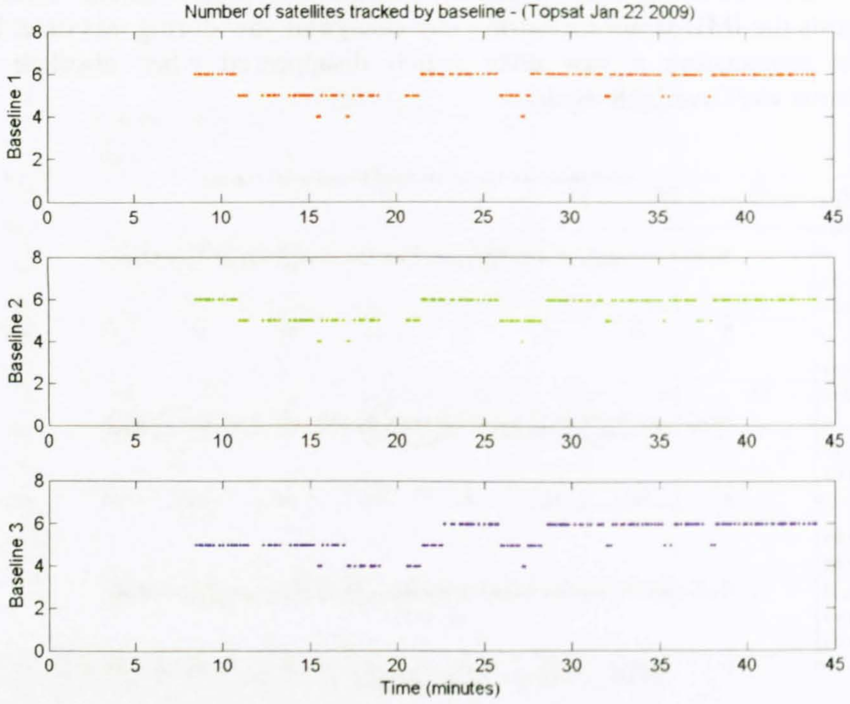

Figure 7-25 Number of satellites tracked 22nd January 2009

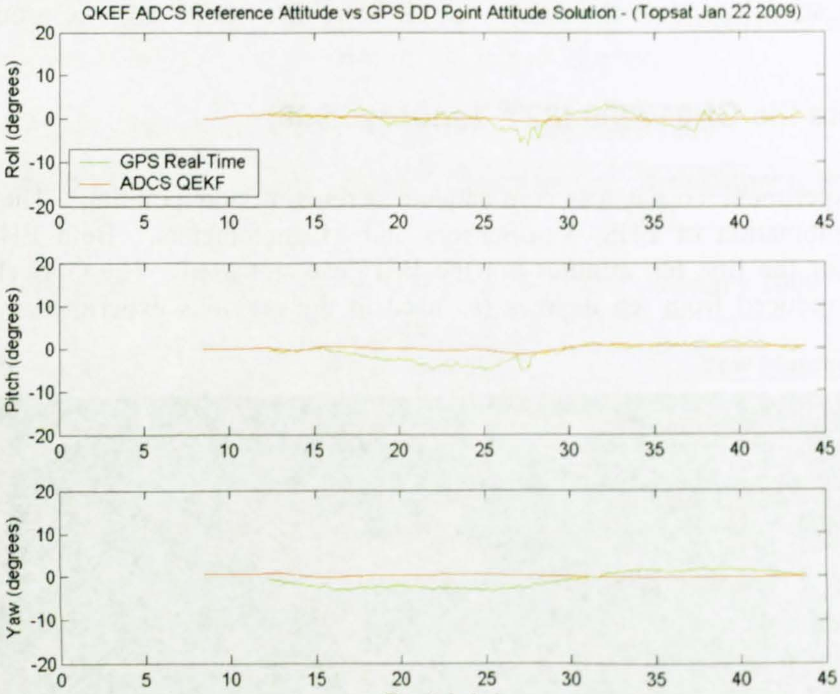

Figure 7-26 Real time GPS attitude point solution 22nd January 2009

The plots in Figure 7-26 show the real-time GPS attitude estimate (green) in comparison with the ADCS attitude solution (red). The GPS attitude pitch and yaw estimates demonstrate an oscillation which is not present in the respective ADCS attitude estimates. This can be seen more clearly in Figure 7-27. The oscillation in yaw may be an error in the ADCS since the ADOP of the GPS yaw estimate suggests the yaw was being determined to within 0.25 degrees (1 sigma), as shown in Table 7-6 and Figure 7-27. The likely explanation for the increased disparity, which in some cases exceeds five degrees, is that the EHS were switched off after around ten minutes into the experiment, due to an error in the schedule file on the OBC. The ADCS would therefore have been based on the combination of Sun-sensors and magnetometers. From Figure 7-27 it can be observed that the GPS-ADCS disparity is greatest at around twenty-five minutes in to the experiment. The GPS residuals, shown in Figure 7-29, show no significant evidence of multipath at this time. This suggests that the GPS attitude estimate was not biased by multipath error. However, examination of the spacecraft's position at this time (see Figure 7-28) shows that it was passing over the North Pole, which would typically cause a loss of observability in the magnetometer estimate. This may have resulted in the five degree disparity between the GPS and ADCS pitch and yaw estimates.

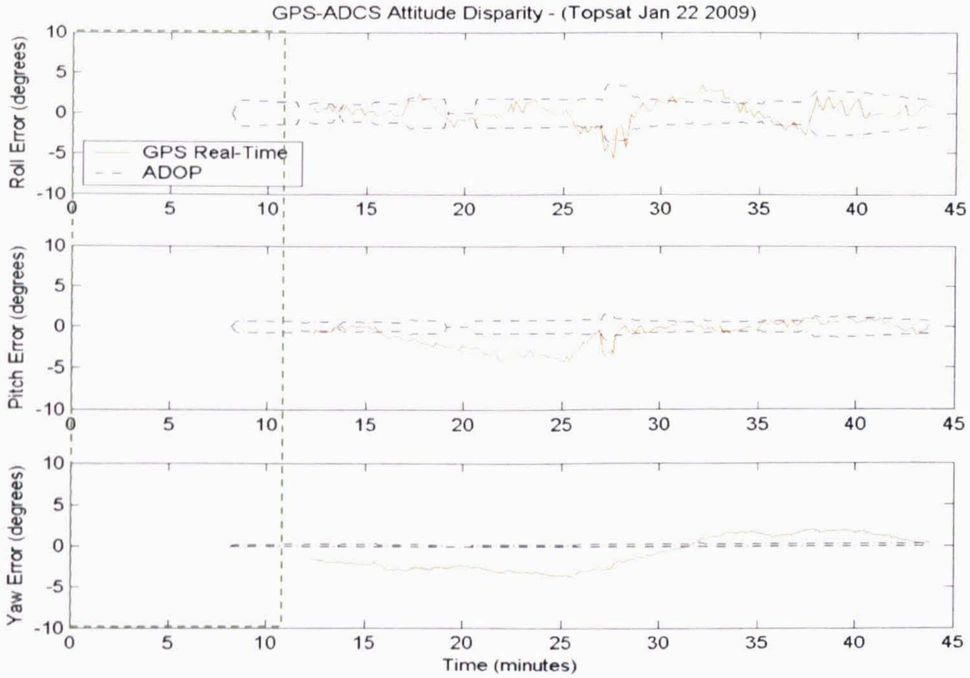

Figure 7-27 GPS-ADCS Attitude Disparity 22nd January 2009

Table 7-5 RMS GPS-ADCS Attitude Disparity (22/01/2009)

Roll Disparity (degrees)	Pitch Disparity (degrees)	Yaw Disparity (degrees)
1.56	1.83	2.17

Table 7-6 Expected Accuracy of GPS attitude solution (22/01/2009)

	Expected Accuracy	
Roll (degrees)	Pitch (degrees)	Yaw (degrees)
1.77	0.80	0.25

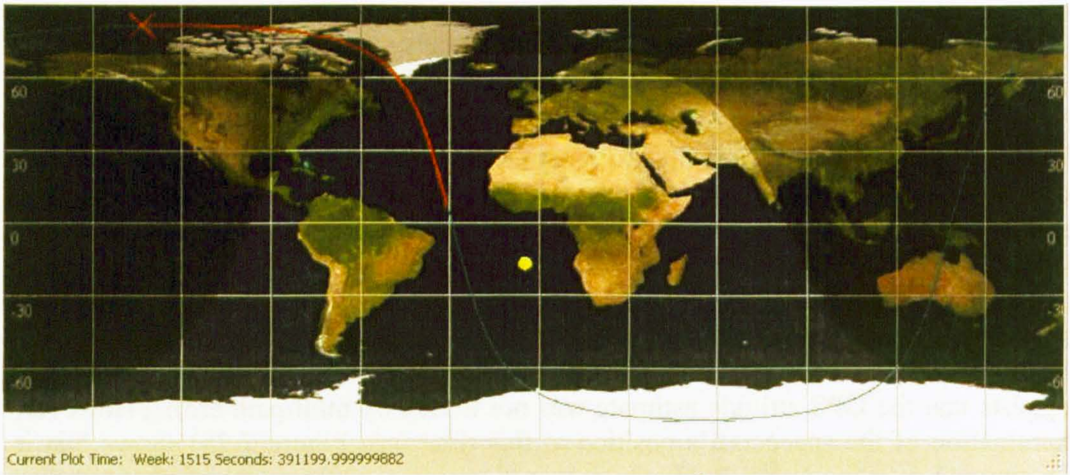

Figure 7-28 Position of Topsat at 25 minutes into 22nd January 2009 experiment

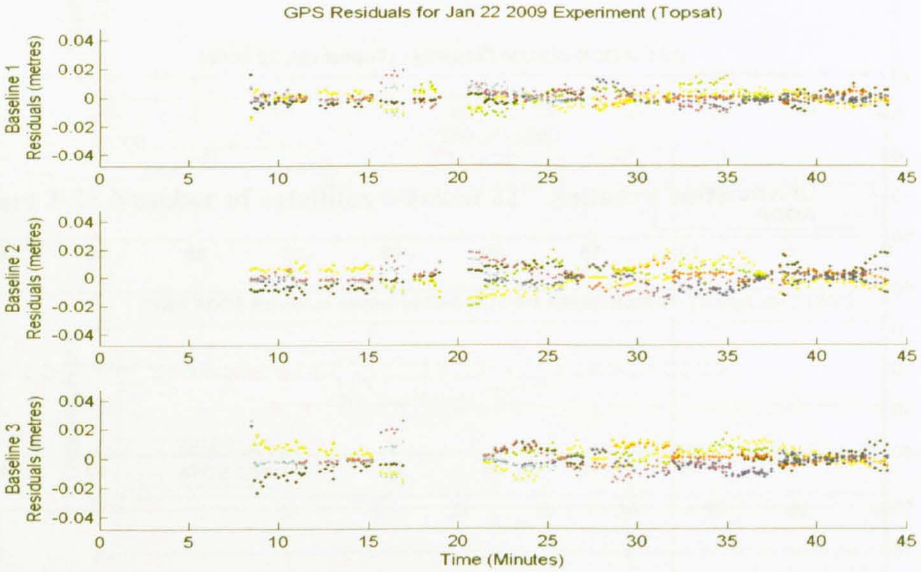

Figure 7-29 GPS residuals 22nd January 2009

The results of this experiment demonstrate that the ability of the GPS attitude sensor to maintain a reliable attitude estimate throughout the whole orbit. This demonstrates an improvement on the standard combination of sun-sensors and magnetometers used on many small satellite missions.

7.4.6 Summary of experiments to date

At the time of writing fifteen real-time GPS attitude experiments have been conducted on Topsat using the modified SGR-20 flight software. Of these fifteen experiments thirteen resulted in the SGR-20 successfully calculating the integer ambiguities and initialising the attitude tracking algorithm. Two of the experiments were not successful. The first, on 14th August 2008, was due to the ten second update rate of the attitude tracking algorithm resulting in the incorrect calculation of the integer ambiguities as part of the attitude tracking algorithm. This problem was fixed by increasing the update rate to 1Hz. The second failure, on 24th February 2009, was due to the satellite acquisition and tracking algorithms on the SGR-20 failing to successfully acquire and track six satellites on all three baselines for the whole of the forty minute experiment. The mean attitude GPS-ADCS disparity in roll, pitch and yaw between the real-time GPS attitude solution and the ADCS QEKF attitude solution for all fifteen experiments is shown in Table 7-7.

Table 7-7 Mean Disparity between GPS and ADCS attitude solutions

	Mean Disparity		
	Roll (degrees)	**Pitch (degrees)**	**Yaw (degrees)**
05/08/2008	1.30	0.32	-0.61
14/08/2008	-	-	-
20/08/2008	1.10	-0.29	-0.61
09/12/2008	-0.07	-2.10	0.36
11/12/2008	-1.54	0.07	0.09
15/12/2008	0.12	-0.12	-1.55
18/12/2008	-0.24	-0.53	0.24
06/01/2009	-0.21	0.48	0.51
08/01/2009	-0.09	-0.05	0.29
13/01/2009	-0.34	-5.16	-0.70
15/01/2009	1.19	-0.39	0.03
20/01/2009	0.85	0.25	-0.96
22/01/2009	0.10	-1.02	-0.99
24/02/2009	-	-	-
26/02/2009	1.74	-0.67	0.44
Mean Disparity	0.30	-0.71	-0.27

The RMS attitude disparity between the real-time GPS double-difference point solution and the ADCS for each of the fifteen successful real time experiments conducted is shown in Table 7-8 below.

Table 7-8 RMS Disparity between GPS and ADCS attitude solutions

	RMS Disparity		
	Roll (degrees)	**Pitch (degrees)**	**Yaw (degrees)**
05/08/2008	2.37	2.23	1.04
14/08/2008	-	-	-
20/08/2008	1.69	2.40	1.36
09/12/2008	2.13	2.23	1.69
11/12/2008	2.61	0.71	2.49
15/12/2008	1.64	1.72	1.91
18/12/2008	1.64	1.02	1.95
06/01/2009	1.25	1.07	1.22
08/01/2009	2.22	1.19	1.40
13/01/2009	2.75	5.51	1.28
15/01/2009	2.48	0.79	0.80
20/01/2009	1.82	0.78	1.45
22/01/2009	1.56	1.83	2.17
24/02/2009	-	-	-
26/02/2009	2.04	1.30	0.91
RMS Disparity (including outlier)	2.06	2.14	1.59
RMS Disparity (ignoring outlier)	1.99	1.56	1.61

The five degree disparity in the pitch axis on 13th January 2009 appears to have been caused by an error in the attitude tracking code. The disparity is not present in the post-processed attitude solution. The error may have been the result of a cycle slip in the real-time attitude tracking algorithm. This could easily be remedied by implementing the double-difference integer tracking algorithm from Chapter 4 and monitoring the residuals of the attitude tracking algorithm. Both these features are planned for a future update of the SGR-20 attitude code. If this 'outlier' is removed from the calculation of mean disparity the resulting mean offsets between the GPS and ADCS attitude solutions are 0.35° in roll, -0.34° in pitch and -0.23° in yaw, and the correspond RMS disparities are 1.99°, 1.56° and 1.61° respectively.

Table 7-9 gives the expected accuracy of the GPS attitude solution for each of the fifteen real-time experiments. These figures were calculated by estimating the measurement noise for each experiment from the GPS carrier phase residuals using the method shown in Chapter 3, and combining this with the ADOP calculated in post-processing (as described in Chapter 2) to give an estimate of the expected attitude error in each axis.

Table 7-9 Expected Accuracy of GPS attitude solution based on ADOP

	Expected Accuracy		
	Roll (deg)	Pitch (deg)	Yaw (deg)
05/08/2008	1.16	0.87	0.28
14/08/2008	1.74	1.16	0.34
20/08/2008	1.28	0.89	0.24
09/12/2008	1.22	0.64	0.34
11/12/2008	0.96	0.57	0.27
15/12/2008	1.52	0.96	0.35
18/12/2008	1.32	1.08	0.38
06/01/2009	0.91	0.61	0.26
08/01/2009	1.63	0.76	0.34
13/01/2009	1.43	0.78	0.30
15/01/2009	1.21	0.74	0.27
20/01/2009	0.80	0.59	0.42
22/01/2009	1.77	0.80	0.25
24/02/2009	1.47	0.85	0.30
26/02/2009	1.80	1.12	0.34
Expected Accuracy	1.38	0.85	0.32

The difference between the overall expected accuracy of the GPS attitude solution shown in Table 7-9 and the RMS disparity between GPS and ADCS (ignoring the outlier on 13th January 2009) is 0.61° in roll, 0.71° in pitch and 1.29° in yaw.

In Chapter 3 it was shown that the ADCS attitude estimate has a standard deviation of around 0.30 degrees in the along-track direction and 0.34 in the across-track direction when DASH2 is functioning. This increases to 0.51 and 0.89 degrees respectively when DASH2 is not functioning. It was also noted that the mean error in the across-track (nominally roll) axis was 1.19 degrees when DASH2 was operating. Analysis of the telemetry from the ADCS on Topsat showed that both EHS were operating during most of the real-time experiments with the exception of 5th August 2008 and 20th January 2009 when DASH2 was malfunctioning. Therefore for most of the real-time experiments there may have been an error in the ADCS roll estimate of up to

1.19 degrees. Based on the expected accuracy of the GPS roll estimate this would lead to an overall RMS disparity of

$$\sqrt{1.19^2 + 1.38^2} = 1.82^{\circ}$$

which is close to the observed RMS roll disparity of 1.99 degrees. This estimate would only be reasonable if the assumed ADCS roll error of 1.19 degrees was correct. Since there is no method of validating the ADCS except through the single-point comparison done by comparing the requested image centre/target with the achieved image centre/target, the extent of any actual bias in the ADCS attitude estimate is unknown.

The same logic can be applied to the disparity between the expected GPS yaw estimate accuracy and the measured GPS-ADCS disparity in yaw. On Topsat the Sun-sensors are the main source of yaw information. According to the ADCS engineers at SSTL the Sun-sensors are accurate to around 2 degrees RMS. Therefore it is likely that the GPS yaw estimate is actually significantly better than the ADCS yaw estimate. This potential benefit of GPS attitude may be a selling point for implementing GPS attitude on future small satellite missions, since many missions require a yaw estimate to better than 0.5 degrees, which GPS should be able to provide without further work.

7.5 Conclusions

The results presented in this chapter demonstrate that the SGR-20 can successfully calculate the attitude of the Topsat microsatellite. It has been shown that this can be achieved in real time at a rate of 1Hz onboard the SGR-20 in orbit.

To allow the aim of demonstrating real-time stand-alone GPS attitude determination in LEO to be met, only Parts I to III of the new IAR algorithm were implemented in the SGR-20 flight software. This was due to the amount of time required for implementing and debugging the C modules that were added to the SGR-20 flight software. The results from Chapter 5 indicated that when tracking six satellites Part I to III of the algorithm could provide a reliable integer ambiguity solution using a single epoch of data, assuming the double-difference RMS measurement noise was less then 8mm. The analysis of spaceflight data showed that the double-difference RMS measurement on Topsat is around 8.5mm. This meant that theoretically there was around a 0.3 percent chance that the IAR algorithm would output an incorrect solution. This was deemed acceptable for testing purposes and to date the single epoch IAR algorithm in the SGR-20 flight software has always calculated the correct integer ambiguity solution and correctly initialised the attitude tracking algorithm. The performance of the whole IAR algorithm including Part IV was instead demonstrated via post-processing of in-orbit data in Chapter 5.

Comparison between the ADCS attitude solution and the real-time GPS attitude solution shows a disparity of around 2.0 degrees in roll, 1.6 degrees in pitch and 1.6 degrees in yaw. However the extent of any unknown errors in the ADCS attitude solution cannot be verified. Analysis of the GPS measurement noise and ADOP suggests the GPS attitude solution may be accurate to 1.4 degrees in roll, 0.9 degrees in pitch and 0.3 degrees in yaw.

These results demonstrate that the SGR-20, even given its limitations such as only tracking six satellites per baseline, can provide a robust attitude estimate. Importantly, this attitude estimate is totally independent from the ADCS attitude since no external aiding is required. These results demonstrate that GPS attitude determination could be used on small satellites to provide a stand-alone estimate of the true attitude either as a back-up to the main ADCS in case of failures or as part of a low-cost satellite design to augment the standard sun-sensor and magnetometer combination which is limited in scope. The independent attitude estimate provided by GPS could also be exploited to provide insight in to the performance of the other attitude sensors typically used on small satellite missions, as was demonstrated in this work.

8 Conclusions and future work

This chapter describes the research contributions provided through this work as well as details of potential areas of interest for future work. The specific goals of this research were as follows:

1. Analysis of spaceflight data from a small satellite, including quantification of measurement errors such as line bias error, multipath and receiver noise.
2. Design and implementation of a robust integer ambiguity resolution technique for single frequency single epoch GPS measurements.
3. Analysis of the performance factors affecting GPS attitude determination on small satellites.
4. Implementation of a robust real time onboard GPS attitude determination system based on the SGR-20.
5. Demonstration of real-time in-orbit GPS attitude determination on a microsatellite, and comparison of the GPS attitude solution with the ADCS reference attitude.

8.1 Research contributions

The summary of significant contributions as a result of this research follows:

8.1.1 Analysis of spaceflight data

The analysis of spaceflight data presented in Chapter 3 used data logged in-orbit from a series of experiments on Topsat to analyse the error sources that affect the performance of the SGR-20 as a GPS attitude sensor.

As with previous research the GPS antenna baselines were calibrated using the ADCS. This demonstrated that there was a rotation between the baselines defined from MCAD drawings of the satellite and those estimated by the calibration process. In previous research such as [Ward, 1996] the reference attitude was an order of magnitude more accurate than the GPS attitude and so the calibration was assumed correct. However for this work it was known that there was a potential bias in the ADCS found by comparing the ADCS attitude solution with ground imagery. Comparison of the estimated rotation required to 'calibrate' the GPS antenna baselines with the known offset in the ADCS attitude showed that the GPS baselines measured from the MCAD drawings may be correct. Without a third independent attitude reference it is impossible to determine where the offset actually lies.

The analysis of the GPS carrier phase measurements showed that the RMS measurement noise for the SGR-20 on Topsat was between 5 and 7mm for each of the three baselines. Baseline 2, which lies diagonally across the space-facing facet, had the highest measurement noise. Analysis of the residuals, including analysis of the cross-correlation between satellites that traversed the same part of the 'sky' on different dates, showed that multipath is definitely present in the carrier phase measurements. This was an interesting result since the GPS patch antennas all have an unimpeded view of the GPS constellation. This suggests that the multipath error was not due to the signal reflecting off surrounding surfaces, but may have been due to differences in the phase response of the different antennas. This conclusion is supported by the fact that baseline 2 demonstrates the largest errors. It is expected that baseline 2 will suffer from the largest disparity between the phase patterns of the antennas due to antennas 1 and 3, which form this baseline, lying on diagonally opposite corners of the space-facing facet.

The analysis in Chapter 3 showed that the line bias on the SGR-20 is arbitrary on start-up and whilst it shows a correlation with temperature, no method for independently calibrating or modelling the line bias has yet been found. Therefore line bias was removed via double-differencing for the purposes of this research.

Details of the analysis of spaceflight data and the demonstration of real-time GPS attitude determination using the SGR-20 on Topsat were presented at NAVITEC 2008 [Duncan *et al*, 2008].

8.1.2 Robust multi-epoch integer ambiguity resolution

A new integer ambiguity resolution algorithm was developed which provides a robust solution to the integer ambiguity problem using only single-frequency measurements over multiple epochs. The performance of this algorithm was demonstrated via a combination of Monte-Carlo simulation and post-processing of data logged in-orbit. The Monte-Carlo simulation tested the performance of the algorithm when subject to levels of receiver noise between 2mm and 10mm. The results of this simulation showed that the algorithm calculated the correct solution in nearly 100% of epochs when tracking six satellites, and in over 95% of epochs when tracking five satellites. In the remaining epochs the algorithm reported 'no solution', and no incorrect solutions were given. The simulation results also showed that the new algorithm can provide the correct integer ambiguity solution using only two epochs (or 20 seconds) of data when tracking six satellites, but a minimum of six epochs (or 60 seconds) of data was required to guarantee a correct solution with only five satellites.

The significant novelties of this new algorithm are:

- A formulation is provided showing how to implement a robust multi-epoch algorithm which permits validation of the trial integer ambiguity solutions over a period chosen by the user.
- The algorithm includes a double-difference integer tracking component. This enables the multi-epoch validation to operate in the high dynamics environment of a satellite in LEO when the GPS satellites are rising and setting over much shorter periods than experienced by ground-based users – for which most previous research has been intended.

- Unlike previous research the multi-epoch component of the algorithm is fully documented and the entire algorithm has been shown to work using a large collection of data logged on a microsatellite in-orbit.
- The algorithm was implemented in the flight software of the SGR-20 and its use in real-time onboard the Topsat microsatellite was demonstrated.

The new robust integer ambiguity resolution algorithm was developed by the author based on a method devised by Dr Hodgart, which was presented at ENC 2006 [Duncan, 2006] and is provided for comparison in Appendix B. The original algorithm's main limitation was that it only provided a list of probable integer ambiguity solutions, of which the correct solution was only one of the solutions. The algorithm was also based on using only a single-epoch of data, and so was not robust. The new algorithm built upon the original by adding the statistical tests for the residuals of the secondary set, the baseline length and the relative geometry. The chi-squared test of the attitude residuals was also added. Most importantly, the algorithm was extended to use multiple epochs of data with the capability of tracking the double-difference integer ambiguities, which led to the greatly improved robustness. The improved robust algorithm was first presented at ION GNSS 2007 [Duncan *et al*, 2007], receiving a best paper award at the conference.

8.1.3 Analysis of the performance factors for GPS attitude on small satellites

The concept of ADOP was used to demonstrate the effect that the coplanar baseline geometry on Topsat has on the achievable attitude accuracy. A numerical simulation showed that the ADOP increased by almost a factor of four due to coplanar baselines, relative to the ADOP that would be achieved with triple orthonormal baselines.

The study of ADOP also highlighted that one of the factors limiting the accuracy of the GPS attitude solution on Topsat is that the SGR-20 can only track up to six satellites on each baseline when in its attitude configuration. A simulation showed that a future GNSS attitude receiver, that is able to track all satellites in view, could achieve an overall attitude accuracy of 0.74 degrees, with the yaw estimate accurate to 0.39 degrees, even with coplanar baselines. This is assuming the same level of measurement noise as Topsat, without any form of multipath mitigation, i.e. with no extra effort required. This would be achievable using only the GPS constellation, and could be improved further if more channels and more GNSS satellites are available.

It was also demonstrated that by using the ADCS to estimate the line bias it is actually the mean GPS-ADCS disparity that is being calculated and this results in both an overly optimistic assessment of the performance of the GPS attitude solution and can also hide potential systematic errors in the ADCS attitude solution, thereby removing much of the benefit of GPS as a stand-alone three-axis attitude sensor.

Finally, a numerical simulation was used to demonstrate that an elevation mask of 20° or less should result in 100% availability of the GPS attitude solution. However, a lower elevation mask would be preferable in order to provide a more accurate attitude solution.

8.1.4 Implementation of a real-time GPS attitude sensor

A major component of this work was the integration of the new robust integer ambiguity resolution algorithm and the attitude point solution algorithm into the flight software of the SGR-20. As a result of this work the SGR-20 can now operate as a real-time stand-alone GPS attitude sensor, thereby achieving one of the main aims of the commissioning of this research.

The new algorithms were implemented as an independent task in the SGR-20 flight software and are fully configurable using the SBPP command formats given in Appendix E. A number of new SBPP output packets have also been defined to allow the real-time GPS attitude solution to be logged as part of the standard log file stored on the OBC. This log file can be downloaded by the SSTL ground-station and displayed via the SGR-PC software used to interface with the SGR-20.

Therefore as a result of this work, GPS attitude determination has progressed from the stage of an interesting research area to an operational reality which can be used on future SSTL small satellite missions.

8.1.5 In-orbit demonstration of stand-alone real-time GPS attitude determination

Using the data collected from the Topsat microsatellite a number of important lessons have been learned. Firstly, it has been shown that a GPS attitude sensor can provide a robust stand-alone three-axis attitude solution suitable for use on a microsatellite. It has been shown for the Topsat microsatellite that this attitude solution is likely to be accurate to better than 1° in the pitch and yaw axes, and just over 1° in the roll axis. In Chapter 3 the accuracy of the ADCS reference attitude was estimated by using a comparison of the targeted image centre and the achieved image centre. This analysis showed that due to the roll Earth Horizon Sensor being non-operational the ADCS had a mean offset of 0.60° in pitch and 0.53° in roll with a 1-sigma uncertainty of 0.51° in pitch and 0.89° in roll. Due to this uncertainty about the accuracy of the ADCS reference attitude the GPS attitude solution can only be shown to agree with the ADCS to around two degrees in all axes.

Importantly it has also been shown that a GPS attitude sensor can successfully track large angle manoeuvres in both roll and pitch. Manoeuvres of up to 30° off-pointing in roll and 20° off-pointing in pitch were successfully tracked. This demonstrates an obvious advantage of GPS attitude over Earth Horizon Sensors which cannot track such manoeuvres because they are limited by their 5° field-of-view. If the accuracy of the GPS attitude solution could be improved to around the 0.1-0.2 degree level as suggest in [Wong, 2004] then GPS attitude should prove to be a viable alternative to Earth Horizon Sensors, which currently obtain an accuracy of around 0.3°.

Whilst the hardware limitations imposed by using the SGR-20 resulted in problems with availability of sufficient satellites for integer ambiguity resolution, there were generally at least 4 satellites, which is sufficient to maintain attitude tracking. All the post-processed and real-time experiments showed 100% availability of the GPS attitude solution once attitude tracking had commenced. The only limitation on the availability of the GPS attitude solution was the requirement that at least five satellites are tracked on each baseline in order for the integer ambiguity resolution algorithm to begin. The availability of the GPS attitude solution should only improve given the development of modern GNSS receiver and the continued development of other GNSS constellations such as Galileo, GLONASS and Compass.

8.2 Future work

8.2.1 Improvements to the SGR-20 flight software

The analysis of the real-time experiments conducted using the SGR-20 on Topsat demonstrated that the performance of the GPS attitude algorithms is currently limited by a number of features in the general SGR-20 flight software.

Firstly, the satellite acquisition and tracking algorithms sometimes failed to assign six satellites to all three baselines when analysis of the data files showed that more than six satellites were above the configured elevation mask. Therefore further work is required to optimise the satellite allocation algorithms to ensure the maximum performance can be achieved.

Secondly, the time to first attitude is currently limited by the long time to first fix and the time taken to download sufficient almanacs to enable switching to the 'Highest Elevation' tracking mode. Recent improvements to the SGR-20 flight software now permit orbital elements and the GPS Almanac to be uploaded to the receiver from the OBC in order to 'Warm Start' the receiver. Ongoing testing has shown this allows the receiver to achieve a position fix in around sixty seconds, and then quickly switch to the 'Highest Elevation' tracking mode. Merging these improvements with the attitude algorithms implemented on the experiment software implemented as part of this work would enable a faster time to first attitude.

Thirdly, the level of receiver noise on the SGR-20 is a function of the bandwidth of the carrier tracking loops. The tracking loops on the SGR-20 are currently second order and therefore result in a steady-state error under constant acceleration. Implementing a third-order tracking loop would reduce the loop bandwidth and therefore should also reduce the receiver noise.

8.2.2 Multipath mitigation

Previous research at Surrey Space Centre presented in [Wong, 2004] and [Hodgart and Wong, 2007] demonstrated that the ADCS reference attitude could be used to generate a multipath map that enabled mitigation of the multipath error. This could potentially result in a GPS attitude accuracy of better than 0.2 degrees for a typical microsatellite.

However, to generate the multipath map measurements must be logged over a long period, typically more than 24 hours. This is so the multipath map can provide an estimate for the multipath error over the entire hemisphere visible to the GPS patch antennas. Also, in [Hodgart and Wong, 2006] it was acknowledged that any systematic error in the ADCS reference attitude would effectively be calibrated in to the GPS attitude solution, removing some of the benefit of having an independent three-axis attitude solution. Therefore a potential area of interest for future work is to determine if the GPS residuals can be used to generate an independent multipath map, possibly through some sort of iterative process. This would allow the benefit of the independence of the GPS attitude solution to be maintained, whilst improving the accuracy to a level where it is comparable with Earth Horizon Sensors.

8.2.3 Future receiver designs

SSTL is currently working on a next-generation FPGA-based GNSS receiver that will be capable of tracking multiple frequencies. Whilst this research has shown that it is possible to robustly solve the integer ambiguity problem and track the attitude using only six single-frequency measurements on L1, there are a number of important benefits relating to GPS attitude determination that may come from a new receiver.

It is expected that the new receiver will have at least eight channels per antenna, and possibly up to twelve. This would permit tracking all satellites in view on all antennas. This would provide an immediate improvement in the accuracy of the GPS attitude solution due to the improvement in dilution of precision gained by tracking more satellites. There would also be a corresponding improvement in the availability of the GPS attitude solution since when tracking so many satellites it is unlikely that the GPS attitude solution will have to be reinitialised due to tracking too few satellites on any baselines.

Being able to track multiple frequencies on each baseline will permit other integer ambiguity resolution techniques to be implemented. Given the short baselines possible on most SSTL satellites it should also be possible to take advantage of L1-L2 wide-lane measurements to remove the need for integer ambiguity resolution altogether. However, it remains to be seen if the power and processing constraints imposed on a space-based GNSS receiver will permit multi-frequency GNSS attitude determination.

An important design consideration for a future GNSS receiver would be to try and eliminate line bias from the carrier phase measurements. Past research has shown that some improvements are possible by using multiplexed RF front-end designs [Cohen, 1992], but this still required in-orbit calibration of the line bias [Lightsey et al, 1994]. Investigation in to the relative phase stability of the new generation of RF front-ends and consideration of the line bias problem when developing the new receiver may lead to a method for eliminating this nuisance parameter without resorting to multiplexing architectures.

8.3 In Closing

Development of the SGR-20 began more than fifteen years ago and has resulted in a number of Ph.D. studies relating to GPS attitude determination for microsatellites. The research presented in this thesis has finally demonstrated the capability of the SGR-20 to provide a robust stand-alone three-axis attitude solution suitable for use on microsatellites. Developing on the work presented in [Purivigraipong, 2000] a real-time GPS attitude implementation has been demonstrated. The results from this Ph.D.

research should encourage developers of small satellites such as SSTL to seriously consider including a GPS attitude sensor as part of their standard ADCS baseline for low-cost small satellite missions. Using the upcoming next-generation GNSS receivers the accuracy of such sensors could provide a robust and accurate single sensor solution for attitude determination on small satellites.

Bibliography

[Arbinger *et al*, 2000] Arbinger, C., Enderle, W. (2000) "Spacecraft Attitude Determination using a Combination of GPS Attitude Sensor and Star Sensor Measurements". *Proceedings of the 13th International Technical Meeting of the Satellite Division of the Institute of Navigation, p.2634-2642,* ION GPS 2000, Salt Lake City, UT, September 2000.

[Brown, 1992] Brown, R. A. (1992). "Instantaneous GPS Attitude Determination". *IEEE PLANS 1992. p.113-120,* Position Location and Navigation Symposium, Monteray, CA, March 1992.

[Brown and Ward, 1990] Brown, R. A., Ward, P. (1990). "A GPS Receiver with Built-In Precision Pointing Capability". *IEEE PLANS 1990, p. 83-93,* Position Location and Navigation Symposium, Las Vegas, NV, March 1990.

[Buist *et al*, 2006] Buist, P., Kumagai, S., Hama, K. (2006). "GPS-Based Attitude Determination in different attitude modes: experimenting with a GPS receiver and a star sensor onboard the SERVIS-1 satellite". *Proceedings of the 6th International ESA Conference on Guidance, Navigation and Control Systems, Published on CD-ROM, p78.1,* Loutraki, Greece, October 2006

[Buist, 2007] Buist, P. (2007) "The Baseline Constrained LAMBDA method for Single Epoch, Single Frequency Attitude Determination Applications", *Proceedings of the 20th International Technical Meeting of the Satellite Division of the Institute of Navigation, p.2962 2973,* ION GNSS 2007, Fort Worth, TX, September 2007

[Buist *et al*, 2008] Buist, P., Giorgi, G. (2008) "Single-epoch, Single-Frequency Standalone Full Attitude Determination", *Proceedings of the 4th ESA Workshop on Satellite Navigation User Equipment Technologies,* NAVITEC 2008, ESTEC, Noordwijk, December 2008

[Carpenter and Hain, 1997] Carpenter, J. R., Hain, R. M. (1997) "Precise Evaluation of Orbital GPS Attitude Determination on the STS-77 GPS Attitude and Navigation Experiment (GANE), *Proceedings of the 1997 National Technical Meeting of the Institute of Navigation, p. 387-397,* Santa Monica, CA, January 1997

[Cohen, 1992] Cohen, C. E. (1992). "Attitude Determination using GPS". Ph.D Dissertation, Department of Aeronautics and Astronautics, Stanford University. Doctor of Philosophy, December 1992

[Cohen *et al*, 1992] Cohen, C. E., Cobb, H. S., Parkinson, B. W. (1992) "Two studies of High Performance Attitude Determination using GPS: Generalizing Wahba's problem for High Output Rates and Evaluation of Static Accuracy Using a Theodolite". *Proceedings of the 5th International Technical Meeting of the Satellite Division of the Institute of Navigation, p. 1197-1203,* ION GPS 1992, Albuquerque, NM, September 1992

[Cohen *et al*, 1993] Cohen, C. E., Lightsey, E. G., Feess, W. A., Parkinson, B. W. (1993). "Space Flight Tests of Attitude Determination Using GPS." *Proceedings of the 6th International Technical Meeting of the Satellite Division of the Institute of Navigation, p.625-632,* ION GPS-94, Salt Lake City, UT, September 1993.

[Comp and Axelrad, 1998] Comp, C. J., Axelrad, P. (1998). "Adaptive SNR-Based Carrier Phase Multipath Mitigation Technique." *IEEE Transactions on Aerospace and Electronic Systems* 34(1): 264-276.

[Conway *et al*, 1996] Conway, A., Montgomery, P., Rock, S., Cannon, R. and Parkinson, B. (1996). "A New Motion-Based Algorithm for GPS Attitude Integer Resolution." *NAVIGATION,* Journal of the Institute of Navigation 43(2): 179-190.

[Crassidis *et al*, 1999] Crassidis, J. L., Lightsey, E.G., and Markley, F.L. (1999). "Efficient and Optimal Attitude Determination Using Recursive Global Positioning System Signal Operations." AIAA Journal of Guidance, Control and Dynamics 22(2): 193-201.

[Crassidis *et al*, 1999b] Crassidis, J. L., Lightsey, E.G., and Markley, F.L. (1999). "Global Positioning System Integer Ambiguity Resolution without Attitude Knowledge." AIAA Journal of Guidance, Control and Dynamics 22(6): 212-218.

[Cross and Ziebart, 2003] Cross, P. and Ziebart, M. (2003) "LEO GPS attitude determination algorithm for a micro-satellite using boom-arm deployed antennas" GPS Solutions 6(4): 242-256. Springer Berlin. March 2003.

[Daganzo and Pasetti, 1998] Daganzo, E., and Pasetti, A. (1998). "Attitude Determination Using GPS by MMS/Sextant/GMV: Summary Report". *ETT/059.98/ED,* August 1998

[Donghyun, 1999] Donghyun, K., Langley, R. (1999). "An Optimized Least-Squares Technique for Improving Ambiguity Resolution and Computational Efficiency". *Proceedings of the 12th International Technical Meeting of the Satellite Division of the Institute of Navigation, p.1579-1588,* ION GPS 99, Nashville, TN, September 1999.

[Duncan *et al*, 2006] Duncan, S. M., Hodgart, M. S., Unwin, M. J. (2006) "Investigation of GPS Attitude Determination for Microsatellites", ENC 2006, Manchester, England, 2006

[Duncan, 2007] Duncan, S. M., Hodgart, M.S., Unwin, M. J., Hebden, R. (2007) "In-Orbit Results from a Space-borne GPS Attitude Experiment", *Proceedings of the 20th International Technical Meeting of the Satellite Division of the Institute of Navigation,* p.2412-2423, ION GNSS 2007, Fort Worth Texas, September 2007

[Duncan *et al*, 2008] Duncan, S. M., Unwin, M. J., Hebden, R., Hodgart, M. S. (2008) "In-Orbit Validation of a GPS Attitude Sensor", *Proceedings of the 4th ESA Workshop on Satellite Navigation User Equipment Technologies, NAVITEC 2008*, ESTEC, Noordwijk, December 2008

[Freesland *et al.*, 1996] Freesland, D., Reiss, R., Young, D., Cooper, J., Adams, A. (1996) "GPS Based Attitude Determination: The REX II Flight Experience", *Proceedings of the 10th Annual AIAA/USU Conference on Small Satellites,* Logan, Utah, August 1996

[Gao Y. *et al*, 1996] Gao, Y., McLellan, J. F., Schleppe, J. B. (1996) "An Optimized GPS Carrier Phase Ambiguity Search Method Focusing on Speed and Reliability". IEEE AES Systems Magazine 11(6):22-26, December 2006.

[Godet *et al*, 1999] Godet, J., Dantepal, J. Grondin, M., Belot, D., Baudenon, L., Sourdois, C., Sebbag, I. (1999). "Multipath Error Analysis and Calibration for GPS Differential Phase". *Proceedings of the 1999 National Technical Meeting of the Institute of Navigation, p.512-530,* ION NTM-99, San Diego, CA, January 1999.

[Gomez, 2002] Gomez, S. F. (2002), "Flying High: GPS on the International Space Station and Crew Return Vehicle", *GPS World Magazine*, June 1992

[Gomez and Lammers, 2004] Gomez, S. F., Lammers, M. L. (2004). "Lessons Learned from Two Years of On-Orbit Global Positioning System Experience on International Space

Station". *Proceedings of the 17th International Technical Meeting of the Satellite Division of the Institute of Navigation,* ION GNSS 2004, Long Beach, CA, September 2004.

[Gomez *et al*, 1995]	Gomez, S. F., Panneton, R. J., Saunders, P. E., Hwu, S. U., and Lu, B. P. (1995). "GPS Multipath Modelling and Verification Using Geometrical Theory of Diffraction". *Proceedings of the 8th International Technical Meeting of the Satellite Division of the Institute of Navigation, p.195-204,* ION GPS-95, Palm Spring, CA, September 1995.
[Han and Rizos, 1996]	Han, S., Rizos, C. (1996) "Integrated Method for Instantaneous Ambiguity Resolution Using New Generation GPS Receivers". *IEEE PLANS 1996, p. 254-261,* Position Location and Navigaiton Symposium, Atlanta, GA, April 1996.
[Hashida, 1997]	Hashida, Y. (1997) "ADCS for Future UoSAT Standard Platform", *Internal Document (Not published),* Surrey Satellite Technology Limited, January 1997
[Hatch, 1991]	Hatch, R. (1991) "Instantaneous Ambiguity Resolution", *Proceedings of IAG Internation Symposium No. 107 on Kinematic Systems in Geodesy, Surveying and Remote Sensing, p. 299-308,* Springer Verlag, New York
[Hatch, 1991]	Hatch, R. (1991). "Ambiguity Resolution While Moving - Experimental Results", *Proceedings of the 4th International Technical Meeting of the Satellite Division of the Institute of Navigation, p. 707-714,* ION GPS 91, Albuquerque, NM, September 1991.
[Hatch, 1994]	Hatch, R. (1994). "Comparison of Several AROF Kinematic Techniques". *Proceedings of the 7th International Technical Meeting of the Satellite Division of the Institute of Navigation, p. 363-370,* ION GPS 94, Salt Lake City, UT, September 1994.
[Hodgart *et al*, 1999]	Hodgart, M. S., Hashida, Y., Steyn, W. H. (1999) "Enhanced Low-Cost Attitude Control of a Microsatellite", *Proceedings of the 4th ESA International Conference on Spacecraft Guidance, Navigation and Control Systems,* ESTEC, Noordwijk, October 1999

[Hodgart, 1982]	Hodgart, M. S. (1982) "Attitude Control and Dynamics of UoSAT Angular Motion", *Radio and Electronic Engineer*, Vol. 52, No. 8-9, Aug-Sep 1982
[Hodgart, 1989]	Hodgart, M. S. (1989) "Gravity Gradient and Magnetorquing Attitude Control for Low-Cost Low-Earth-Orbit Satellites: The UoSAT Experience", Ph.D. Thesis, University of Surrey, 1989
[Hodgart *et al*, 2000]	Hodgart, M. S., Purivigraipong, S. (2000). "New Approach to Resolving instantaneous integer ambiguity resolution for spacecraft attitude determination using GPS signals". *IEEE PLANS 2000, p. 132-139*, Position Location and Navigation Symposium, San Diego, CA, March 2000.
[Hodgart and Wong, 2006]	Hodgart, M. S., Wong, R. (2006) "Statistically Optimised In-Flight Estimation of GPS Carrier Phase Multipath for LEO Satellite Attitude Determination", *Navigation*, Journal of the Institute of Navigation, Vol. 53, No. 3, Fall 2006.
[Hofmann-Wellenhof, 2001]	Hofmann-Wellenhof, B., Lichtenegger, H., Collins, J. (2001). "GPS Theory and Practice". New York, Springer-Verlag/Wien.
[Kaplan, 1996]	Kaplan, E. D. (1996). "Understanding GPS Principles and Applications". Artech House Publishers.
[Kee *et al*, 2003]	Kee, C., Jang, J., Sohn, Y. (2003) "Efficient Attitude Determination Algorithm Using Geometrical Concept: SNUGLAD", *Proceedings of the 2003 National Technical Meeting of the Institute of Navigation, p. 142-151*, ION NTM 2003, Anaheim, CA, January 2003
[Kee *et al.*, 2007]	Kee, C., Kim, D., Jang, J. (2007) "Efficient Ambiguity Search Technique Using Separated Decision Variables", *NAVIGATION, The Journal of Navigation*, Vol. 60, pg 147-157, January 2007
[Kim *et al.*, 2004}	Kim, U. S., De Lorenzo, D., Gautier, J., Enge, P. (2004) "Phase Effects Analysis of Patch Antenna CRPAs for JPALS", *Proceedings of the 17th International Technical Meeting of the Satellite Division of the Institude of Navigation, p. 1531-1538, ION GNSS 2004*, Long Beach, CA, September 2004
[Knight, 1994]	Knight, D. (1994). "A New Method of Instantaneous Ambiguity Resolution" *Proceedings of the 7th International Technical Meeting of the Satellite*

Division of the Institute of Navigation, p. 707-716, ION GPS-94, Salt Lake City, UT, September 1994.

[Lightsey *et al.*, 1994] Lightsey, G. E., Cohen, C. E., Parkinson, B. W. (1994) "Analysis of Spacecraft Attitude Measurements using Onboard GPS", *Proceedings of the 17th Annual AAS Rocky Mountain Guidance and Control Conference, p. 521-532*, Keystone, CO, February 1994.

[Lightsey, 1997] Lightsey, G. (1997). "Development and Flight Demonstration of a GPS Receiver for Space", Ph.D dissertation, Stanford University. 1997.

[Lopes and Milani, 2000] Lopes, R. V. F. a. Milani, P. G. (2000). "Consistent On-Board Multipath Calibration for GPS-Based Spacecraft Attitude Determination". *Proceedings of the 13th International Technical Meeting of the Satellite Division of the Institute of Navigation, p. 2216-2226,* ION GPS 2000, Salt Lake City, UT, September 2000.

[Lu, 1995] Lu, G. (1995). "Development of a GPS Multi-Antenna System for Attitude Determination", Ph.D. dissertation, University of Calgary. 1995.

[Martin-Neira *et al*, 1995] Martin-Neira, M., Toledo, M., Pelaez, A. (1995). "The Null Space Method for GPS Integer Ambiguity Resolution". *Proceedings of DSNS'95*, Bergen, Norway, April 1995.

[Misra and Enge, 2001] Misra, P., Enge, P. (2001). "Global Positioning System - Signals, Measurements, and Performance". *Ganga-Jamuna Press*, Lincoln, Massachussetts. 2001

[Monikes *et al*, 2005] Monikes, R., Wendel, J., Trommer, G. F. (2005) "A Modified LAMBDA Method for Ambiguity Resolution in the Presence of Position Domain Constraints." *Proceedings of the 18th International Technical Meeting of the Satellite Division of the Institute of Navigation, p. 81-87, ION GNSS 2005,* Long Beach, CA, September 2005.

[Moon and Verhagen, 2006] Moon, Y., Verhagen, S. (2006) "Integer Ambiguity Estimation and Validation in Attitude Determination Environments", *Proceedings of the 19th International Technical Meeting of the Satellite Division of the Institute of Navigation, p. 335-344,* ION GNSS 2006, Fort Worth, TX, September 2006.

[Morros, 1995] Morros, D. (1995). "Phase Difference for Attitude Determination using a Dual Antenna GPS Receiver", M.Sc. Dissertation, University of Surrey. 1995.

[NGA, 2004] National Geospatial-Intelligence Agency, "DoD – World Geodetic System 1984", http://earth-info.nga.mil/GandG/publications/tr8350.2/tr8350_2.html

[Pratt *et al*, 1997] Pratt, M., Burke, B. and Misra, P. (1997). "Single-Epoch Integer Ambiguity Resolution with GPS L1-L2 Carrier Phase Measurements". *Proceedings of the 10th International Technical Meeting of the Satellite Division of the Institute of Navigation, p. 1737-1746,* ION GPS-97, Kansas City, MO, September 1997.

[Purivigraipong, 1998] Purivigraipong, S., Hashida, Y., Unwin, M. J. (1998). "Novel Algorithms for Modelling Vector Observations for Spacecraft Attitude Determination Using GPS Signals". *Proceedings of the 11th International Technical Meeting of the Satellite Division of the Institute of Navigation, p. 1773-1782,* ION GPS 1998, Nashville, TN, September 1998.

[Purivigraipong, 1999] Purivigraipong, S., Hashida, Y., Unwin, M. J. (1999). "GPS Attitude Determination for Microsatellites". *Proceedings of the 12th International Technical Meeting of the Satellite Division of the Institute of Navigation, p. 2017-2026,* ION GPS 1999, Nashville, TN, September 1999.

[Purivigraipong, 1999b] Purivigraipong, S., Hodgart, M. S., Hashida, Y., Unwin, M. J. (1999). "New Approach to Achieving Stand Alone GPS Attitude Determination using Dual Short Baselines for Small-Satellites". *Proceedings of the 13th Annual AIAA/USU Conference on Small Satellites,* Logan, UT, August 1999.

[Purivigraipong, 2000] Purivigraipong, S. (2000). "Study of Spacecraft Attitude Determination from Phase Information of GPS Signals. Surrey Space Centre", *Ph.D Thesis,* University of Surrey. Doctor of Philosophy, 2000.

[Purivigraipong, 2000b] Purivigraipong, S., Hashida, Y., Unwin, M. J. (2000). "Demonstrating GPS Attitude Determination from UoSat-12 Flight Data". *Proceedings of the 13th International Technical Meeting of the Satellite Division of the Institute of Navigation, p. 2625-2633,* ION GPS 2000, Salt Lake City, UT, September 2000.

[Quinn, 1993] Quinn, P. G. (1993). "Instantaneous GPS Attitude Determination". *Proceedings of the 6th International Technical Meeting of the Satellite Division of the Institute of Navigation, p. 603-615,* ION GPS 1993, Salt Lake City, UT, September 1993.

[Ray and Cannon, 1999] Ray, J. K., Cannon, M. E. (1999). "Characterization of GPS Carrier Phase Multipath". *Proceedings of the 1999 National Technical Meeting of the Institute of Navigation, p. 343-352,* ION NTM 1999, San Diego, CA, January 1999.

[Reichert and Axelrad, 1997] Reichert, A. K., Axelrad, P. (1997). "Algorithms for Calibration of Multipath Errors Using Micro-mechanical Gyros", Draper Lab.

[Reichert, 1999] Reichert, A. K. (1999). "Correction Algorithms for GPS Carrier Phase Multipath Utilizing the Signal-to-noise Ratio and Spatial Correlation". *Ph.D Thesis,* Department of Aerospace Engineering Sciences, University of Colorado. Doctor of Philosophy, 1999.

[Schuster and Oh, 1981] Schuster, M. D., Oh, S. D. (1981). "Three-Axis Attitude Determination from Vector Observations" *Journal of Guidance and Control* 4(1):70-77. January-February 1981.

[Simsky *et al*, 2005] Simsky, S., Vander Kuylen, L. and Boon, F. (2005). "Single-board Attitude Determination System Based on the PolaRx2@ GPS Receiver". *Proceedings of ENC GNSS 2005*, Munich, Germany, July 2005.

[Souza, 2004] Souza, E. M. (2004). "Multipath Reduction from GPS Double Differences using Wavelets: How far can we go?" *Proceedings of the 17th Internation Technical Meeting of the Satellite Division of the Institute of Navigation, p. 2563-2571,* Long Beach, CA, September 2004.

[SSTL, 1999] SSTL (1999) "SGR PLL Implementation", Reference Document P0524/018, Surrey Satellite Technology Limited, March 1999.

[SSTL, 2009a] SSTL (2009) "Star Tracker - Altair HB+ Datasheet", http://www.sstl.co.uk/assets_sstl/Downloads/starcamera%20altairHBplus%20v1_00.pdf, Surrey Satellite Technology Limited, 2009

[SSTL, 2009b] SSTL (2009) "SGR-10/20 User Manual", *Internal Document ST# 0000628*, Surrey Satellite Technology Limited, 2009

[Steyn, 1995] Steyn, W. H. (1995) "A Multi-mode Attitude Determination and Control System for Small Satellites", Ph.D. Dissertation, University of Stellenbosch, 1995

[Steyn, 1998] Steyn, W. H. (1998) "AODCS System Assessment for UoSAT-12", *Internal Document*, Surrey Satellite Technology Limited, October 1998

[Steyn and Hashida, 1999] Steyn, W. H., Hashida, Y. (1999) "In-Orbit Attitude and Orbit Control Commissioning of UoSAT-12", *Proceedings of the 4th ESA International Conference on Spacecraft Guidance, Navigation and Control Systems*, ESTEC, Noordwijk, October 1999

[Strang and Borre, 1997] Strang, G., Borre, K. (1997) "Linear algebra, Geodesy and GPS" *Wellesley-Cambridge Press*, Wellesley, MA, ISBN 0906140863

[Teunissen, 1994] Teunissen, P. J. G. (2004) "A New Method for Fast Carrier Phase Ambiguity Estimation". *IEEE PLANS 1994, p. 562-573*, Position Location and Navigation Symposium, Las Vegas, NV, April 1994.

[Teunissen, 1995] Teunissen, P. J. G. (1995). "The least-squares ambiguity decorrelation adjustment: a method for fast GPS integer ambiguity resolution". Delft Geodetic Computing Centre, Delft University of Technology, Journal of Geodesy 70: 65-82.

[Teunissen, 1998] Teunissen, P. J. G. (1998). "Success Probability of integer GPS ambiguity rounding and bootstrapping." Journal of Geodesy 72: 606-612.

[Teunissen, 2001] Teunissen, P. J. G. (2001). "Statistical GNSS Carrier Phase Ambiguity Resolution: A Review". *Proceedings of the 11th IEEE Signal Processing Workshop, p. 4-12*, 2001.

[Um and Lightsey, 2000] Um, J., Lightsey, E. G. (2000). "Space Flight Test Results for the SOAR Experiment". *Proceedings of the 13th International Technical Meeting of the Satellite Division of the Institute of Navigation, p. 2243-2251*, ION GPS 2000, Salt Lake City, UT, September 2000.

[Unwin, 1995] Unwin, M. J. (1995). "The Design and Implementation of a Small Satellite Navigation Unit Based on a Global Positioning System Receiver", *Ph.D. Dissertation*, University of Surrey, 1995.

[Urhan, 2002] Urhan, H. (2002) "Engineering Study of the GPS System for Satellite Attitude Determination", *M.Sc. Dissertation*, University of Surrey, August 2002

[Verhagen & Teunissen, 2004] Verhagen, S., Teunissen, P. J. G. (2004) "PDF Evaluation of the Integer Ambiguity Residuals", *Proceedings V Hotine-Marussi Symposium of Theoretical and Computational Geodesy, p. 120-128*, 2004

[Wahba, 1965] Wahba, G. (1965). "A Least Squares Estimate of Spacecraft Attitude." SIAM Review 7(3): 409.

[Ward, 1996] Ward, L. M. (1996). "Spacecraft Attitude Determination using GPS: Methodology and Results". *Ph.D. Dissertation*, Department of Aerospace Engineering Sciences, University of Colorado. Doctor of Philosophy. 1996

[Weill, 1995] Weill, L. R. (1995). "A Pointing System Requiring No Ambiguity Resolution: Theory, Design, and Performance". *Proceedings of the 1995 National Technical Meeting of the Institute of Navigation, p. 803-812*, Anaheim, CA, January 1995.

[Wertz, 1978] Wertz, J. R. (1978). "Spacecraft Attitude Determination and Control". Kluwer Academic Publishers, Boston, MA, 1978.

[Wong, 2004] Wong, R. T. M. (2004). "GPS Carrier Phase Multipath Mitigation by Spectral Analysis for LEO Satellite". *Ph.D. Dissertation*, University of Surrey. 2004.

[Yoon and Lundberg, 2001] Yoon, S., Lundberg, J. B. (2001) "Euler Angle Dilution of Precision in GPS Attitude Determination", *IEEE Transactions on Aerospace and Electronic Systems*, Vol. 37, No. 3, July 2001

Appendix A MATLAB-based GPS attitude simulator

This appendix describes the MATLAB based GPS attitude simulator developed to allow repeatable testing of the algorithms studied. MATLAB was chosen as the preferred tool since it was available at Surrey Space Centre and enabled fast implementation and testing of the various algorithms devised as part of this work.

The MATLAB based simulator simulates the true constellation geometry for a satellite in Low Earth Orbit. It generates realistic single-difference carrier phase measurements for any number of baselines. The simulator allows both receiver noise and multipath to be simulated based on the model presented in Chapter 2. The simulator allows the spacecraft attitude to be changed on an epoch-by-epoch basis permitting simulation of large angle manoeuvres like those seen on Topsat. The simulator also provides truth data such as the true integer ambiguities and the orbit-referenced baseline vectors to aid in the analysis of the various algorithms tested.

A general overview of the simulation is shown in Figure A-1, and each stage is outlined in the following sections.

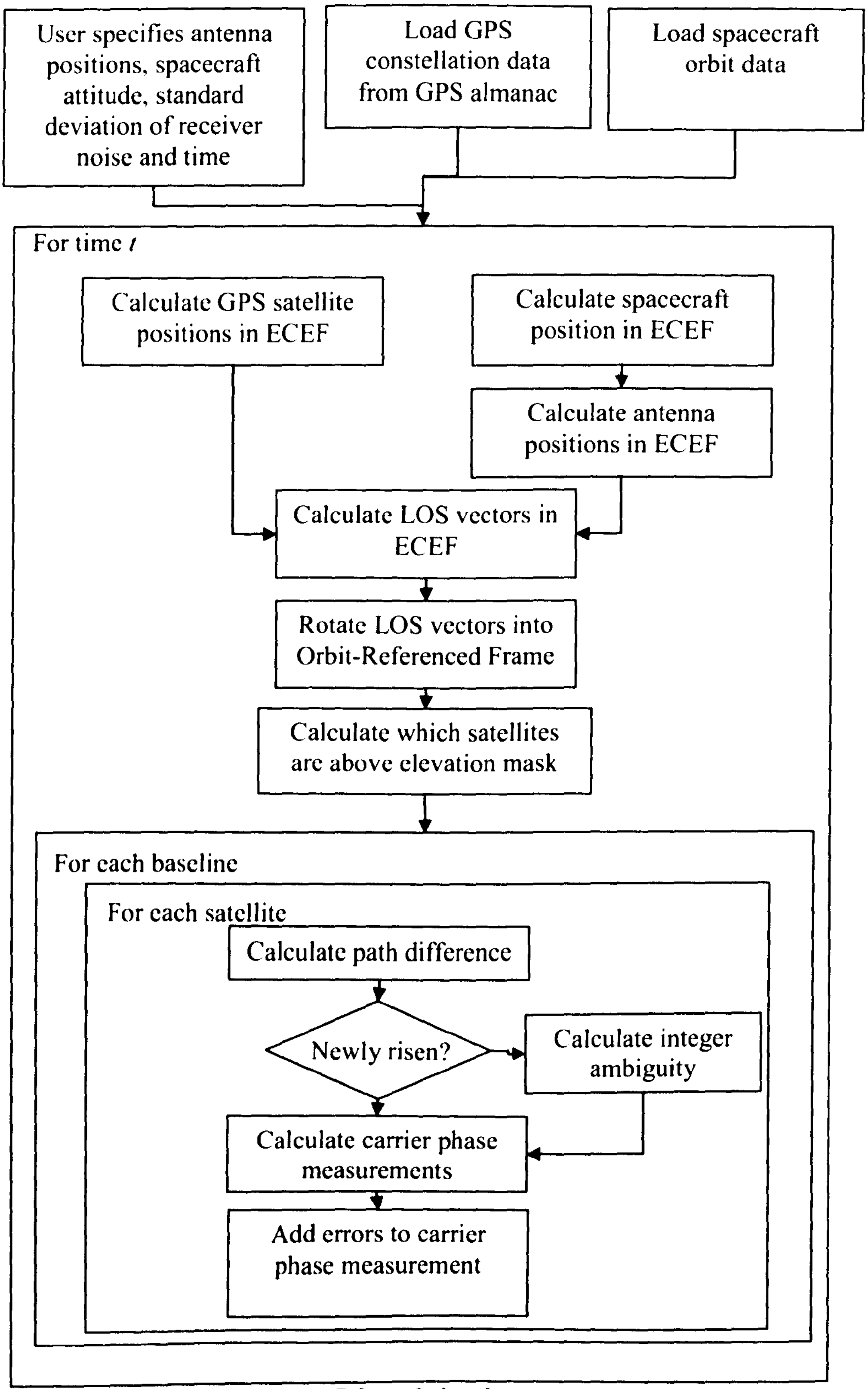

Figure A-1 Overview of MATLAB based simulator

A.1 Simulating the GPS constellation

The MATLAB based simulator uses a Yuma format GPS almanac provided by the user to calculate the position of the entire GPS constellation for a given epoch. The GPS satellite positions are calculated in the Earth-Centred-Earth-Fixed (ECEF) frame. This method was chosen rather than generating random constellation geometry in each epoch. It should provide a more realistic simulation of the effects of constellation geometry on integer ambiguity resolution and attitude determination, meaning that the simulation results should more closely match the results achievable in orbit.

The MATLAB scripts used to calculate the position of the GPS satellites were taken from [Strang and Borre, 1997]. The scripts use the information provided by the Yuma format GPS almanac to calculate the position of each GPS satellite at a time specified by the simulation. The almanac used for all simulations is given at the end of this appendix.

A.2 Simulating spacecraft motion

The routines used to simulate the position of the GPS satellites were also used to simulate the orbital position of a small satellite in LEO. This was achieved by generating a Yuma format GPS almanac file describing the orbital parameters of a typical SSTL mission i.e. a 686km Sun-Synchronous orbit. The Yuma format GPS almanac file used is shown in Figure A-2 below.

```
******** Week  338 almanac for Topsat ********
ID:                          35
Health:                      000
Eccentricity:                0.0016453
Time of Applicability(s):   503808.0000
Orbital Inclination(rad):    1.71308603939299
Rate of Right Ascen(r/s):   -0.7600316584E-008
SQRT(A)  (m 1/2):            2657.81865446083
Right Ascen at Week(rad):   2.41346223360878
Argument of Perigee(rad):   -0.909812213796612
Mean Anom(rad):             0.909309558972038E+001
Af0(s):                      0.3719329834E-004
Af1(s/s):                    0.3637978807E-011
week:                        338
```

Figure A-2 Yuma format GPS almanac used to simulate spacecraft orbit

A.3 Generation of carrier phase measurements and LOS vectors

The simulator calculates the position of the GPS satellites and the user position for a given epoch k as described above.

The LOS vectors are generated by calculating the vector relating the user position $\mathbf{x}_{user}$ and the GPS satellite position $\mathbf{x}_{GPS,j}$ and normalising it.

$$\mathbf{s}_{i,j,ECEF}[k] = \frac{\mathbf{x}_{GPS,j}[k] - \mathbf{x}_{user}[k]}{\left\| \mathbf{x}_{GPS,j}[k] - \mathbf{x}_{user}[k] \right\|} \qquad \textbf{A-1}$$

The LOS vectors are then rotated into the orbit-referenced frame

$$\mathbf{s}_{i,j(O)}[k] = \mathbf{T}[k]\mathbf{s}_{i,j,ECEF}[k] \qquad \textbf{A-2}$$

where $\mathbf{T}$ is calculated as shown in Appendix C. The satellites in view are determined assuming a nadir pointing attitude for the spacecraft and an elevation mask of zero degrees with respect to the –Z facet of the spacecraft as shown in Figure A-3.

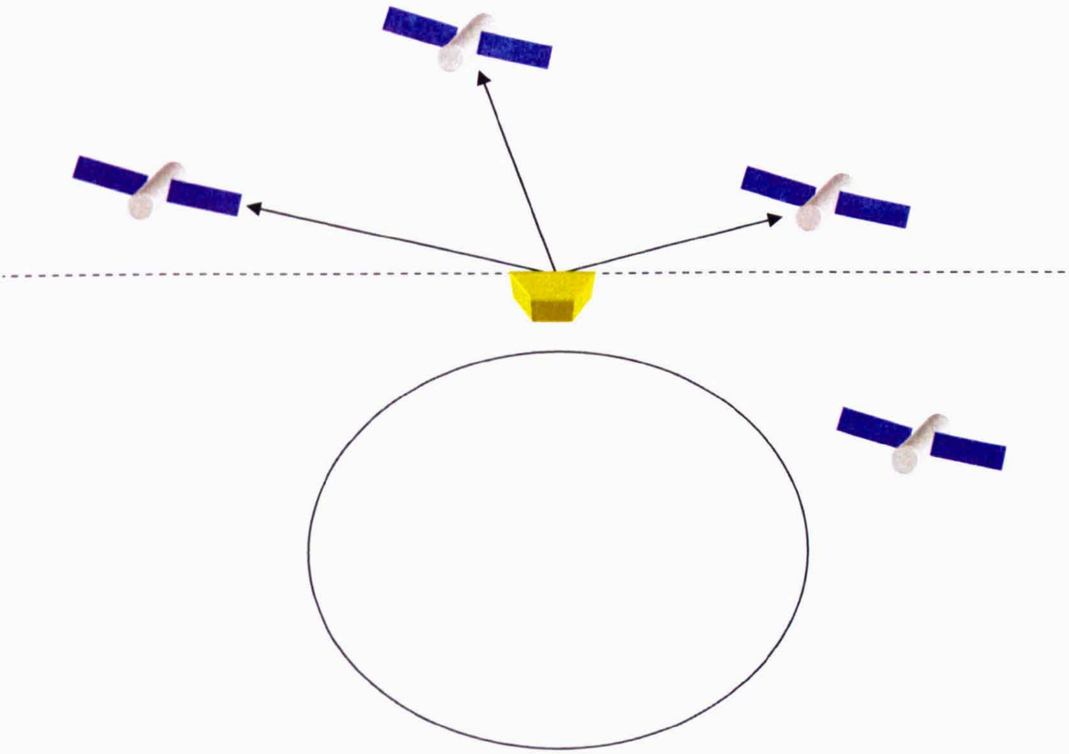

Figure A-3 Satellite visibility is calculated based on an elevation mask

For each baseline the orbit-referenced baseline vector is calculated according to

$$\mathbf{b}_{i(O)}[k] = \mathbf{A}^{T}[k]\mathbf{b}_{i(B)} \qquad \textbf{A-3}$$

where $\mathbf{b}_{i,(B)}$ is calculated from the antenna positions passed to the simulator as inputs.

The true path difference (in cycles) for each satellite on each baseline is then calculated as

$$\vec{r}_{i,j}[k] = \mathbf{b}^T_{i(O)}[k]\mathbf{s}_{i,j(O)}[k] \tag{A-4}$$

The simulator maintains a log of which satellites were visible in the previous epoch and uses this to determine if a satellite has just risen. If the satellite has just risen the simulator calculates its integer ambiguity according to

$$N_{i,j} = round\left(\vec{r}_{i,j}[k]\right) \tag{A-5}$$

Each integer is stored in a look-up table and a validity flag is set. If the satellite was present in the previous epoch, but has set in the current epoch then the integer value is cleared from the look-up table, and the validity flag is cleared to say it is invalid.

Next the accumulated carrier phase measurement is calculated using

$$\bar{r}_{i,j}[k] = \vec{r}_{i,j}[k] + N_{i,j} \tag{A-6}$$

Note that the same integer ambiguity is used in each epoch to replicate the accumulated carrier phase measurements output by the SGR-20. Finally receiver noise and multipath (if required) are added to the measurements as described in the next sections.

A.4 Simulating Receiver Noise

As described in Chapter 2, the term *receiver noise* is used to define zero mean random noise having a Gaussian distribution with a known standard deviation. The MATLAB based simulator requires the user to specify the standard deviation of the receiver noise. Given a standard deviation by the user the simulation uses the MATLAB 'randn' function to generate thirty-two vectors (one per simulated GPS satellite) each containing zero mean random noise with a Gaussian distribution and a standard deviation of unity. Each vector contains 86,400 epochs of random noise to allow the simulation to run for one whole day if required. All the vectors are then scaled using the standard deviation specified by the user.

In any particular epoch k a sample of the receiver noise from the vector relating to each satellite is added to the accumulated carrier phase measurement

$$\bar{r}_{i,j}[k] = \vec{r}_{i,j}[k] + N_{i,j} + v_{i,j}[k] \tag{A-7}$$

To demonstrate the effect of receiver noise on the GPS residuals (as calculated in Chapter 3) the MATLAB-based simulator was used to simulate one hour of constellation motion sampled at ten second intervals. Four millimetres of receiver noise was added to the single-difference carrier phase measurements. The procedure detailed in Chapter 3 was used to calculate the GPS residuals and the results are shown in Figure A-4 below.

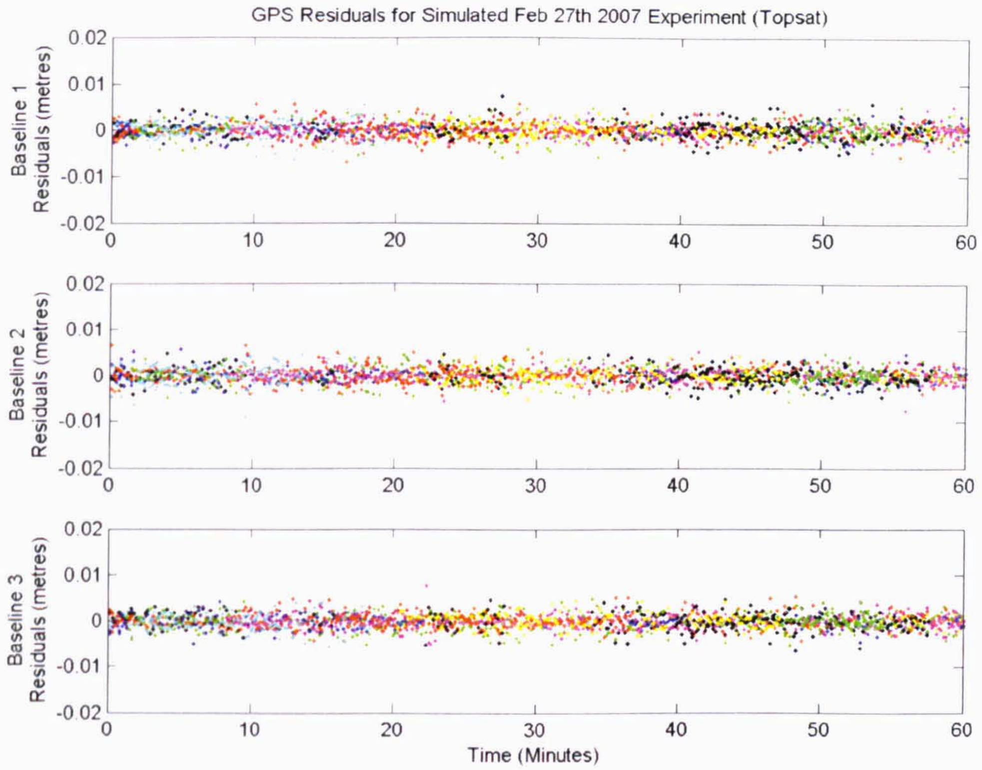

Figure A-4 GPS residuals for simulated 27th February 2007 experiment with receiver noise only

Note that since the measurement errors are due to receiver noise, which has a Gaussian distribution with zero mean, the GPS residuals are also Gaussian with zero mean.

A.5 Simulating multipath

A common method for simulating multipath is to use a Gauss-Markov process with a time period of around five minutes [Ward, 1996]. However, for a small spacecraft it has been shown [Wong, 2004] that the multipath is fixed relative to the spacecraft's structure, meaning that the multipath error is spatially correlated as well as being correlated in time. Using a Gauss Markov process only simulates the time correlation, and does not simulate any correlation between the incident angle of the incoming signal and the multipath error.

Therefore to better replicate the multipath error experienced by a small satellite a simulated multipath map was created. [Wong, 2004] showed that the spatial correlation of the multipath error allowed it to be mapped as a function of the azimuth and elevation of the incoming signal. Wong then used this multipath map as a form of look-up table to apply corrections to the carrier phase measurements. Here the process is reversed. Using a simulated multipath map, multipath error is applied to the carrier phase measurements based on the azimuth and elevation of the LOS vector for each satellite. This is based on a function

$$u_{i,j}[k]=f(\theta,\phi) \qquad \textbf{A-8}$$

where the multipath error $u_{i,j}[k]$ is calculated from a look-up table which is indexed by the azimuth (θ) and elevation (ϕ) of the LOS vector for satellite j on baseline i.

A.5.1 Generating the multipath look-up table

During the development of their latest patch antenna SSTL performed a series of measurements in an anechoic chamber facility. The main purpose of these tests was to measure the gain of a new antenna design and compare it with the gain of a heritage patch antenna. However, these tests also included measuring the phase response of both antennas to see how the measured phase varies depending on the incident signal direction. To calculate the phase response a measurement probe is moved in a sphere around the antenna under test and takes measurements in the near field of the antenna.

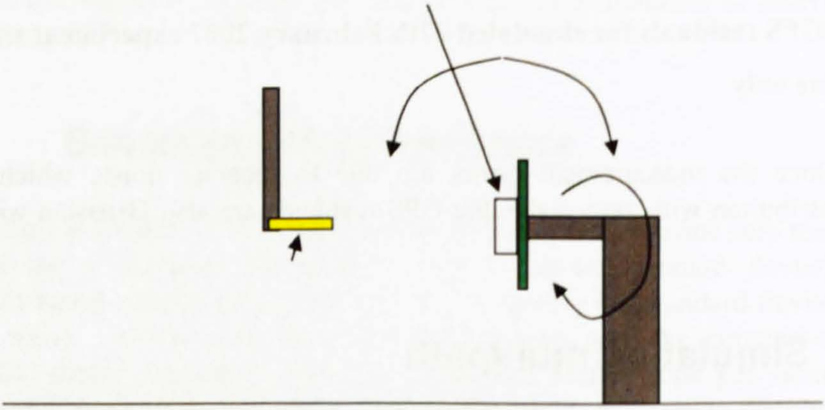

Figure A-5 Measuring the antenna phase response

These measurements are then used to calculate the far-field phase response using a series of complex transforms. The result is a phase error plot such as that shown in Figure A-6.

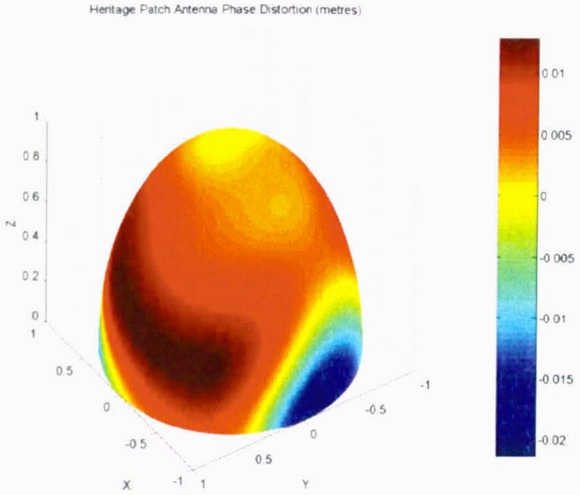

Figure A-6 Hemi-spherical projection of patch antenna phase error

The plot in Figure A-6 shows the phase error for a single patch antenna as a function of azimuth and elevation (with zero degrees azimuth at (-1, 0, 0) and zero degrees elevation at z = 0). Note that in certain directions the phase error can exceed 2cm. The map is not a true reflection of the antenna phase error on TopSat since the lack of a sufficient ground-plane along two sides of each patch antenna (due to their positions in the corners of the –Z facet) will likely result in a dramatically different phase error.

The effect of the phase error of the antennas is worsened for GPS attitude determination since measurements from multiple antennas are differenced. It is assumed that each antenna will have a different phase error due to its different location on the spacecraft. Therefore to approximate the errors likely to be experienced on TopSat the phase error map was rotated 180 degrees in azimuth and differenced from the un-rotated map to match the orientations of the patch antennas on TopSat. The result is shown in Figure A-7.

To demonstrate the effect of multipath on the GPS residuals the MATLAB-based simulator was used to simulate one hour of constellation motion sampled at ten second intervals. Four millimetres of receiver noise was added to the single-difference carrier phase measurements as with the receiver noise only simulation. The multipath map described above was used as a look-up table to add multipath error to each carrier phase measurement depending on the azimuth and elevation of its LOS vector. Again the GPS residuals were calculated using the method in Chapter 3 and the results are plotted in Figure A-8.

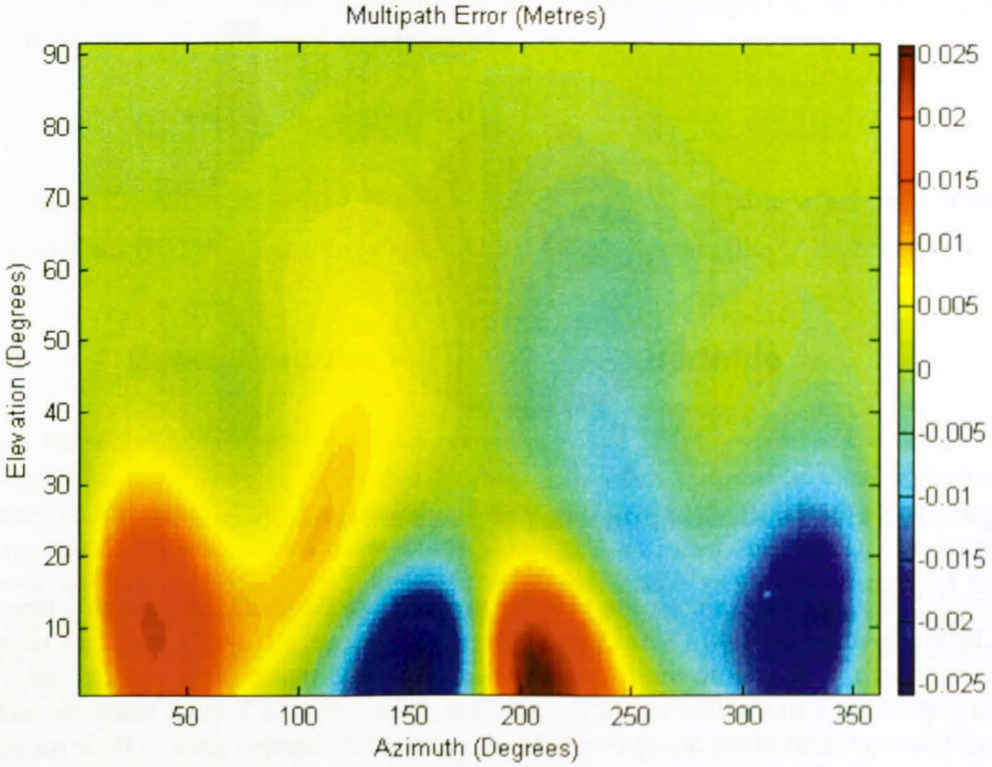

Figure A-7 Simulated multipath map generated from anechoic chamber measurements

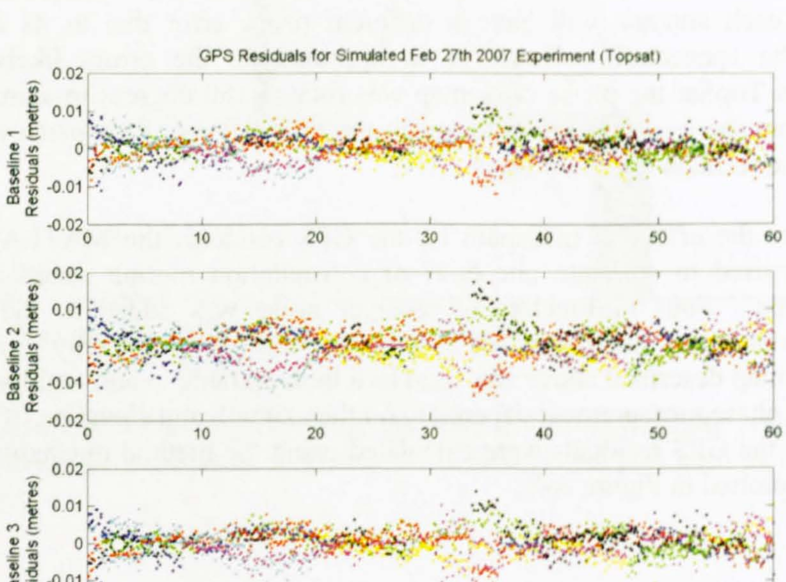

Figure A-8 GPS residuals for simulated 27th February 2007 experiment with receiver noise and multipath

The different coloured GPS residuals in Figure A-8 each relate to a different GPS satellite and hence carrier phase difference measurement. It is obvious from the above plot that the individual GPS residuals are now correlated, which was not the case for the receiver noise only simulation. This demonstrates that in the presence of multipath (which is a spatially correlated error) the GPS residuals become correlated. Note that this correlation appears to be a time correlation due to the relative motion of the receiver and the GPS constellation.

A.6 Effect of ADCS Error on GPS-ADCS Residuals

A series of simulations was conducted to establish the effect an error in the ADCS attitude solution would have on the GPS-ADCS disparity as calculated in Chapter 3. The MATLAB-based simulator was used to generate one hour of constellation motion. The simulation was configured to add 1.4mm of receiver noise to the single-difference carrier phase measurements. Multipath was not simulated. The ADCS attitude from the experiment conducted on 27th February 2007 was used as an input to the MATLAB-based simulator. A constant error of 1.5 degrees was added to the roll value reported by the ADCS. The GPS-ADCS disparity was then calculated using the method shown in Chapter 3. The simulation was repeated with a 1.5 degree error in pitch and again with a 1.5 degree error in yaw. The results are shown in the figures below.

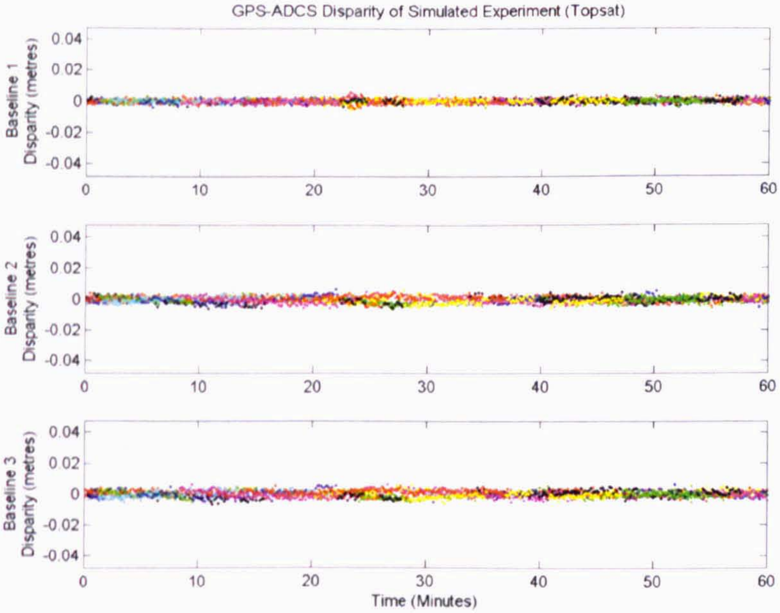

Figure A-9 GPS-ADCS disparity when ADCS roll estimate is subject to 1.5 degree error

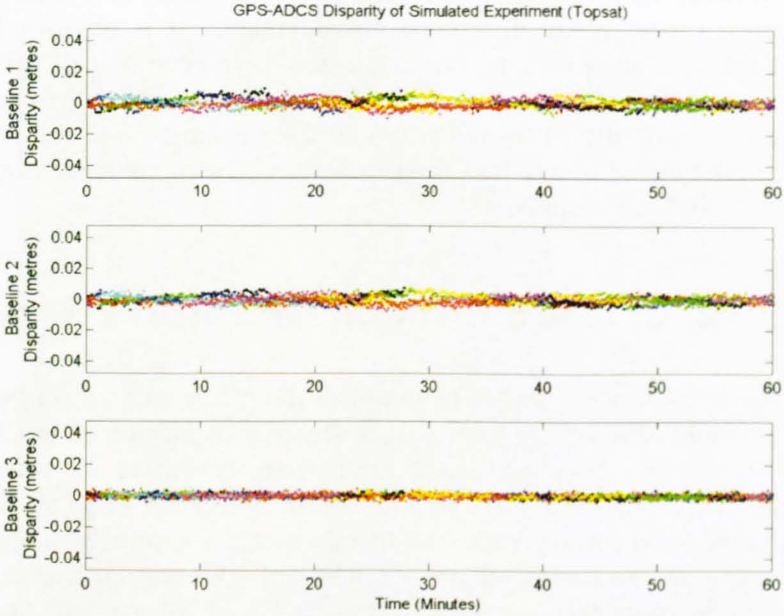

Figure A-10 GPS-ADCS disparity when ADCS pitch estimate is subject to 1.5 degree error

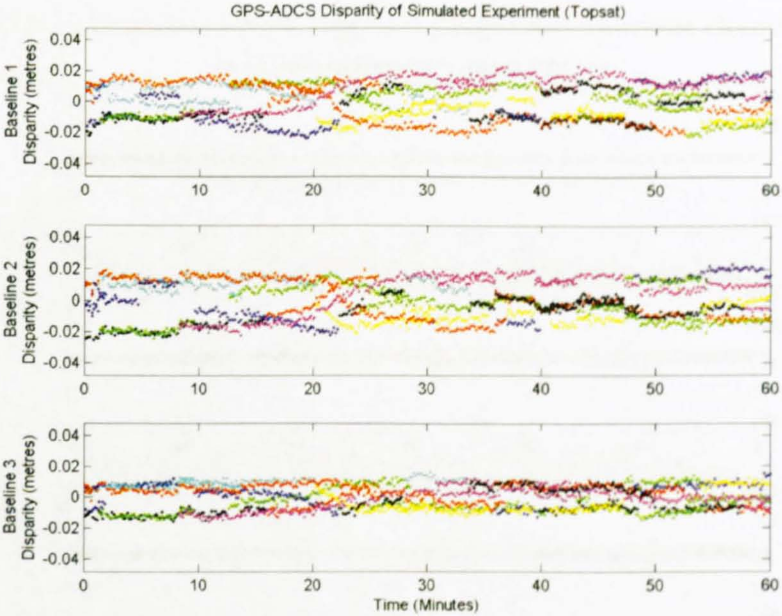

Figure A-11 GPS-ADCS disparity when ADCS yaw estimate is subject to 1.5 degree error

The above figures show that the effect of an ADCS error is dependent on which axis the error is present. The geometry of the baselines when the spacecraft is maintaining a nadir pointing attitude means that an ADCS roll error couples into baselines 2 and 3, whereas an ADCS pitch error couples into baselines 1 and 2. In both cases for a 1.5 degree error the effect on the GPS-ADCS is subtle, but there is an observable correlation in the disparities.

The effect of an ADCS yaw error is more pronounced and couples in to all three baselines. As can be seen from the above figures a 1.5 degree error in yaw can result in GPS-ADCS disparities of centimetres, which could be misinterpreted as multipath if the ADCS attitude solution is relied on too heavily.

A.7 Yuma format GPS Almanac used in simulations

```
******** Week  338 almanac for PRN-01 ********
ID:                         01
Health:                     000
Eccentricity:               0.6318092346E-002
Time of Applicability(s):  503808.0000
Orbital Inclination(rad):   0.9866876018
Rate of Right Ascen(r/s):  -0.7600316584E-008
SQRT(A)  (m 1/2):           5153.638672
Right Ascen at Week(rad):  -0.1968275991E+001
Argument of Perigee(rad):  -1.707152089
Mean Anom(rad):            -0.1272841157E+001
Af0(s):                     0.3719329834E-004
Af1(s/s):                   0.3637978807E-011
week:                        338

******** Week  338 almanac for PRN-02 ********
ID:                         02
Health:                     000
Eccentricity:               0.9141445160E-002
Time of Applicability(s):  503808.0000
Orbital Inclination(rad):   0.9511124301
Rate of Right Ascen(r/s):  -0.8263201338E-008
SQRT(A)  (m 1/2):           5153.590820
Right Ascen at Week(rad):   0.2182517979E+001
Argument of Perigee(rad):   1.978523627
Mean Anom(rad):             0.1886912466E+000
Af0(s):                    -0.1811981201E-004
Af1(s/s):                   0.0000000000E+000
week:                        338

******** Week  338 almanac for PRN-03 ********
ID:                         03
Health:                     000
Eccentricity:               0.7876873016E-002
Time of Applicability(s):  503808.0000
Orbital Inclination(rad):   0.9263590136
Rate of Right Ascen(r/s):  -0.8114623721E-008
SQRT(A)  (m 1/2):           5153.616699
Right Ascen at Week(rad):   0.1046903688E+001
Argument of Perigee(rad):   0.662592815
Mean Anom(rad):            -0.6815327587E+000
Af0(s):                     0.7534027100E-004
Af1(s/s):                   0.3637978807E-011
week:                        338

******** Week  338 almanac for PRN-04 ********
ID:                         04
Health:                     000
Eccentricity:               0.7454395294E-002
Time of Applicability(s):  503808.0000
Orbital Inclination(rad):   0.9506869901
Rate of Right Ascen(r/s):  -0.8274630386E-008
SQRT(A)  (m 1/2):           5153.731934
Right Ascen at Week(rad):   0.2202285584E+001
Argument of Perigee(rad):   0.145160422
Mean Anom(rad):             0.2494106703E+001
Af0(s):                     0.1525878906E-003
Af1(s/s):                   0.1091393642E-010
week:                        338

******** Week  338 almanac for PRN-05 ********
ID:                         05
Health:                     000
Eccentricity:               0.6813049316E-002
Time of Applicability(s):  503808.0000
Orbital Inclination(rad):   0.9380256565
Rate of Right Ascen(r/s):  -0.8103194673E-008
SQRT(A)  (m 1/2):           5153.600586
Right Ascen at Week(rad):   0.8525652499E-002
Argument of Perigee(rad):   1.039268613
Mean Anom(rad):             0.2222819804E+001
Af0(s):                    -0.5369186401E-003
Af1(s/s):                   0.9094947018E-010
week:                        338

******** Week  338 almanac for PRN-06 ********
ID:                         06
Health:                     000
Eccentricity:               0.5989551544E-002
Time of Applicability(s):  503808.0000
Orbital Inclination(rad):   0.9338311778
Rate of Right Ascen(r/s):  -0.8046049436E-008
```

```
******** Week  338 almanac for PRN-17 ********
ID:                         17
Health:                     000
Eccentricity:               0.1850128174E-002
Time of Applicability(s):  503808.0000
Orbital Inclination(rad):   0.9602504016
Rate of Right Ascen(r/s):  -0.7771752296E-008
SQRT(A)  (m 1/2):           5153.607910
Right Ascen at Week(rad):   0.1135503812E+001
Argument of Perigee(rad):   2.761678867
Mean Anom(rad):             0.1243646461E+001
Af0(s):                     0.5245208740E-004
Af1(s/s):                   0.7275957614E-011
week:                        338

******** Week  338 almanac for PRN-18 ********
ID:                         18
Health:                     000
Eccentricity:               0.6727695465E-002
Time of Applicability(s):  503808.0000
Orbital Inclination(rad):   0.9593455926
Rate of Right Ascen(r/s):  -0.7920329914E-008
SQRT(A)  (m 1/2):           5153.615723
Right Ascen at Week(rad):  -0.3008347547E+001
Argument of Perigee(rad):  -2.692015317
Mean Anom(rad):             0.2025385691E+001
Af0(s):                    -0.2212524414E-003
Af1(s/s):                  -0.3637978807E-011
week:                        338

******** Week  338 almanac for PRN-19 ********
ID:                         19
Health:                     000
Eccentricity:               0.3172397614E-002
Time of Applicability(s):  503808.0000
Orbital Inclination(rad):   0.9582130834
Rate of Right Ascen(r/s):  -0.7851755629E-008
SQRT(A)  (m 1/2):           5153.519531
Right Ascen at Week(rad):   0.1195303221E+001
Argument of Perigee(rad):  -1.351585753
Mean Anom(rad):             0.6873443587E+000
Af0(s):                    -0.2098083496E-004
Af1(s/s):                   0.0000000000E+000
week:                        338

******** Week  338 almanac for PRN-20 ********
ID:                         20
Health:                     000
Eccentricity:               0.2719879150E-002
Time of Applicability(s):  503808.0000
Orbital Inclination(rad):   0.9589381290
Rate of Right Ascen(r/s):  -0.7943188009E-008
SQRT(A)  (m 1/2):           5153.494141
Right Ascen at Week(rad):  -0.3061130568E+001
Argument of Perigee(rad):   1.330866152
Mean Anom(rad):             0.1891749225E+001
Af0(s):                    -0.3242492676E-004
Af1(s/s):                   0.0000000000E+000
week:                        338
******** Week  338 almanac for PRN-21 ********
ID:                         21
Health:                     000
Eccentricity:               0.1067066193E-001
Time of Applicability(s):  503808.0000
Orbital Inclination(rad):   0.9442814219
Rate of Right Ascen(r/s):  -0.8331775623E-008
SQRT(A)  (m 1/2):           5153.672363
Right Ascen at Week(rad):   0.2223138884E+001
Argument of Perigee(rad):  -3.021145201
Mean Anom(rad):            -0.2915601256E+001
Af0(s):                     0.6675720215E-005
Af1(s/s):                   0.3637978807E-011
week:                        338

******** Week  338 almanac for PRN-22 ********
ID:                         22
Health:                     000
Eccentricity:               0.4838943481E-002
Time of Applicability(s):  503808.0000
Orbital Inclination(rad):   0.9568528739
Rate of Right Ascen(r/s):  -0.7954617056E-008
SQRT(A)  (m 1/2):           5153.637207
```

```
SQRT(A)  (m 1/2):           5153.546875
Right Ascen at Week(rad):   0.1104721207E+001
Argument of Perigee(rad):  -1.852165330
Mean Anom(rad):            -0.2768151098E+001
Af0(s):                     0.3337860107E-003
Af1(s/s):                   0.3274180926E-010
week:                        338

******** Week  338 almanac for PRN-07 ********
ID:                         07
Health:                     000
Eccentricity:               0.1173067093E-001
Time of Applicability(s):  503808.0000
Orbital Inclination(rad):   0.9353771428
Rate of Right Ascen(r/s):  -0.7977475151E-008
SQRT(A)  (m 1/2):           5158.748047
Right Ascen at Week(rad):   0.1078280261E+001
Argument of Perigee(rad):  -1.852276558
Mean Anom(rad):            -0.1709250452E+001
Af0(s):                     0.4978179932E-003
Af1(s/s):                   0.7275957614E-011
week:                        338

******** Week  338 almanac for PRN-08 ********
ID:                         08
Health:                     000
Eccentricity:               0.9485721588E-002
Time of Applicability(s):  503808.0000
Orbital Inclination(rad):   0.9716653758
Rate of Right Ascen(r/s):  -0.8023191341E-008
SQRT(A)  (m 1/2):           5153.605469
Right Ascen at Week(rad):  -0.9177418316E+000
Argument of Perigee(rad):   2.638955536
Mean Anom(rad):            -0.2749293171E+001
Af0(s):                    -0.5722045898E-004
Af1(s/s):                   0.0000000000E+000
week:                        338

******** Week  338 almanac for PRN-09 ********
ID:                         09
Health:                     000
Eccentricity:               0.1754999161E-001
Time of Applicability(s):  503808.0000
Orbital Inclination(rad):   0.9591059081
Rate of Right Ascen(r/s):  -0.8160339911E-008
SQRT(A)  (m 1/2):           5153.589355
Right Ascen at Week(rad):  -0.9957857257E+000
Argument of Perigee(rad):   1.218319300
Mean Anom(rad):            -0.3069442377E+001
Af0(s):                     0.8583068848E-005
Af1(s/s):                   0.0000000000E+000
week:                        338

******** Week  338 almanac for PRN-10 ********
ID:                         10
Health:                     000
Eccentricity:               0.7071018219E-002
Time of Applicability(s):  503808.0000
Orbital Inclination(rad):   0.9753325487
Rate of Right Ascen(r/s):  -0.7783181344E-008
SQRT(A)  (m 1/2):           5153.513184
Right Ascen at Week(rad):  -0.3031559118E+001
Argument of Perigee(rad):   0.389809385
Mean Anom(rad):             0.4755587617E+000
Af0(s):                     0.7915496826E-004
Af1(s/s):                   0.0000000000E+000
week:                        338
******** Week  338 almanac for PRN-11 ********
ID:                         11
Health:                     000
Eccentricity:               0.5326271057E-002
Time of Applicability(s):  503808.0000
Orbital Inclination(rad):   0.8980762428
Rate of Right Ascen(r/s):  -0.8766079428E-008
SQRT(A)  (m 1/2):           5153.623047
Right Ascen at Week(rad):   0.2042988270E+001
Argument of Perigee(rad):   0.353177355
Mean Anom(rad):            -0.2209039069E+001
Af0(s):                     0.3080368042E-003
Af1(s/s):                   0.3637978807E-011
week:                        338

******** Week  338 almanac for PRN-13 ********
ID:                         13
Health:                     000
Eccentricity:               0.2675056458E-002
Time of Applicability(s):  503808.0000
Orbital Inclination(rad):   0.9908880726
Rate of Right Ascen(r/s):  -0.7554600394E-008
SQRT(A)  (m 1/2):           5153.545410
Right Ascen at Week(rad):  -0.1983034938E+001
Argument of Perigee(rad):   1.077524881
Mean Anom(rad):             0.4898252324E+000
Af0(s):                     0.4196166992E-004
Af1(s/s):                   0.3637978807E-011
week:                        338

******** Week  338 almanac for PRN-14 ********
ID:                         14
Health:                     000
Eccentricity:               0.2383232117E-002
Time of Applicability(s):  503808.0000
```

```
Right Ascen at Week(rad):  -0.3000007650E+001
Argument of Perigee(rad):  -1.560234854
Mean Anom(rad):             0.2937865324E+000
Af0(s):                     0.6961822510E-004
Af1(s/s):                   0.3637978807E-011
week:                        338

******** Week  338 almanac for PRN-23 ********
ID:                         23
Health:                     000
Eccentricity:               0.4168987274E-002
Time of Applicability(s):  503808.0000
Orbital Inclination(rad):   0.9673390706
Rate of Right Ascen(r/s):  -0.7794610391E-008
SQRT(A)  (m 1/2):           5153.545898
Right Ascen at Week(rad):  -0.2007488375E+001
Argument of Perigee(rad):   2.425412003
Mean Anom(rad):            -0.3112172130E+000
Af0(s):                     0.1497268677E-003
Af1(s/s):                   0.0000000000E+000
week:                        338

******** Week  338 almanac for PRN-24 ********
ID:                         24
Health:                     000
Eccentricity:               0.8968830109E-002
Time of Applicability(s):  503808.0000
Orbital Inclination(rad):   0.9609634630
Rate of Right Ascen(r/s):  -0.8148910863E-008
SQRT(A)  (m 1/2):           5153.736816
Right Ascen at Week(rad):   0.2235089029E+001
Argument of Perigee(rad):  -0.963331321
Mean Anom(rad):            -0.2050953286E+001
Af0(s):                     0.8678436279E-004
Af1(s/s):                   0.3637978807E-011
week:                        338

******** Week  338 almanac for PRN-25 ********
ID:                         25
Health:                     000
Eccentricity:               0.1258659363E-001
Time of Applicability(s):  503808.0000
Orbital Inclination(rad):   0.9524007343
Rate of Right Ascen(r/s):  -0.8228914196E-008
SQRT(A)  (m 1/2):           5153.640625
Right Ascen at Week(rad):  -0.1049718108E+001
Argument of Perigee(rad):  -1.387248560
Mean Anom(rad):            -0.2370041139E+001
Af0(s):                    -0.1010894775E-003
Af1(s/s):                   0.3637978807E-010
week:                        338

******** Week  338 almanac for PRN-26 ********
ID:                         26
Health:                     000
Eccentricity:               0.1693630219E-001
Time of Applicability(s):  503808.0000
Orbital Inclination(rad):   0.9890604783
Rate of Right Ascen(r/s):  -0.7577458489E-008
SQRT(A)  (m 1/2):           5153.619141
Right Ascen at Week(rad):  -0.1981979203E+001
Argument of Perigee(rad):   0.751871171
Mean Anom(rad):            -0.1201831628E+001
Af0(s):                    -0.4005432129E-004
Af1(s/s):                  -0.7275957614E-011
week:                        338

******** Week  338 almanac for PRN-27 ********
ID:                         27
Health:                     000
Eccentricity:               0.1979541779E-001
Time of Applicability(s):  503808.0000
Orbital Inclination(rad):   0.9569487477
Rate of Right Ascen(r/s):  -0.8160339911E-008
SQRT(A)  (m 1/2):           5153.632812
Right Ascen at Week(rad):  -0.1018339662E+001
Argument of Perigee(rad):  -1.955382088
Mean Anom(rad):             0.2340130386E+001
Af0(s):                     0.3623962402E-004
Af1(s/s):                   0.0000000000E+000
week:                        338

******** Week  338 almanac for PRN-28 ********
ID:                         28
Health:                     000
Eccentricity:               0.1103687286E-001
Time of Applicability(s):  503808.0000
Orbital Inclination(rad):   0.9605380230
Rate of Right Ascen(r/s):  -0.7840326581E-008
SQRT(A)  (m 1/2):           5153.611816
Right Ascen at Week(rad):   0.1067565990E+000
Argument of Perigee(rad):  -2.285471459
Mean Anom(rad):             0.1179785523E+001
Af0(s):                     0.3337860107E-004
Af1(s/s):                   0.0000000000E+000
week:                        338

******** Week  338 almanac for PRN-29 ********
ID:                         29
Health:                     000
Eccentricity:               0.9426593781E-002
Time of Applicability(s):  503808.0000
```

```
Orbital Inclination(rad):    0.9850996920
Rate of Right Ascen(r/s):   -0.7600316584E-008
SQRT(A)  (m 1/2):            5153.575195
Right Ascen at Week(rad):   -0.1995651331E+001
Argument of Perigee(rad):   -1.970293835
Mean Anom(rad):             -0.3819541005E+000
Af0(s):                     -0.1907348633E-004
Af1(s/s):                    0.0000000000E+000
week:                         338

******** Week  338 almanac for PRN-15 ********
ID:                          15
Health:                      000
Eccentricity:                0.9411811829E-002
Time of Applicability(s):   503808.0000
Orbital Inclination(rad):    0.9577816513
Rate of Right Ascen(r/s):   -0.8194627053E-008
SQRT(A)  (m 1/2):            5153.654785
Right Ascen at Week(rad):    0.2259011040E+001
Argument of Perigee(rad):    2.552085260
Mean Anom(rad):             -0.2635566247E+001
Af0(s):                      0.5674362183E-003
Af1(s/s):                    0.7275957614E-011
week:                         338

******** Week  338 almanac for PRN-16 ********
ID:                          16
Health:                      000
Eccentricity:                0.3179073334E-002
Time of Applicability(s):   503808.0000
Orbital Inclination(rad):    0.9624854596
Rate of Right Ascen(r/s):   -0.7840326581E-008
SQRT(A)  (m 1/2):            5153.612305
Right Ascen at Week(rad):    0.9702802990E-001
Argument of Perigee(rad):   -0.937181368
Mean Anom(rad):              0.2129707245E+001
Af0(s):                      0.2670288086E-004
Af1(s/s):                    0.3637978807E-011
week:                         338
```

```
Orbital Inclination(rad):    0.9858067612
Rate of Right Ascen(r/s):   -0.7600316584E-008
SQRT(A)  (m 1/2):            5153.652832
Right Ascen at Week(rad):   -0.2016310262E+001
Argument of Perigee(rad):   -0.970531593
Mean Anom(rad):              0.7153155397E+000
Af0(s):                      0.5369186401E-003
Af1(s/s):                    0.1091393642E-010
week:                         338

******** Week  338 almanac for PRN-30 ********
ID:                          30
Health:                      000
Eccentricity:                0.8715152740E-002
Time of Applicability(s):   503808.0000
Orbital Inclination(rad):    0.9446709092
Rate of Right Ascen(r/s):   -0.8023191341E-008
SQRT(A)  (m 1/2):            5153.534180
Right Ascen at Week(rad):    0.5430838769E-001
Argument of Perigee(rad):    1.292541724
Mean Anom(rad):              0.1525984314E+001
Af0(s):                      0.2574920654E-004
Af1(s/s):                    0.3637978807E-011
week:                         338
```

Appendix B Attitude Determination using the Standard Method (ADSM)

This method, devised by Dr Hodgart improves on the 'Attitude Determination by Direct Orthogonalisation' (ADDO) method presented in [Purivigraipong, 2000] and [Urhan, 2003]. It can incorporate information from as many measurements as are available whilst still maintaining the speed of the two-dimensional integer search. This improved method, which we have termed 'Attitude Determination using the Standard Method' (ADSM) was inspired by a method for single-axis attitude determination contained in [Wertz, 1978]. This algorithm formed the basis of the work presented in the author's transfer report, which was then improved on to form the method presented in Chapter 4. It is included in its entirety to allow comparison with the improved algorithm implemented by the author as part of this research.

B.1 Part I – Solving for the unknown baseline

Any arbitrary 3-vector $\mathbf{b}$ can be expressed as a linear combination of any two other 3-vectors providing that they are not collinear,

$$\mathbf{b} = \lambda_1 \mathbf{v}_1 + \lambda_2 \mathbf{v}_2 + \lambda_{12}(\mathbf{v}_1 \times \mathbf{v}_2) \qquad \textbf{B-1}$$

where $\mathbf{v}_1$ and $\mathbf{v}_2$ are double-differenced LOS vectors and $\mathbf{b}$ is the unknown baseline vector. Note that the third axis of the vector is described by the cross product of the two vectors.

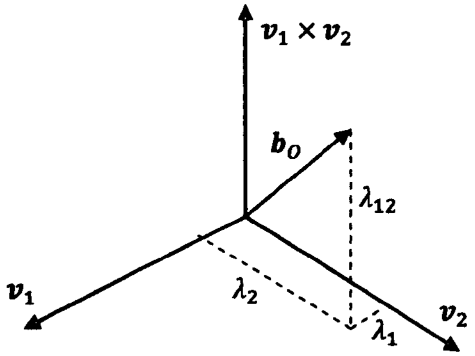

Figure B-1 Illustration of baseline vector equation

The coefficients $\lambda_1, \lambda_2, \lambda_{12}$ can be found from

$$\begin{aligned} \mathbf{b}^T \mathbf{v}_1 &= \lambda_1 \mathbf{v}_1^T \mathbf{v}_1 + \lambda_2 \mathbf{v}_2^T \mathbf{v}_1 \\ \mathbf{b}^T \mathbf{v}_2 &= \lambda_1 \mathbf{v}_1^T \mathbf{v}_2 + \lambda_2 \mathbf{v}_2^T \mathbf{v}_2 \end{aligned} \qquad \textbf{B-2}$$

or equivalently

$$\Delta \bar{r}_1 = \lambda_1 \mathbf{v}_1^T \mathbf{v}_1 + \lambda_2 \mathbf{v}_2^T \mathbf{v}_1 \qquad \textbf{B-3}$$

$$\Delta\bar{r}_2 = \lambda_1 \mathbf{v}_1^T \mathbf{v}_2 + \lambda_2 \mathbf{v}_2^T \mathbf{v}_2$$

Defining

$$\begin{aligned} a_{11} &= \mathbf{v}_1^T \mathbf{v}_1 \\ a_{22} &= \mathbf{v}_2^T \mathbf{v}_2 \\ a_{12} &= \mathbf{v}_1^T \mathbf{v}_2 \end{aligned} \tag{B-4}$$

leads to

$$\begin{aligned} \Delta\bar{r}_1 &= \lambda_1 a_{11} + \lambda_2 a_{12} \\ \Delta\bar{r}_2 &= \lambda_1 a_{12} + \lambda_2 a_{22} \end{aligned} \tag{B-5}$$

and rearranging for λ_1, λ_2 gives

$$\begin{aligned} \lambda_1 &= \frac{\Delta\bar{r}_1 a_{22} - \Delta\bar{r}_2 a_{12}}{a_{11}a_{22} - a_{12}^2} \\ \lambda_2 &= \frac{\Delta\bar{r}_2 a_{11} - \Delta\bar{r}_1 a_{12}}{a_{11}a_{22} - a_{12}^2} \end{aligned} \tag{B-6}$$

The third component λ_{12} can be determined, and the baseline vector $\mathbf{b}$ fully defined, by exploiting the known magnitude of $\mathbf{b}$ after determining λ_1 and λ_2. The component normal to the plane has a magnitude

$$\left\|\mathbf{b}_\perp\right\| = \sqrt{\left\|\mathbf{b}\right\|^2 - \lambda_1 \bar{r}_1 - \lambda_2 \bar{r}_2} \tag{B-7}$$

The third component λ_{12} is then given by

$$\lambda_{12} = \pm\sqrt{\frac{\left\|\mathbf{b}\right\|^2 - \lambda_1 \bar{r}_1 - \lambda_2 \bar{r}_2}{a_{11}a_{22} - a_{12}^2}} \tag{B-8}$$

Equation B-8 contains an ambiguity, requiring two solutions for $\mathbf{b}$ to be calculated,

$$\begin{aligned} \mathbf{b}^+ &= \lambda_1 \mathbf{v}_1 + \lambda_2 \mathbf{v}_2 + \left|\lambda_{12}\right|(\mathbf{v}_1 \times \mathbf{v}_2) \\ \mathbf{b}^- &= \lambda_1 \mathbf{v}_1 + \lambda_2 \mathbf{v}_2 - \left|\lambda_{12}\right|(\mathbf{v}_1 \times \mathbf{v}_2) \end{aligned} \tag{B-9}$$

Only one of the above solutions is correct. Further information is required to determine the correct solution.

B.2 Integer Search

The carrier phase measurements are ambiguous to a number of integer cycles. Therefore, the integer corrections to the carrier phase measurements must be determined. In a single epoch there is insufficient information to estimate the integers directly (a *float solution*) so an integer ambiguity search is conducted. Using the method described above the unknown baseline pointing can be estimated using just two measurements. This means that only two integers need to be determined in order to solve for the baseline pointing. Therefore a two dimensional integer search is performed. Trial measurements are constructed by applying an integer correction to the double-difference carrier phase measurements $\Delta\bar{r}_j$:

$$\begin{aligned}\Delta\tilde{r}_1 &= \Delta\bar{r}_1 - \Delta\tilde{N}_1 \\ \Delta\tilde{r}_2 &= \Delta\bar{r}_2 - \Delta\tilde{N}_2\end{aligned} \qquad \textbf{B-10}$$

where $\Delta\tilde{N}_1$ and $\Delta\tilde{N}_2$ are the trial integer ambiguities, and $\Delta\tilde{r}_1$ and $\Delta\tilde{r}_2$ are the trial corrected carrier phase measurements.

B.2.1 Solving for the baseline using the primary set

A two-dimension integer search is conducted over the range $\Delta N_{j,\min} \le \Delta\tilde{N}_j \le \Delta N_{j,\max}$ for $j = 1,2$. The trial integer ambiguities are used to calculate the trial parameters $\tilde{\lambda}_1$ and $\tilde{\lambda}_2$:

$$\begin{aligned}\tilde{\lambda}_1 &= \frac{\Delta\tilde{r}_1 a_{22} - \Delta\tilde{r}_2 a_{12}}{a_{11}a_{22} - a_{12}^2} \\ \tilde{\lambda}_2 &= \frac{\Delta\tilde{r}_2 a_{11} - \Delta\tilde{r}_1 a_{12}}{a_{11}a_{22} - a_{12}^2}\end{aligned} \qquad \textbf{B-11}$$

from which the third trial parameter can be solved for using

$$\tilde{\lambda}_{12} = \pm\sqrt{\frac{\left\|\mathbf{b}_{(B)}\right\|^2 - \tilde{\lambda}_1\Delta\tilde{r}_1 - \tilde{\lambda}_2\Delta\tilde{r}_2}{a_{11}a_{22} - a_{12}^2}} \qquad \textbf{B-12}$$

leading to two equations for $\hat{\mathbf{b}}_{(O)}$

$$\begin{aligned}\tilde{\mathbf{b}}_{(O)}^{+} &= \tilde{\lambda}_1\mathbf{v}_1 + \tilde{\lambda}_2\mathbf{v}_2 + \left|\tilde{\lambda}_{12}\right|(\mathbf{v}_1 \times \mathbf{v}_2) \\ \tilde{\mathbf{b}}_{(O)}^{-} &= \tilde{\lambda}_1\mathbf{v}_1 + \tilde{\lambda}_2\mathbf{v}_2 - \left|\tilde{\lambda}_{12}\right|(\mathbf{v}_1 \times \mathbf{v}_2)\end{aligned} \qquad \textbf{B-13}$$

Measurement errors can affect the trial pointing solutions provided by Equation B-13. The trial baseline solutions can be improved by incorporating the third measurement $\Delta\bar{r}_3$. From,

$$\begin{aligned}\mathbf{v}_3^T\tilde{\mathbf{b}}_{(O)}^{+} &= \Delta\bar{r}_3 - \Delta\tilde{N}_3 = \tilde{\lambda}_1\mathbf{v}_1^T\mathbf{v}_3 + \tilde{\lambda}_2\mathbf{v}_2^T\mathbf{v}_3 + \left|\tilde{\lambda}_{12}\right|(\mathbf{v}_1 \times \mathbf{v}_2)^T\mathbf{v}_3 \\ \mathbf{v}_3^T\tilde{\mathbf{b}}_{(O)}^{-} &= \Delta\bar{r}_3 - \Delta\tilde{N}_3 = \tilde{\lambda}_1\mathbf{v}_1^T\mathbf{v}_3 + \tilde{\lambda}_2\mathbf{v}_2^T\mathbf{v}_3 - \left|\tilde{\lambda}_{12}\right|(\mathbf{v}_1 \times \mathbf{v}_2)^T\mathbf{v}_3\end{aligned} \qquad \textbf{B-14}$$

the third integer ambiguity $\Delta\tilde{N}_3$ can be solved for using

$$\Delta\tilde{N}_3^+ = round\left(\Delta\bar{r}_3 - \mathbf{v}_3^T\tilde{\mathbf{b}}_{(O)}^+\right) \qquad \textbf{B-15}$$
$$\Delta\tilde{N}_3^- = round\left(\Delta\bar{r}_3 - \mathbf{v}_3^T\tilde{\mathbf{b}}_{(O)}^-\right)$$

and then the third measurement can be used to improve the estimate for the baseline pointing according to

$$\tilde{\mathbf{b}}_{(O)}^+ = \begin{bmatrix} \mathbf{v}_1^T \\ \mathbf{v}_2^T \\ \mathbf{v}_3^T \end{bmatrix}^{-1} \begin{bmatrix} \Delta\bar{r}_1 - \Delta\tilde{N}_1 \\ \Delta\bar{r}_2 - \Delta\tilde{N}_2 \\ \Delta\bar{r}_3 - \Delta\tilde{N}_3^+ \end{bmatrix} \qquad \textbf{B-16}$$
$$\tilde{\mathbf{b}}_{(O)}^- = \begin{bmatrix} \mathbf{v}_1^T \\ \mathbf{v}_2^T \\ \mathbf{v}_3^T \end{bmatrix}^{-1} \begin{bmatrix} \Delta\bar{r}_1 - \Delta\tilde{N}_1 \\ \Delta\bar{r}_2 - \Delta\tilde{N}_2 \\ \Delta\bar{r}_3 - \Delta\tilde{N}_3^- \end{bmatrix}$$

Both potential baseline solutions are placed in a list, along with their corresponding integer ambiguities. All of the entries in the list should be possible solutions to the baseline pointing and integer ambiguities, but one of them will be the correct solution. At this point not all the available measurements are used, and there is additional information to be gained from the remaining measurements in the secondary set.

B.2.2 Solution for the secondary set

By conducting an integer search for the primary set of measurements a list of potential solutions for the baseline pointing and integer ambiguities has been created. The next step is to use the additional information present in the measurements in the secondary set to improve upon the baseline pointing solution.

For each measurement in the secondary set, $\Delta\bar{r}_j$, the baseline pointing estimated from the primary set is used to solve for the corresponding integer ambiguity $\Delta\tilde{N}_j$

$$\Delta\tilde{N}_j^{(m)} = round\left(\Delta\bar{r}_j - \mathbf{v}_j^T\tilde{\mathbf{b}}_{(O)}^{(m)}\right) \qquad \textbf{B-17}$$

where the superscript (m) acts as an index to the list of potential solutions generated using the primary set. Using each extra measurement and its corresponding integer, in turn, an updated trial baseline pointing is calculated using:

$$\tilde{\mathbf{b}}_{(O)}^{(m)} = \left(\mathbf{H}_j^T\mathbf{H}_j\right)^{-1}\mathbf{H}_j^T\bar{\mathbf{r}} \qquad \textbf{B-18}$$

where

$$\mathbf{H}_j = \begin{bmatrix} \mathbf{v}_1^T \\ \mathbf{v}_2^T \\ \vdots \\ \mathbf{v}_j^T \end{bmatrix} \qquad \bar{\mathbf{r}} = \begin{bmatrix} \Delta\bar{r}_1 - \Delta\tilde{N}_1 \\ \Delta\bar{r}_2 - \Delta\tilde{N}_2 \\ \vdots \\ \Delta\bar{r}_j - \Delta\tilde{N}_j \end{bmatrix} \qquad \textbf{B-19}$$

and j is the additional measurement from the secondary set. Rather than recalculate the entire least squares estimation in Equation B-18 for each new measurement an iterative update procedure is performed that reduces the computational requirements.

B.2.3 Iterative Update Method

The first part of the procedure is to calculate the following parameters based on the measurements from the primary set:

$$\begin{aligned} \mathbf{G}_3 &= \sum_{i=1}^{3} \mathbf{v}_i \mathbf{v}_i^T \\ \bar{\mathbf{z}}_3 &= \sum_{i=1}^{3} \mathbf{v}_i \Delta\bar{r}_i \\ \mathbf{z}_3^{(m)} &= \bar{\mathbf{z}}_3 + \sum_{i=1}^{3} \mathbf{v}_i \Delta N_i^{(m)} \end{aligned} \qquad \textbf{B-20}$$

where the superscript (m) indicates that $\mathbf{z}_3$ must be calculated for each potential solution in the list generated using the primary set. Note that the first two equations in Equation B-20 are only dependent on the measurements and so can be precalculated prior to the integer search and then applied to the entire list of solutions.

For each measurement j in the secondary set calculate

$$\begin{aligned} \mathbf{G}_j &= \mathbf{G}_{j-1} + \mathbf{v}_j \mathbf{v}_j^T \\ \bar{\mathbf{z}}_j &= \bar{\mathbf{z}}_{j-1} + \mathbf{v}_j \Delta\bar{r}_j \end{aligned} \qquad \textbf{B-21}$$

and using the integer ambiguity calculated in Equation B-17, update each entry in the list according to

$$\mathbf{z}_j^{(m)} = \bar{\mathbf{z}}_j + \mathbf{v}_j \Delta N_j^{(m)} \qquad \textbf{B-22}$$

An improved estimate for each trial baseline pointing can then be determined using

$$\tilde{\mathbf{b}}_{j(0)}^{(m)} = \mathbf{G}_j^{-1} \mathbf{z}_j^{(m)} \qquad \textbf{B-23}$$

Finally, in order to rank each trial solution, a cost is calculated by comparing the length of the baseline calculated in Equation B-23 with the known baseline length,

$$\varepsilon^{(m)} = \left| \left\| \mathbf{b}_{(B)} \right\| - \left\| \widetilde{\mathbf{b}}^{(m)}_{j(O)} \right\| \right| \qquad \text{B-24}$$

where the correct baseline estimate should have the length closest (allowing for measurement noise) to the body-referenced baseline. This leads to the correct solution being ranked at the top of the list of potential solutions.

B.2.4 Summary

At this point a list of potential solutions has been constructed. The solutions in the list are ranked according to the cost function given in Equation B-24, so that ideally the correct solution is at the top of the list. In the presence of errors it is likely that the correct solution is near the top of the list, but not at the very top. Therefore additional information is required in order to identify the correct solution in the list.

B.3 Part II – Combining candidate baseline solutions

The method outlined above called Part I, is run for each available baseline, generating a list of potential baseline vectors for each baseline. In Part II of the algorithm, the lists from two baselines are combined by selecting pairs of solutions (one from each list) and calculating an additional cost function based on the relative geometry of the baselines.

If the relative geometry of the antennas remains constant i.e. they are mounted on a rigid platform, then the pre-surveyed antenna positions can be used to calculate the baseline vectors in body-referenced coordinates. These baseline vectors will have a known relative geometry. This can be used to help identify the correct solution in the multiple lists from Part I by combining the solutions from different lists and comparing their relative geometry with the known relative geometry of the body-referenced baselines.

B.3.1 Virtual Baseline Method

This method, presented in [Purivigraipong, 2000] uses the known geometry of two arbitrary baselines to calculate a virtual baseline. The virtual baseline is defined as

$$\Delta\mathbf{b}_{12(B)} = \mathbf{b}_{1(B)} - \mathbf{b}_{2(B)} \qquad \text{B-25}$$

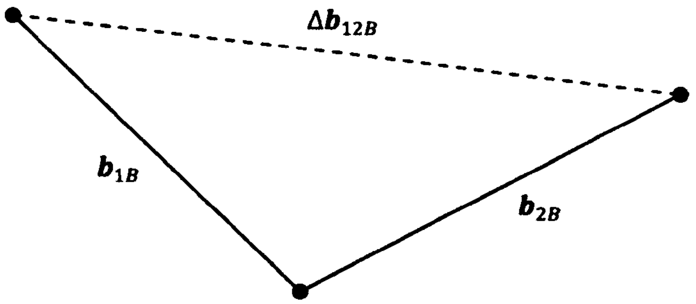

Figure B-2 Virtual Baseline

Next a potential solution from the list for baseline 1 and a potential solution from the list for baseline 2 are selected. Using these values a trial virtual baseline can be calculated according to:

$$\Delta\tilde{\mathbf{b}}_{12(O)} = \tilde{\mathbf{b}}_{1(O)} - \tilde{\mathbf{b}}_{2(O)} \tag{B-26}$$

A goodness of fit test can then be conducted by comparing the lengths of the known virtual baseline the trial virtual baseline:

$$\varepsilon = \left|\Delta\tilde{\mathbf{b}}_{12(O)} - \Delta\tilde{\mathbf{b}}_{12(B)}\right| \tag{B-27}$$

The two potential baseline solutions $\tilde{\mathbf{b}}_{1(O)}$ and $\tilde{\mathbf{b}}_{2(O)}$ are then placed in a second list of candidate baseline pairs. Each candidate pair is ranked according to the sum of the cost calculated for each potential baseline solution in Equation B-24 and the cost calculated in Equation B-27. This method can be extended to any number of baselines by taking each possible pairing and using the virtual baseline to calculate a cost.

B.4 Part III – Solving for Attitude

For each entry in the list generated in Part II the estimated baseline vectors $\tilde{\mathbf{b}}^{(m)}_{1(O)},\ldots,\tilde{\mathbf{b}}^{(m)}_{l(O)}$ are used to estimate the attitude matrix $\hat{\mathbf{A}}$, where the superscript (m) indicates an index to the list. Methods for estimating the attitude from a set of vectors are given in Chapter 2. Using the estimated attitude a cost for each entry in the list can be calculated from

$$\varepsilon^{(m)} = \sum\left\|\tilde{\mathbf{b}}^{(m)}_{i(O)} - \hat{\mathbf{A}}^{(m)}\mathbf{b}^{(m)}_{i(B)}\right\|^2 \tag{B-28}$$

where the most likely solution is the entry in the list that minimises the cost when using all available baselines.

B.5 Conclusions

This method was implemented and tested during the initial work conducted as part of this research and the results are documented in the author's transfer report. The main conclusion of the testing was that this method provided an improvement on the ADDO method implemented in [Purivigraipong, 2000]. However, it still had the problem that for a single epoch the solution that minimises the cost is not necessarily the correct solution. Therefore further work was undertaken to build on the above method in order to provide a robust integer ambiguity resolution algorithm. This work resulted in the method presented in Chapter 4.

Appendix C Orbit-Referenced Frame (ORF)

In order to estimate the attitude the LOS vectors logged from the SGR-20 must be rotated from the standard WGS-84 reference frame into the orbit-referenced frame described in Chapter 2.

Assuming that the SGR-20's position $\mathbf{x}_{\mathrm{WGS\text{-}84}}$ and velocity $\mathbf{x}'_{\mathrm{WGS\text{-}84}}$ in the WGS-84 reference frame are known, the velocity vector is corrected to account for the rotation of the Earth. The corrected velocity is calculated using

$$\mathbf{x}'^{*}_{\mathrm{WGS\text{-}84}} = \mathbf{x}'_{\mathrm{WGS\text{-}84}} + \left(\omega_{Earth} \times \mathbf{x}_{\mathrm{WGS\text{-}84}}\right) \qquad \text{C-1}$$

where $\omega_{Earth} = 7.2921151467 \times 10^{-5}$ radians/second is the Earth rotation rate. The basis vectors of the orbit-referenced frame are then calculated as

$$\hat{\mathbf{R}} = -\frac{\mathbf{x}_{\mathrm{WGS\text{-}84}}}{\left\|\mathbf{x}_{\mathrm{WGS\text{-}84}}\right\|} \quad \hat{\mathbf{W}} = -\frac{\mathbf{x}_{\mathrm{WGS\text{-}84}} \times \mathbf{x}'^{*}_{\mathrm{WGS\text{-}84}}}{\left\|\mathbf{x}_{\mathrm{WGS\text{-}84}} \times \mathbf{x}'^{*}_{\mathrm{WGS\text{-}84}}\right\|} \quad \hat{\mathbf{S}} = \hat{\mathbf{W}} \times \hat{\mathbf{R}} \qquad \text{C-2}$$

which can be used to form a rotation matrix

$$\mathbf{T} = \left\lfloor \hat{\mathbf{R}} \middle| \hat{\mathbf{S}} \middle| \hat{\mathbf{W}} \right\rfloor \qquad \text{C-3}$$

which defines the rotation between the WGS-84 and Orbit-referenced frames

$$\mathbf{s}_{i,j(O)} = \mathbf{T}\mathbf{s}_{i,j(WGS-84)} \qquad \text{C-4}$$

When post-processing the LOS vectors logged in the GPS binary log are stored in the WGS-84 frame and the required rotation is calculated using a MATLAB script. For real-time attitude determination the rotation is calculated onboard the SGR-20 using the most recent position and velocity solution. Testing has shown that using the GPS position and velocity vectors to calculate the orbit-referenced frame matches the orbit-referenced frame used by the ADCS (which is derived from NORAD two-line elements) to 0.009 degrees.

Experiment log

The following table contains details of each in-orbit experiment conducted on the Topsat microsatellite at the time of writing. In-orbit experiments are ongoing.

Date	GPS Week	GPS Second	Epoch (UTC)	EHS Start (Mins from epoch)	IMU Start (Mins from Epoch)	EHS End (Mins from Epoch)	IMU End (Mins from Epoch)	El Mask	Code Version	Mode	Notes
09/02/2007	1413	478677	12:57:43		00:12:17		00:24:02	0	2.81_9	Data logging	1
22/02/2007	1415	411740	18:22:20	-7.42	00:12:10	32.42	00:24:05	0	2.81_9	Data logging	
27/02/2007	1416	215600	11:53:20	-5.42	00:14:25	34.42	00:26:05	0	2.81_9	Data logging	
01/03/2007	1416	391909	12:51:49	-5.07	00:14:41	34.77	00:26:25	0	2.81_9	Data logging	
01/05/2007	1425	238120	18:08:40	-5.58	00:14:20	34.25	00:25:59	0	2.81_9	Data logging	
09/05/2007	1426	319860	16:51:00	-4.50	n/a	35.33	n/a	0	2.81_9	Data logging	
25/05/2007	1428	443100	03:04:46	-3.18	n/a	36.57	n/a	0	2.81_9	Data logging	
25/05/2007	1428	496030	17:46:56	-5.35	n/a	34.40	n/a	0	2.81_9	Data logging	
26/05/2007	1428	528947	02:55:33	-4.05	n/a	35.78	n/a	0	2.81_9	Data logging	
26/05/2007	1428	581681	17:34:27	-2.87	n/a	36.88	n/a	0	2.81_9	Data logging	
20/06/2007	1432	280488	05:54:34	0.18	00:19:56	39.93	00:31:40	10	2.81_9	Data logging	2
04/07/2007	1434	297243	10:34:03	-6.30	00:13:27	33.45	00:25:09	10	2.81_9	Data logging	
10/07/2007	1435	231247	16:14:07	-3.95	00:15:53	35.88	00:27:34	10	2.81_9	Data logging	
05/08/2008	1491	251899	21:58:05	2.25	00:17:10	37.25	00:28:55	5	2.84_15	Real-time Attitude	
14/08/2008	1492	423110	21:31:36	3.73	00:18:44	38.90	00:30:24	5	2.84_15	Real-time Attitude	
20/08/2008	1493	333530	20:38:36	1.73	00:16:39	36.90	00:28:24	5	2.84_15	Real-time Attitude	
09/12/2008	1509	244460	19:54:06	1.32	00:16:09	36.23	00:27:54	5	2.84_15	Real-time Attitude	
11/12/2008	1509	404300	16:18:06	2.32	00:17:09	37.32	00:28:54	5	2.84_15	Real-time Attitude	

15/12/2008	1510	149030	17:23:36	1.82	00:16:39	36.90	00:28:24	5	2.84_15	Real-time Attitude	
18/12/2008	1510	409453	17:43:59	1.43	00:16:16	36.52	00:28:01	5	2.84_15	Real-time Attitude	
06/01/2009	1513	241489	19:04:34	0.77	00:15:41	35.93	00:27:26	5	2.84_15	Real-time Attitude	
08/01/2009	1513	407327	17:08:32	1.80	00:16:48	36.97	00:28:27	5	2.84_15	Real-time Attitude	
13/01/2009	1514	234830	17:13:35	1.75	n/a	36.75	n/a	5	2.84_15	Real-time Attitude	
15/01/2009	1514	382820	10:20:05	0.25	n/a	35.25	n/a	5	2.84_15	Real-time Attitude	3
20/01/2009	1515	210650	10:30:35	-0.25	n/a	34.75	n/a	5	2.84_15	Real-time Attitude	4
22/01/2009	1515	389713	12:14:58	-24.72	n/a	10.28	n/a	5	2.84_15	Real-time Attitude	5
24/02/2009	1520	212953	11:08:58	1.45	n/a	36.37	n/a	5	2.84_15	Real-time Attitude	
26/02/2009	1520	360877	04:14:22	0.97	n/a	35.97	n/a	5	2.84_15	Real-time Attitude	6

Notes:

1. This first upload of the SGR-20 flight software only included the modifications required to log single-difference carrier phase measurements via Packet 0x65. This experiment highlighted a problem with the processor loading that meant that when the SGR-20 was tracking on all twenty four channels the spare processing was reaching zero, and this was resulting in lost data from Packet 0x65. This issue was fixed and the code re-uploaded.
2. In this experiment the SGR-20 was configured with a single master and a single slave antenna forming one baseline. This allowed the receiver to track up to twelve satellites on this single baseline. The single-difference carrier phase measurements were logged via Packet 0x65 and the data was used in post-processing to examine the possibility of calculating a carrier-phase only float solution. The data was also shared with Peter Buist of Delft University who was working on a constrained LAMBDA method at the time. However, due to the lack of code-phase measurements and the limited number of epochs with common satellites he was not able to successfully use the data.

Appendix D Packet formats

All communication with the SGR-20 GPS receiver is performed via the SGR Binary Packet Protocol (SBPP) format. This packet format is used for both commanding the GPS receiver and for logging the data output.

As part of the implementation of the new flight software for real-time onboard GPS attitude determination a number of new SBPP commands and data logging packets were implemented. This appendix details all the new commands and data packets implemented, including a description of their function and details of their structure.

D.1 Attitude commands

The following packets were implemented to allow commanding and testing of the onboard attitude determination algorithms.

D.1.1 Attitude setup command (0xdc)

The Attitude Setup Command (0xdc) is used to command the mode of the GPS attitude code. Using this command the code can be set to operate in either an integer ambiguity resolution only mode (for testing), or a nominal three-axis attitude mode (which performs integer ambiguity resolution when necessary, and attitude tracking when initialised). The attitude code can be enabled or disabled and the assumed standard deviation of the measurement noise can be configured. The code can also be commanded to use test data input via command (0xdf) – the format of which is shown in Table D-2.

Table D-1 Format of attitude setup command (0xdc)

Byte Index	Type	Description	Units
0	byte	Use Test Data flag 0 - Use real data 1 - Use Test data	-
1	byte	Run Attitude Flag 0 – Disable GPS attitude code 1 – Enable GPS attitude code	-
2	byte	Select mode of attitude code 0 – Integer Ambiguity Resolution Test Mode 1 – Three Axis Attitude Mode	-
3-6	float	Assumed carrier phase measurement noise standard deviation	Metres

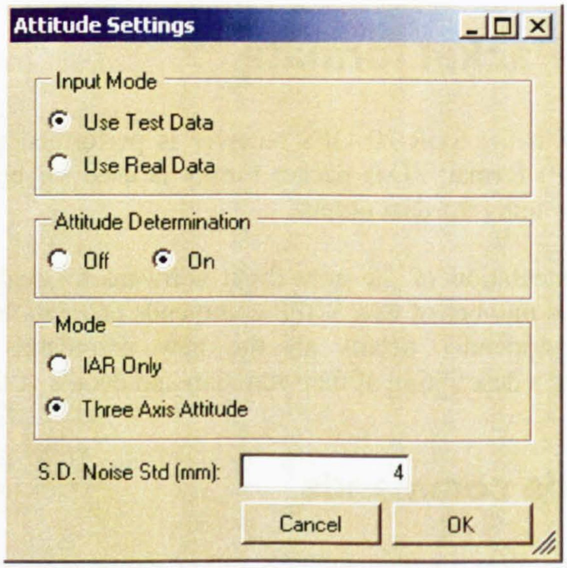

Attitude Settings

Input Mode

● Use Test Data

○ Use Real Data

Attitude Determination

○ Off ● On

Mode

○ IAR Only

● Three Axis Attitude

S.D. Noise Std (mm): 4

Figure D-1 IAR setup window allows configuration of attitude determination on SGR-20

D.1.2 Attitude test data command (0xdf)

The attitude test data command (0xdf) allows test data to be fed into the GPS attitude determination code via the communications interfaces of the SGR-20. This test data is input into the algorithms in place of real data, and permits testing of the entire algorithm since the test data follow the same route through the algorithms that real data would. This command is typically used to permit hardware-in-the-loop simulation which is described in the next section. It also permits data logged in orbit to be post-processed via an SGR-20 on the ground.

Table D-2 Format of attitude test data command (0xdf)

Byte Index	**Type**	**Description**	**Units**
0-7	double	GPS Seconds	Seconds
8	Byte	Number of measurements on Baseline 1	-
9	byte	Number of measurements on Baseline 2	-
10	byte	Number of measurements on Baseline 3	-
The following bytes are repeated for each of the three baselines and depend on the number of measurement on each baselines			
11-14	float	Accumulated Carrier Phase Difference Measurement	Metres
15-16	Short	LOS X Component in ORF (*32767)	-
17-18	Short	LOS Y Component in ORF (*32767)	-
19-20	Short	LOS Z Component in ORF (*32767)	-
21-22	short	PRN of satellite	-

D.2 Attitude data packets

The following packets were implemented to allow in-orbit logging of the GPS carrier phase measurements and the status of the onboard attitude determination algorithms.

D.2.1 Single-difference accumulated carrier phase (0x65)

As part of this work a new accumulated carrier phase measurement packet (Packet 0x65) was implemented to simplify the post-processing of the measurements in MATLAB. This packet contains single-difference accumulated carrier phase measurements for all three baselines. Each packet is time-stamped with the GPS seconds into Week that the raw measurements were latched. This aids synchronisation with the LOS vectors when post-processing the data in MATLAB. The length of time each satellite has been tracked is also included in the packet. This is useful for debugging purposes. The format of Packet 0x65 is given in the table below.

Table D-3 Format of accumulated carrier phase measurements packet (0x65)

Byte Index	Type	Description	Units
0-7	double	GPS Seconds	Seconds
The following bytes are repeated for each of the three baselines			
11-14	long	Measurement validity flags	-
15	byte	Number of measurements	-
The following bytes are repeated depending on the number of measurements on the baseline			
16	byte	PRN of satellite tracked	-
17-18	short	Length of time satellite has been tracked	Seconds
19-22	float	Accumulated carrier phase difference	Metres

Packets 0x10 (Position, Velocity and Time) and 0x41 (Line-of-sight Vectors) are also used in post-processing. The format of these packets is defined in [SSTL, 2009].

D.2.2 Attitude status packet (0x66)

Packet 0x66 (Attitude Status) was implemented to allow the status of the integer ambiguity resolution and attitude tracking algorithms to be monitored. This packet contains information about the status of the integer ambiguity resolution and attitude determination algorithms, including the current estimated integer ambiguities, the current baseline vectors in the orbit-referenced frame and the current attitude output as roll, pitch and yaw in degrees.

A corresponding display was also implemented in SGR-PC in order to parse the SBPP data and display the status of the GPS attitude solution. The format of Packet 0x66 is described in Table D-4 below.

Table D-4 Format of attitude status packet (0x66)

Byte Index	**Type**	**Description**	**Units**
0-7	double	GPS Seconds	Seconds
8-9	short	Integer ambiguity resolution status 0 – Integer Ambiguity Resolution not started 1 – 2 – 3 -	-
9-10	short	Attitude Tracking Status 0 - Attitude Off	-
The following bytes are repeated for each of the three baselines			
11-14	long	Integer Ambiguity Valid Flags	-
15-47	32*byte	Integer Ambiguities (one per byte)	-
48-51	float	Baseline X component in ORF	Metres
52-55	float	Baseline Y component in ORF	Metres
56-59	float	Baseline Z component in ORF	Metres
60-63	float	Roll estimate	Degrees
64-67	float	Pitch estimate	Degrees
68-71	float	Yaw estimate	Degrees
The following bytes are not repeated for each baseline			
72-73	short	Attitude Validity 0 – Invalid 1 - Valid	-
74-75	short	Number of times integer ambiguity algorithm has run since last power on	-

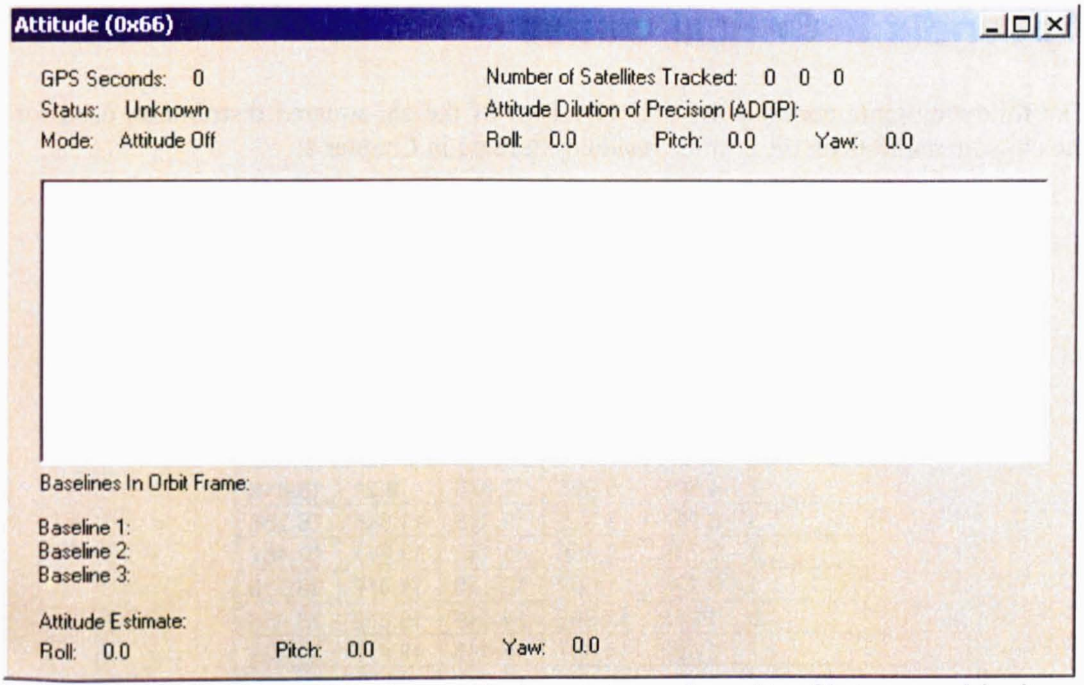

GPS Seconds: 0
Status: Unknown
Mode: Attitude Off

Number of Satellites Tracked: 0 0 0
Attitude Dilution of Precision (ADOP):
Roll: 0.0 Pitch: 0.0 Yaw: 0.0

Baselines In Orbit Frame:

Baseline 1:
Baseline 2:
Baseline 3:

Attitude Estimate:
Roll: 0.0 Pitch: 0.0 Yaw: 0.0

Figure D-2 SGR-PC modification to display status and results of integer ambiguity resolution and tracking

Appendix E Critical values

The following table contains the critical values of the chi-squared distribution used for the chi-squared tests on the attitude residuals defined in Chapter 4.

Table E-1 Critical values of the chi-squared distribution

	Probability of exceeding the critical value				
Degrees of freedom	**0.10**	**0.05**	**0.025**	**0.01**	**0.001**
1	2.706	3.841	5.024	6.635	10.828
2	4.605	5.991	7.378	9.21	13.816
3	6.251	7.815	9.348	11.345	16.266
4	7.779	9.488	11.143	13.277	18.467
5	9.236	11.07	12.833	15.086	20.515
6	10.65	12.592	14.449	16.812	22.458
7	12.02	14.067	16.013	18.475	24.322
8	13.36	15.507	17.535	20.09	26.125
9	14.68	16.919	19.023	21.666	27.877
10	15.99	18.307	20.483	23.209	29.588
11	17.28	19.675	21.92	24.725	31.264
12	18.55	21.026	23.337	26.217	32.91
13	19.81	22.362	24.736	27.688	34.528
14	21.06	23.685	26.119	29.141	36.123
15	22.31	24.996	27.488	30.578	37.697